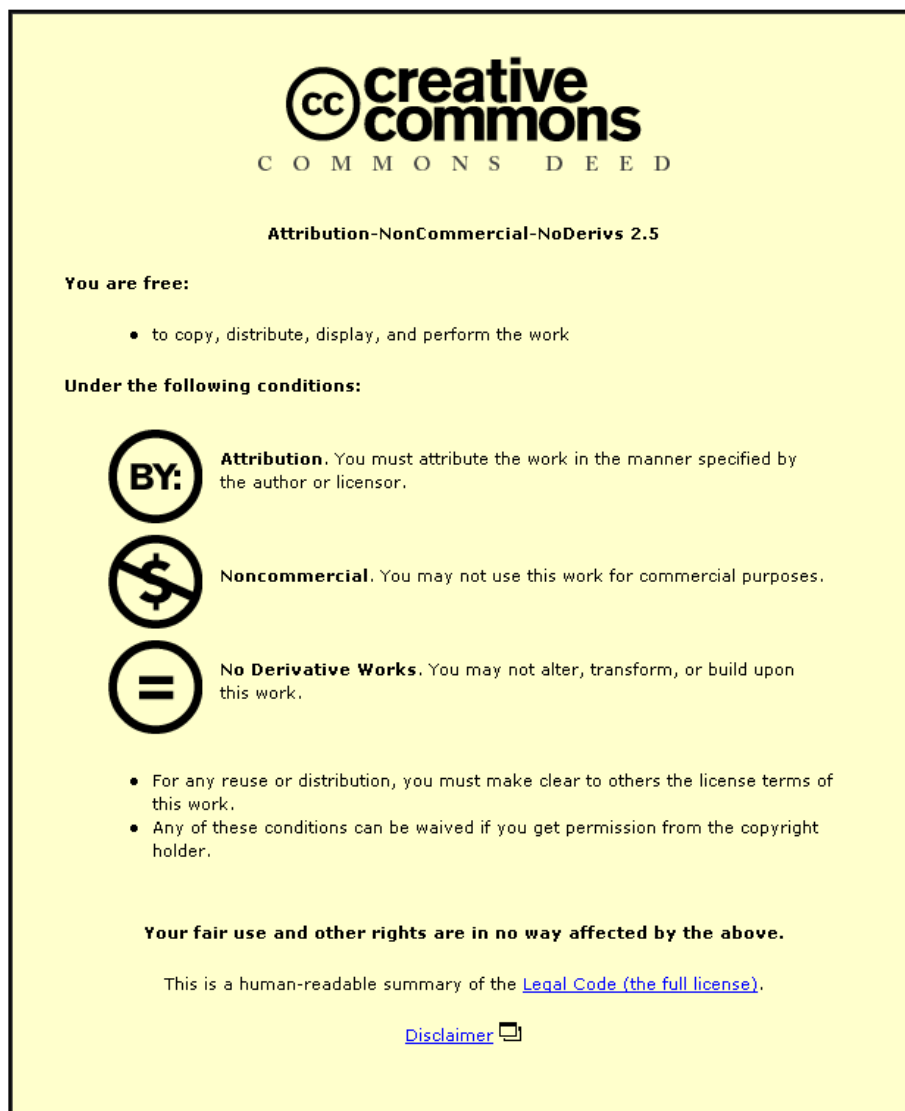


This item was submitted to Loughborough's Institutional Repository (<https://dspace.lboro.ac.uk/>) by the author and is made available under the following Creative Commons Licence conditions.



For the full text of this licence, please go to:
<http://creativecommons.org/licenses/by-nc-nd/2.5/>

**Comparative Performance of a Novel Oscillating Water Column Wave Energy
Converter**

**By
Julian Edward Sydney Minns**

A doctoral thesis

**Submitted in partial fulfilment of the requirements for the award of
Doctor of Philosophy of Loughborough University**

16th April 2012

© Julian Edward Sydney Minns 2012

Dedicated with love to
Pavčina, Eliška and Minka

Certificate of originality

This is to certify that I am responsible for the work submitted in this thesis, that the original work is my own except as specified in acknowledgements, footnotes or references, and that neither the thesis or the original work contained therein has been submitted to this or any other institution for a degree.

Signed:

Date: 3rd May 2012

Abstract

This thesis presents research which shows that a helically configured Oscillating Water Column (OWC) could deliver improved performance compared to a conventional tube OWC, whilst saving a significant amount of draft. It is anticipated that savings in the deployment costs for this compact machine will outweigh any additional manufacturing costs.

In order to prove the benefits of the helical concept, its performance relative to a conventional plain tube OWC was investigated in detail using scaled physical models. These models evolved during the course of the study, and refined models were developed. A variable impedance turbine simulator was also developed to test the models at their optimum conditions. The tests themselves were also refined leading to a high degree of confidence in the final result.

A mathematical model was also adapted to model the performance of the physical models, and to help understand the physical processes involved in the system.

With this series of improving physical models and tests, it has been shown that it is possible to achieve a 27% reduction in draft, with a 24% increase in power output.

Acknowledgements

I wish to thank the many people that facilitated his work that is presented in this thesis.

First of all, my supervisors: Simon Watson and Les Duckers whose friendship, guidance and encouragement throughout the course of my studies have brought me to this point. Simon also helped me to develop the mathematical model presented in Chapter 6.

Several masters students assisted in producing components for the test rig: AJ Ahluwalia manufactured the prototype helical models, Paul Marshall designed and built the wave probes, and Bob Haken updated the data acquisition system and integrated the spinning simulator. Bob Haken and Oliver Scheidegger helped run the Edinburgh tests.

The technicians at both Loughborough and Coventry Universities helped run and adjust equipment and produced high quality models, sensors as well as the spinning turbine simulator.

The Edinburgh University Wave Energy Group was welcoming hosts and helped me to set up and use their tank. Jamie Taylor and Stephen Salter were both very encouraging and gave insightful, timely advice about the tests and future development of the helical concept. Greg Payne, Gorge Lucas and Remy Pascal were also generous with their time and advice, and kept the tests running smoothly by quickly solving problems with the tank.

My IT Power Ltd colleagues have been very patient with me during the write up of the thesis, and I would like to especially mention Jamie O’Nians and Jeremy Thake who have been kind enough to let me take the time off to complete the work, and

Mark Leybourne who has helped me to understand many of the trickier parts of wave energy conversion.

My parents have given me endless encouragement throughout the PhD and their faith in my ability to complete my research gave me the stamina to see it through.

Finally I would not have been able to do this work without the support and sacrifice of my wife, Pavlína, and daughters, Eliška and Minka.

My grateful thanks go to all of these for giving me the chance to work on the most interesting and enjoyable project of my career to date.

Ned Minns, April 2012

Contents

Chapter 1: Introduction.....	1
1. Overview.....	1
1.1. Scope	1
1.2. Novelty	1
1.3. Thesis overview.....	2
1.4. Wave energy in context.....	2
1.5. OWC introduction	4
1.6. Novel helical design.....	8
Chapter 2: Background and Literature Review.....	11
2. Introduction	11
2.1. Climate change.....	11
2.2. Wave resource definition	15
2.3. Technology	22
2.4. Device modelling	35
2.5. Conclusions.....	54
Chapter 3: Flume Tests.....	56
3. Introduction	56
3.2. Power calculation	58
3.3. Turbine simulator calibration	60
3.4. Flume experiments	65
3.5. Conclusions.....	86
Chapter 4: Impedance Calibration of Models	89

4.	Introduction	89
4.1.	System impedance	89
4.2.	Scaling.....	90
4.3.	Objectives.....	91
4.4.	Determining the frictional resistance.....	92
4.5.	Results	98
4.6.	Conclusions.....	110
Chapter 5: Wide Tank Tests.....		114
5.	Introduction	114
5.1.	Equipment	114
5.2.	Test protocol.....	140
5.3.	Results of the first Edinburgh tests	143
5.4.	Results of the second Edinburgh tests	155
5.5.	Conclusions.....	176
Chapter 6: Mathematical Modelling of a model OWC		178
6.	Introduction	178
6.1.	Mathematical model	178
6.2.	Calculation of pneumatic power and efficiency.....	184
6.3.	Radiation damping and turbine damping	185
6.4.	Results and discussion.....	186
6.5.	Conclusions.....	196
Chapter 7: Conclusions and further research.....		198
7.	Introduction	198
7.1.	General.....	198

7.2.	Helical Configuration	198
7.3.	Spinning Simulator	199
7.4.	Mathematical Model	200
7.5.	Further Research.....	200
7.6.	Final Thoughts.....	201
	Appendix A: References.....	202
	Appendix B: Nomenclature and acronyms	209
	Appendix C: List of papers	212
	Appendix D: List of promising wave technologies	219

Chapter 1: Introduction

1. Overview

This thesis contains details of the PhD work carried out by the author, including an overview of wave energy in general and OWCs in particular; the results of a series of experiments to determine the performance of a novel OWC; and a mathematical model of the OWC models tested.

1.1. Scope

The primary goal of the PhD was to prove that a helically configured Oscillating Water Column (OWC) will deliver comparable performance to a conventional tube OWC, whilst saving a significant amount of draft. It is hoped that savings in the deployment costs and improvements to the capacity factor for this compact machine will outweigh any additional manufacturing costs due to incorporating helical fins.

In order to evaluate the benefits of the helical concept, it was investigated in detail using scaled physical models. A mathematical model was also adapted to model the performance of the physical models and provide insights into the way the concept functions.

With a series of improving physical models and test conditions, it has been shown that it is possible to achieve a 27% reduction in draft, with a 24% increase in power output.

A variable impedance turbine simulator was also developed to test the models at their optimum conditions.

1.2. Novelty

The novel aspect of the PhD is the configuration of the internal water path of the OWC, which is helical and will be described in detail later. The benefits of this design

were first publicly described by the author in 2008 at the World Renewable Energy Conference (Duckers et al 2008).

1.3. Thesis overview

Chapter 1 introduces the basic principles of OWCs and the novel helical concept, as well as a brief summary of the case for developing wave energy devices. Chapter 2 Elaborates on this background and contains a review of literature relevant to the modelling carried out in this thesis. Chapters 3, 4 and 5 describe experimental tests first in a flumes, and then in a wide tank. Chapter 4 also covers the scaling of the results and discusses some of the reasons for the improved performance of the helical design. Chapter 5 includes more on the scaling of the results and also describes a variable impedance turbine simulator. In Chapter 6 a mathematical model is described and finally the conclusions are given in Chapter 7

An Appendix listing promising Wave Energy Converters (WECs) has been included as Appendix D.

1.4. Wave energy in context

1.4.1. Climate

Northern Europe has some of the most accessible and copious wave energy available in the world as can be seen in Figure 1.1:

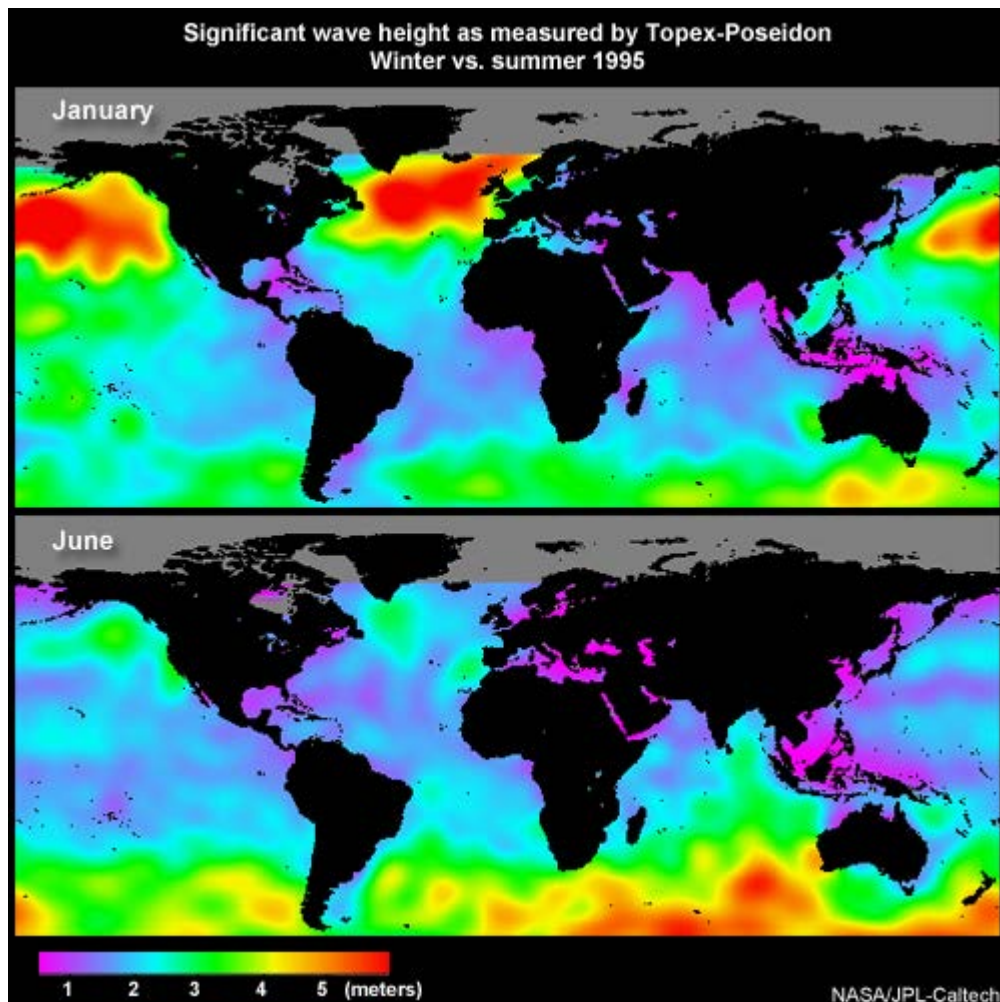


Figure 1.1 World wave energy resource from TOPEX. (eumetsat 2009).

Along with southern Australia and Portugal, the UK is ideally placed in the world, with an excellent wave climate relatively close to centres of population and the national grid. In addition, The Carbon Trust estimates that if the UK utilised all of the practicable wave energy that is available, it could produce about 50TWh/year which is equivalent to 14.5% of the UK's 2010 electricity consumption (Carbon Trust, 2011).

This is a goal well worth striving for as diversity of supply helps to offset the variation in availability of renewable energy sources as well as variations in demand. Waves are a stored and concentrated form of solar energy, as they are created by wind, but persist long after that wind has died away, so they are a potential source of

energy/power that are available when other sources, like wind and solar, may not be.

1.4.2. Economic conditions

Historically over 1000 devices have been suggested over hundreds of years. In modern times, wave energy has been seen as an expensive alternative to fossil fuels, so wave energy development has been linked to periods of high oil prices, such as during the '70's.

With peak oil occurring imminently and gas supply issues, countries worldwide are experiencing increasing energy costs. This added concern about the effects of global warming means there is renewed interest in renewable sources, including wave energy.

It will be some time before wave energy converters are financially viable in their own right, but with sensible government investment via the Carbon Trust, the Technology Strategy Board (TSB) and from Europe under its Framework Programme, and the careful use of systems such as carbon trading and multiple Renewable Obligation Certificates (ROCs), wave energy is set to be a major source of the UK's electrical power in the future.

The UK government has reiterated its intention to support marine renewables, and the industry has recently benefited from £12M from the TSB. Other funding includes that for early stage development and academia through the research councils and grants for R&D, currently administered by the Regional Development Agencies (RDAs). The UK is ideally placed to capitalise on its current position in the world, and an announcement is expected at the time of writing on the future of government support for the sector.

1.5. OWC introduction

This section introduces the principles by which an OWC works, and also outlines some of the problems associated with floating devices.

1.5.1. Operating Principle

As a wave passes the tube of an OWC, air is forced up through a bi-directional air turbine (Figure 1.2). As the following trough passes, air is sucked back down through the turbine. Generally, the turbine is self-rectifying and spins the same way whichever direction the air flows.

We can make the analogy to water in a U-tube where the coupling length (L_c) can be altered so that the water column resonates at a certain frequency.

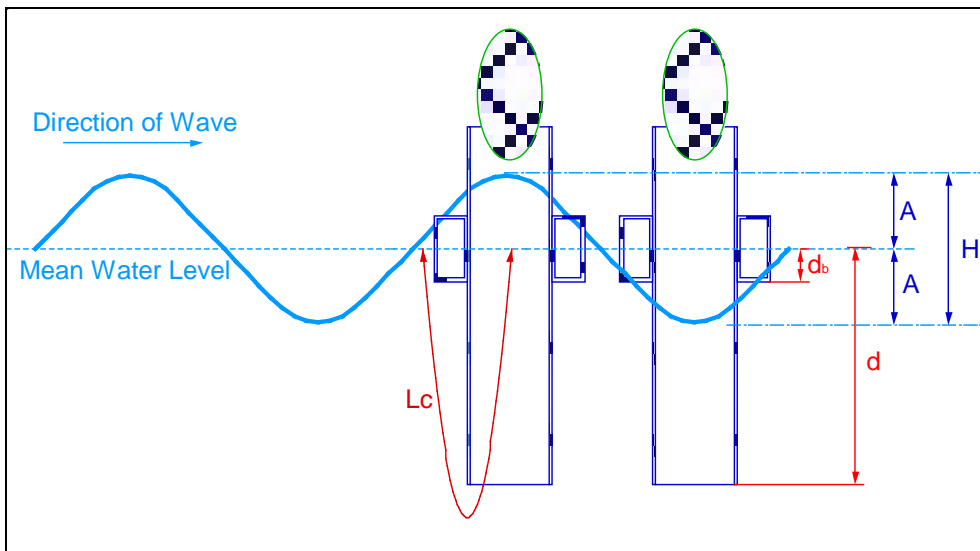


Figure 1.2 OWC Schematic.

Continuing the U-tube analogy, the device can be tuned to the period of an incoming wave by choosing a coupling length L_c such that:

$$L_c = \frac{gT^2}{2\pi^2} \quad (1-1)$$

(White 1985 and Ward-Smith and Chapter 1980)

Which describes the resonant length of a U-tube, where T is the period of oscillation and g is acceleration due to gravity.

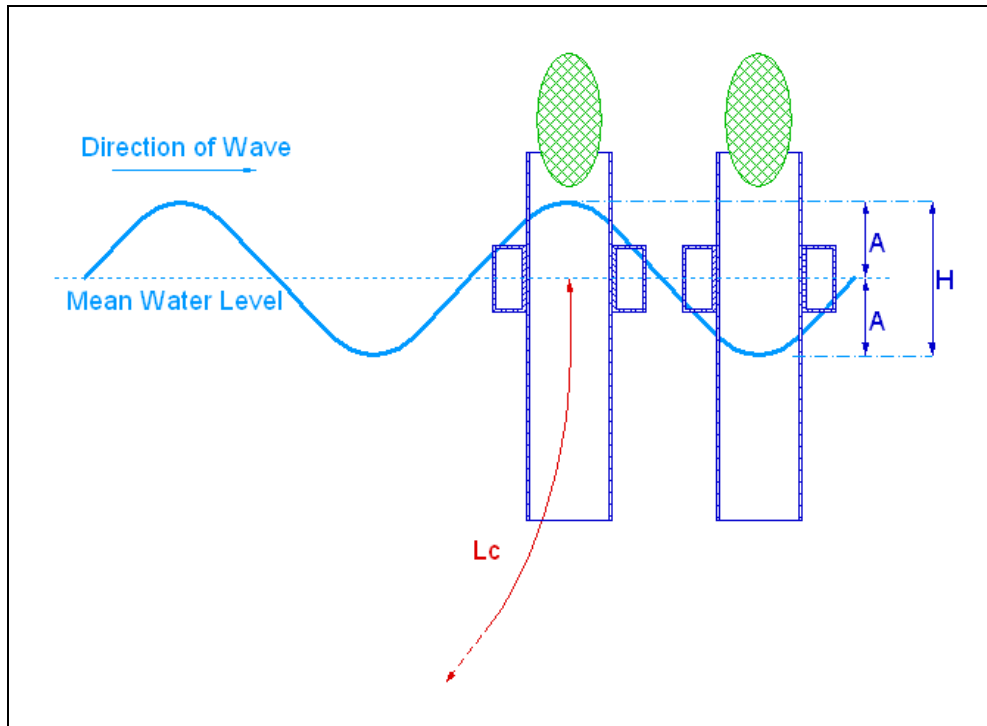


Figure 1.3 Realistic resonant path.

In reality, the streamlines for the water flowing into the OWC are more like the one shown in Figure 1.3, (Knott and Mackley 1979) where L_c varies not only with the draft of the tube, but also with the amount of water entrained by the system. One of the aims of this thesis is to determine the relationship between draft and the resonant period of the system, and this is examined in Chapter 5. The hypothesis is that the relationship will have the same form as equation 1-1.

1.5.2. Heave

A full sized OWC would very likely be a floating device, however the models tested in this PhD were fixed as it is the fundamental relationship between an OWC with helical fins and one without that is under investigation. One problem with small floating OWCs is that they move up and down (heave) as waves pass them. This reduces the amplitude of the wave that is actually captured by the device. The amplitude of displacement (A_d) is subtracted from the amplitude of the wave (A) to give the amplitude captured (A_c).

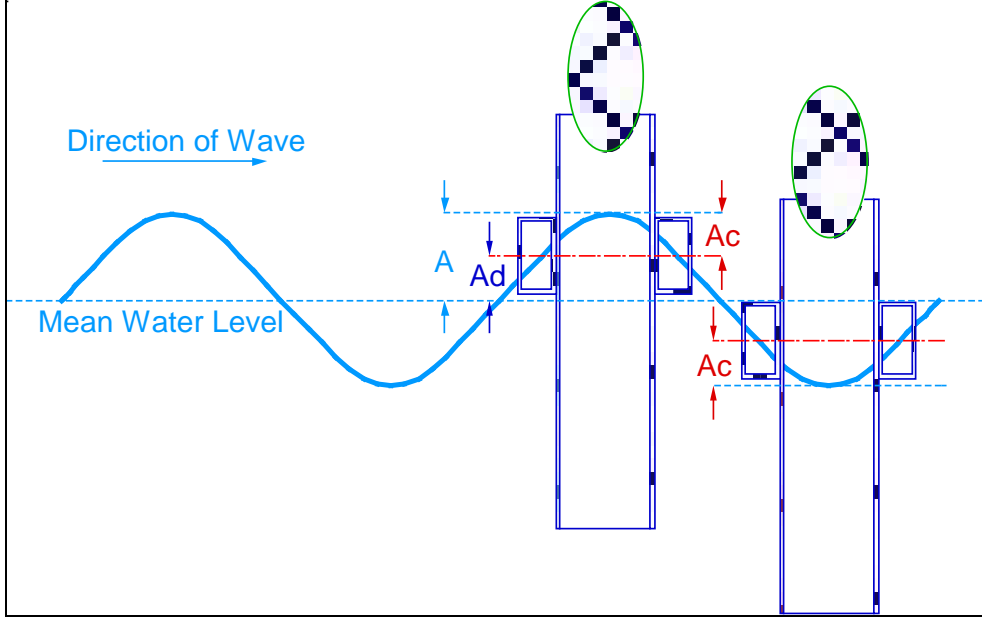


Figure 1.4 The heave effect.

Figure 1.4 is illustrative only: In reality, the motion of the device would be out of phase with the incident wave in a similar way to the water level, which is discussed in section 5.3.3.

This heave effect could be minimized by tuning the bodily motion to a different frequency to that of the energy capture by adjusting the buoyancy and the ballast to resonate at a different period:

$$\omega_0 = \left(\frac{\rho g S_a + K}{m + A} \right) \quad (1-2)$$

Where ω_0 is the natural frequency in heave, ρ is the density of water, S_a is the water plane area of the body, K is the spring constant (due to the restoring force of gravity), m is the mass of the structure and A is the amplitude of the wave (Falcao 2010).

In simple terms, increasing amount and distribution of the buoyancy would increase both S and K (in equation 1-2) and minimising the amount of ballast and structural

mass, m , will increase the natural frequency of heave, ω_0 . If this were set to a low period, and the coupling length were set (according to equation 1-1) to the wave period associated with the highest annual energy yield, then the body motions would create a relative motion between the internal water surface and the body at low periods, and the oscillation of the water in the column would do the same at higher periods, thus extending the range of periods over which the machine converts electricity.

Vijaayakrishna et al (2004) suggest the opposite strategy such that the heave motions would be used to produce power by making the entire structure resonate at the wave period associated with the highest annual power yield, and this is another potential solution.

This thesis investigates the comparative performance of helical OWCs for the fixed case. It is assumed that this comparison will translate in a similar fashion for floating machines since the motions of each of the configurations is expected to be similar, however, this will have to be verified by future research.

1.6. Novel helical design

Following on from the author's MSc dissertation, it was decided to investigate the design of a helical path OWC. The novel aspect of the OWC is the helical nature of the internal ducts. This helical path will enable such a device to be tuned to a local wave climate, whilst being shorter and easier to deploy than the equivalent machine without a helix.

1.6.1. Helical Water Path

The Helical OWC is basically a standard OWC with a helix, or series of helices, inside the tube. Figure 1.5 shows a cutaway view of a conceptualisation of the device. In this example there are two helical fins that execute one full turn round the inside of the OWC tube. At full scale, the central spine will be buoyant as well as helping with construction of the fins which become more complex to manufacture as they get closer to the middle. The fins are expected to improve the structural integrity

of the device since they will provide lateral support to the tube itself. A buoyant ring will also be required around the upper part of the cylinder for support and stability. This could be reduced in size if the fins and outer cylinder were also buoyant. For example, using polyurethane coated foam would give buoyancy to the entire structure.

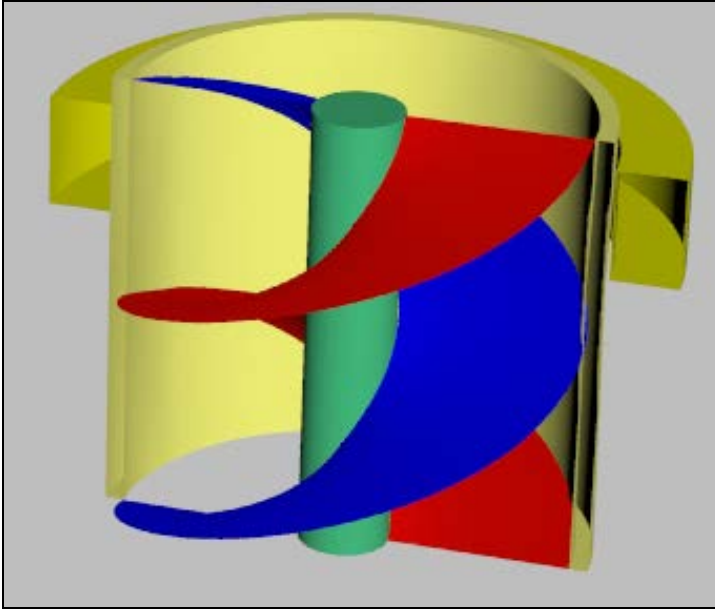


Figure 1.5 Cutaway view of a Helical Path OWC.

A bi-directional turbine and generator would be mounted on top of the structure, contained within a cowling to direct the flow of air through the turbine. Ideally, this entire power unit (turbine, generator & cowl) would be removable to aid maintenance and could be moved in its entirety to a stable ship or to shore for easier access.

The water inside the device has to travel up a helical path L described by:

$$L = \sqrt{(nC)^2 + d^2} \quad (1-3)$$

Where L is the distance that the water travels through the helix, C is the circumference at $D/\sqrt{2}$ (corresponding to the diameter that bisects the horizontal

cross sectional area of the OWC (Chapter 4) and d is the draft when the device is at rest (all in metres) and n is the number of turns made by the wetted part of the helix, again at rest.

As discussed in Chapter 5, a conventional OWC will have an $L \approx 0.4L_c$, but using a helix will enable $L > 0.4L_c$. This will shorten the draft of the device, while maintaining the coupling length which, in turn, will make transportation and deployment easier and also allow the device to be used in shallower seas. It will also make it possible to tune the supporting buoyancy and the water column to a wider range of different frequencies as draft and L_c are no longer coupled.

This helical concept was thoroughly tested, and these tests show that the helical concept is an improvement over the standard plain tube OWC. The background to and results of these tests comprise the rest of this thesis.

Chapter 2: Background and Literature Review

2. Introduction

This chapter is intended to present the general arguments for wave energy, as well as the theory and experimental rationale required for this thesis. It also contains a summary of the different resource measuring methods, and of device categorisation. This should be read in conjunction with Appendix D which is a list of promising wave energy converters, courtesy of IT Power Ltd. Methods for testing a helical OWC are presented and numerical methods for the performance analysis of such a device are suggested.

2.1. Climate change

The Intergovernmental Panel on Climate Change (IPCC 2007a, IPCC 2007b and IPCC 2007c) reports have convincingly set out the arguments stating that human activity associated with industrialisation and population growth in the 20th Century are contributing to major changes in the world's climatic systems. They draw their data from many peer reviewed studies and aggregate the results together in Assessment Reports by four working groups, investigating the science behind climate change, the impacts of climate change, the mitigation of climate change, and the aggregation of results, from around the world and across disciplines. Apart from a few sceptics these reports are widely regarded by the scientific community as reflecting the true state of affairs and the IPCC itself has “high confidence” in its conclusions.

2.1.1. Why marine renewable energy?

With climate change; security of supply concerns; rising energy demand; and limited fossil fuel resources, alternative sources of energy are required. Pacala and Sokolow (2004) hypothesise that existing technologies can mitigate the additional demand in the next 40 years or so, with high rates of expansion of these technologies. New technologies will be needed if demand is to be met after this

period and we will need to bring these technologies to commercial readiness if they are to be useful for the next tranche of technologies. Marine energy could be part of this mix if it is developed now.

2.1.2. With 50 TWh/y of wave energy and 21TWh/y of tidal practicably available in the UK (Carbon Trust 2011), marine energy has the potential to provide 20% of the UK's energy demand (Carbon Trust 2011). The Carbon Trust also estimates that marine energy could realistically provide 1/6th of the 2020 20% target, i.e. 3% of the UK's electricity demand (Carbon Trust 2006).

Figure 2.1 Shows predictions for the UK's installed capacity over the next 10 years. It is worth noting that following BWEA's projection involves installing an average of 1MW per week for the 5 year period 2015-2020.

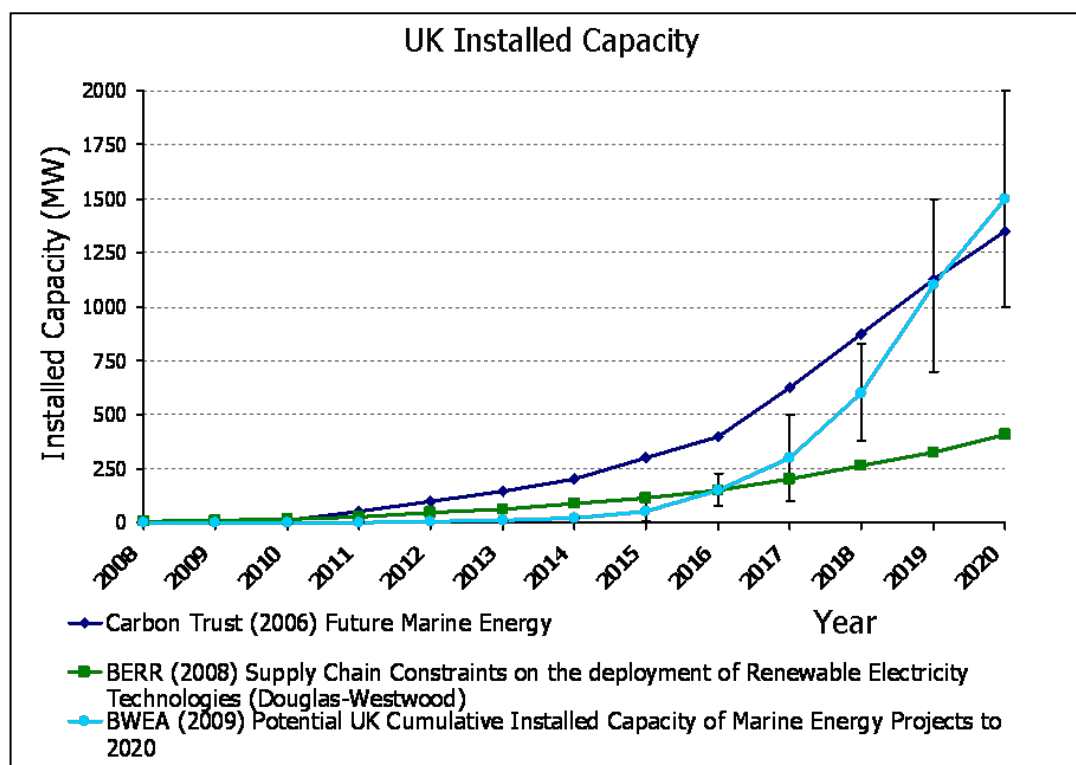


Figure 2.1 Predictions for wave and tidal installed capacity by 2020 (Carbon Trust 2006, BERR 2008 & BWEA 2009).

The cost of wave energy is currently about 38-48p/kWh, whereas for tidal stream it is

about 29-33p/kWh (Carbon Trust 2011). With a discount rate of 15% (representing the reduction in cost between generations of devices), these will reduce to around 28p/kWh for wave and 16p/kWh for tidal by the time 400MW of installed capacity has been installed (Carbon Trust 2011). If other countries install significant quantities of marine renewables, there is scope for these costs to fall even further, especially for wave machines (Carbon Trust 2011).

2.1.3. Why wave energy?

It has been reliably shown that 50TWh/year (14% of the UK's annual usage) (Carbon Trust 2011) is practicably available from the waves surrounding the UK shores. As devices evolve, this energy will be used to help fulfil the renewable energy contribution to reducing carbon emissions. In addition, new technologies will be required during the 50 year Socolow / Pacala period in order to continue reduce carbon emissions in real terms. It may be that wave energy is expensive for the first few generations of device, but eventually it will be cost effective. The Stern report estimated this financial cost of stabilising at 500-550ppm CO_{2e} at 1% of GDP vs. 3% of GDP for mitigating the effects of continued climate change (Stern 2006). The GDP for the UK was about £ 1,400 trillion in 2011 (ONS 2012), so the potential budget for stabilisation is £14Trillion.

The author's view is that it is vital to reduce emissions and to stabilise the world's climate. This will have costs, some personal, like changing lifestyles (possibly by adopting personal carbon allowances), and some financial, like investing in new technologies.

From a wave energy point of view, climate change may provide some benefits since there is evidence that the average wave power, at least in winter, is increasing. Figure 2.2 shows that the waves we are likely to exploit have already increased in Significant Wave Height (H_s) by between 5 and 15% between 1985 and 1996.

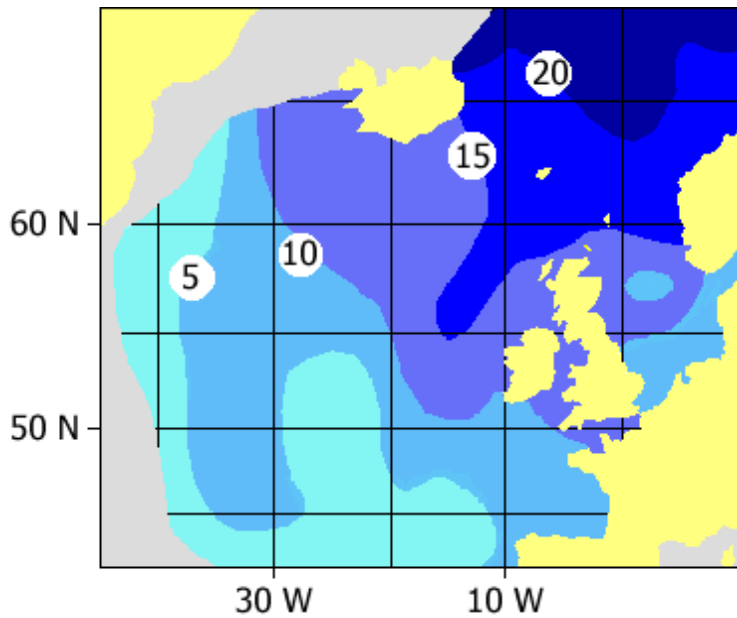


Figure 2.2 The percentage increase in the significant wave height in the North Atlantic in winter (December-February) between the periods 1985 to 1989 and 1991 to 1996. (Hulme et al, 2002).

11 years is not a long period, but the UKCIP02 report (Hulme et al, 2002) shows this trend continuing, with Atlantic wind speeds generally increasing on average, but with large increases in winter being balanced by some decreases in summer and autumn. Thus the yield from wave energy converters can be expected to increase in the future.

The corollary of this winter increase is that there are likely to be more extreme events, so it is vital that any WECs deployed are designed to survive these extreme conditions.

Another benefit of investing in new technologies is that the UK will retain its place as world leaders in marine energy. These technologies and expertise can then be exported around the world, thus improving the national economy and providing jobs. With marine devices this is likely to be a particularly welcome boost to the nation's flagging shipbuilding industry.

2.2. Wave resource definition

2.2.1. On/Near/Off-Shore

There are three general regions where wave energy converters can be deployed and these are onshore, nearshore and offshore. The nearshore and offshore regions are differentiated by water depth, with the transition being in 30-50m of water. Offshore is where the waves are unaffected by water depth, (i.e. where $\text{depth} > \lambda/2$ and $\lambda = \text{wavelength}$) (EMEC 2009) and nearshore is the region where the depth of water has shoaled to such an extent that it slows down the incident waves. Nearshore and onshore are also typically in shallow enough water for a device to be fixed to the seabed, which can enhance performance significantly.

From these definitions, it is clear that the actual distance from shore is immaterial; offshore conditions can be found within 10 miles of the Cornish coast, whereas nearshore or offshore conditions persist for much of the southern North Sea.

Although there is an advantage in being able to fix a device to the shoreline or seabed (because of the stable base that the power take off (PTO) can mechanically react against) there is significantly less energy available in nearshore and onshore wave climates. This is primarily due to interaction with the seabed and the shallow water wave phase velocity, c , is governed by the equation (Open University 1989 & EMEC 2009):

$$c = \sqrt{gz} \text{ ms}^{-1} \quad (2-1)$$

Where z is the mean water depth, g is acceleration due to gravity.

For intermediate depths, the phase velocity is:

$$c = \frac{gT}{2\pi} \tanh(\kappa z) \quad (2-2)$$

Where the wave number, $\kappa=2\pi/\lambda$ and T is the wave period.

Whereas offshore, the phase velocity is defined as:

$$c = \frac{gT}{2\pi} \text{ ms}^{-1} \quad (2-3)$$

In deep water, the whole wave, from peak to trough, moves at the same velocity, whereas in shallow water, the top of each wave travels faster than the bottom and they start to shed energy to the seabed via friction and by breaking.

It can be seen from Figure 2.3 that the offshore region is well worth exploiting, even with additional constraints experienced by floating devices, that are discussed later in the chapter.

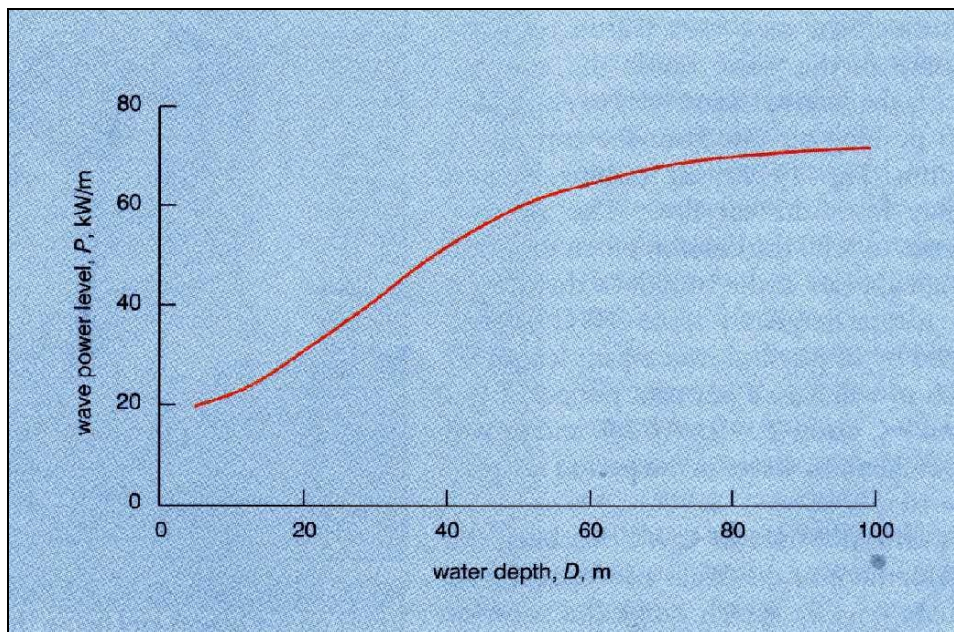


Figure 2.3 Wave power against water depth for a site to the west of the Hebrides in the North Atlantic (Duckers 2004).

2.2.2. Basic wave theory

Plane regular waves can be described in detail in terms of their surface elevation and the motions of particles within the water column. It is possible to superimpose several waves onto each other to form irregular seas, and if a spreading function is added in, these can be used to simulate realistic seas. Figure 2.4 shows the main defining characteristics of a wave.

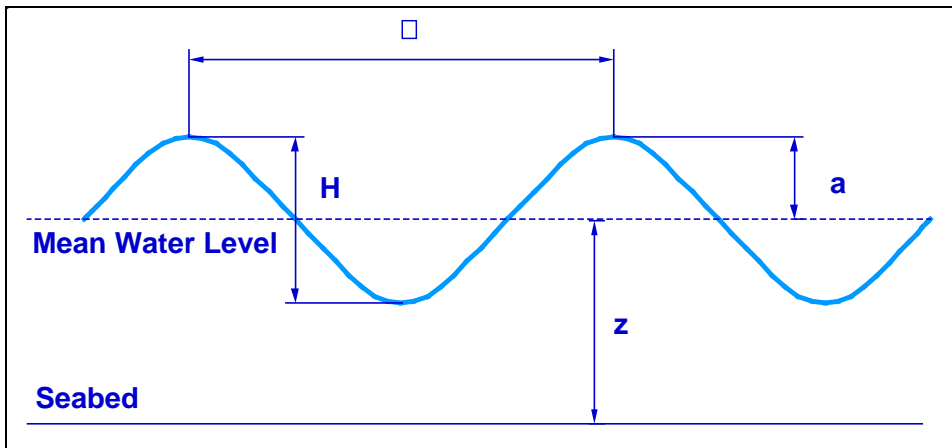


Figure 2.4 Diagram showing wave parameters. The waveheight H is twice amplitude, a , of the wave. The period, T , is the time it takes for one wavelength λ to pass a certain point.

Once waves become steep, as they do when in shallow water, they become non-linear, and the standard linear theory has to be modified. Breaking waves are highly non linear, and cause many of the extreme loads on offshore structures.

The main purpose of this study is to compare the performance of different OWC configurations, so plain regular waves were used, both in the physical and mathematical simulations.

When scaling up the results, it was assumed that the performance of the OWCs in plain waves represents that in the corresponding bin of a polychromatic Bretschneider Spectrum. The Bretschneider spectrum is defined as:

$$S(f) = \frac{5}{16} \frac{H_s^2}{f} \left(\frac{f_p}{f} \right)^4 \exp \left[-\frac{5}{4} \left(\frac{f_p}{f} \right)^4 \right] \quad (2-4)$$

Where $S(f)$ is the spectral variance density (m^2/Hz), H_s is the significant wave height, f_p is the frequency at which the variance of the spectrum is a maximum and f is the frequency and the inverse of the period, T (EMEC 2009).

2.2.3. Wave / Particle motion

Wave power is measured in kW/m. This is the power that is contained in each metre of wave crest. This power is primarily exhibited as circular particle motions (Figure 2.5) with both potential and kinetic energy that decay exponentially with depth. These particle movements are described by the Airy wave equations (Tucker and Pitt 2001).

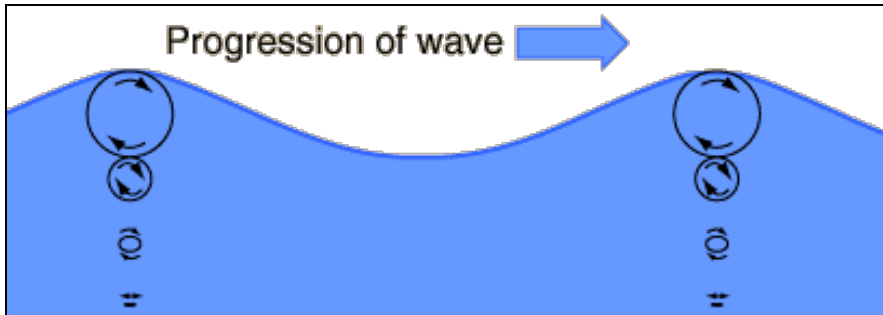


Figure 2.5 Circular nature of water particles in waves (Open University 1989).

The Airy equations describe linear waves, and the Stokes wave equations are higher order expressions that describe non-linear waves. The higher order of the equation that is used, the better the correlation between the result and reality (McCormick 1981).

The figure quoted for wave power in Figure 2.3 is the total power per metre of wave crest, from the surface to the sea bed. In practice, because of the exponential nature of the decay in energy with depth, 80% of the power is found within 1/2 of a

wavelength of the surface, and 99% is found within 1 wavelength of the surface. In deep water (Tucker and Pitt 2001),

$$\chi \approx \zeta \propto A \exp(kz) \quad (2-5)$$

Where

χ is the horizontal displacement of the particles,

ζ is the vertical displacement of the particles

A is the amplitude

k is the wave number, $2\pi/\lambda$

and z is the depth, where z=0 is the water surface, and z is taken as negative

The kinetic energy is proportional to the square of the velocity, and potential is proportional to the particle displacement, so the smaller the motion, the less energy is available.

2.2.4. Monochromatic power calculation

The power flux available in a monochromic wave can be calculated using:

$$P_i = \left(\frac{\rho g^2}{32\pi} \right) TH^2 \approx 0.98TH^2 (kW / m) \quad (2-6)$$

Where T is the period and H is the wave height. The full derivation can be found in Falnes 2002.

2.2.5. Polychromatic power calculation

The power flux available in a polychromic wave can be calculated using:

$$P_i = \left(\frac{\rho g^2}{64\pi} \right) T_e H_s^2 \approx 0.49T_e H_s^2 (kW / m) \quad (2-7)$$

Where T_e is the energy period and H_s is the significant wave height. The full derivation can be found in Chapter 2 of Tucker and Pitt (2001).

The results of equation 2-6 and 2-7 are given as kW/m of wave crest, meaning that the power available at a device can be easily calculated based on its width, or in the case of an attenuator or point absorber, its capture width, which is described in section 2.4.2.

2.2.6. Wave Trains and Seas

An additional complication with sea waves is illustrated in Figure 2.6. Waves can often come from many directions at the same time (Kofoed and Frigaard 2006).

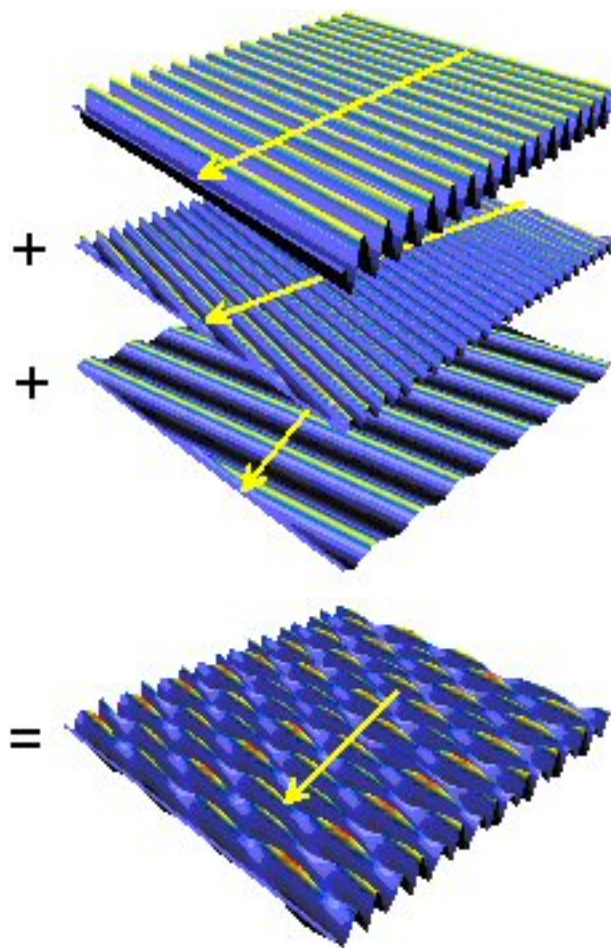


Figure 2.6 A complex sea derived from simple wave trains (Carbon Trust 2006).

This effect means that wave energy converters have to be able to convert waves coming from many directions, or risk losing some of the available power. It also means that waves arriving at a converter are effectively random and this randomness makes effective control difficult as it is impossible to predict what the next wave will be.

In practice, and due to bathymetry and the fact that waves are created by wind, the power producing waves often come from an arc, rather than from all points of the compass. For example, Wave Hub (a test site of the north coast of Cornwall) has South-Westerly prevailing winds, and most of the waves come from an arc 30 degrees either side of West-South-West (SWRDA 2004). Waves from an easterly direction will necessarily be smaller as they do not have the fetch (distance), time or strength of wind to grow. This means that directional wave energy devices like Pelamis, Wave Dragon or OWEL (See Appendix D for a list of promising devices) can be considered for deployment in many sites, especially if they are able to turn to some degree.

Also in practice, most waves are similar to the preceding one, i.e. not completely random, allowing an auto-regressive control algorithm to be used.

However, the complex nature of waves means that extreme waves can form with very little warning, and it is for this reason that survivability must be one of the primary design parameters.

2.2.7. Wave climate modelling

It is not intended to model wave climates as part of this PhD, but rather to use one of the standard spectra that exist. The three main ones are the Peirson-Moskowitz (PM) spectrum for fully developed deep-water waves; the Bretschneider spectrum (equation 2-4) for a realistic spread of waves (including those still being formed, those in the fully developed PM range and those that are decaying); and the

JONSWAP spectrum for fetch limited waves (Tucker and Pitt 2001). These spectra can be used mathematically as described by Tucker and Pitt or reproduced to scale in a wave tank.

For the purposes of this PhD, monochromatic waves, and the Bretschneider spectrum were the most appropriate. Plain, regular waves were used for the physical and mathematical modelling as they enable a more fundamental understanding of the models to be developed. The Bretschneider spectrum closely resembles a realistic sea (EMEC 2009), and is used for the scaling analysis in chapter 5. Any further tests should be done in a scaled Bretschneider sea as advocated by Brian Holmes and EMEC (2009), to predict the general performance of wave energy devices.

Responses to a wave climate can be simulated in scaled physical models in a number of ways. Testing at a range of periods and heights and then weighting the result by the annual probability that that H-T pair will occur and finally summing the results gives indicative results. Ideally the desired spectrum should be simulated in a tank, with directional elements in order that it closely represents the conditions at a specific site, but this is beyond the scope of this PhD.

2.3. Technology

There have been many devices for capturing wave energy, but there was a real effort in the late 70s and early 80s to develop some early concepts. This effort was stopped when the UK government of the day withdrew funding and support for research. Some of these ideas were revived in the last 20 years or so and several others have emerged. The UK is seen as leading the world in wave energy converter development, and government funding is once again available to fund this promising industry.

OWCs were first used to power navigation buoys (Falcao 2010) using simple impulse turbines, and have since been developed into a successful category of WEC. This is expanded on in section 2.3.3.

2.3.1. Device Categorisation:

There are several ways to categorise WECs. These can be based on their location, their primary energy capture system, and their power take off (PTO). To fully categorise a device, all three should be stated.

2.3.1.1. Primary energy capture categorisation

To start with a basic principle, any device that can make a wave can also absorb energy from waves (McCormick 1981). These devices can be subdivided into four capture methods, attenuators, terminators, Quasi Point Absorbers and point absorbers. Attenuators lie normal to the prevailing wave crests. Terminators lie parallel to the wave crests and are long in comparison to the wavelength e.g. a harbour wall, or a beach. Point absorbers are small compared to the wavelength ($D < 0.2\lambda$ (Cruz 2008)) and absorb energy at a particular point, e.g. buoys. Quasi Point Absorbers are those that, due to their width, act like point absorbers in large waves, and terminators in smaller waves (e.g. Oyster a bottom fixed flap device (Royal Soc)). This is shown schematically in Figure 2.7.

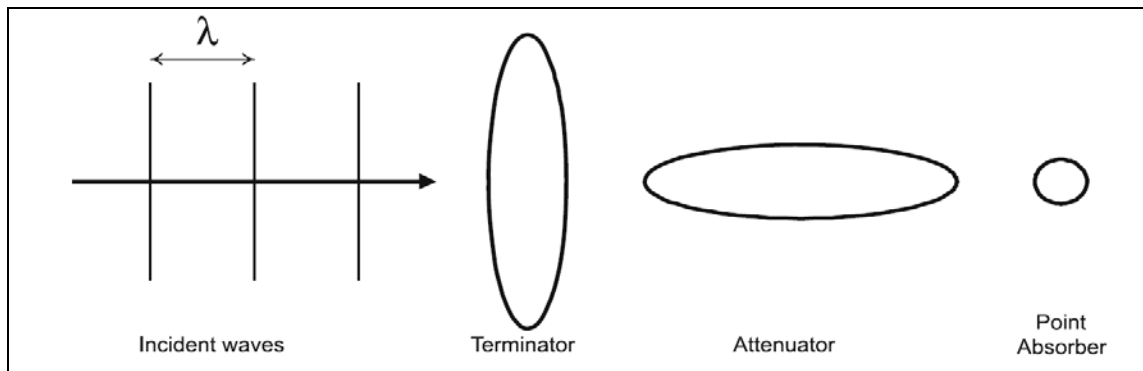


Figure 2.7 Schematic showing scale and orientation of a terminator, attenuator and a point absorber (Cruz 2008).

2.3.1.2. Device location categories

Like the resource, devices can also be defined as onshore, nearshore or offshore, but in this case the distinction is largely due to the way devices are fixed to the

seabed.

Onshore devices can be built into the shoreline or structures such as breakwaters. In the case of breakwaters, significant capital costs can be saved as the structure only needs to be modified, and not built from scratch. Nearshore (up to 30m water depth) devices can rest on the seabed. Devices fixed in one way or the other can react against the seabed which can deliver high efficiencies when compared to the equivalent floating structures. This is because a bottom fixed device has a fixed side and a moving side with the PTO absorbing the relative motion between the two sides. A floating device also has two sides, however they are both floating in a similar manner, and the side that experiences most movement will tend to pull the other along, rather than create a differential movement between them. The relative motion between them will therefore be smaller than for a fixed device, and the energy capture will be reduced as a result.

Offshore devices must be moored to the seabed, which requires special skills and equipment to design and deploy. They must also incorporate something for the PTO to react against, or there will not be any power extraction.

In the case of a floating OWC, the reaction is provided by the inertia of the structure. This creates a phase difference between the waves and the structure, and therefore the internal water surface rises and falls as it does for a fixed OWC. The relative internal change in water level is likely to be less than for a fixed machine as the structure will also be moving.

2.3.1.3. Power Take Off (PTO) Categories

The PTO generally converts motion into another form of energy: McCormick (1981) lists Mechanical, Pneumatic, Hydraulic and Piezoelectric amongst others. These PTOs can be used to generate electricity, pressurise a water system for reverse osmosis or to produce a fuel such as hydrogen.

The pneumatic systems are most appropriate for this thesis, and examples of appropriate air turbines are given below.

McCormick (1981) also shows that the power removed from the air is:

$$P = \Delta p \cdot Q \quad (2-8)$$

Where P (W) is the power, Δp (Pa) is the pressure drop across the turbine and Q (m^3/s) is the flowrate.

2.3.2. State of the art full scale wave energy converters (WECs)

There are many devices that are vying for supremacy in the wave industry at the moment, and a list of the current leaders with some other promising machines is included in Appendix D.

The current front runners with devices successfully deployed are Pelamis, PowerBuoy, OE Buoy and Oyster with Wavegen's shoreline devices successfully filling their onshore niche. Other devices that look promising, based on their technology readiness level (TRL), are, Oceanlynx, Wave Bob, Wave Dragon and Fred Olsen. There are some other devices that could break the mould of conventional thinking and they have been included in Appendix D. These include Wave star, CETO, OWEL, AWSIII, Anaconda, Wave Treader and Wave Rotor.

An onshore or nearshore device could be fixed to the seabed (as discussed above), and the proximity to shore means that the power transmission cost is minimised. It is sometimes possible to locate the PTO and electronic components onshore. An offshore location gives access to the more highly energetic waves, so there are benefits to both positions.

This and the list in Appendix D is a brief overview to show the diversity of devices being developed at the moment. There are many others, including some whose development has stopped, but it is clear that there is not one standard design that has been settled on (like a three-bladed upstream wind turbine). The Author's prognosis is that there will be technology convergence towards a preferred capture method for each of the regions: Onshore, Nearshore and Offshore.

2.3.3. OWC Comparison

There are two broad categories of OWC: Fixed and Floating. Floating versions can be placed in the more energetic offshore locations, and the fixed ones can take advantage of the vicinity of the shore and use the seabed to react against. The results, where published, are presented below.

Here are some examples of these types of machine:

Fixed OWCs

Wavegen's machines exemplify the state of the art for Onshore OWCs (see Figure 2.8). Their Mutriku plant was commissioned in late 2011 and their Siadar project in is the largest consented wave energy project in the world in 2012.



Figure 2.8 Wavegen's Limpet is the prototype for the current generation of commercial devices and completed its 10th year of operation in 2011 (Wavegen n.d.).

Many other similar onshore or nearshore devices have been developed all over the world, including Pico, Russia, China and Japan and the one shown in Figure 2.9 which was built in Vizhinjam in India in 1990.



Figure 2.9 Vizhinjam OWC (Leipzig university n.d.).

Floating OWCs

Ocean Energy are demonstrating their 1:4 scale device off the Irish coast (see Figure 2.10) based on the Japanese bent backward duct buoy (BBDB) concept. It has been in the water since December 2006.

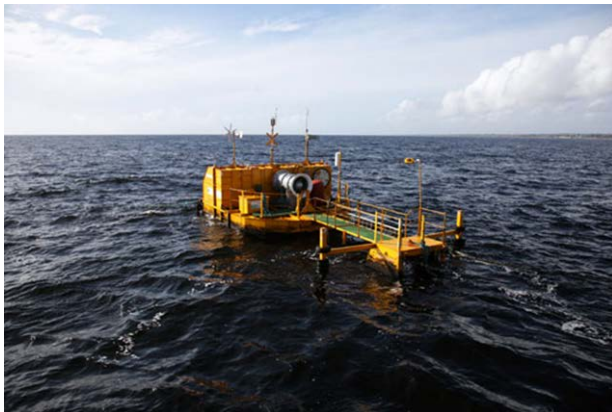


Figure 2.10 OE Buoy (Ocean Energy n.d.).

Oceanlinx have tested three devices including the version shown in Figure 2.11 and have tested two different turbines: the Dennis Auld, and the Hydro Air.



Figure 2.11 Oceanlinx mark 2 (Oceanlinx 2010).

There are several other floating OWCs worth noting: Embley Energy's machine (Figure 2.12) has not yet been tested, but is a simple robust machine. The Mighty Whale was deployed in Japan, but was not considered a success.

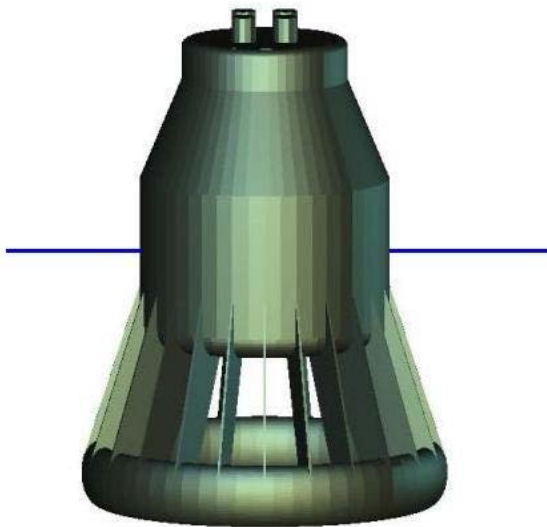


Figure 2.12 Embley Energy's OWC.

2.3.4. Large Scale OWC results

Babarit et al (2012) show that OWCs are amongst the most promising devices commercially. Figure 2.13 shows that the absorbed energy per mass is the highest for floating OWCs compared to all the others analysed. This is a good metric when analysing the cost of electricity of a device, and shows that floating OWCs should deliver a good levelised cost of energy (p/kWh) compared to other devices.

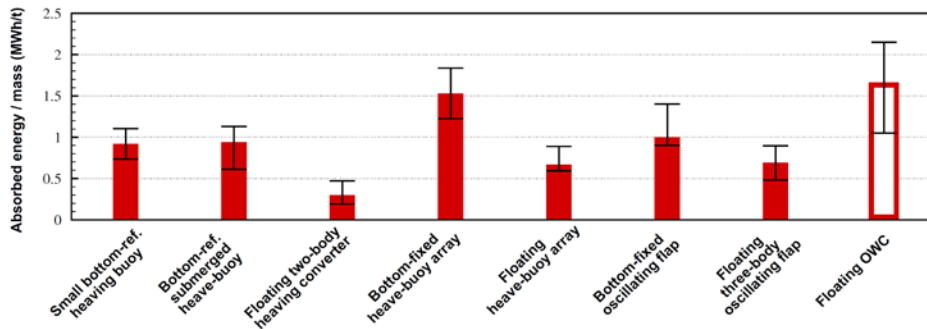


Figure 2.13 Absorbed Energy/mass for a selection of WECs (Babarit et al 2011).

It should be noted that the method used led to greater uncertainty for the OWC than the others (hence the size of error bar and colour of the OWC histogram bar). The absorbed power must also be converted to electricity, and an air turbine in an OWC may not be as efficient as some other methods like hydraulic pumps. The main mass of a floating OWC is made of simple structural members, whereas complex structures add significantly to the cost of construction. The author's recent experience gives prices of £2,800/tonne to £4,500/tonne for fabricated steel depending on the complexity of the component. This analysis leaves out the cost of a power line, which would be similar in all cases, but also omits the cost of moorings or bottom fixing. Again the author's recent experience shows that bottom fixing is a much more costly option to mooring with standard anchors. There is therefore some uncertainty about the validity of Figure 2.13, however it is a good indicator that OWCs are worth developing further. This view is echoed in Dalton and Lewis (2011) where they show that floating OWCs perform well commercially compared to other devices, especially after a number of MWs have been installed and full use has been made of the learning from previous projects.

Much useful technical information has been published on the Islay OWC and on Limpet with most of the other developers keeping their detailed results confidential.

Following trials with the Islay OWC, Limpet was designed with several modifications to improve performance: the concrete structure at the top of the opening was given a rounded profile to reduce vortex shedding (Müller and Whittaker 1995 and Cuan et al 2002), and the back wall of the chamber was angled at 40° to reduce loads and improve the flow of the water inside the machine.

Cuan et al (2001) also report on the air to mechanical efficiency of the Wells turbine which is about 50% at rated power, and rises to 65% in lower wave energy conditions.

Arup reported on the average performance of OWCs and shows that the average efficiency for Wavegen's Limpet is 8% and for the Vizhinjam OWC it is 6.3% (Arup 2007). Arup also say that Wavegen's turbine's peak efficiency was 70% for outflow and 30% for inflow, and that the low average performance was due to the mismatch between the climate and the device. This highlights the necessity to design an OWC for the climate it will experience, and also to match the turbine to the output of the OWC.

2.3.5. OWC turbine variations

There are currently four types of air turbine that could be used for a floating OWC.

2.3.5.1. Wells turbine

A Wells turbine (Figure 2.14) is a self-rectifying reaction turbine that has good impedance characteristics (independent of flowrate) and a high rotational speed (meaning that no gearbox is required), but is less good at start-up due to the blades stalling at low rotational speeds. Wells turbines are symmetrical about their chord, which is parallel to the direction of rotation. This geometry means that their

performance is highly dependent on Reynolds number: effectively, they require a very specific flow regime to deliver peak efficiencies (Curran et al 1997) as in slow flows, the incident angle is too low (and produces no net lift), and for high flows it is too high (leading to stall) (Setoguchi et al 2004). Their performance can be improved by allowing the blades to pivot with the air flow, and the optimum pitch angle ($2-10^\circ$) (Setoguchi et al 2003 & Falcao et al 2004) needs to be determined experimentally as it is also dependant on the dimensions of the plenum chamber (Setoguchi et al 2004). Brito-Melo et al (2002) also show that altering the blade profile can delay the onset of stall to provide a wider range of flow conditions that the turbine can function in.

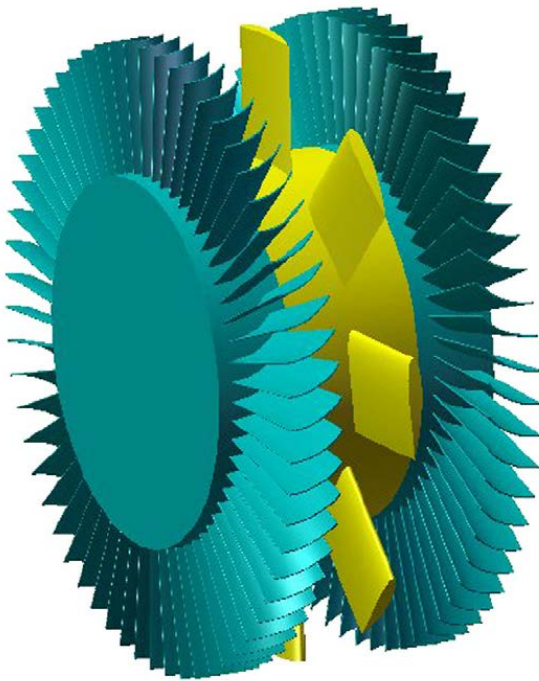


Figure 2.14 Wells Turbine with guide vanes (Falcao 2010).

2.3.5.2. Impulse turbine

An impulse turbine (similar to a steam impulse turbine) can also self rectify if guide fins are fitted on both sides of the turbine (see Figure 2.15). These perform better at low and high flowrates (Masuda 2001) as their performance is not affected by

Reynolds number (Setoguci et al 2004) and they do not suffer from stall. These turbines would need a gearbox for generating electricity as they rotate slower than a Wells turbine in the 100s of RPM, implying another expensive layer of machinery to install (Falcao et al 2004). In general, impulse turbines have lower peak efficiencies than Wells turbines but, nevertheless, these impulse turbines have been used in other OWC designs (Johnson et al 2001) due to their higher average efficiency over a wide range of operating conditions.

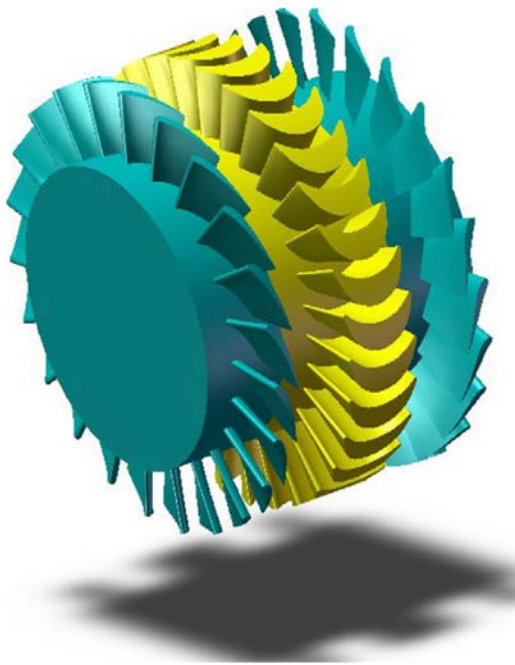


Figure 2.15 Impulse Turbine with guide vanes (Falcao 2010).

A variation of the impulse turbine is the Dresser-Rand Hydro-Air Turbine (Figure 2.16) that uses an annular duct with reducing area to accelerate air flow, and the same on the outlet, that acts like a draft tube to decrease the flow – and pressure. This enhances performance in both directions.

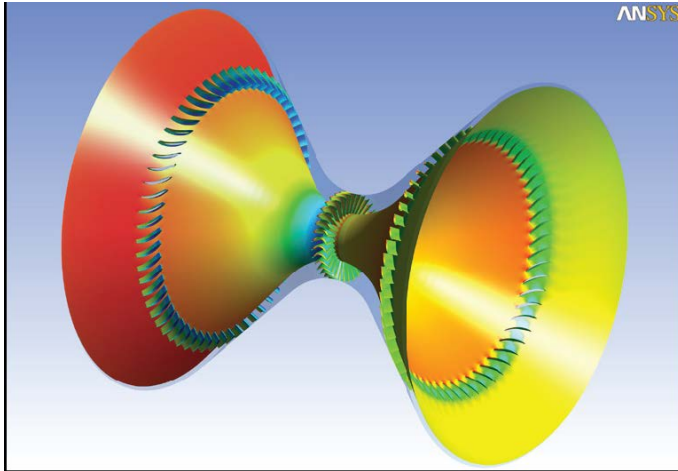


Figure 2.16 Dresser-Rand HydroAir Turbine (Dresser Rand 2010).

2.3.5.3. Reaction turbine

The Dennis-Auld turbine (Figure 2.17) is a reaction turbine that uses variable pitch blades to account for the reciprocating airflow. There is significant complexity in the spinning, rotating actuator system, but reaction turbines are more efficient than impulse turbines, so this turbine should also be investigated.

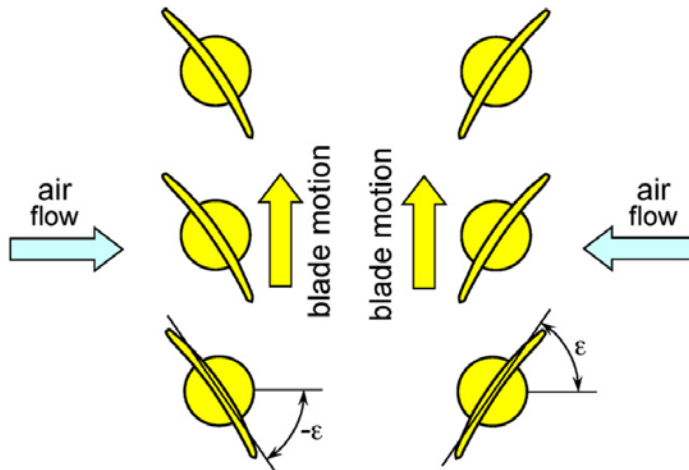


Figure 2.17 Dennis-Auld air turbine. The rotor blades pivot rapidly between extreme positions when the air flow is reversed. (Falcao 2010).

A standard unidirectional turbine (impulse or reaction) could be used (Johnson et al 2001), but the valves and ducts involved in rectifying the airflow are generally thought to make this configuration impractical (Falcao et al 2004).

A Wells or impulse turbine will be chosen as part of the design process for a full scale machine, but for the purposes of this PhD it was assumed that a Wells turbine will be used.

2.3.6. Control methods

The function of the control system is to get the best performance out of a device, and to ensure that it survives stormy seas.

Matching the turbine impedance to the radiation impedance (Falnes 2002) of the machine gives the greatest efficiency (discussed in detail in Chapters 5 and 6), meaning that an adjustable impedance turbine is desirable in a large scale OWC.

Falnes proposed a control regime called 'latching' (Falnes 2002), and Lopes et al (2009) describe using the principle to achieve an increase of 2.5 times the maximum efficiencies over those of a "non-latching" version. Actually achieving this with a floating OWC would be practically impossible as it relies on holding the floating object at both the top and bottom of its cycle.

It is possible, however, to approach this latching regime by using bypass and cut-off valves (Lopes et al, 2009) and altering the speed of the turbine to alter the impedance of the device. When to do this depends on the phase difference between the internal and external water levels, and these are difficult to measure externally, since this involves short term prediction of the incident wave and internally, because the extreme pressure fluctuations inside the plenum chamber make it difficult to assess the correct moment to release the latch (Lopes et al, 2009).

Once it has been decided to add a control mechanism to a system that needs to react in a specific way depending on the wave conditions in the next 5-15 seconds, which is the range of periods in a realistic sea, there are four ways to achieve it:

1. One could try to mathematically predict the next wave, but in a random, multidirectional sea this is pretty much impossible in the time available.
2. A large array of wave monitors could be placed around a wave device or farm, but this is a highly complex system and it would probably be better to spend the money on another wave device
3. Iterative control searches for the best performance in current conditions, and there are techniques such as genetic control analysis that ensure that the global peak performance has been reached, and not just a local one (Gunn et al 2008).
4. A predictive control system could be used, which uses a simple auto-regressive control regime to predict the next wave from the preceding few. Improvements in performance of 40% have been gained when using auto-regressive control instead of no control (Mundon et al 2005), so it is likely that a predictive control algorithm will be used for the full scale machine.

The peak performance of the models tested here will be determined by manually altering the turbine simulator impedance.

2.4. Device modelling

2.4.1. Methods of modelling

Broadly there are two methods for determining device performance: mathematical and physical modelling. Both have their advantages and disadvantages.

Physical modelling is good for reproducing complex systems and their results, but requires careful planning to ensure that the results are valid – see the scaling laws section below. It is not possible to comply with all of the scaling laws at the same

time, so numerical modelling is often used to increase confidence in the results. It is also true that an understanding of the theory informs experiments, and suggests areas of interest to test. Physical modelling is quite time consuming but, as Froude said, “one can make one’s mistakes in private and for a fraction of the cost of full scale tests” (Chakrabarti 1994).

The data gathered are typically used (Vassalos 1999):

- To gain a detailed understanding of a device and thereby choose a configuration for development;
- To identify the principle characteristics exhibited by a device;
- To accumulate a data bank;
- To confirm theoretical results;
- To validate a numerical model;
- To predict large scale performance.

Mathematical modelling often needs validation or calibration by physical models. For example, the actual response amplitude operators (RAO’s which define the motions in six degrees of freedom and are similar to dynamic amplification factors) are often not known and physical models can be used to confirm the mathematical model and increase confidence in the results. Mathematical modelling also requires time, both for setting up and then running tests, but the right model can produce large numbers of results quickly, and these are often good enough to use in the design process. A computer with significant capacity is also required for modelling or test runs become prohibitively long.

In general, both physical and mathematical modelling are used in order to take advantage of both systems, and to increase the certainty in the scaled results.

2.4.2. Hydrodynamics

The purpose of any modelling exercise is to model the flows within and around the

device and structural motions to understand the power that can be extracted by the machine and the loads that will be experienced in service. These are governed by the hydrodynamics of the system, and an overview is given here:

The flow in an OWC is unsteady in that the flow varies with time for any given point in the system. This reciprocating flow means that the flow regime is constantly altering and new features are being formed. This is true of the water particle motions outside the OWC too. Both effects have been described in detail by Knott and others in a number of papers (e.g. Knott and Mackley 1979, Knott and Fowler 1980 and Müller and Whittaker 1995). This work is directly relevant to the current work as it describes many of the hydrodynamic effects experienced by an OWC.

2.4.2.1. Entry Shape

The entry shape is important as reciprocating particles move past the entry at the base of an OWC and this governs that pattern of flow within. In general, eddies are detrimental to the operation of an OWC as they dissipate energy that would otherwise pass through the system (Knott and Mackley 1979). If the entry is sharp, rather than rounded with a flared bell mouth entry, then more eddies will be generated as flow separation will be more common. Knott and Mackley also observed that vortex rings formed within the tube without a bell mouth on the up-stroke and the flow was forced into the centre of the tube by these vortices. On the down-stroke, the vortices were moved to the centre of the tube and they caused the flow to be constricted to an outer annulus. Both of these cases meant that energy was lost due to the additional friction of water passing through the constricted area caused by the vortices. These effects become more pronounced as the particle motions become larger, i.e. as H increases.

A similar effect was recorded by Müller and Whittaker (1995) during an analysis of the Islay OWC. The shape of the entry caused vortices to form inside the chamber on the in-stroke and outside on the out-stroke. As with Knott and Flower's

conclusions, they determined that this reduced the effective size of the inlet (by 20-30% in their case) and reduced the power transfer into the machine.

Müller and Whittaker go on to point out that flow separation and vortex shedding are phenomena dependant on the Reynolds Number. Their model was scaled using Froude criteria and so there is a factor of $X^{1.5}$ for the Reynolds number (where X is the scale factor). They explain that this means that the onset of separation and vortices would actually occur in smaller flows at full scale.

Sarmiento uses an energy balance approach to show that eddy losses are the main reason that the full theoretical efficiency of a physical OWC cannot be achieved (Sarmiento 1992), as they were not modelled using the techniques common at the time. The eddies completely disappeared when the bell mouth was added, and in addition, the flow was effectively at-rest compared to the complex motions present in the straight tube at the top and bottom of the stroke. These represent a large reduction in losses when moving to the bell mouth entry.

Falnes (Falnes 2002) shows that the Keulegan-Carpenter number can be used to identify whether there is likely to be vortex shedding at the entry:

$$N_{KC} = \pi \frac{|\hat{x}|}{r_{entry}} \quad (2-9)$$

Where N_{KC} is the Keulegan-Carpenter number, \hat{x} is the maximum displacement of the reciprocating flow and r_{entry} is the radius of the entry.

When $N_{KC} < \pi$, laminar flow occurs, but if $N_{KC} \geq \pi$, then vortex shedding will occur with significant viscous losses.

Therefore for laminar conditions to exist and for the absence of vortex shedding,

$$\frac{|\hat{x}|}{r_{entry}} < 1 \quad (2-10)$$

Knott and Flower (1980) state that this ratio should be less than 5 whereas Knott and Mackley also observed that flow separation can occur with a bell mouth of $r_{\text{entry}}=30\text{mm}$ and \hat{x} of 60mm, i.e. a ratio of 2. This satisfies the condition described in (2-9) for vortex shedding, but not the higher value of 5. This suggests that a certain element of vortex shedding is allowable before the losses begin to affect energy transfer.

A full explanation of the Keulegan-Carpenter number can be found in Keulegan and Carpenter 1958 and its application in Falnes 2002.

Eddies can be expected at both the mouth edge of the models and at the start of the helical fins within, and the results of Knott and Fowler and Müller and Whittaker emphasise that the entry should be the focus of design optimisation in the next phase of development.

Weber and Thomas (2001) show in their 2-D and 3-D OWC optimisation models that a 2D OWC with a forward facing opening performs significantly better than a vertically mounted circular tube, and this may be because the forward facing design creates fewer eddies. It would be useful to try to develop a floating directional OWC to see if the performance is improved, or perhaps to consider an underwater structure for directing more of the energy flux into the OWC. The same paper by Weber and Thomas also underlines the importance of optimising all of the operational parameters at the same time as they all affect the performance of the overall device. In this case, the important parameters are the damping of the turbine, the impedance of the collector tube, and the wave input in terms of period and height. Ocean Lynx have also opted for a version of this forward-facing opening design. The tests undertaken for this PhD compare the relative performance of OWC water column configurations, and for ease of construction and comparison, a bottom opening OWC was used.

2.4.3. Helical Fins

In plain tube OWCs, the flow within the chamber is more or less vertical (Knott and Mackley 1979). Adding in the helical fins not only adds an opportunity to create vortices (as described above), but will also modify the flow from purely axial to one that has both an axial and rotational element. In this case the rotation will be about the central vertical axis, and the resultant centripetal forces are likely to create a similar free surface profile as that exhibited by a forced vortex in a vertical cylinder.

This profile means that the mean displacement along each fin is likely to be further away from the central vertical axis than the centreline of the fin. This is similar to the effect of a swirl inducing stator, as fitted to ships, which increases the diameter of the stream tube (Zondervan et al 2011). This is important as the mean displacement can be used to estimate the power production. In Chapter four, the radius of this mean displacement path is deduced.

The fins may also act as lifting surfaces in the same way that an inclined flat plate generates lift when dragged through water (e.g. Massey 1989). In this case a pressure differential could be developed across the fin which would tend to increase any movement of the structure of the device as the lift would likely be generated in the same direction as the flow. Once again this indicates the necessity to optimise the shape of the fins to achieve the optimum performance. For a fixed device, there is likely to be little net impact as each helical tube contains an upper and lower face of a fin and so it will not be investigated as part of the current work.

2.4.4. Capture width

Falnes (2002) defines the width of a wave that an ideal point absorber interacts with as the absorption width, or capture width (CW), and shows that it is:

$$CW = \frac{\lambda}{2\pi} \quad (2-11)$$

Where λ is the wavelength. As an example, a 120m long wave gives a capture width of 19m.

Falnes goes on to show that the theoretical maximum power converted by a point absorber operating in heave is:

$$P_{(\max)} = 0.5 \frac{\lambda}{2\pi} P_i \quad (2-12)$$

i.e. $\frac{1}{2}$ of the incident power in the capture width, where P_i is the power in a unit length of wave crest in kW/m.

Using surge instead of heave results in:

$$P_{(\max)} = 0.5 \frac{\lambda}{\pi} P_i \quad (2-13)$$

i.e. 100% of the power in the capture width.

And using both surge and heave:

$$P_{(\max)} = 0.5 \frac{3\lambda}{2\pi} P_i \quad (2-14)$$

A point absorber must be small compared to the wavelength in order to take advantage of this property, and they are usually defined as having a diameter of less than $\frac{1}{4}$ of a wavelength ($< \lambda/4$) (Cruz 2008).

It is clear that a machine capable of operating in both heave and pitch will be more effective at capturing energy than one operating only in heave. It is a goal of the

development of this OWC to try to achieve this.

2.4.5. Physical Modelling

Physical modelling is a useful technique for understanding complex systems which cannot be reliably modelled numerically. In the context of ocean systems, any device that floats or extracts energy from surface waves should go through a process of physical modelling. This process provides a good indication of performance, motions and loading, and these can be scaled up to aid the design process and to predict full scale techno-economic performance.

The results of physical modelling are often used to validate a numerical model, or to provide empirical data for use in a semi-empirical numerical model. These numerical models are then used to scale up the results with confidence and can be compared to mathematical predictions based on the physical results. Importantly, physical models are often used to select the optimum physical characteristics of a device.

Physical models are also a useful tool when understanding the fundamental phenomena that occur in a machine. A well conducted series of tests can be used to build up a detailed understanding of how the various phenomena interact and this is invaluable when designing large scale machines. A series of tests should therefore include investigations that identify the effects of altering one parameter at a time. Examples include limiting the degrees of freedom (direction) in which a model can move; altering the geometry and orientation of the model; and varying certain physical properties like the power-take-off (PTO) damping and the input wave.

2.4.5.1. Previous studies

There have been numerous studies of OWCs over the years, and these have focussed on every element of the system, from the hydrodynamics of a simple tube described in section 2.4.2 to the shape of the OWC Chamber (eg Dizadji and Sajadian 2011 and Müller and Whittaker 1995) to the effectiveness of the PTO (e.g.

Curran et al 1998, Falcao et al 2010 and Korde 1997) and the optimisation of the control regime (e.g. Falcao and Justino 1998, Falnes 2002a and Sarmento et al 1990). These have been developed into techno economic models (e.g. Dalton and Lewis 2011, Babarit et al 2012 and Arup 2007).

The most relevant work for informing this current work is that done on small scale models, and a brief overview is given here:

Sarmiento (1992) carried out a series of experiments to determine the efficiency of an OWC and to validate a numerical model. He measured the reflected and transmitted waves and used an energy balance method to calculate the absorbed power. He also calculated the efficiency and observed that this was lower than in the absorbed power. He concludes that the difference was dissipated in other losses, largely by vortex shedding. He also tried two different versions of the model, one with a bottom opening, and the other with a rear wall that reached the floor of the flume. He showed that the maximum efficiency for the bottom opening version was 50% and the one with a rear wall was 100%. The models tested in this PhD are of the bottom opening kind and therefore the maximum efficiency that can be expected is 50%. He showed that the depth of the device affected the period that the maximum efficiency occurred at, with minimal change to the maximum value. He explains that deeper machines have more water entrained in them, and hence higher inertial values. This decreases the natural frequency and also narrows the breadth of the curve. Sarmento is presumably referring here to the fact that mechanical resonant frequencies are proportional to $1/\sqrt{m}$ (Main 1998):

$$\omega_0 = \frac{1}{2\pi} \sqrt{\frac{K}{m}} \quad (2-15)$$

Where ω_0 is the natural frequency, K is the spring constant and m is the mass.

Since the mass is governed by and proportional to the length of the OWC, the length of the tube clearly affects the resonant length. The relationship is likely to be:

$$\omega_0 \propto \frac{1}{\sqrt{L}} \quad (2-16)$$

This can be written in terms of the period:

$$L \propto T_{res}^2 \quad (2-17)$$

Which corroborates the hypothesis that the draft will be related to the coupling length in a similar form to equation 1-1. This is discussed in detail in Chapter 5.

Using a helix will reduce the draft without reducing the resonant length, so it removes the proportional relationship between L and m as the amount of water in the system was less but L was constant. It is thought possible that the resonant period will change whilst the breadth of the response is kept as wide as for the plain tube version with the equivalent draft.

Ajai Ahluwalia describes some initial tests on the helical OWC in Ahluwalia 2006. His tests were inconclusive, but showed that the double twist helical model (the fins executed 2 turns from bottom to top of the model) performed less well than the single twist model (the fins executed one turn from the bottom to the top of the model) or the plain tube model with no helix inside. These tests did not achieve peak performance, highlighting the importance of matching the turbine simulator impedance to the radiation damping of the OWC (Falnes 2002). The models were used for the early tests in the current project, and my thanks go to Ajai for his work.

Everyone who has compared physical and numerical models of OWC has achieved a reasonable degree of correlation between the results (e.g. Sarmiento 1992, Lopes 2009, and Curran et al 1997), so it can be expected that a similar effect will be found

in the current work. The difference between the numerical and physical results is usually put down to the fact that the eddy losses aren't described adequately in the numerical models (Sarmiento 1992). Zhang et al (2011) confirmed this when they used a CFD analysis to compare the results of Evans and Porter's potential flow model (Evans and Porter 1995) with both Morris-Thomas et al's physical model results (Morris-Thomas 2007) and their own CFD model. Even this advanced procedure resulted in an overestimate compared to the physical results, although it was much closer than the potential flow model by Evans and Porter. It is expected that the numerical model developed as part of this current work will overestimate the results to some degree, but that the numerical and physical results will be reasonably close.

2.4.5.2. Wave measurement

In order to calculate the efficiency of the device, the incident wave power must be known. The wave height and period must be known to calculate this.

Waves in a flume or tank are naturally altered when a model is put into the water. It is possible to use 2 (monochromatic) or 3 (polychromatic) probes to calculate the reflected wave, however building and integrating a system of this type is beyond the scope of this PhD.

If the waves can be created in a repeatable fashion, then the tank can be calibrated at a particular point without a model, and the calibrated values of H and T can be used to calculate the incident power.

Measurement is usually done with wave probes using two wires that pierce the water surface. These probes can be resistive or capacitive, and in both cases, the voltage varies as the water rises and falls and is measured. The probes can be calibrated to produce a (linear) transfer function which shows that the relationship between voltage and surface elevation. With this relationship known, it is possible to

measure waves to within a ± 1 mm accuracy (Kofoed and Frigaard 2006). This error is due to the meniscus caused by surface tension. The voltage – elevation relationship becomes non-linear towards the end of the probes, especially in the last 10% of the length, so it is better to use the middle 50% of the probe's length for the best accuracy.

Wave probes of this type require frequent recalibration as they suffer from oxidation and deposition from the water that alter the conductive properties of the metal. If a DC current is used, then they can also suffer from the anode-cathode effect where material from the anode is deposited onto the cathode. It is usual to use an AC system whether using a resistive or capacitive system. The AC frequency used determines the resolution of the data, so it should be significantly higher than the wave frequency.

2.4.5.3. Scaling Laws

In order for physical modelling to be useful, there are detailed laws of similarity that must be followed. Usually the model is geometrically similar to the large scale prototype. The model also has to be dynamically and kinematically similar (Chakrabarti 1994 & Chanson 1999) for motions, velocities and forces to be scaled up.

Types of similarity

- Geometric Similarity: All lengths are scaled with a geometric scale factor of 1:X and all angles are the same, so the model and prototype are the same shape.
- Kinematic Similarity: All the motions of the model are similar to those of the prototype so that the magnitude and direction of velocity and acceleration are scaled correctly.
- Dynamic Similarity: Forces and pressures are similar for the model and are scaled to represent the magnitude of the prototype forces.

Standard dimensionless numbers are used to ensure that similarity exists. Each of these parameters is linked to a certain phenomenon and must have the same value at model scale and prototype scale to ensure similarity.

Typical parameters used for ocean engineering are:

Name	Property	Note: It is impossible for all of these corresponding numbers to be the same for a given test, and it is important that the limitations (scale effects) of the test are understood. The larger the scale factor, the larger the discrepancy between the properties.
Reynolds Number	Inertia/Viscosity	
Froude Number	Inertia/Gravity	
Weber Number	Surface Tension	
Keulegan Carpenter Number	Inertia/Drag	
Mach Number	Elasticity	
Euler Number	Pressure	

Table 2-1 Typical dimensionless groups used in scaling.

The most significant property is chosen as the primary scale factor and any limiting scale effects can be accounted for in order to draw useful data from the models.

For example, in naval architecture, Froude number similarity is used as the inertial and gravitational forces dominate the system and it can be assumed that elastic, surface tension and pressure forces are negligible in comparison. The scaled results are corrected using empirical data relating to viscous drag. At small scale, the surface tension becomes significant, limiting the scale of model that can usefully be used. Scaling air compressibility for a WEC using an air turbine PTO is challenging as air flow scales with Reynolds number, and there may well be significant viscous damping of the structure. These problems can be addressed in various ways, either by altering the test strategy, experimental set-up, or with post test analysis, e.g. computational fluid dynamics (CFD), which can be calibrated using a small scale physical model and used to scale up the results.

Recommendations for tests that achieve these aims can be found in (EMEC 2009, Vassalos 1999 & IEA-OES 2003). If these recommendations and scaling laws are followed then a high degree of confidence in the results can be expected.

As discussed above, the Keulegan-Carpenter number is important if eddy losses are to be eliminated from the models.

Froude Number Scaling

The Froude number, Fr , indicates the relative importance of inertial forces acting on a fluid vs. the gravitational force due to its weight. It is defined as:

$$Fr = \sqrt{\frac{\text{inertial force}}{\text{gravity force}}} = \sqrt{\frac{\rho L^2 u^2}{\rho L^3 g}} = \frac{u}{\sqrt{gL}} \quad (2-18)$$

Where u = characteristic velocity and L = characteristic length

For similarity, the Froude number of the model, Fr_m , and prototype, Fr_p , must be the same, therefore

$$Fr_m = \frac{u_m}{\sqrt{gL_m}} = \frac{u_p}{\sqrt{gL_p}} = Fr_p \quad (2-19)$$

Reynolds Number Scaling

The Reynolds number of the model becomes the most important parameter when viscous forces are dominant. The Reynolds number indicates the relative importance of the inertial forces acting on the fluid vs. the viscous forces. i.e.

$$Re = \frac{\text{inertial force}}{\text{viscous force}} = \frac{\rho L^2 u^2}{\mu u L} = \frac{\rho u L}{\mu} = \frac{u L}{\nu} \quad (2-20)$$

Where u = velocity, L = length,

$$\mu = \frac{\tau}{\left(\frac{du}{dy}\right)} = \text{dynamic viscosity (the ratio of the shear stress and the velocity,}$$

gradient perpendicular to the flow) and $\nu = \mu/\rho$ = kinematic viscosity (Massey 1989).

As with Froude number similitude, the Reynolds number at model scale Re_m , must equal the full scale, prototype Reynolds number, Re_p :

$$Re_m = \frac{u_m L_m}{\nu_m} = \frac{u_p L_p}{\nu_p} = Re_p \quad (2-21)$$

In wave energy applications, Reynolds number similitude is not often used as it is generally accepted that the inertial forces dominate (EMEC 2009 & Chakrabarti 1994). Viscous forces are present, however, both when movement of the water or structure becomes significant, and also in the air flow.

It is not possible to have Froude number and Reynolds number similarity at the same time so, as with naval architecture, the usual course of action is to use Froude number scaling, and to try to compensate for Reynolds number effects afterwards.

To highlight the differences, the geometric, kinematic and dynamic scale factors for both Froude and Reynolds number similitude are summarised in Table 2-2.

Characteristic	Dimension	Froude No.	Reynolds No.
Geometric			
Length	[L]	X	X
Area	[L ²]	X ²	X ²
Volume	[L ³]	X ³	X ³
Rotation	[L ⁰]	—	—
Kinematic			
Time	[T]	\sqrt{X}	X ²
Velocity	[LT ⁻¹]	\sqrt{X}	X ⁻¹
Acceleration	[LT ⁻²]	—	X ⁻³
Volume Flow	[L ³ T ⁻¹]	X ^{2.5}	X
Dynamic			
Mass	[M]	X ³	X ³
Force	[MLT ⁻²]	X ³	—
Pressure	[ML ⁻¹ T ⁻²]	X	X ⁻²
Power	[ML ² T ⁻³]	X ^{3.5}	X ⁻¹

Table 2-2, Similitude scaling ratios.

2.4.5.4. Power Scaling Example

For Froude number similarity and a 1:50 scale model, the average power at model scale (say 0.5W) can be used to predict full-scale performance. Power scales with X^{3.5}, Power = 50^{3.5} x 0.5W = 442kW. In reality, the air power cannot be properly scaled by using this method as discussed above. The performance of the device will be less than this when factors such as air compressibility, turbine and generator losses are taken into account. Nevertheless, this method gives a useful estimate of the power output for a full scale machine.

Air at small scale is effectively incompressible, which leads to an over-estimate of device performance when using this method to scale up. Weber (2007) estimates that the mean annual performance may over-estimated by about 10%. This can easily be incorporated into the scaling of power and is used in Chapter 5.

Weber simulated the effect of compressibility at small scale using an additional volume of air attached between the water chamber and the PTO to increase the effective air volume being compressed and so reproduce compressible effects. He concludes that this is impractical for floating models as volume required is large (200 – 700 litres) and the pipe work required to link a barrel to the model dominates the motions of the device, altering its performance. It is not considered necessary to reproduce this method for the current device as the comparative performance will not be affected by the incompressibility of air.

2.4.6. Mathematical Modelling

2.4.6.1. Introduction

There are several numerical techniques for modelling an OWC. Theoretical models are fluid flow models that are developed from fundamental principles, including conservation of mass, momentum and energy. A basic model for fluid flow can be made using Bernoulli's principle of conservation of energy and Newton's laws of motion. For more complex models, Navier-Stokes equations are required but these are complex and computationally expensive (in both time and hardware) and are the basis of CFD. They can be simplified into the Euler equations by neglecting the viscosity term and simplified further by neglecting vorticity, which is the basis of potential flow theory.

Potential flow theory has traditionally been used to solve simple flow problems before the advent of CFD and is still used as a good compromise between accuracy and expense (time, software and hardware) to solve complex flow problems today (Evans and Porter 1995).

Another good compromise is to make the analogy between a forced oscillator and an OWC. In this case, the free surface is replaced by a massless piston, actuated by the force of the waves impinging on the machine. The force of the waves is equated

to the inertia of the water inside the column and the added mass outside; the damping force (due to friction and radiation of waves); and the restoring force due to the compressibility of the system, (notably of the air in the plenum chamber). This method was developed by Evans (1978) and has been developed since and described in many papers and textbooks e.g. Korde 1997, Watabe 2007, Brendmo McCormick 1981, and Lopes et al 2009. Lopes notes that an important adjustment of this method is to include a non-linear term to account for the eddy losses.

Sarmiento shows that the difference on power production between linear waves and nonlinear waves is minimal (Sarmiento 1992), and the use of linear waves is acceptable in numerical simulations. In the current work, some of the waves generated in the flumes and tanks were non-linear, either due to the steepness of the waves, or due to the wavelength – tank depth ratio. Based on Sarmiento's conclusions, it was expected that the physical and numerical results would be directly comparable.

2.4.6.2. Mathematical Models

Mathematical modelling is a useful technique that allows for device optimisation, simulation and scaling.

The usual techniques for modelling OWCs and other WECs are:

- Forced Oscillator
- Potential Flow
- CFD (Navier Stokes)

Forced Oscillator

Forced Oscillation models assume that the system is entirely linear, so they have to be calibrated using empirical data before they can be used. These models are best suited for simulation of full scale systems as they are quick to run, so changes to wave input or control strategies can be readily tested.

A simplistic model (e.g. Falcao 2007, Brendmo et al 1996, McCormick 1981 and Curran Et al 1997) can be built up from Newton's first and second laws in the same way that the equation of motion is derived:

$$F_e = F_m + F_d + F_s \quad (2-22)$$

i.e. the excitation force equals the inertial force plus the spring force plus the damping force. This can be re-written as:

$$F_e = m\ddot{x} + d\dot{x} + kx \quad (2-23)$$

and with care, and calibration from physical modelling results, a numerical model of the system can be built up that accounts for many of the non-linearities in a WEC system.

The details are explained in many texts, but Watabe has produced a clear example of how this analysis can be used to model a fixed OWC (Watabe 2007). This is the method used in this thesis and is described in detail in Chapter 6 and was modified to simulate the performance of the models.

Potential Flow

Potential flow models are also reasonably quick to run, and like forced oscillation models, assume that the input wave is linear (e.g. Evans and Porter 1995 and Falnes 2007). Potential flow theory is a simplified version of the Navier Stokes equations, and assumes that viscosity and vorticity are negligible. Many commercial programs use potential flow to solve problems (e.g. WAMIT, Ansys AQWA, DNV and Orcaflex) and typically use the Boundary Element Method to solve for forces and pressures at boundaries, making them reasonably quick to run as they do not solve for the fluid flow in the whole domain. This makes them more useful for evaluating the performance of devices which have mechanical PTOs rather than pneumatic

ones as an assumption has to be made about the position of the free surface within the OWC chamber, the compressibility of air and the turbine characteristics. They are also useful for modelling mooring and panel loads. Panel loads are the distributed loads experienced by surfaces of vessels floating in the sea. They can be due to impact or differential hydrostatic pressure across a wall. These methods tend to give frequency domain, or time-averaged, solutions meaning that they do not identify any of the non-linearities in the system, like transient events.

Navier Stokes

CFD codes generally solve the Navier Stokes equations for a system. This gives the closest approximation to a physical system, but requires a significant amount of processing power to solve problems in reasonable timescales as it solves in the time domain. CFD models can provide good results, especially for fixed models, but they also require validation to ensure that the results are sound. CFD models are very good for optimising the geometry of a device, and also for scaling up results with confidence. However, modelling the effect of waves and the two phase flow characteristics of OWC devices using a CFD code is very challenging. The Navier Stokes equations can be simplified by omitting the viscous terms (Euler) or by linearising them (Stokes). Both of these simplifications speed up the computation time required.

2.5. Conclusions

2.5.1. About 14% of the UK's electricity could be produced from wave energy.

2.5.2. To ensure valid comparison, the models were fixed with:

- a) The same draft
- b) The same resonant frequency

In all cases, it was important to test at optimum performance (i.e. peak efficiency), so the optimum PTO impedance should be used.

2.5.3. The shape of the models will affect their efficiency, so curved inlets should be used. Although a side entry OWC would perform better than a bottom opening one, a bottom opening version will be used as it is easier to ensure similarity between the models with a helix and those without.

2.5.4. A forced oscillator model will be used for numerical analysis of the device.

Chapter 3: Flume Tests

3. Introduction

This chapter presents the results of preliminary model OWC tests at Coventry University during the period 6th - 10th November 2006. These tests were designed to test the experimental set up, familiarise the author with the models and tank testing, and to prepare for more conclusive tests. These conclusive tests were carried out with an improved setup and are described in Chapter 5.

Three model OWCs were tested in a wave flume at Coventry University (Figure 3.1). The aim of the tests was to compare the performance of three models to determine the effect on performance of introducing a helical structure into the tube.

The hypothesis to be tested was that since the water path is compressed into a helix, the resonant coupling length could be achieved in a device with a shallower draft. Energy in water waves decreases exponentially with depth below the surface, so reducing the draft of an OWC could expose it to a greater incident energy density. If the performance of a helical vs. a plain OWC of the same resonant coupling length could be shown to be similar, or better, then there could be significant savings to be made in deploying these more compact devices.



Figure 3.1 Three model OWCs: Plain tube (P) (left), double twist (D) with a turbine simulator and pressure taps fitted (centre), single twist (S) (right).

In order to simulate the performance of a Wells turbine (which is characterised by constant impedance at constant rotational speed (Figure 3.2), three rubber discs with a cross cut into each of them (concentric with the centre) were used.

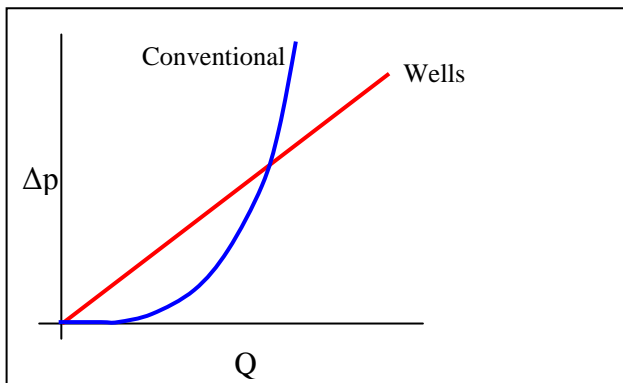


Figure 3.2: Impedance characteristics for a conventional reaction air and Wells turbine (Curran et al 1998 and Gato and Falcao 1999) showing pressure drop (Δp) against flow rate (Q).

These crosses formed four flaps (Figure 3.3 and Figure 3.1) that were free to open and close as dictated by the flow rate, thus altering the cross sectional area of the hole through the simulator. As the area of this hole increases with flow rate, the impedance remains constant, unlike an orifice plate where the impedance increases in proportion to the square of the flow rate (Ower and Pankhurst 1977). The slits of

the three crosses were 10cm, 12.5cm and 15cm long (measured from the centre to the end of the slit, see Figure 3.3) and the simulators will be referred to by these dimensions from now on. The 15cm simulator is shown in Figure 3.1.

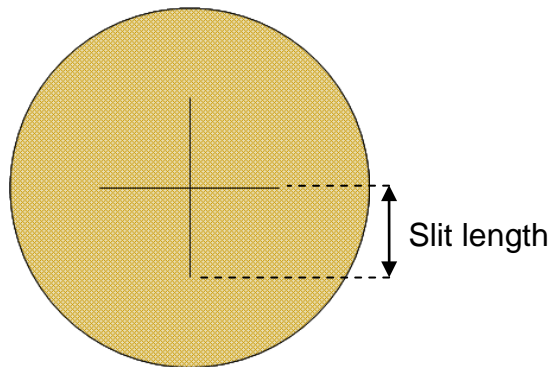


Figure 3.3 Schematic of the rubber slotted simulators.

3.1.1. Key

As shorthand, the following abbreviations have been allocated to the model / simulator combinations:

Slit length	10cm	12.5cm	15cm
Plain	P10	P12.5	P15
Single twist helix	S10	S12.5	S15
Double twist helix	D10	D12.5	D15

Table 3-1 Key to abbreviated names.

3.2. Power calculation

These Wells turbine simulators were calibrated to define the relationship between pressure drop, Δp , and flow rate, Q . This allowed the measurement of Δp across the simulator during the tests to determine Q and therefore the power, P_{air} , available in the air flow where:

$$P_{air} = Fv \quad (3-1)$$

where F =force on the simulator disc, v =velocity of the air flowing through the simulator disc and:

$$F = \Delta p A_d \quad (3-2)$$

where A_d = cross sectional area of simulator disc and:

$$Q = A_d v \quad (3-3)$$

Therefore P_{air} is:

$$P_{air} = \Delta p Q \quad (3-4)$$

and

$$Z = \frac{\Delta p}{Q} \quad (3-5)$$

(Price et al 2009) Where Z is the impedance (also known as the applied damping) of the turbine.

So finally P_{air} is:

$$P_{air} = \frac{\Delta p^2}{Z} \quad (3-6)$$

Expression 3-6 was divided by the calculated power of the incoming wave (equation 2-6) to generate instantaneous efficiencies:

$$\eta = \frac{P_{air}}{DP_i} = \frac{\Delta p^2}{Z \cdot 0.14 \cdot 0.98 H^2 T} \quad (3-7)$$

For monochromatic waves, where D = the model diameter, 0.14m.

3.3. Turbine simulator calibration

The turbine simulators were calibrated against an orifice plate to enable the determination of the flow rate through the simulators by measuring only the pressure difference across them. The test rig is shown in Figure 3.4.

3.3.1. Method

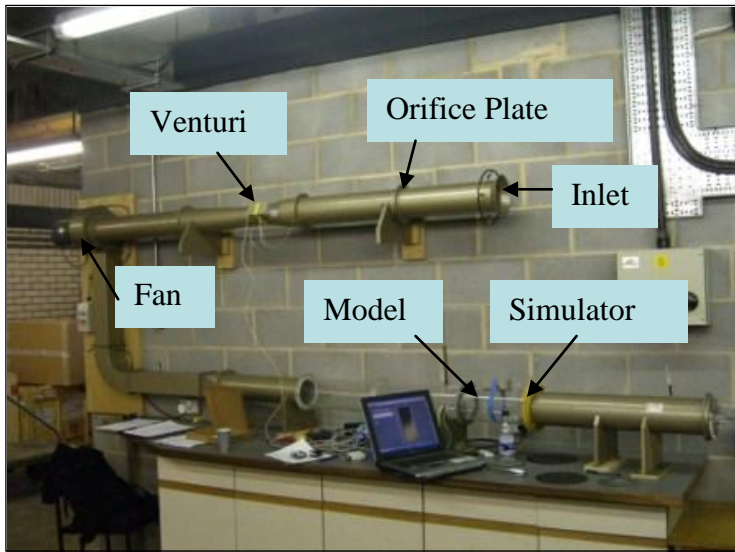


Figure 3.4 Calibration rig with the various components labelled.

Firstly an orifice plate was calibrated against a known Venturi to determine its Coefficient of Discharge (C_d), and using Bernoulli's equation, the flow rate for a series of pressure drops across the plate was calculated (Ower and Pankhurst 1977 & Massey 1989).

$$\frac{p_1}{\rho_a} + \frac{u_1^2}{2} + gz_1 = \frac{p_2}{\rho_a} + \frac{u_2^2}{2} + gz_2 \quad (3-8)$$

Where p_1 is the upstream pressure, p_2 is the downstream pressure, u_1 is the upstream velocity, u_2 is the downstream velocity, z_1 is the upstream height above datum, z_2 is the downstream height above datum and ρ_a is the density of air.

The difference in head due to gravity is considered negligible, so this can be re-written:

$$Q = C_d \cdot A_1 \left[\frac{2}{\rho_a} \frac{(p_1 - p_2)}{(A_1 / A_2)^2 - 1} \right]^{\frac{1}{2}} \quad (3-9)$$

Where the A_1 is the area of the pipe, and A_2 is the area of the orifice is area, and C_d is the Coefficient of Discharge.

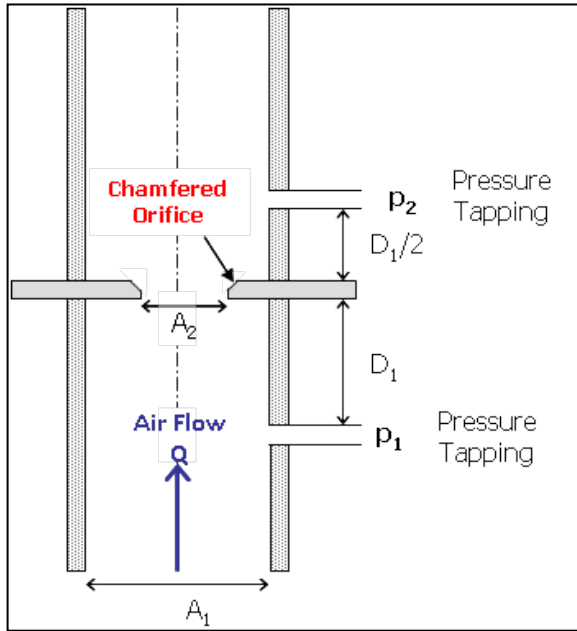


Figure 3.5 Schematic of a standard orifice plate showing variables in equation 7

This orifice plate was then used to measure the flow rate through the simulator discs at various pressure drops between 70 and 480Pa. The results are presented below.

3.3.2. Instrumentation

Two ± 10 mbar differential sensors from Sensor Technics (Datasheet for BSDX0010d4d) were used. The 12 bit analogue to digital converter gave 4096 steps over the 20 mbar range of the sensor, meaning that each step was 4.9×10^{-3} mbar, or 0.49 Pa, which was considered sufficient for these experiments. According to their specification, these sensors were accurate to within $\pm 1\%$ of the full scale range for the conditions in which they were used. These sensors were chosen as the maximum pressure expected was expected to be significantly smaller than that created by a column of water of equal height to the largest wave which was about 0.1 m. The pressure at the bottom of 0.1 m of water ($p = \rho gh = 1000 \times 9.81 \times 0.1 \approx 100$ mbar), and the pressure drop across the simulator was not expected to be more than 10% of this. The electronics for the sensors were set up by AJ Ahluwalia and are described in detail in (Ahluwalia 2006).

The sensors were attached to the pressure taps on the calibration rig and models by short, flexible, small bore pipes (Tygon R-3603) designed to transfer pressure readings without distortion due to compression in the connecting pipes. The simulator pressure taps were mounted 10 mm either side of the simulator disc.

The sensors were connected to a 12 bit LabView data logger sampling at 50 Hz.

The data were captured and recorded by a LabView program that was written for the purpose.

3.3.3. Calibration results

Three simulators were calibrated against an orifice plate with a known C_d of 0.63, to give the graph in Figure 3.6 below. Each of the simulators had a cross cut across the centre with cut lengths of 10 cm, 12.5 cm and 15 cm respectively.

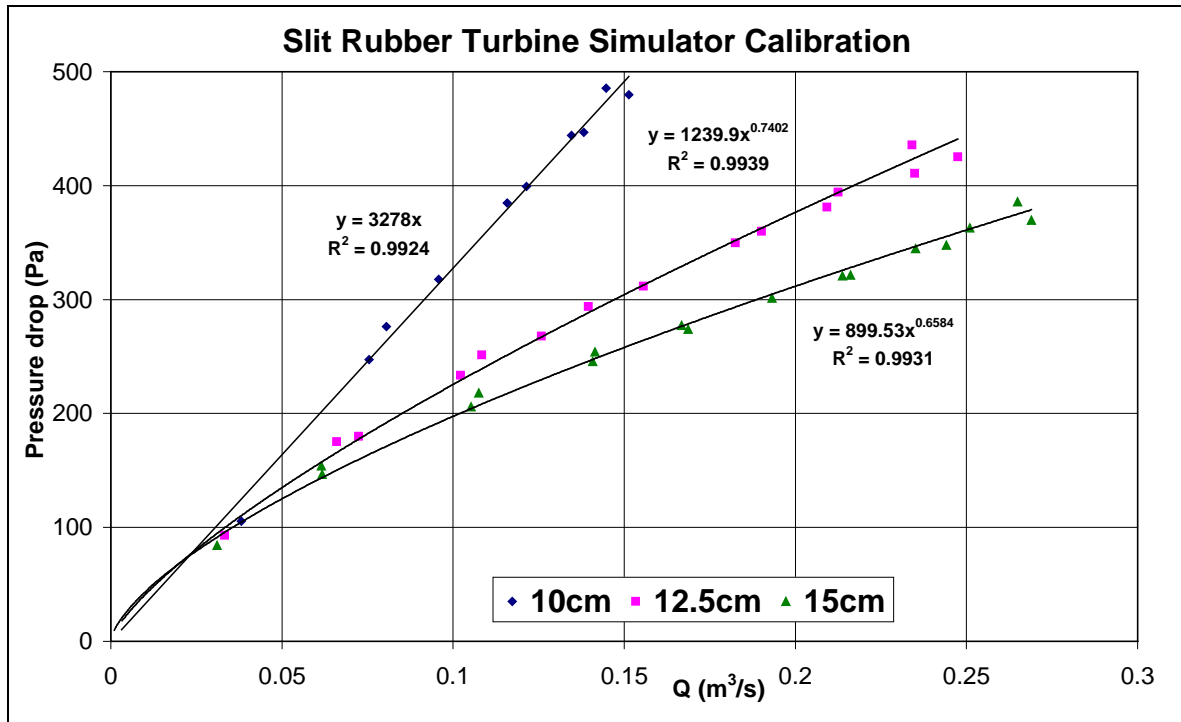


Figure 3.6 Characterisation of the three simulator discs showing pressure drop against flow rate.

The impedance, Z , is given by $\Delta p/Q$, so the gradient of the lines gives the value of Z for each of the simulators.

The 10cm simulator showed a linear response (i.e. constant Z) across the range of pressure drops tested, whereas the other two showed some non-linearity below around 200Pa. This would suggest that the 12.5cm and 15cm simulator discs displayed varying stiffness below 200Pa with slightly stiffer behaviour at lower values of Δp than at higher values – perhaps as the faces of the cuts were in contact at these low pressure drops and the increase in friction increased the impedance. Another possibility is that since the rubber drooped somewhat at rest, especially for the 15cm version, then a certain pressure differential was required to close the slits before then opening the simulator the other way. The simulators were calibrated in a horizontal orientation (due to the test rig) where this effect would have led to the shape of the graphs in Figure 3.6. When used with the model OWCs, they were mounted vertically, and the reciprocating nature of the flow would have meant that at low flowrates, the impedance was not consistent for both directions. In turn this led

to higher flowrates in the downward direction, giving the higher peak pressures in the downward direction as shown in Figure 3.16 below. This asymmetric pressure drop is not representative of a real turbine, and is a reason for choosing a different simulator for later tests.

It should be noted that a root mean squared (RMS) Δp greater than 6.7Pa (for P10 at a wave period of 0.935s), was never achieved during the flume tests, so all of the results below are based on the extrapolations shown in Figure 3.6. It is also interesting that the lines converged in this region, giving similar gradients and therefore values for Z for the all of the simulators.

Using the equations in Figure 3.6, 6.7Pa, the flowrate through the 10cm simulator was $0.02\text{m}^3/\text{s}$.

Differentiating the three equations in Figure 3.6 gives the gradients (i.e. impedances) of the lines and these were:

Slot length	Gradient at $0.02\text{m}^3/\text{s}$ ($\text{Pa.s}/\text{m}^3$)
10cm	3278
12.5cm	2522
15cm	2237

Table 3-2 Slotted simulator impedances at low flowrates.

There is clearly a difference between the models' performances with the different simulators fitted, so the small differences here are critical to performance. The fitted lines are a source of errors in the results in section 3.4.5. and it was determined to find a better simulator method for the tests outlined in Chapter 5.

These errors notwithstanding, the simulators clearly provided different impedances for the models and so the results are still useful for comparing the effect of using low

impedance and high impedance simulators, and for testing the different models against each other with the same impedance.

It was clear that future simulators should be more representative at working pressures. To facilitate this, a stiffer material and smaller diameter could be used in order to ensure that they retain a linear pressure-flow relationship over the flow regime of interest, and that they don't droop under their own weight. Another possibility is to use a spinning, slotted simulator which also has constant impedance at constant RPM (White 1991). This solution was eventually used in the later tests as described in Chapter 5.

3.4. Flume experiments

3.4.1. Models

The models were designed and drawn using Solid Edge, and the resulting 3D images were then made in the rapid prototyping facilities at Loughborough University.

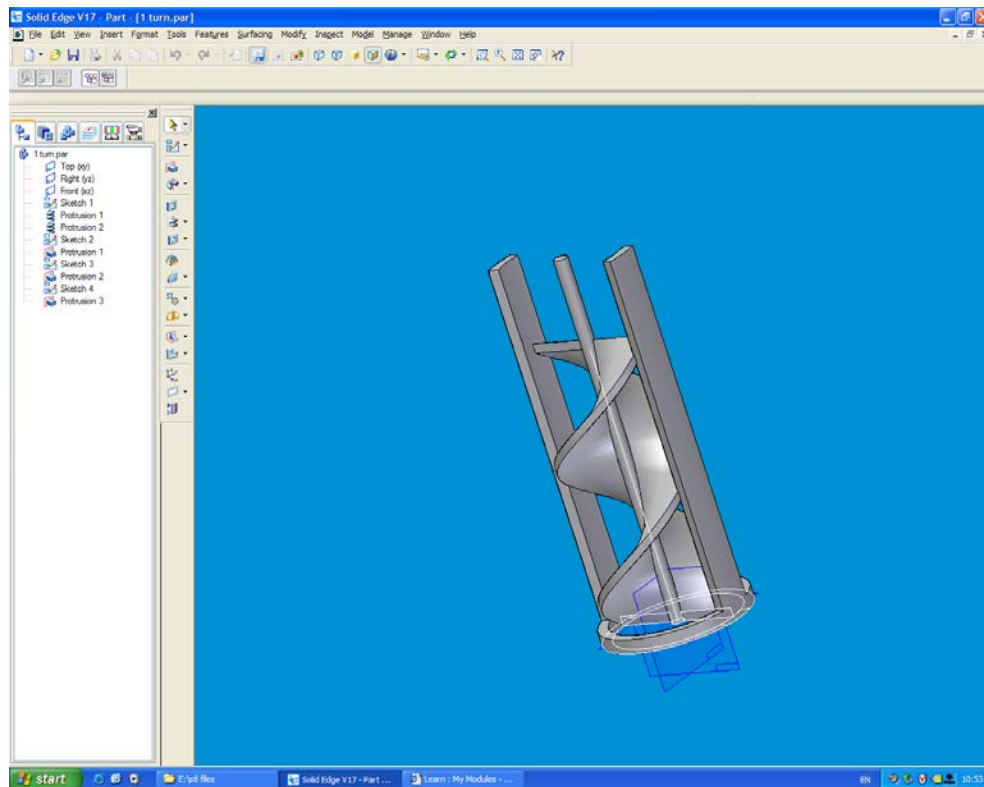


Figure 3.7: Solid Edge 3D view of the single twist model.

The rapid prototyping involves sintering successive layers of powder in a fluidised bed. After each layer is sintered, the platen on which the model stands is lowered by about one millimetre and the next layer is sintered to it. This process leaves steps in the material as shown in Figure 3.8.



Figure 3.8: Detail of stepped construction of fins within one of the model OWC tubes with an internal helix.

The surfaces were filled with a combination paint and filler, but this still left steps in the helical fins. This had the effect of increasing the viscous damping and raising the surface roughness to a level that made Reynolds number scaling impossible as described in Chapter 2. The decision was taken to use a smoother finish for future tests.

Following painting, walls cut from a Perspex tube were fitted to each side of the model and fixed in place using waterproof silicone sealant.



Figure 3.9: Three OWC models, assembled: plain tube (left), single twist helix (centre), double twist helix (right).

3.4.2. Setup

When preparing the flume, it was first necessary to repair the seal around the paddle. Some rubber was sourced and new seals that work on the same principle as windscreen wipers were made. This allowed tests to be run with minimal flow through the tank, and eliminate the steepening of the waves that occurred due to the waves running in the opposite direction to the current that was observed in the initial, pre-test trials of the flume

The next task was to build a beach to absorb as much of the energy that reached the end of the tank as possible. A perfect absorber allows tests to be carried out for longer, giving longer data sets. The beach was made from coarse, sharp hardcore about 30mm across, laid with a shallow incline starting about 1.5m from the end of the tank. The top of the beach can be seen in Figure 3.10.



Figure 3.10 Rear end of flume, showing beach.

In tests, more than 90% of the wave height was removed by the beach, except for the very longest period waves, where this was reduced to about 70%. In order to minimise this effect, periods of less than 1.5s were used where possible, and the test times for wave periods greater than 1.5s were reduced to 4 wave periods following the initial setting up of the waves in the flume.

Finally, prior to commencing the tests, the variator (which controls the speed of oscillation of the wave-making paddle) was calibrated to allow the accurate selection of a particular wave period.

This was done by setting the dial, and then timing 20 waves and then calculating the average. To check the consistency and ensure accuracy, the calibration was repeated 3 times for each period and the average of the three periods noted was plotted against dial setting in Figure 3.11.

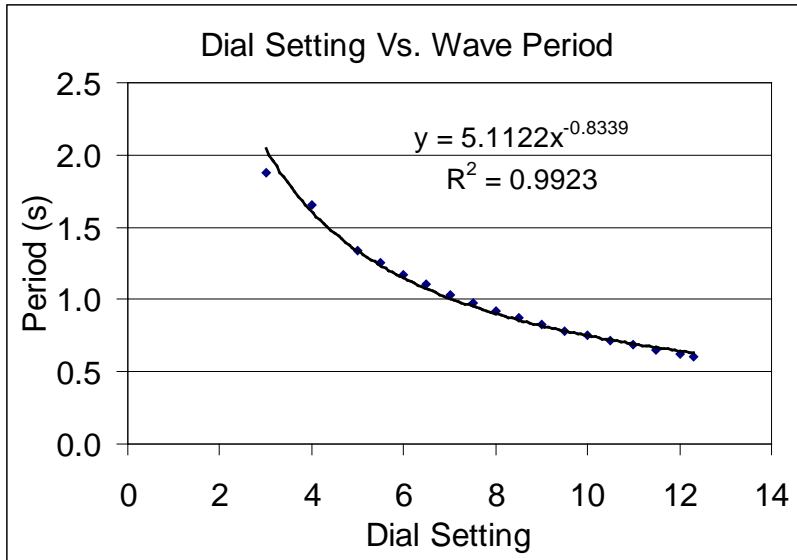


Figure 3.11 Variator dial to period transfer function.

The same process was carried out for the wave height. Although possible, it was not practical to alter the position of the crank that moved the wave flap. The crank was positioned by moving a bolt along a slot in a spinning disk. Once moved, accurate repositioning of the crank was considered unlikely, so it was decided to use only one crank position.

Figure 3.12 shows the effect on wave height of removing the model from the flume.

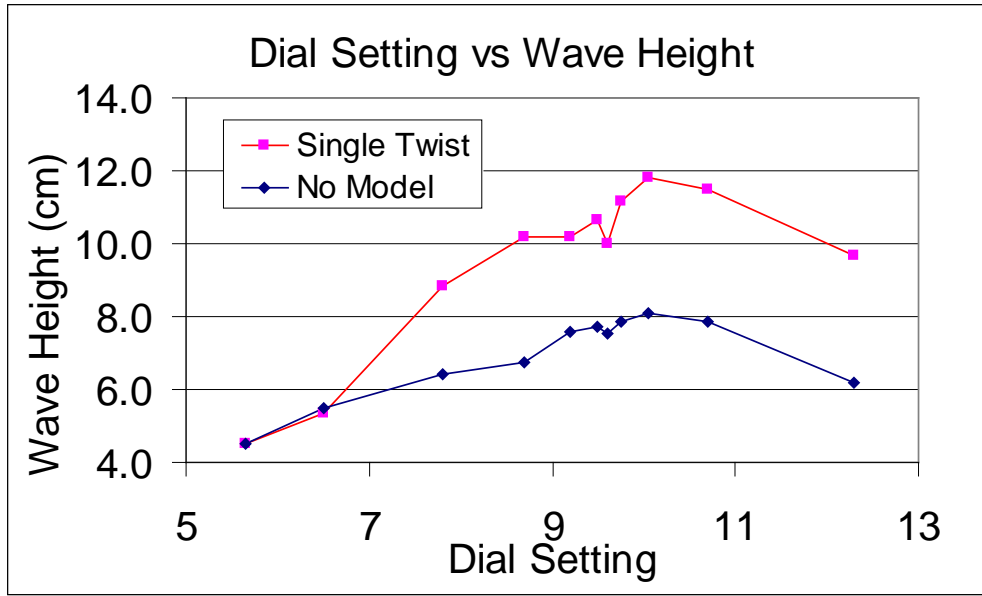


Figure 3.12 Wave height vs. dial setting.

The model was clamped in position on the flume. The draft of the model could be adjusted using vertical screw adjusters, thus allowing a high degree of accuracy when selecting a draft (Figure 3.13).

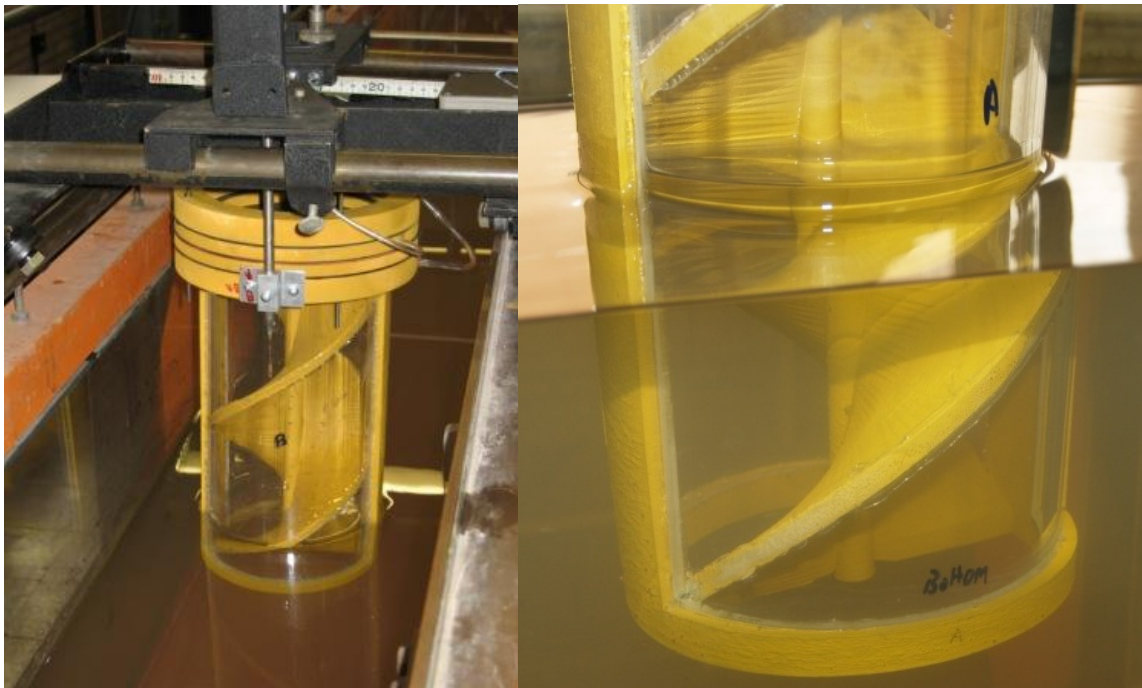


Figure 3.13 Flume, showing model in test position (left) and close up (right).

The series of periods from 0.605s to 1.88s were chosen based on the theoretical resonant coupling length. The series had more points taken near the expected region of resonance, in order to define the peak performance more precisely.

In order to carry out the tests at least two people were needed, due to the length of the tank (Figure 3.14); one person to set and run the variator, and another to run the data acquisition software.



Figure 3.14 Long view of flume showing incident waves, model and laptop with data acquisition software.

3.4.3. Instrumentation

The same pressure transducers and data logger that were used for the calibration tests were used again, and the LabVIEW program was modified to present more of the data in real time as well as carrying out more of the calculations in real time.

3.4.4. Method

Two groups of tests were carried out:

1. All three models with the 10cm simulator
2. All three models with the 15cm simulator

There was slight leakage around the seal of the wave maker, so the level of the water fixed using the flume's overflow water-level regulator.

There was no time to test with the 12.5cm simulator,

A range of plain, regular waves were used with periods between 0.605s and 1.88s. The pressure drop across the simulator was noted, and the RMS value calculated. By inserting these values and their corresponding flow rates, from the calibration in section 3.3, into equation 3-6, the power available in the air flow was measured by the simulator.

Note on shallow water

Taking shallow water to be $\lambda/4$, where λ is the wavelength of the incident waves, it should be noted that when using a water depth of 380mm, every test with $T > 0.975$ s occurred in shallow water. This is because the wavelength increases with period, whereas the depth remained constant.

Shallow water effects include slowing the wave velocity, c (i.e. reducing the wavelength), and increasing the wave height, H . In general, shallow water reduces the power of a wave as described in (Duckers 2004). This will have skewed the

results at higher periods, to give higher incident powers, but this effect would have been comparable between the models.

In order to test like for like machines, and ensure that the resonant period was the same, the coupling length was made the same using the equation 1-1 ($L_c = gT^2/2\pi^2$). A period of 0.775s was chosen as the centre of the available range of the wave-maker (0.605s – 0.975s), giving L_c as 0.298m and when calculating the helical element of L_c , half of the model diameter was used.

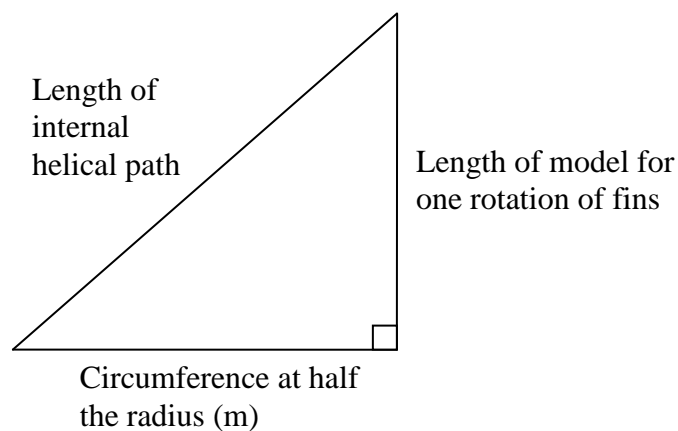


Figure 3.15 Pythagoras' equation was used to calculate internal path length.

The helical length is directly proportional to vertical length, so the draft representing half of the water path length L_c can be calculated and yielded the drafts in Table 3-3:

Model	Draft (m)
P (Plain Tube)	0.148
S (Single Twist Helix)	0.130
D (Double Twist Helix)	0.104

Table 3-3 Model drafts.

The draft is the distance from the still water level to the bottom of the tube.

3.4.5. Results

3.4.5.1. Pressure time-series

A sample plot of the pressure drop across the 10cm simulator is shown in Figure 3.16.

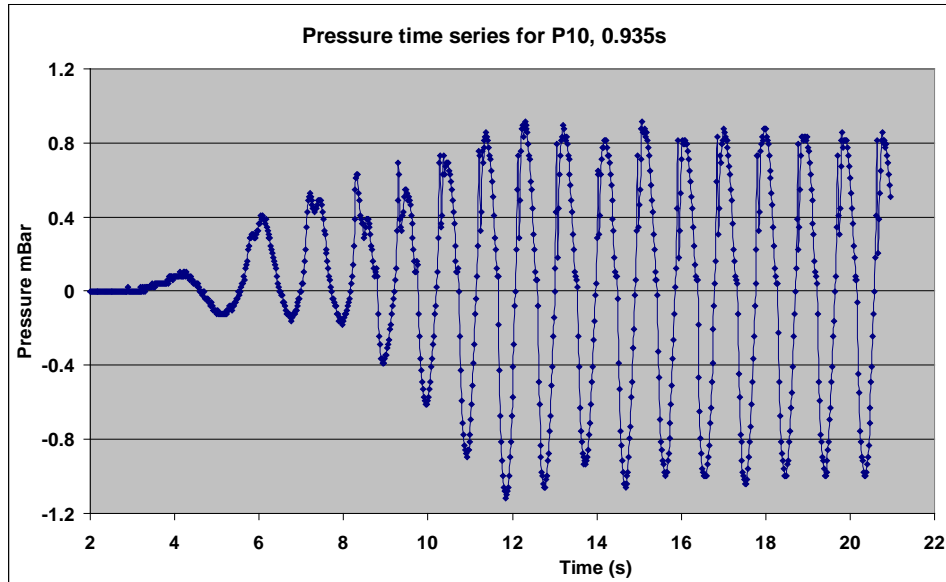


Figure 3.16: Sample differential pressure time series.

The RMS value of the pressure drop was calculated between the zero up-crossing at 12s and the one at 20.5s, giving a value of 0.67mbar in this case.

The instantaneous power was calculated using equation 3-4:

$$P_{air} = \Delta p Q$$

Where Δp was the instantaneous pressure drop from the sensors and Q was the instantaneous flowrate. The flowrate was calculated from the instantaneous pressure drop using the equations in Figure 3.6.

The RMS of the power was calculated, also for a whole number of wavelengths (between 12s and 20.5 s in the case above), and plotted against the wave period in Figure 3.17.

3.4.5.2. Power

Figure 3.17 presents the power collected by each of the three models over a range of incident wave time periods and shows that Model P outperforms the other two models regardless of the turbine simulator used.

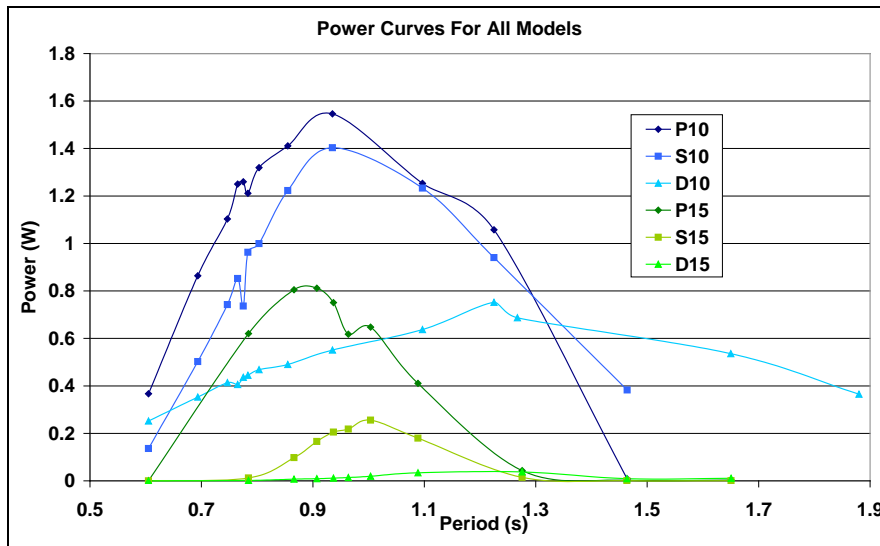


Figure 3.17 Power curves for all three models.

The differential pressures for S15 and D15 were very low: The maximum value for S15 was 37Pa, and for D15 it was 17Pa. These are right at the bottom of the range of the +/-1000Pa sensors, so their accuracy is in doubt. More sensitive sensors were purchased for the tests in Chapter 5.

However, the curves for P10 and S10 are clearly comparable, with S giving almost the same power output as P, but with 12% less draft. Taking the areas under the power curves in Figure 3.17 and using P10 and P15 as controls, shows that S10

provides 90% of the energy of P10, whereas S15 only produces 23% of the energy of P15.

Simulator	10cm	15cm
P	100%	100%
S	90%	23%
D	80%	6%

Table 3-4 Table showing comparative energy provided by the single twist and double twist models compared to the plain tube model.

Judging by the differences in performance between P10 → P15 and S10 → S15, it would appear that the correct turbine / helix combination could give at least comparable performance to a similar Plain tube OWC.

This showed that the helical concept had potential merit and it was decided to arrange more tests, to see if the comparative performance of the helical models could be improved upon with optimised configurations of model and simulator. These tests are described in Chapter 5.

The output of the models with the 15cm simulator fitted is uniformly lower than that of the models with the 10cm simulator fitted. This indicates that this simulator is delivering a sub-optimal impedance, and as the 15cm simulator has a larger area, the impedance must be too low rather than too high. The 15cm simulator therefore has very little damping effect, so the prime damping influence on the results is the helix, which could explain the different P_{\max} periods that maximum power occurs at for the different models in these three tests: as damping increases, the period of the peak response is expected to rise (Main 1998 & Braddick 1965).

$$\omega^2 = \frac{K}{m} - \frac{b^2}{4m^2} \quad (3-10)$$

Where ω is the frequency for maximum amplitude of the system, K is the spring rate, m is the mass of the water in the model plus the added mass of water entrained outside the model and b is the damping coefficient. This shows that, if all else remains the same, then as b increases so ω must decrease.

It is worth noting that there is no sign of any significant improvement in performance due to the base of the models being closer to the surface, which is one of the premises of the helical design. This may be due to the proximity of the flume floor and walls which artificially focused more energy into the models than would naturally enter the system.

The relationship between the power curves shows that the 10cm simulator created a larger pressure drop than the 15cm one, as was expected (Figure 3.17). This has the effect of giving a higher power output and, again, suggests the need to optimise the simulator / model systems in order to achieve and compare the best possible performances.

It is interesting to note that the P_{\max} period for Model D is almost identical for the two simulators, suggesting that the helix itself must be the dominant damping factor in both situations. The response is more consistent across the range of periods and this property should be explored. As a configuration it should probably be discarded; it is unlikely that the double twist model will ever compare favourably with the plain and single twist versions, without increasing the damping of the turbine to such an extent that their efficiencies would drop to match that of Model D and would therefore be below their optimum level. This effect can also be seen in Ahluwalia's results (Ahluwalia 2006) where Model D outperformed Model P and Model S with the 7.5cm simulator. An intermediate model with 1.5 twists was considered worth investigating in future tests.

3.4.5.3. Incident Power

The wave heights were measured by eye using a ruler at the same position as the model for each of the wave time periods that were used and plotted in Figure 3.12.

It is usual to assume that the incident power on a wave device is the power contained in a device width (198mm) of wave crest. In this case however, due to the blockage of the flume by the model, it is suspected that much more of the generated energy was incident on the model, especially since using a wave front of 198mm generates “efficiencies” of over 200%.

Therefore the whole power in the width of the tank has been used for efficiency calculations and is shown in Figure 3.18.

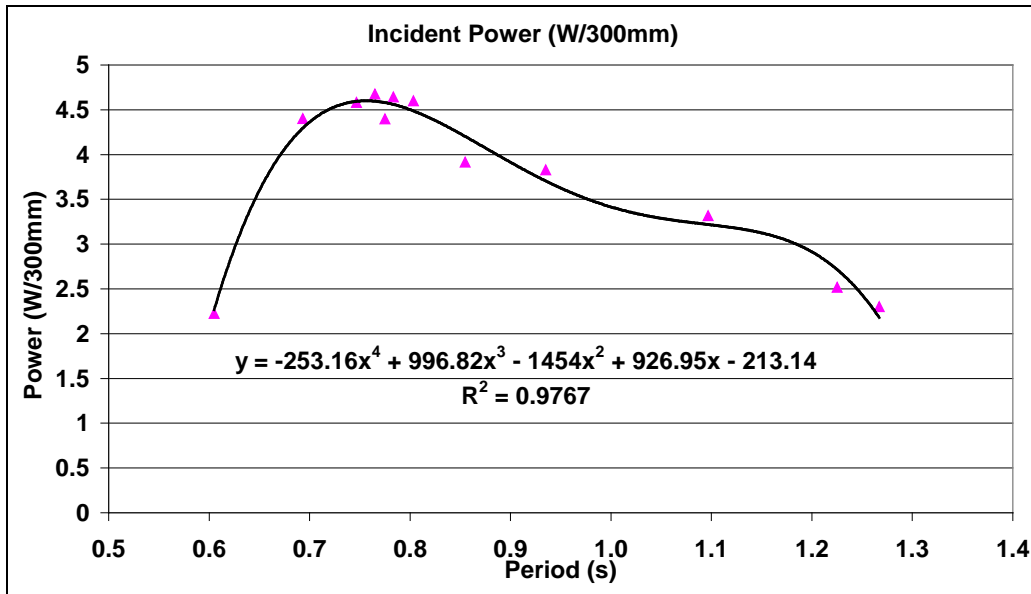


Figure 3.18 Incident wave power with no model in flume.

Equation 3-7 was therefore modified to:

$$\eta = \frac{P_{air}}{DP_{wave}} = \frac{\Delta p^2}{Z \cdot 0.3 \cdot 0.98 H^2 T} \quad (3-11)$$

In real waves, power rises with the square of H until the waves in the field are fully developed. The input power curve in Figure 3.18 will have distorted the output power curves from the models, meaning that the maximum power measures does not occur at, or even near, the period of resonance.

The line fitted to the curve in Figure 3.18 was used in the efficiency calculations. However, as noted above, it is likely that less than 100% of the incident power in the width of the tank interacted with the model, leading to slightly underestimated efficiencies. This effect is comparable for all of the models as they are geometrically identical, and the drafts only differ by 42mm, which is small compared to the depth of the flume. The assumption was made that the comparison between the models is still valid, and the recommendation was made to use a larger tank for the tests presented in Chapter 5.

3.4.5.4. Extension of the incident power data

After the experimental data had been collected, it was found that wave heights for the higher periods had not been measured, so the incident power curve was extended as shown below in Figure 3.19 using wave height data from previous experiments. The three points on the right are new, the others are the same as in Figure 3.18. It is not absolutely certain that the crank of the wave-maker was set to the same excursion for these tests, so the results above a period of 1.267s are useful for comparison, but the absolute results should be treated with caution.

The fitted relationship from Figure 3.19 for periods above 1.267s was used to determine the incident wave power, and from Figure 3.18 for periods below 1.267s.

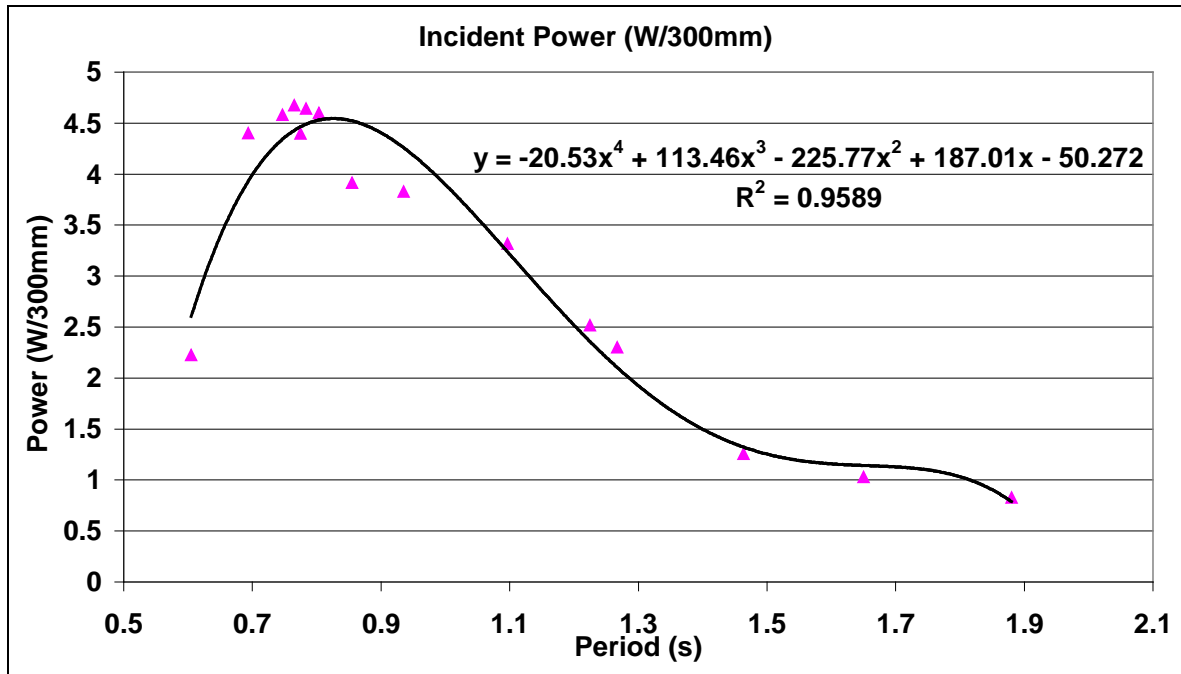


Figure 3.19 Extended incident wave power curve. Data from this graph only used for tests with periods between 1.267s and 1.88s.

3.4.5.5. Efficiency

The incident power was calculated from the relationships described above. The power removed by the simulator was calculated as described in the calibration section, and then the efficiency was calculated using equation 3-11:

$$\eta = \frac{P_{air}}{DP_{wave}} = \frac{\Delta p^2}{Z \cdot 0.3 \cdot 0.98 H^2 T}$$

The efficiency curves shown in Figure 3.20 are useful for performance comparison between the models and also show the peak performance period.

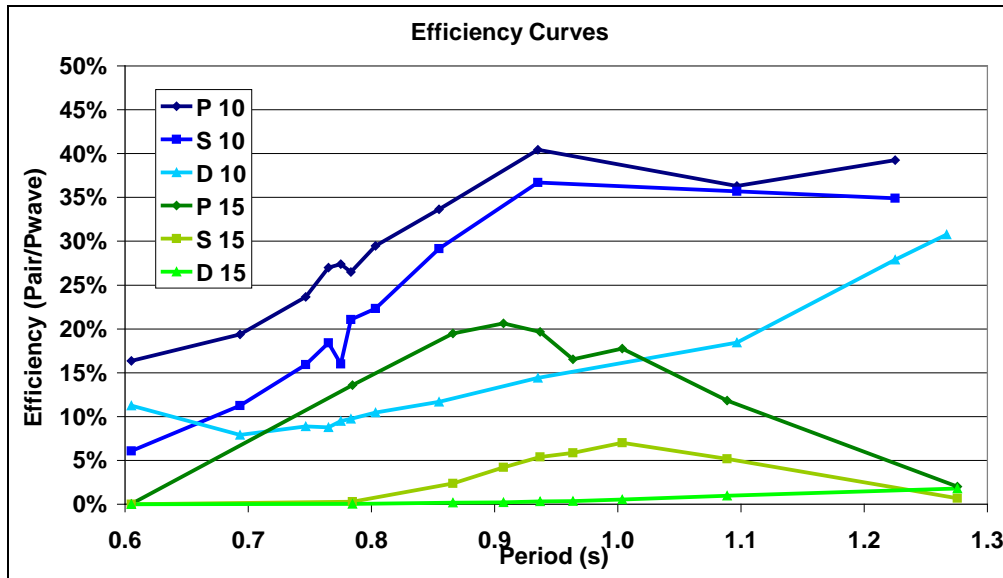


Figure 3.20: Efficiency curves for all models

The efficiency curves (Figure 3.20) for the 10cm simulator show that the power curves (Figure 3.17) would look very different if the models were tested in waves more representative of a realistic sea-state: significantly more incident power would have been available at higher time periods, and this combined with the higher efficiencies for higher periods in Figure 3.20 would give broader power curves.

The efficiency curves in Figure 3.20 also demonstrate that the P and S models perform in a similar way with the higher impedance (10cm) simulator, but not with the 15cm simulator. P15 is much better than S15, whereas P10 is only slightly better than S10, and the difference between them is the impedance of the turbine. This suggests that, with the correct impedance matching, it may be possible to increase the performance of all of the models, and that the single twist tube may even outperform the plain tube.

Peak efficiency, i.e. that at resonance, in all cases occurs at higher values of period than those expected from calculations using equation 1-1 as shown in Table 3-5.

Model	Draft = $L_c/2$	Calc'd T_{res}	T_{res} (10cm)	T_{res} (15cm)
P (Plain Tube)	0.148m	0.775s	0.935s	0.907s
S (Single Helix)	0.130m	0.775s	0.935s	1.004s
D (Double Helix)	0.104m	0.775s	>1.3s	>1.3s

Table 3-5: Table showing calculated and measured resonant periods (T_{res}) for the two different turbine simulators.

Possible reasons for this are:

1. In calculating $L_{c(res)}$ only the shortest path from the inside of the model to the outside was calculated – effectively following the inside and then outside faces of the plain model, or the centreline of the helix and the outside faces of the helical models. The coupling length clearly follows a longer path following (using the plain model as an example) the centreline of the device, passing some distance under the base, and then interacting with the water some distance away from the model (Figure 1.3).
2. The sides of the flume may have acted as “harbour walls” in a similar manner to the Limpet OWC (Cuan et al 2002). These harbour walls alter the response of these devices as standing waves are set up in the channel. Whenever the length of these walls matches an odd multiple of the quarter wavelength of the incident waves, an anti-node is set up at the OWC entry (Hunter 1991). The walls may also have influenced the peak efficiencies shown in Figure 3.21 as more energy was directed into each model due to the blockage of the flume by the model. This should not affect the comparison of the models as the effect will have been similar for all of the models as the geometry of the models is similar and the draft only varies by 42mm across all three models.
3. Heavily damped systems have higher resonant periods than lightly damped ones; this is particularly visible in the results for the 15cm simulator in Figure 3.20. The damping of the models is discussed in Chapters 2, 5 and 6, however the three main elements of damping are the radiation damping and the viscous

resistance of the model and the impedance of the turbine. It is a combination of the first two of these that are responsible for the difference in $T_{(res)}$.

3.4.5.6. Discussion of L_c

The fact that η_{max} (the maximum efficiency) occurs at the same period for P10 and S10 suggests that the error in calculating L_c is largely due to an underestimation of the external path, which would be similar for all of the models. However, the fact that η_{max} is so different for the two Model D configurations, compared to the Model P and Model S ones would suggest that calculation of the internal path may also be in error. The relationship between draft and resonant period is an important one and is discussed further in Chapter 5.

It may be that the impedance of the simulators is dominating with the 10cm simulator results, and the impedance of the model is dominating with the 15cm simulator results, and that the impedance of the double helix model is dominant in both cases. This suggests that the simulator impedance will have to dominate the model impedance in order for it to have a significant effect on performance.

A suggestion for future tests is to take readings of optimised performance at two depths for each model. This will yield η_{max} data that can be used to compare L_c values for the different configurations, and a firmer understanding of the relationship between the models and their resonant characteristics can be developed.

Another suggestion is to conduct tests to determine the impedance of the models so that they can be compared with the impedance of the simulators. One method for achieving this is described in Chapter 4 and another in Chapter 6.

3.4.5.7. Extension of efficiency curves

As an indication of performance at higher periods, the efficiency curves based on the extrapolated incident power curve are shown in Figure 3.21.

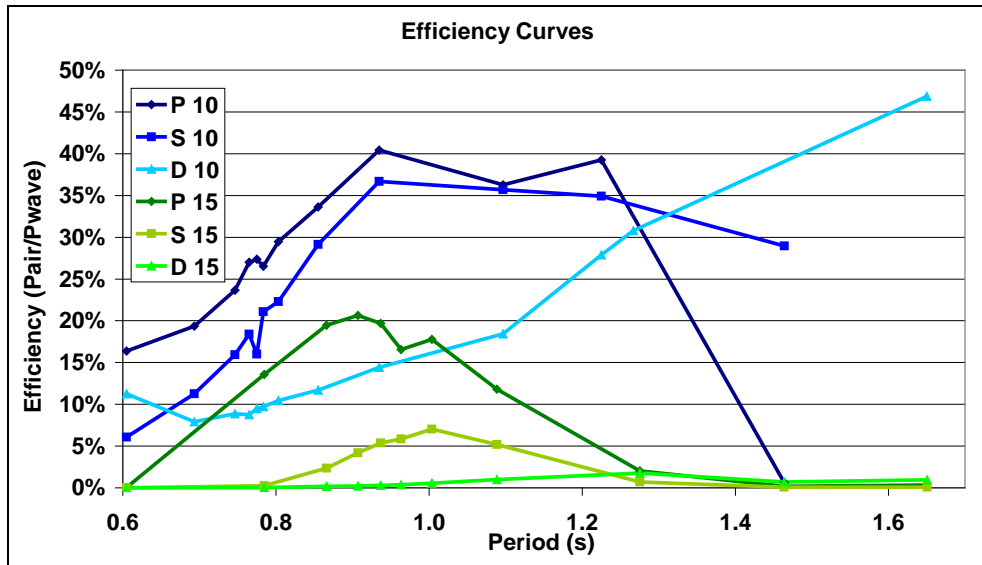


Figure 3.21 Extended efficiency curves for all models.

These extended results should be treated with caution as the efficiency above a period of 1.267s was based on the extended incident power curves. The final point to the right of the series indicates that the helical models may outperform the plain tube model at higher periods, and this again highlighted the need for more tests on optimised models with similar resonant periods and in a large tank.

3.4.6. Errors

5. At ± 10 mbar or ± 100 Pa, the transducers were somewhat oversized, and all the measured results were calculated from an extrapolated part of the simulator $Q/\Delta p$ calibration graphs. This leads to an element of uncertainty in the data as the relationship between Q and Δp is not precisely defined. The maximum recorded pressure was 6.7 Pa which is 0.67 mbar. Thus a range of ± 1 or 2 mbar would be more appropriate for next round of experiments. This requires a transducer that is 5 or 10 times as sensitive as the ones used. The errors would have been similar for each model using the same simulator, so the families for curves are still useful for comparison.
6. According to the datasheet (Sensortek datasheet for BSDX0010d4d), the pressure transducers were accurate to within $\pm 1\%$ of the full scale for the conditions in which they were used. This was ± 2 Pa in this case.

7. The 12 bit data logger digitised the signal voltage in steps of 0.49Pa which is considered negligible.
8. The incident power reduced as the period increased above a period of about 0.75s, unlike a wind generated wave which rises according to $P=H^2T$. This will have narrowed the power curves described above, and shifted the power maxima to a lower value of T. Converting the power data to efficiencies ensures that they are useful for comparison. A more realistic set of periods/heights is recommended for the next set of tests.
9. The flume undoubtedly affected the results, since the water was “shallow” for many of the tests and the sides were close to the model. This affected the nature of the incoming waves and made it difficult to separate the response of the model and the response of the flume. In addition the tests were monochromatic and if these results were applied to a spectrum, the results would be somewhat different to those generated from a simulated polychromatic climate. This is discussed further in Chapter 5.
10. The water level was not fixed for the 10cm simulator tests, as the overflow regulator of the flume was blocked, so the water feed had to be carefully adjusted at the bottom of its range to keep the level fixed. This led to the curves for these experiments being less smooth than the 15cm ones. Trends were clearly visible nevertheless.

3.5. Conclusions

The preliminary results suggested that the helical idea could have the potential to yield a shorter device whilst delivering similar performance. It was clear that tests in a wide tank would be necessary to confirm this potential.

Specifically:

1. The impedance of each of the model / simulator pairs is different, and the impedance of the Double Twist model appears dominant in all cases. See Table 3-2, repeated here:

Slot length	Gradient at $0.02\text{m}^3/\text{s}$ (Pa.s/m^3)
10cm	3278
12.5cm	2522
15cm	2237

The experiments with the slit simulators did not provide evidence that the correct impedance had been achieved, so it wasn't clear if the models were performing at their optimum. The performance of the Plain Tube and Single Twist models was very similar when using the 10cm simulator, suggesting that the simulator was more closely matched to the Plain Tube and Single Twist models in this case than when the 15cm one was fitted.

2. Impedance matching of the whole model/simulator system to a range of sea states could yield a more efficient device, especially if a realistic turbine could be simulated and its impedance varied in real time.
3. A 12% saving in draft was achieved between the Plain Tube and Single Twist models when fitted with the 10cm simulator, whilst achieving a similar performance. This may be improved with optimisation.
4. As can be seen from the efficiency curves in Figure 3.21, resonance was not at the expected period. It is possible that this is due to the constraints of the flume meaning that it was difficult to separate device effects from the flume effects. The first stage of the next set of tests should determine a constant period for peak performance.
5. Introducing the helices introduced an element of centripetal force to the water motion; this may have extended the effective internal water path somewhat by moving the centre of mass of the water towards the outside of the helix. More tests are required to evaluate the effect of this on the coupling length and resonant period.
6. Further tests are worthwhile, including using an improved simulator, a larger and polychromatic tank and more sensitive pressure transducers to determine the scalable performance of the models.

7. More tests would be worthwhile to determine the impedance of the models so that it can be compared with the impedance of the simulators, and these are described in Chapter 5.

In view of the tank limitations, it was decided that the next stage should be to prepare the models for use in a wide tank. In order to minimise configurations, the smallest number of models would need to be tested, so it was resolved that the next steps should be to try to determine the ideal helix angle, and then to try to predict the optimum turbine damping.

Chapter 4: Impedance Calibration of Models

4. Introduction

In this chapter, the viscous resistance of the models was measured, and scaled up to inform the prediction of full scale output and optimum turbine impedance.

4.1. System impedance

Following on from the first set of flume tests, an attempt was made to predict the ideal helix angle, and also the ideal turbine impedance for the helical design. The objective was to end up with one or two helical designs, whose performance could be evaluated against the plain tube, used as a control, with a reasonable degree of confidence that they are comparable and close to the optimum helical shape.

The impedance of the system has three components, the model resistance, which is the resistance due to the viscous interaction of the water with the OWC; the radiation damping, which is the impedance due to waves created by the model in response to an initial displacing force; and finally the impedance of the turbine simulator (Falnes 2002 and Brendmo et al 1996).

These impedances must be added together to obtain the impedance of the whole system and can be expressed as (Falnes 2002):

$$Z_{tot} = Z_r + R_f + Z_s \quad (4-1)$$

Where Z_r is the radiation damping; R_f is the viscous resistance and Z_s is the impedance of the simulator (Figure 4.1):

An analogy exists between a wave energy converter and a transmission line, in that the impedance at the end of the line must match that of the load for maximum power transfer. In the same way, the impedance of the turbine should match the radiation

damping of the OWC in order to transfer maximum power through the system (Falnes 2002 and Brendmo et al 1996), i.e.:

$$Z_r = Z_s \quad (4-2)$$

The radiation damping of the models was measured in a later set of experiments, and is presented in Chapter 6 where it is compared to the impedance of the turbine simulators.

In order that the maximum energy is transferred to the turbine, R_f should be as low as possible. Impedance tests were carried out to determine the resistance of the models and compare the sensitivity of the system to variations in the resistance of the helical fins. The goal was to identify the minimum model resistance, and therefore the optimum helix angle.

4.2. Scaling

In section, 3.4.5.2 using the plain model as a control, and taking the area under the power curves in Chapter 3, the single helix model was shown to perform 90% and the double twist model 80% as efficiently as the plain model. Due to the excessive roughness of the fins in the helical models, it is thought that some improvement in this relative performance may be achieved. This is discussed later in this chapter with reference to the Reynolds numbers of the models and it appears that in scaling up the impedances, the models are favoured over the prototypes, as indicated by Knott and Flower (1980), leading to the expectation of further performance gains at prototype scale.

4.3. Objectives

4.3.1. Determining Impedance

It is important to understand the effect of model impedance in order to predict the potential conversion efficiency of future models and eventually a full scale prototype. As well as the radiation damping, the impedance has two further elements: the model's viscous resistance and the turbine impedance. The viscous resistance must be as low as possible to maximise the energy reaching the turbine.

The three impedances are shown schematically in Figure 4.1, where the internal water surface has been given a vertical displacement to depth d (the displacement of the internal and external water heights is nearly in phase):

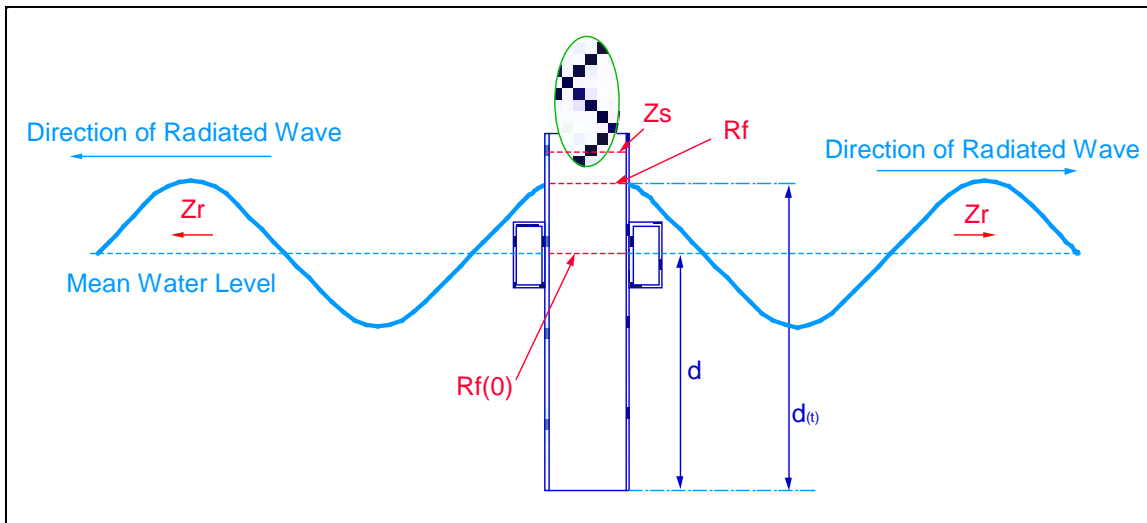


Figure 4.1 Schematic showing components of model impedance.

The green oval represents a turbo-generator at the top of the device, and Z_s is the turbine impedance. d is the draft at rest, and $d_{(t)}$ is the instantaneous wetted depth. R_f is the resistance due to friction of the tube. This varies with length and is a maximum when d is also at a maximum, so a reference value of $R_{f(0)}$ is also shown. Z_r is the radiation damping.

Any floating object, including wave energy converters radiates waves. This process results in energy being lost to the OWC and is referred to as radiation damping and this is discussed in detail in Chapter 6.

$Z_s \approx \text{Constant}$ for a Wells turbine, but R_f will change as the depth of water changes through the cycle since there is a variable velocity and length of wetted water path within the OWC. It is interesting to note that flowrate and pressure drop are greatest when $R_f = R_{f(0)}$ and 0 when $R_f = R_{f(\max)}$ or $R_f = R_{f(\min)}$. The maximum flowrate experienced at $R_{f(0)}$ is likely to be a state close to that for which the turbine will be designed, so it was decided to compare this value to the simulator impedances when examining the sensitivity of the system to varying flowrate and resistance.

Comparing the performance of the models in this way also gave an insight into whether the helical design was worthy of further study.

4.4. Determining the frictional resistance

4.4.1. Equipment

Tank Setup

In order to determine the impedance of the helix, the models were mounted vertically in a dam across the flume such that the only way for water to flow is through the model (Figure 4.2). With steady state flow, the head difference across the dam will give the pressure difference caused by the model.

For a given model $d_{(\text{mean})}$, (Figure 4.1) the head loss is dependent on the flow rate since the head loss through a pipe is given by Darcy's equation (Massey 1989):

$$H_f = \frac{f l u^2}{D_h \cdot 2g} = \frac{\Delta p}{\rho g} \quad (4-3)$$

Where f is the friction factor; Δp is the pressure drop along the pipe; l is the length of the pipe (i.e. d_{mean}), D_h is the hydraulic diameter (used for non-circular ducts); ρ is the density of water; g is the acceleration due to gravity and \bar{u} is the average velocity of the water.

The hydraulic diameter is given by (Massey 1989):

$$D_h = \frac{4A}{P_d} \quad (4-4)$$

Where A is the area of the section at a tangent to the flow through one side of the helix and P_d is the perimeter around area A .

The assumption has been made that:

$$R_f = \frac{\Delta p}{Q} \quad (4-5)$$

Combining Equations 4-3 and 4-5 gives:

$$R_f = \frac{H_f \rho g}{Q} \quad (4-6)$$

For steady state flow.

Figure 4.2 and Figure 4.3 show the experimental setup to determine the head loss due to friction and the flowrate.

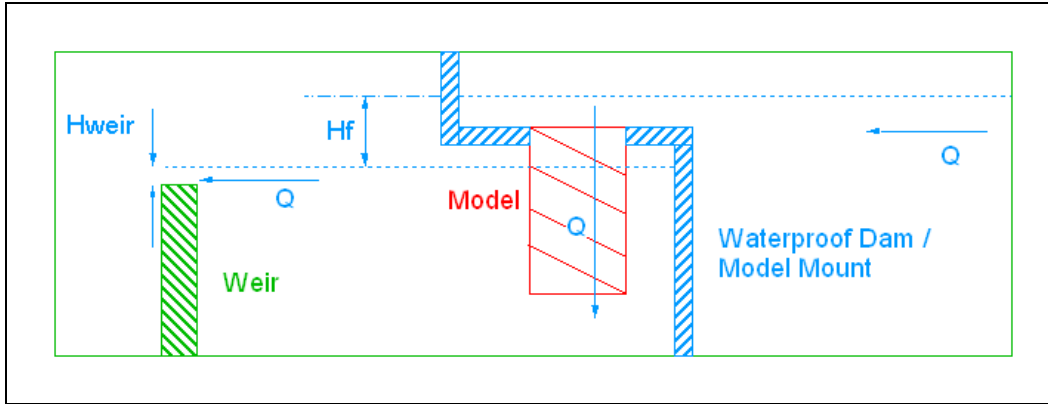


Figure 4.2 Flume set up to measure model impedance.

This set up required significant flow rates, so the data had to be extrapolated into the region of lower flow rates to include those that would be achieved in the test tank (Figure 4.6). A typical flowrate in the model during the tank tests was $0.0027\text{m}^3/\text{s}$, but the full range was 0.0007 to $0.003\text{m}^3/\text{s}$. H_f was chosen such that the top of the model was always covered by water at the lower level. The upper level was only limited by the depth of the tank.



Figure 4.3 Pictures of V-Notch weir (left), both sides of the dam (centre) and model under test (right).

The impedance of the model was measured using the whole length of the model and $R_{f(0)}$ was calculated from this value assuming a linear relationship between $R_{f(0)}$ and $R_{f(d)}$.

Δp and Q are known for the turbine simulators, so it was possible to make a comparison between Z_s and R_f .

Models

The same three models were used for this test as for the earlier flume tests described in Chapter 3.

4.4.2. Method

Measure head difference across dam

H_f was measured in still water on either side of the dam using a pair of meter rules and a spirit level across the dam. The bottom of the model was never allowed to be above the lower water level as this would have distorted the head measured across the model. When correcting the impedance for length, the length of the model was thus constant at 300mm as the water had to flow through the entire length, regardless of the height of the water either side.



Figure 4.4 Dam showing difference in water level on either side.

4.4.3. Measurement of flow rate

The flow rate was measured in various different ways for the different models as different pumps had to be used to achieve the correct flow rates. A lower capacity pump running at high power was used to pump water from the sump to the head of the tank for the double model, and a high capacity pump, running at low power was used for the same purpose for the other two models. The high capacity pump delivered too high a flowrate for the double twist model, so the low capacity one had

to be used. Unfortunately, this pump did not give a high enough flowrate for the other two models, hence the different instruments used to calculate the flowrates.

A calibrated venturi-meter was attached to the feed of the smaller pump and flowrate values were read from this for the double twist model. There was a piezometer attached to the feed of the larger pump, and this was used for the single model. Unfortunately, the piezometer stopped working during the first readings for the plain tube so another method of determining Q had to be used:

Fortunately, the outflow from the experiment was a V-notch weir. The height of water behind the v-notch weir was measured for all readings, giving two possibilities for determining Q for the plain tube:

- Using the theoretical relationship between water height above the bottom of the V-notch ($H_{(weir)}$) and flowrate over a v-notch weir ($Q_{calc'd}$).
- Correlating the height behind the weir ($H_{(weir)}$) with the flowrate already measured for the single twist model ($Q_{correlate}$). The single twist results were used as they were closest to the plain model flowrates.

4.4.3.1. V-notch weir calculation

The Coefficient of discharge, C_d for the weir was calculated to be 0.3 and then the flowrate was calculated using the theoretical formula for flow through a weir (Massey 1989):

$$Q = C_d \cdot \frac{8}{15} \cdot \tan\left(\frac{\theta}{2}\right) \cdot \sqrt{2g} \cdot H_{Weir}^{\frac{5}{2}} \quad (4-7)$$

Where θ is the angle of the V notch weir.

4.4.3.2. Correlated Flowrate

The readings of H_{weir} vs. flowrate for the single model were plotted and, using a least squares fit to derive the formula for the relationships in Figure 4.5, alternative values of R_f for the models were obtained.

Both of these were used to determine Q for the plain model.

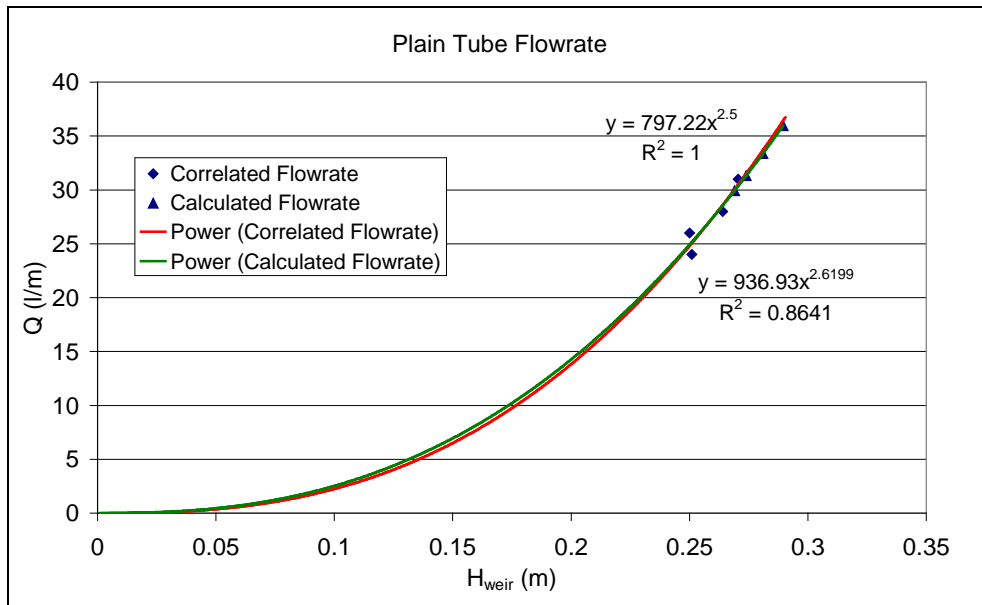


Figure 4.5 Plain tube flowrate estimation.

Both of these flowrate data sets are very similar, giving confidence that both methods have merit. In order to use both sets of data, both sets of flowrate were plotted against Δp and an average of the two impedances was used to determine the plain tube impedances (Figure 4.6).

4.4.3.3. Leaky dam

There was a small amount of leakage round the dam, and by closing the hole in the dam, setting a representative head of 378mm and using the venturi meter, this was measured as $0.0025 \text{ m}^3/\text{s}$, which was a 5% - 10% of the flowrate during the impedance tests. This will have varied a little with the different heads behind the dam (291mm to 473mm), but this value was deemed to be accurate enough for all

situations, and was subtracted from the measured results to get the actual flow through the model.

4.5. Results

4.5.1. Impedance Results

After measuring the values for the head loss (H_f) and by inference Δp , the pressure drop values were calculated in terms of unit length of model (i.e. Pa/m). Thus impedance has units of $(\text{Pa/m}) \cdot (\text{s/m}^3) = \text{Pa} \cdot \text{s/m}^4$ giving a value that is easily applicable to the different drafts that were used during the tests described in Chapter 3 and 5.

Figure 4.6 shows a plot of pressure drop against flow rate for the three different models.

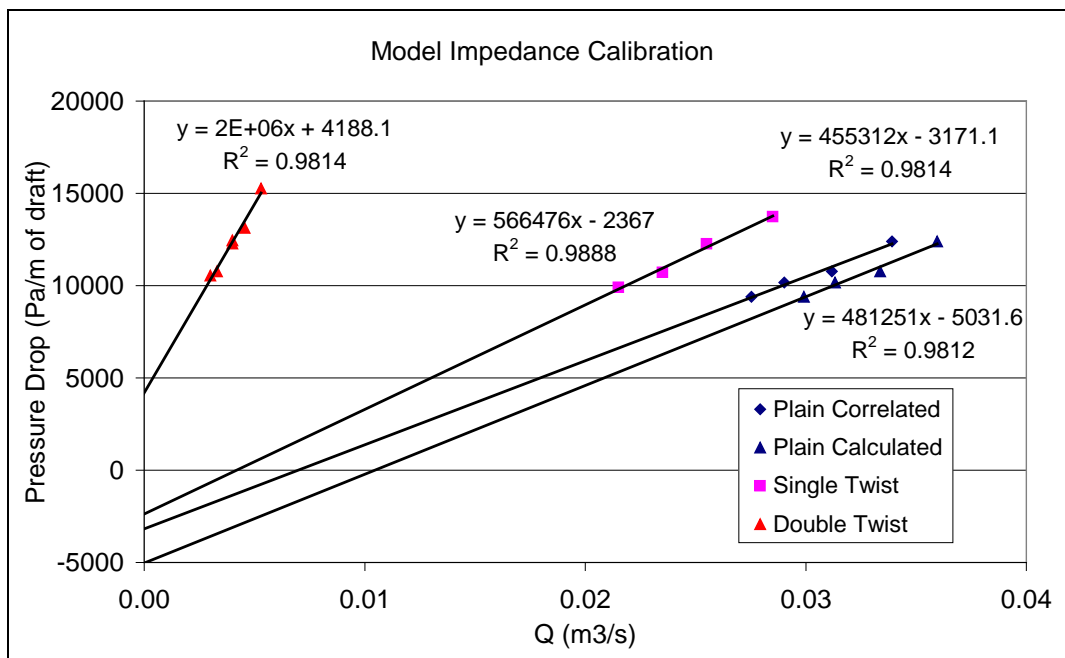


Figure 4.6 Plot of pressure drop (proportional to measured head loss) as a function of flow rate for the three models used to infer model impedances.

The impedances of the models are given by the gradients of the black lines which are linear least squares fits to the data points. The lines should be linear and pass through the origin, (equation 4-5) but there is obviously an experimental error, probably due to the difficulty of obtaining accurate results for the flowrate. The results for H_f were reliable with an error estimated at $\pm 2\text{mm}$.

There is clearly a difference between the lines derived using the venturi (used for the double model) and those derived using the piezometer (used for the others), but there is clearly also a straight line relationship in the region tested as predicted by equation 4-5.

It was decided to use the resistance values shown in Figure 4.6 which are the gradients in the equations. The zero error may have been due to a systematic error in all the results obtained, i.e. a shift upwards for the venturi, and downwards for the piezometer, while the gradients remained the same. This casts doubt on the calibration, however no better results were achievable since the flowrates couldn't be dropped any further with the test rig that was available. It can be seen that both of the plain tube resistances are similar, so an average was used.

4.5.1.1. Resistance per unit length ($R_{f(x)}$)

$R_{f(x)}$ is the impedance per unit length of the model. It is useful as it enables any draft to be analysed, by multiplying $R_{f(x)}$ by the draft to get $R_{f(0)}$ as in Table 4-1:

Model	$R_{f(x)}$ (Pa.s/m ³ /m)	Draft (m) for $T_{\text{res}} = 1.17\text{s}$	$R_{f(0)}$ (Pa/m ³ /s)
Double	2000000	0.1	200000
Single	566476	0.139	78740
Plain	468282	0.191	89442

Table 4-1 Model impedances adjusted for draft.

The impedances of the turbine simulators were calculated during the calibration process described in section 3.3.3 and they are shown again in Table 4-2:

Simulator	Zs (Pa.s/m ³)
15cm	2237
10cm	3278

Table 4-2 Turbine Simulator Impedances.

4.5.1.2. Impedance comparison

In order to compare the effect of altering the impedance of the configurations, the impedance was compared to the overall power available.

The pneumatic power available across a range of monochromatic waves (from the flume tests described in Chapter 3) is shown graphically in Figure 4.7:

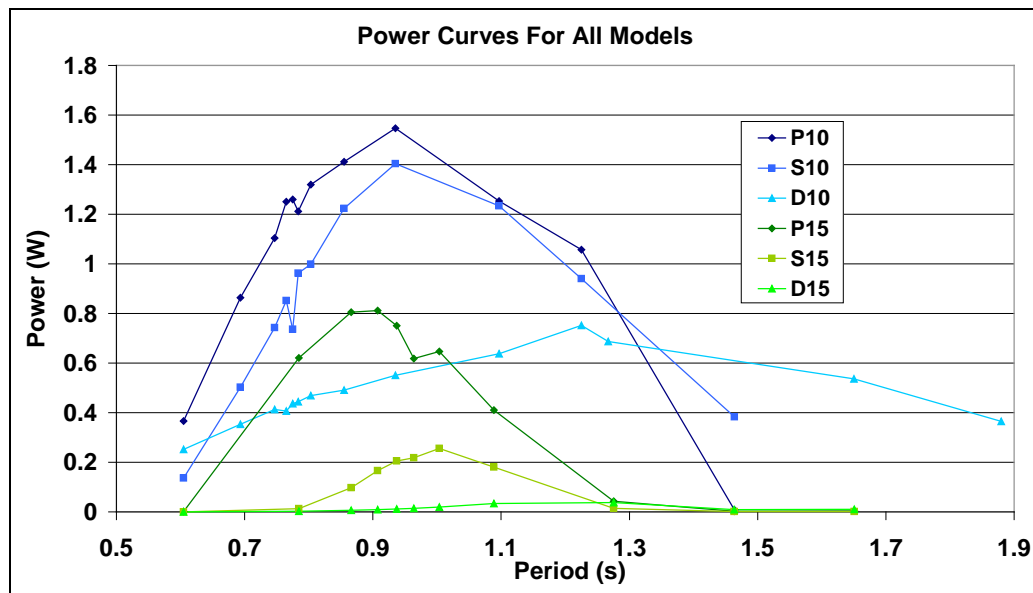


Figure 4.7 Power curves from flume experiments.

The pneumatic energy (Ws) available across the spectrum is the area under the curves in Figure 4.7. It should be noted that the curve for the double twist model is much broader than for the other models, and the whole width of the double twist

curve was used as the results for the other configurations were low or near zero in the extended region.

$R_{f(0)} + Z_s$ was calculated for each of the model configurations and the results are presented in Table 4-3 along with the total pneumatic energy available:

	R_f From Table 4-1	Z_s From Table 4-2	$R_f + Z_s$ (Pa.s/m ³)	Energy across the spectrum (Ws)
D10	200000	3278	203278	0.6912
S10	78740	3278	82018	0.7838
P10	89442	3278	92720	0.8672
D15	200000	2237	202237	0.0174
S15	78740	2237	80977	0.0699
P15	89442	2237	91679	0.3060

Table 4-3 Model impedance vs. power available.

Graphically the relationship between Z and the power available is more obvious as can be seen in Figure 4.8:

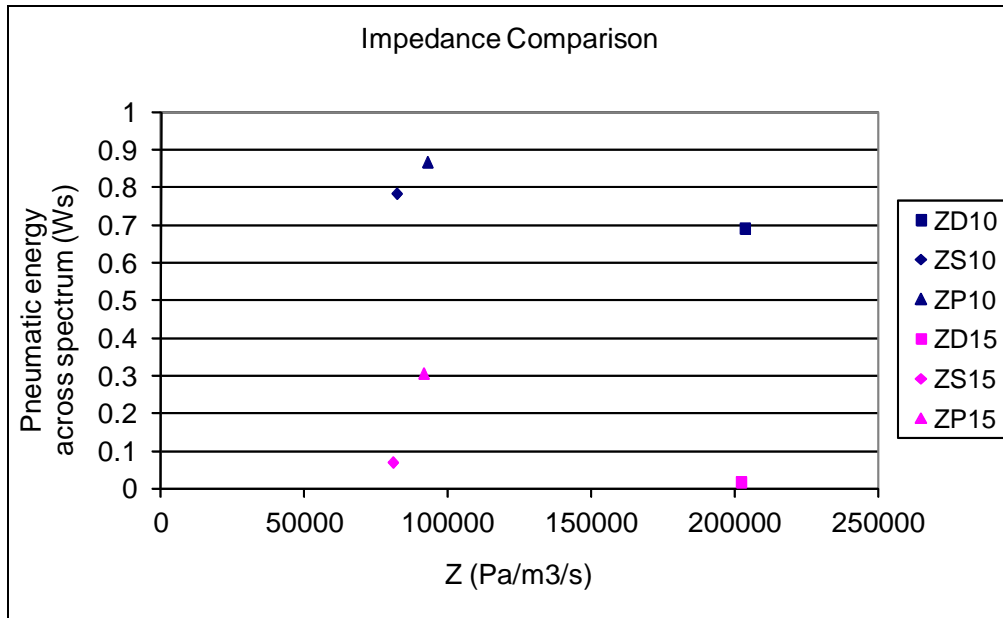


Figure 4.8 Model impedance ($Z=R_f(0) + Z_s$) vs. power available.

It is clear from Figure 4.8 and Table 4-3 that the impedance of the single tube at its operating draft is lower than the plain tube. This was an unexpected result. The implication is that although the single twist has a higher per metre of draft value for R_f (Table 4-1), its actual value under test is reduced to below that of the plain tube due to the relationship between coupling length and draft. This is also clearly not the case for the double twist, where the impedance is much higher.

There is no clear relationship between the results meaning that they cannot be used to estimate the ideal helix to choose. However since the double twist model has such a large impedance, it was decided to use a 1.5 twist model for future experiments with the expectation that it would deliver better performance than the double model, and would therefore be closer to the ideal shape.

It was also clear from Figure 4.8 that the impedance of the turbine simulator dominates the overall efficiency of the system. This is a useful result as it is possible to adjust the turbine impedance (at the design stage and to some extent during operation as well) and suggests that this will be a useful control method as explained by Falcao (1999) and others. Using a higher impedance turbine will generate a

higher Δp and therefore a higher pneumatic power. There should be an optimum turbine impedance close to the value of Z_r . A new simulator system was therefore recommended that could achieve these impedances in future tests.

If there is an optimum $R_{f(0)}$ for the wet part of the OWC, it is likely to be as low as possible, transferring as much energy through to the turbine. Thus the main design criterion should be to minimise the impedance of the model, suggesting that the single helix was worth further investigation.

4.5.2. Scaling Results

4.5.2.1. Froude Number Scaling

The Froude number is used for scaling flows where the significant forces are inertial and gravitational. Typical applications for this type of scaling are those where a body interacts with water at a free surface, for example modelling the drag due to waves caused by the passage of a ship (Massey 1989), or in reverse, waves being absorbed by a wave energy converter. As discussed in Chapter 2, this is widely considered to be the most important scaling factor for wave energy converters.

The Froude number is defined in chapter 2 as:

$$Fr = \frac{c}{\sqrt{gD}}$$

Where c is the wave phase velocity and D is the diameter of the model. The suffixes m for model and p for prototype have been used in this analysis.

Full scale wave machines are tuned to the predominant wave period. A period, T , of 7s has been chosen for the prototype as it is a common wave for much of the world including Africa, India and Eastern Japan, as well as inshore locations around the UK (KNMI n.d.). Time scales as $S^{0.5}$ (see chapter 2) and for the design period of the

models $T_m=1.17s$ this gives a scale factor of 1:36. The phase velocity is defined in equation 2-3 as:

$$c = \frac{gT}{2\pi}$$

So the Froude numbers can be compared for a 1:36 scale model and a prototype:

	Fr_m X= 1:36	Fr_p
Velocity, V (m/s)	1.83	10.92
Diameter, D (m)	0.14	5
Froude Number	1.562	1.559

Table 4-4 Comparison of Froude numbers.

Since $Fr_m = Fr_p$, the models have dynamic similarity and, as noted, except for viscous effects, results obtained with these models in an appropriate tank, with scaled waves, would be scalable to prototype size. Weber (2007) shows that the compressibility of air does not scale with the Froude number. However, as discussed in Chapter 5, it is expected that the scaling error due to compressibility will be similar for all of the models since the volume of air and velocities are similar for all of the models.

4.5.2.2. Reynolds Number Scaling (Massey 1989)

In order to investigate the level of error that could be introduced into any scaled results, an analysis of the Reynolds number was carried out. Recalling equation 2.20:

$$Re = \frac{VL}{\nu}$$

Where L is a representative length (the pipe diameter in this case), V is the average velocity along a pipe, and ν is the kinematic viscosity of the fluid.

$$V = \frac{L}{t} \quad (4-8)$$

Where $t = T/2$.

The value of V for the plain tube was taken as the average of the vertical velocity of a particle at the water surface for a wave of $H=3.2\text{m}$ and 7s which is 0.922m/s for the plain tube prototype. 1:36 scaled waves were used for the models.

This velocity was adjusted to include the longer water path of the helical designs, (described in Figure 3.15), and these are shown in Table 4-5.

L in this case is the hydraulic diameter, D_h (equation 4-4), which is used when comparing circular and noncircular pipes and ducts.

The following assumptions were made:

The kinematic viscosity of fresh water = $1.16 \times 10^{-6} \text{ m}^2/\text{s}$ at 20°C ;

The kinematic viscosity of sea water = $1.004 \times 10^{-6} \text{ m}^2/\text{s}$ at 16°C .

The following definitions were used:

ε = absolute roughness of the interior of the models;

r (the relative roughness) = ε/D_h

Using $\varepsilon=0.05\text{mm}$ for the prototypes (commercial steel (Massey 1989)), $\varepsilon=0.001\text{mm}$ (Perspex (Massey 1989)) for the plain model and $\varepsilon \approx 0.5\text{mm}$ (size of steps) for the helical models, the values of Re and r are shown in Table 4-5:

	$L = D_h \text{ (m)}$	$V \text{ m/s}$	Re	Re_p/Re_m	$r=\epsilon/D_h$ Rough finish	$r=\epsilon/D_h$ Smooth finish
Model						
Plain	0.140	0.156	18,631	246	7.0×10^{-6}	
Single	0.170	0.215	15,599	242	0.0059	12.0×10^{-6}
Double	0.128	0.335	18,347	242	0.0078	16.0×10^{-6}
Prototype						
Plain	5	0.922	4.5×10^6		10.0×10^{-6}	
Single	5.95	1.274	3.8×10^6		18.6×10^{-6}	
Double	4.50	1.985	4.4×10^6		22.2×10^{-6}	

Table 4-5 Reynolds number scaling of the OWC models up to prototype size.

The high r values for the helical models are due to the excessive roughness of the fins where the steps were not smoothed down.

If the helical models had been sanded down and had a fine gloss paint finish, then the absolute roughness would be similar to that of the Perspex tube i.e. $\epsilon=0.001\text{mm}$ and so the single would have a relative roughness of 12×10^{-6} and the double of 16×10^{-6} (shown in Table 4-5). These are comparable with the plain tube prototype, and the models would all be in the transition region (see Figure 4.9), meaning that while the results still could not be scaled, the viscous effects could be considered to vary in a similar way for all of the models, and also that the comparative performance can be expected to scale up. The next set of models were prepared in this way.

With a factor of about 240 between Re_p and Re_m , as well as dissimilar roughnesses, the models do not satisfy Reynolds number scaling. However useful conclusions can still be drawn from these results if they are plotted on a Moody diagram (see Figure 4.9):

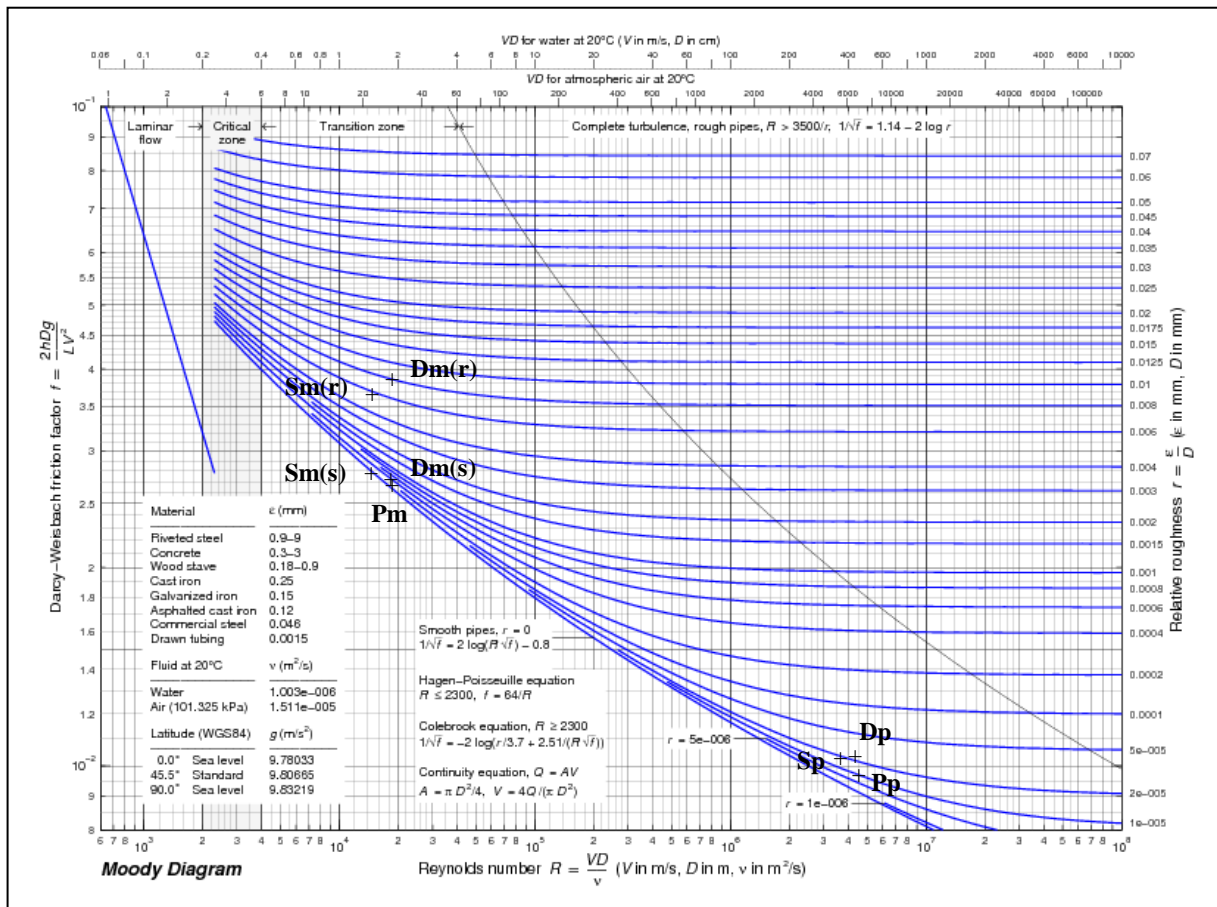


Figure 4.9 Moody Diagram (including some typical roughness values) (Webscripts n.d.).

S, D and P represent the OWC configurations and the suffixes 'm' and 'p' denote model and prototype respectively. The additional suffix '(s)' shows the position of the models if the surfaces of the fins were smoothed off versus the actual positions which are shown by '(r)' for rough.

It is important to note that the Moody diagram and Darcy's equation are for steady state flow in a straight pipe, but using these methods gives an indication of the comparable performance between the models and also how this comparative performance will scale up.

4.5.2.3. Scaling performance

Flow in the laminar region is dominated by viscous forces (friction and eddies), and flow in the turbulent region is dominated by inertial forces. Both types of force are significant in the transition zone (Massey 1989). The Froude number is used to scale

inertial effects, and the Reynolds number is used to scale viscous effects (Knott and Flower 1980). Since the points are closer to the laminar side of the zone (opposite the grey line in Figure 4.9), it is likely that the viscous forces dominate the inertial forces for both models and prototypes.

It is interesting to note that the flow within the single helix model also has a lower Reynolds number than the double and plain models because the hydraulic diameter, D_h , is larger for the single model. The head loss due to friction, H_f , is inversely proportional to D_h , (equation 4-3) so an optimised single twist model could be expected to perform better than the other two models.

The relative positions of the points plotted in Figure 4.9 also indicate that the comparative results should scale up. i.e. if the single twist proves better at small scale, then it will also be better at large scale.

From Table 2-2, it can be seen that velocity scales with X^{-1} and deduced using dimensional analysis that viscosity scales with X^4 , where X is the scale factor described in section 2.4.5.3. For Re to be accurately scaled from the prototype to the model, the model velocity should have been faster and the viscosity lower:

	Prototype values	Theoretical 1:36 scale values	Actual model values
Velocity V (m/s)	0.457	16.45	0.008
Kinematic viscosity ν (m^2/s)	1.004×10^{-6}	598×10^{-15}	1.16×10^{-6}

Table 4-6 Comparative values of velocity and viscosity using Reynolds scaling.

The increased velocity that was required at model scale would increase the losses due to friction, but the lower viscosity would reduce the same losses if they were implemented for the model. Knott and Flower (1980) suggested that Re losses would be reduced at large scale since eddy separation would be delayed at the

higher Re numbers of the full scale machines. They also added the caveat that this required confirmation with further experimental work. It would be interesting to carry out a sensitivity analysis of these two parameters to see whether the net effect of not using the correct Reynolds scaling would increase or decrease performance at full scale.

Head loss due to friction

Darcy's equation states that the head loss due to friction is (equation 4-3):

$$H_f = \frac{f l u^2}{D_h \cdot 2g} = \frac{\Delta p}{\rho g}$$

Form the moody diagram, the plain tube has a (dimensionless) friction factor of about 2.65×10^{-1} , whereas the helical models are around 3.75×10^{-1} . From Darcy's Equation, the friction factor is proportional to Δp , so it can be deduced that Δp will be reduced if the helical models had similar roughness (r) values as the plain model (as indicated by $S_{m(s)}$ and $D_{m(s)}$ in Figure 4.9).

Viscous resistance

Equation 4-6 shows that if H_f is reduced, then R_f will also reduce and so better comparative performance can be expected from these models. i.e. the 80% and 90% figures quoted in section 3.4.5.2 can be expected to rise. This was a powerful argument for continuing the work on the helical models.

The sensitivity of this change can only be determined by constructing and testing new models as the flow rate will also change with H_f but it was determined that the next generation of models should have smooth fins to give a similar r value to the plain model.

4.5.2.4. Turbine Impedance Scaling

It is useful to be able to scale impedance as the ideal impedance can be estimated

for larger scale models and a demonstrator based on smaller models. The scale index is therefore calculated here.

As described in the literature review, when using Reynolds scaling, mass scales with X^3 , Length with X and Time with $X^{0.5}$ (Rao 1996).

From Table 2-2 in Chapter 2, we can derive scale factors for Δp , Q and Z . These are shown in Table 4-7, we expect the impedance to scale up with the same factor for all of the models.

Parameter	Scale factor	Scale factor for 1:36 scale.
Δp	Scales with F/A $M.L^{-1}.T^{-2} \rightarrow X$	$\Delta p_p = \Delta p_m.36$
Q	Scales with m^3/s $L^3.T^{-1} \rightarrow X^{2.5}$	$Q_p = Q_m.36^{2.5}$
Z	$\Delta p/Q \rightarrow X^{-1.5}$	$Z_p = Z_m.36^{-1.5} = Z_m \times 4.63 \times 10^{-3}$

Table 4-7 Impedance scaling.

So the impedances of the full scale prototypes will be 0.0046 times of the impedances of the models.

4.6. Conclusions

4.6.1. Viscous Resistance

The impedance resistance of the single tube model was shown to be lower than that of the other two models. This indicates that it is likely perform better under ideal conditions than either of the other models.

An analysis of the extreme relative roughness of the fins of the helical models compared to the plain model suggests that significant improvement in performance could be obtained by using smooth fins. The size of this improvement will be

assessed when new models with smooth fins are tested.

Since the tube is not converting any energy itself, its resistance, R_f , should be lowered as much as possible to allow the energy to reach the turbine.

4.6.2. Performance

No optimum performance was observed in these tests. As the impedance rises, the energy converted increases as described in section 3.4.5, and which was also the case in previous tests by Ahluwalia (2007).

For the condition $Z=0$, (where Z is the turbine simulator impedance) there will be no pressure drop generated for any flow. For the condition $Z=\infty$, there will be no flow for any pressure differential. For both of these conditions, there will be no power produced, and they are analogous to the short circuit and open circuit conditions in electronics (Hughes 2002).

There will be an optimum impedance that allows for the highest possible efficiency of conversion of wave power to pneumatic power as described by Falnes (2002), Falcao and Justino (1999) and Curran et al (1998), amongst others.

So a new method for determining the pneumatic power simulating the turbine must be introduced into the model that allows the determination of the optimum impedance. The models should be compared using their best possible performances, or the comparison is not valid. Identifying and implementing the optimum simulator impedance was made a priority for the tests outlined in Chapter 5.

At full scale, achieving optimum performance is the goal of the control strategy. A, and as changing Z_s clearly affects the overall performance of the system considerably, it is likely to form a significant part of the control system. Falnes (2002)

shows that the optimum $Z_s=Z_r$ (the radiation damping). If Z_r is known, it is therefore possible to design for a particular Z_s by choosing an appropriate turbine specification. With the correct control mechanism (e.g. variable pitch turbine), it will be possible to alter Z_s in service, and possibly even within a wave cycle, to optimise performance. Z_r can be measured using the method described by Brendmo and carried out in Chapter 6 of this thesis.

4.6.3. Scaling

The models were successfully scaled using Froude number criteria, but not using Reynolds number criteria. These two are mutually exclusive at this scale.

The excessive surface roughness of the helical models suggests that there should be an improvement in relative performance of the helical models vs. the plain model, if the fins were smoothed to a finish similar to Perspex.

The relative performance of the models is expected to scale up, and to be augmented (for all models) by the fact that the Reynolds numbers of the models was low compared to the prototypes. Thus if a helical model proves to be better at small scale, it will also be better at full scale.

4.6.4. Designs for next models

The next set of models will be similar in scale to the existing ones, but they will have smooth surfaces throughout. Without an optimum impedance to aim for, it was decided to make a 1.5 twist helix OWC model. The Double twist model appears over damped in all conditions (Figure 4.8) and an intermediate model was considered more promising.

4.6.5. Optimisation

Identifying the optimum turbine impedance was set as a critical task. The models should be compared using their best possible conversion efficiencies or the

comparison will not be valid.

A new shape or configuration, e.g. having the inlet facing the waves or a more hydrodynamically shaped inlet, may help to improve the amount of energy reaching the turbine (Knott & Mackley 1979 and Knott and Flower 1980). A wall, or similar construction behind the OWC would also improve its performance (Sarmiento 1992).

Chapter 5: Wide Tank Tests

5. Introduction

The tests described in this chapter were designed to conclusively determine the comparative performance between the helical concept and a standard non-helical OWC tube. A spinning turbine simulator with variable impedance was used to determine the optimum performance of each model, so that a fair comparison could be made between them. The models were improved to reduce the viscous losses described in chapter 4 and Edinburgh University's curved basin was used to ensure that tank effects were minimized.

Two sets of tank tests were carried out during 2008. The initial tests were used to test the experimental set up; gain understanding of the fundamental working of helical OWCs and to gather initial results. During the second set of tests, the single twist helix was shown to perform 24% better than the plain model as well as having a 27% shorter draft.

5.1. Equipment

5.1.1. Data Acquisition System

The Data Acquisition System (DAQ) was fundamental to the experiments. It was based on the same hardware and software as the DAQ used for the flume tests outlined in Chapter 3. The interface card was a 12 bit analogue to digital system, and this was controlled by a program written in LabVIEW. It not only collected and processed data in real time, but was also the interface for controlling the speed of the spinners used as the improved turbine simulators, and described in section 5.1.6.

5.1.1.1. DAQ updates from Coventry flume tests

The LabVIEW DAQ was upgraded for the calibration of the spinners and Edinburgh tests, and three new major elements were incorporated into the DAQ:

- Add a speed controller for the spinners.
- Add a speed regulator
- Design the program such that the efficiency was calculated in real time.

Two screens were designed to make the system simple and quick to use. The first (Figure 5.1) was for static data that remains the same for each individual test (H, T, draft, model, etc) and the second (Figure 5.2) was for running the tests and monitoring live test data.

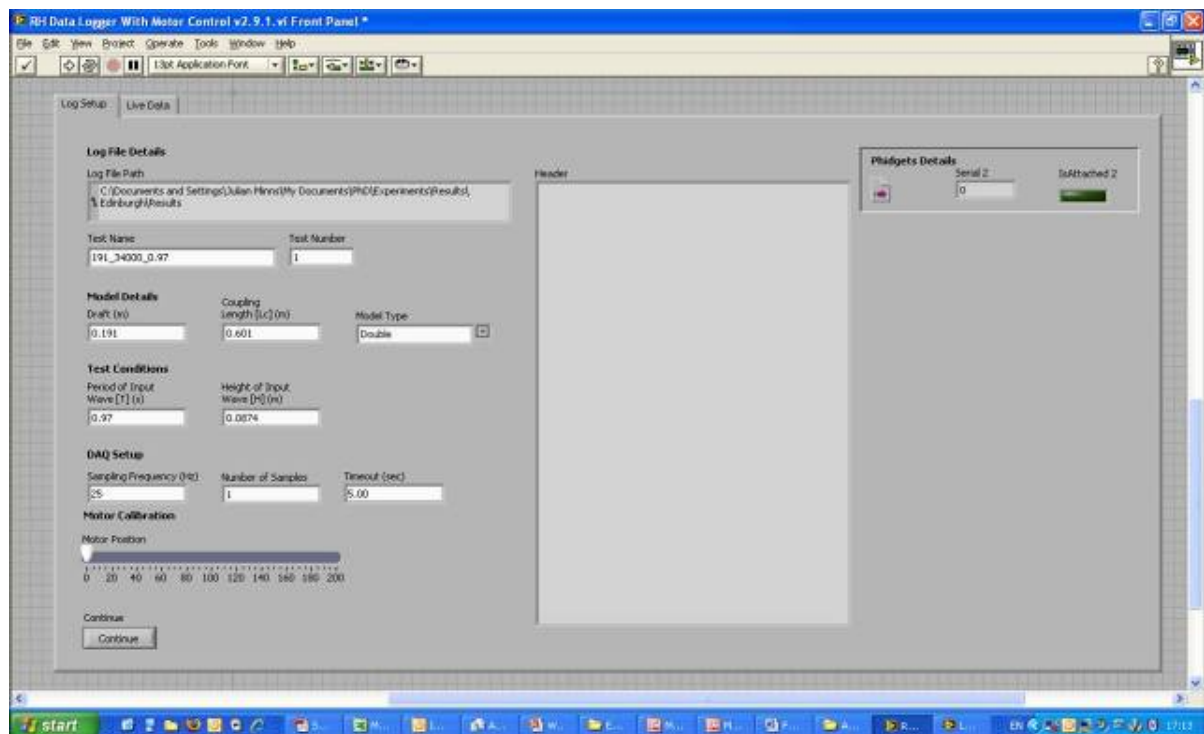


Figure 5.1 LabVIEW first screen.

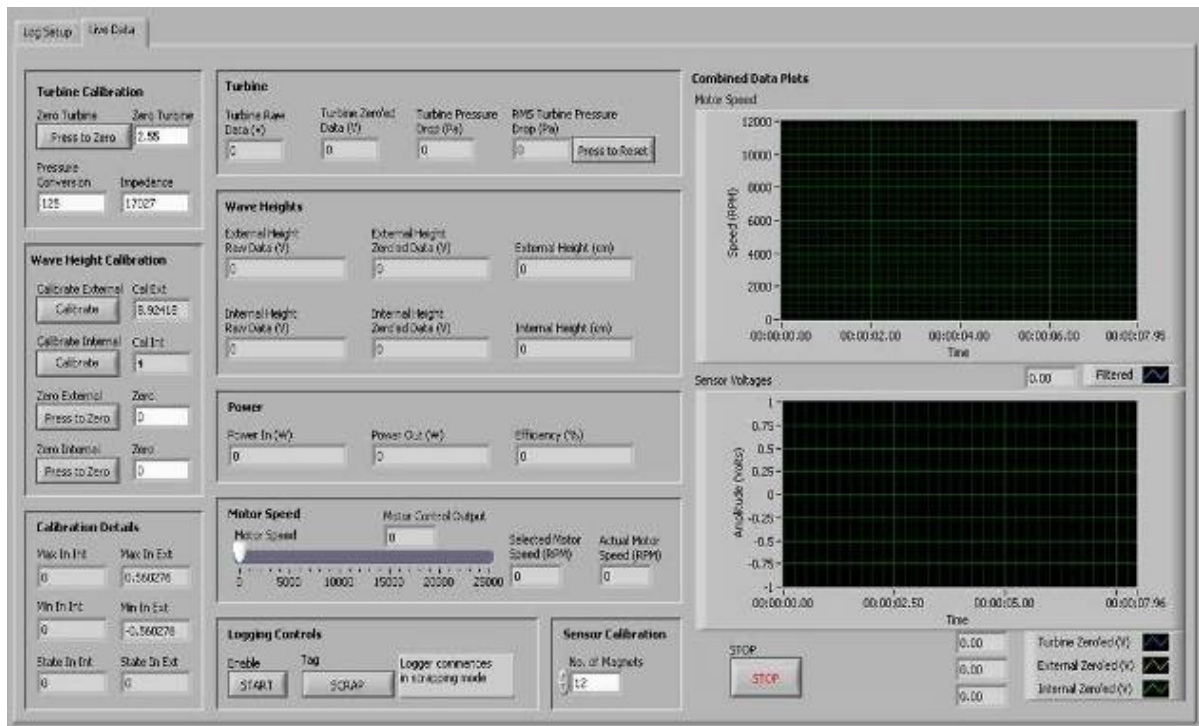


Figure 5.2 LabVIEW second screen.

The most important features of the DAQ are displayed on the second screen, where the impedance is set, the spinner speed is adjusted, the wave probes can be calibrated, and live data can be viewed as oscilloscope plots and as numerical displays. Once the efficiency value became steady, data were recorded for the period of the test.

Speed controller and regulator

The impedance of the spinning simulators, described in section 5.1.6, is proportional to the rotational speed (White 1991). The speed was initially controlled by simply adjusting the voltage supplied to a motor. A sliding input calibrated by speed was added to the LabVIEW program to control the voltage. Unfortunately, this was unstable and resulted in speed fluctuations of ± 350 rpm (over a base speed of 8,000 RPM – 12,000 RPM), which was considered significant, so a speed regulator was developed.

In LabVIEW, it is possible to run a counter and timer at the same time, and this was used to measure the frequency of the rotation of the disks using a hall sensor and magnets attached to the disks. This was then compared to the selected speed, and an adjustment was made as required. The high frequency of the magnetic pulses (up to 2,400Hz) meant that rapid voltage alterations were achievable, and that the speed, and therefore the impedance, was steady.

The speed was cross-checked from time to time during calibration and the tests using an optical counter, designed for adjusting the timing of a car engine.

Efficiency calculation

It is very useful to understand the performance of models during each test run. This allows the experimenter to make early decisions about the effectiveness of a configuration, and to adjust the test schedule during the limited time available in the lab.

To this end, an efficiency calculation was incorporated into the LabVIEW DAQ program.

As discussed per equation 3.6,

$$P_{air} = \sqrt{\left(\frac{\Delta p^2}{Z_s}\right)^2} \quad (5-1)$$

Where P_{air} is the power available in the air flow, Δp^2 is the square of the instantaneous pressure drop across the turbine simulator and Z_s is the impedance of the spinning turbine simulator. P_{air} is taken as the RMS value of $\Delta p^2/Z_s$ as this is the value that is used to calculate power in oscillating systems (Croft et al 2001).

The incident power in a monochromatic wave for a model width of 0.14m is (Falnes 2002):

$$P_{wave} = 0.14 \times 0.976 \cdot H^2 \cdot T \quad (5-2)$$

And so the model efficiency is, η , is given by:

$$\eta = \frac{P_{air}}{P_{wave}} \quad (5-3)$$

The simulators were calibrated (section 5.1.6.3) and the impedance was calculated from this calibration. The same wave height, H and wave period, T set for the run were entered into the LabVIEW program and by measuring Δp , the efficiency was calculated in real time. This meant that post processing was kept to a minimum, and had the added benefit that it was easy to see when a steady state had been reached as the efficiency value attained a steady value and this indicator was used to start the test run.

DAQ performance

The DAQ performed well during the tests and allowed a large number of tests to be undertaken in a limited time.

5.1.2. Pressure Sensors

Following the experience in the flume, described in Chapter 3, where the sensors were operating at the bottom of their range, new +/-2.5 mbar differential sensors (HCLA02X5EB), again from Sensor Technics, were used. A simple circuit specified by the manufacturer was required to use the sensor, and attach the 3 leads: 5v

power, +ve signal and common earth. The National Instruments DAQ card (NI USB-6008) had a 12 bit analogue to digital converter giving 4096 quantisation steps over the 5V range of the sensor. However the useful range was described as 0.5-4.5V giving 3276 steps for 5mbar=500Pa. This gives steps of $500\text{Pa}/3276=0.153\text{Pa}$ giving good resolution, even for small pressure differences. The sampling rate was 25Hz. The sensors were mounted in plastic boxes to protect them and attached to the pressure taps on the models by short, flexible, small bore pipes (Tygon R-3603) designed to transfer pressure readings without distortion due to flexing and distension of the tubes.

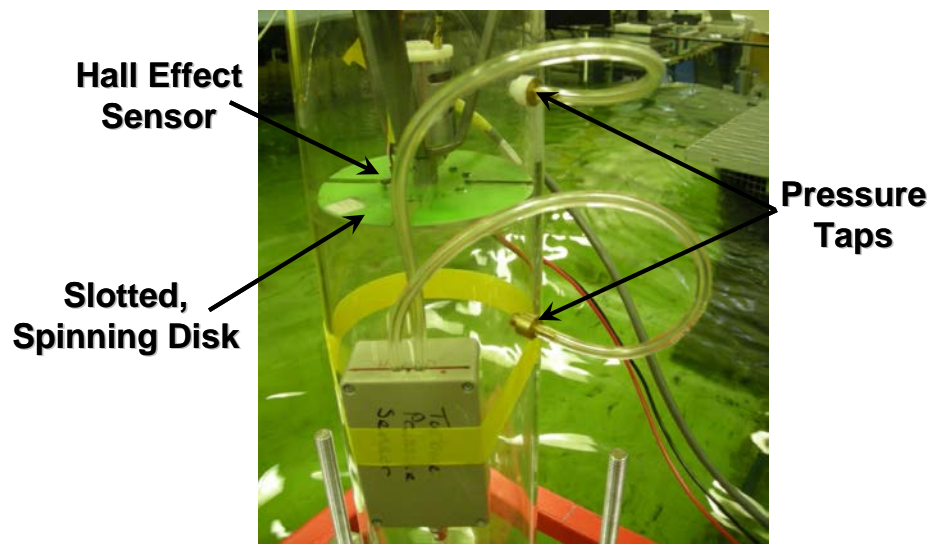


Figure 5.3 Simulator pressure measurement and speed regulator.

5.1.3. Wave probes

Two resistive wave probes, developed as an M.Eng. student project, and described by Marshall (2007) were used in these wide tank tests. Essentially they measure voltage using a circuit that includes two separate metal probes submerged in the water: The higher the water level, the lower the resistance between the probes. The probes were calibrated by moving them up 10cm above their operating position, and then down to 10cm below their operating position. The voltage was taken at each of these positions and the difference in voltage used to calculate the relationship between the voltage and the water level and thus the wave height at any instant.

The probe's normal operating position was with the still water level half way along its length. These probes were used to investigate the water elevation and phase differences in the system.

Similar probes were connected into Edinburgh University's DAQ and were used to calibrate the tank. These readings were used to calculate the incident power and efficiency in conjunction with the author's DAQ described above.

5.1.4. Wave probes of this type must be zeroed regularly as the zero reading drifts with time due to oxidation and impurities building up on the probes and altering the resistance. The probes were zeroed after every second or third test, and calibrated at least once per day. There was little difference between the calibrations (i.e. the relationship between the change in voltage compared to the change in depth), however the zero was seen to alter, so the re-zeroing was a useful exercise.

However the wave probes performed erratically, especially during the second set of tests: one wave probe channel failed altogether, and the other gave low readings. Unfortunately, there was insufficient time to repair the solid state circuitry, so the wide tank tests went ahead in Edinburgh with one malfunctioning wave-probe. The data gathered allowed the phase difference between the water inside the OWC and outside it to be analysed, so this was not a critical problem, and this is discussed in section 5.4.2.

5.1.5. Models

The same model designs were used as for the Coventry flume tests, but three new ones were made, and the fins were smoothed and filled to reduce their surface roughness, and then sprayed with gloss paint to make the surface as close as possible to the Perspex tube of the plain model.

The original plain model was used, and an additional 1.5 twist model added as an

intermediary between the single and double twist models. Figure 5.4 shows the original plain and new single twist models.

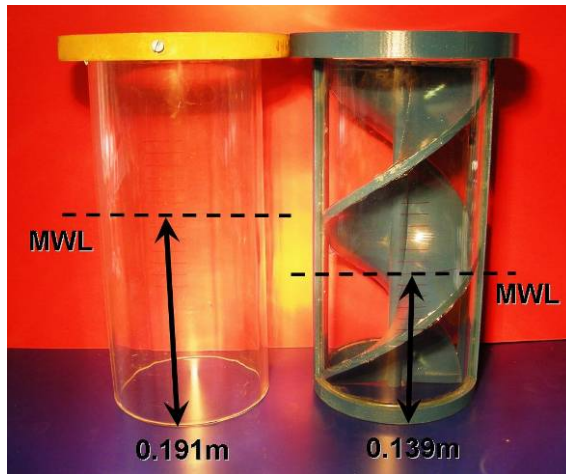


Figure 5.4 Plain and single twist models showing drafts for equivalent resonant periods. MWL=Mean Water Level.

5.1.6. Spinning turbine simulators

It was identified during the previous work that a better turbine simulator was required for the wide tank tests, and various options were considered:

Options

Various turbine simulators were considered for this round of tests:

1. A standard orifice or slotted plate.
2. A porous mat.
3. Slotted flaps made from rubber, metal, or some other flexible material.
4. Pitot tubes & pressure sensors across a valve.
5. A spinning simulator.

Options 1-3 would have involved a significant time to change between the required impedances as a physical item would have to be replaced for each impedance used. This would have meant that it was likely that many unnecessary tests would have to have been run to determine the ideal impedance, in order to save time on swapping from one simulator to another.

Option 4 was the second choice: The valve could have been automated and quick to change, but the pitot tubes were an extra expense and would have added unnecessary complication: the flow would have to have been measured by one Pitot tube in one direction and another in reverse flow. Also, Pitot tubes work best in laminar flow conditions, and these were not guaranteed.

Option 5 gave a relatively simple variable impedance simulator, (with similar characteristics to a Wells turbine) that was used to alter impedance for iterative searches for the best performance. A further development could be to incorporate a real time control system to simulate varying the turbine impedance within a cycle. At full scale this is likely be achieved by altering the pitch of blades or fins, and with valve control of the air flow (e.g. Falcao and Justino 1999) but at this small scale, a motor was used, with voltage control and speed sensing, to rapidly move between rotational speeds.

5.1.6.1. Spinning simulator concept

The concept described in Option 5 above can effectively be thought of as a Wells turbine with flat blades. This type of simulator has been used successfully when model testing the Clam WEC (Bellamy et al 1985). The simulator is spun using a motor, and the impedance varies linearly with flow rate: As the rotational speed of the disk increases, the effective solidity of the disk also increases (White 1991). This means that a fixed impedance can be chosen at will and using an iterative test protocol, the optimum performance can be determined. A more sophisticated setup could include a variable speed simulator that automatically tunes the system to the prevailing conditions.

The spinner was turned by a 7.2V, 19.7W DC motor. This was fixed in the model by a steel bracket and the spinner was attached directly to the shaft of the motor as shown in Figure 5.3.

Several speed control options were tried: First of all, a simple voltage control was used, however this produced speed fluctuations, and a speed regulator was clearly required. Next a slotted disc, L.E.D. and light sensor were tried, but this setup suffered from interference from room lighting, which caused the speed to fluctuate unpredictably. Using a cowl was considered and rejected as it could interrupt the airflow, and there could be no guarantee that light would not filter in and affect the sensor during the tests. It was also considered desirable to be able to see the simulator in operation. Finally, a Hall effect sensor and 12 small magnets were used to sense the speed. This proved more robust, and the speed was controlled via a feedback loop to within ± 50 rpm in the worst case, even at speeds in excess of 12,000rpm.

Figure 5.3 also shows the motor, fixed to its bracket, and the spinner bolted to the axle of an electric motor. A Hall effect sensor and 12 magnets were used to govern the rotational speed of the simulator, and a differential pressure sensor was used to measure the pressure drop across the simulator.

The product of the pressure drop across the simulator and the air flow rate through it gives the power available in the air flow through the simulator.

5.1.6.2. Simulator designs

Two simulators were fabricated: four-bladed and six-bladed, and these were attached to the motor which has a top speed of 20,000RPM.

During calibration, the maximum speed obtainable was 9,000 rpm. This was largely due to vibrations in the handmade spinners, which meant that they periodically brushed against the inside of the duct causing them to fluctuate in speed. This limited the maximum speed (which was measured at 14,000rpm outside the duct) and therefore the impedance. The drag on the spinning simulators accounts for the remaining 6,000 rpm. A third rotor, with four slots, was therefore designed to increase the impedance by a factor of 2.

White (1991) has shown that the impedance of a Wells turbine is related to its solidity:

$$Z_s \propto \left(\frac{1}{S_a} \right)^{1.65} \quad (5-4)$$

where S_a is the solidity of the rotor, (this is the area of the annulus swept by the blades excluding the hub divided by the area of the blades themselves A solidity of 1 indicates complete blockage). In order to double the impedance, this relationship can be used to determine the solidity of a simulator with double the impedance:

$$\frac{Z_s}{2.Z_s} = \frac{\left(\frac{1}{S_{a1}} \right)^{1.65}}{\left(\frac{1}{S_{a2}} \right)^{1.65}}$$

$$\frac{S_{a1}}{\sqrt[1.65]{2}} = 0.657 S_{a1} = S_{a2} \quad (5-5)$$

This relationship was used to design the 4 slot simulator which is shown with the six-bladed design in Figure 5.5. The new simulator was slotted rather than bladed as this was the most effective way to achieve the required solidity. The 12 magnets for the Hall effect sensor can also be seen:

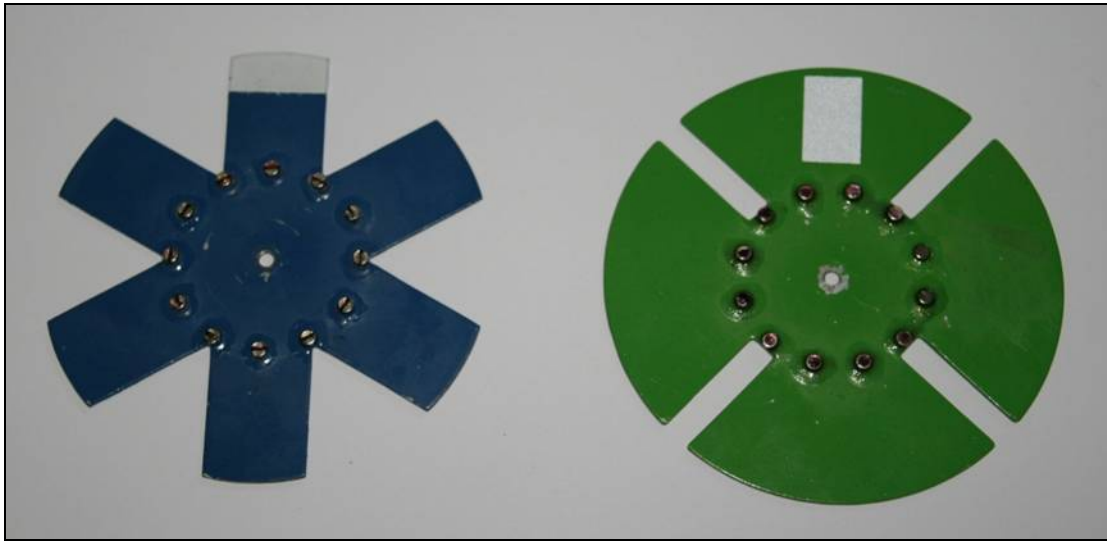


Figure 5.5: 6-Blade and 4-slot turbine simulators.

The 4-slot simulator has twice the impedance of the 6-bladed one.

5.1.6.3. Simulator calibration

The flow through the simulator and the pressure drop across it were measured at various rotational speeds to calibrate it. As discussed in Chapter 2, the impedance was then found using the expression:

$$Z_s = \frac{\Delta p}{Q}$$

The accepted convention for measuring flow rate through an orifice plate dictates

that the pressure taps should be placed $1D$ upstream and $0.5D$ downstream, where D is the internal pipe diameter (British Standards Institute 1987 and Figure 3.5). This is not possible with a single differential pressure sensor in bi-directional flow. As a compromise, the taps were mounted $0.5D$ either side of the simulator, meaning that the differential pressure measured was slightly lower than the maximum, and therefore that the power calculated would also be somewhat lower. This was accepted as the comparative performance of the models was the primary objective of the tests and this comparison would not be affected by the lower power value.

The six-bladed turbine simulator was calibrated under steady-state flow conditions in the same rig as the flexible slotted simulators described in Chapter 3 (Figure 5.6).



Figure 5.6: Calibration rig including strobe lamp used to double check the RPM.

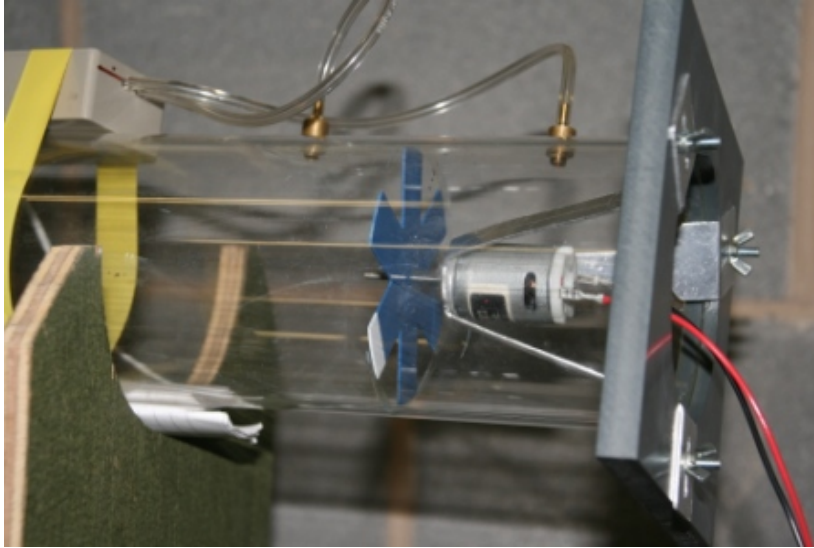


Figure 5.7: Spinner in calibration rig.

Simulator Calibration Results

In a similar set of experiments to those described in Chapter 3, the spinner was run with a selection of fixed voltage inputs, and a series of flow rates was produced, using the fan in the test rig, for each of these voltages. The family of $\Delta p/Q$ curves was then plotted as shown in Figure 5.8.

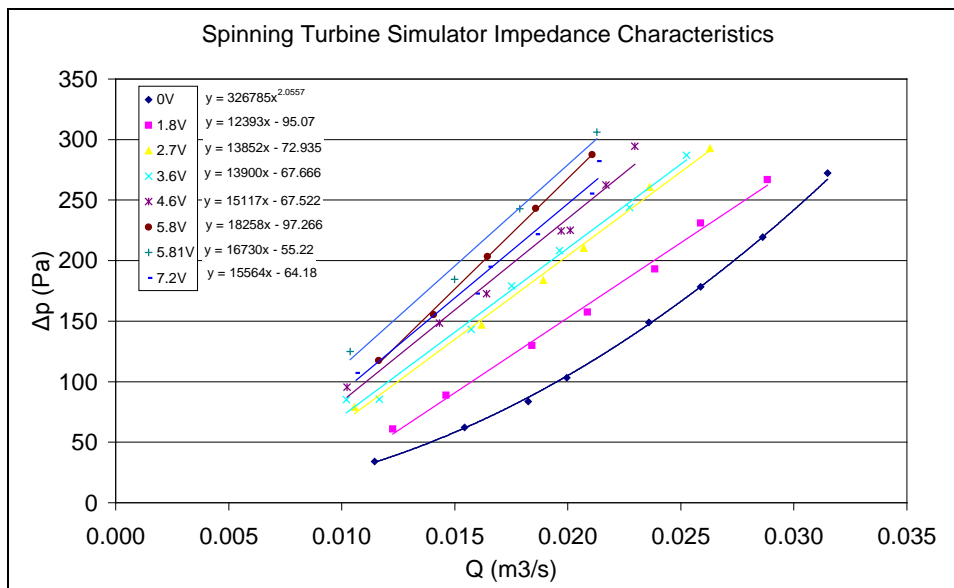


Figure 5.8: $\Delta p/Q$ curves for the six-bladed spinner.

Using a fixed voltage input resulted in a slight variation in speed but it can be seen from the results that the predicted proportional relationship still exists, i.e. a fixed speed results in a fixed impedance irrespective of flow rate.

The 0V (no rotation) results clearly show a curve, and the rotational speed was so unsteady at 7.2V, due to the spinner brushing the wall of the duct, that these two results were omitted when plotting the Z_s /RPM line in Figure 5.9 below.

The tests in the Edinburgh University wave tank resulted in flow rates between 0.001 and 0.003 m³/s which are clearly below the range of the calibration rig.

The lines in Figure 5.8 should pass through the origin since there is no pressure differential when the flowrate is zero, and this suggests that the gradients, i.e. the impedances, Z_s , in the operating region are likely to be lower than those measured, and also may be on a curved part of the graph. With no way to reduce the flow further in the calibration tests, the results obtained were used and the error was presumed to be proportionally similar for all of the speeds. Any curvature of the lines in the region 0-0.003 m³/s was considered likely to be slight so the fixed speed -fixed Z_s relationship was still assumed to be valid.

However the value of Z_s in the operating region is likely to have been lower than that used to calculate P_{air} , and therefore efficiency. With no better equipment available, it was not possible to evaluate this error.

The important characteristic of the simulators is to provide a variable and repeatable impedance so that the models could be compared at their maximum operating efficiency and this characteristic is supported by these results.

The relationship between impedance and speed was plotted and the formula for the fitted line used to determine the impedance at various speeds during the tests.

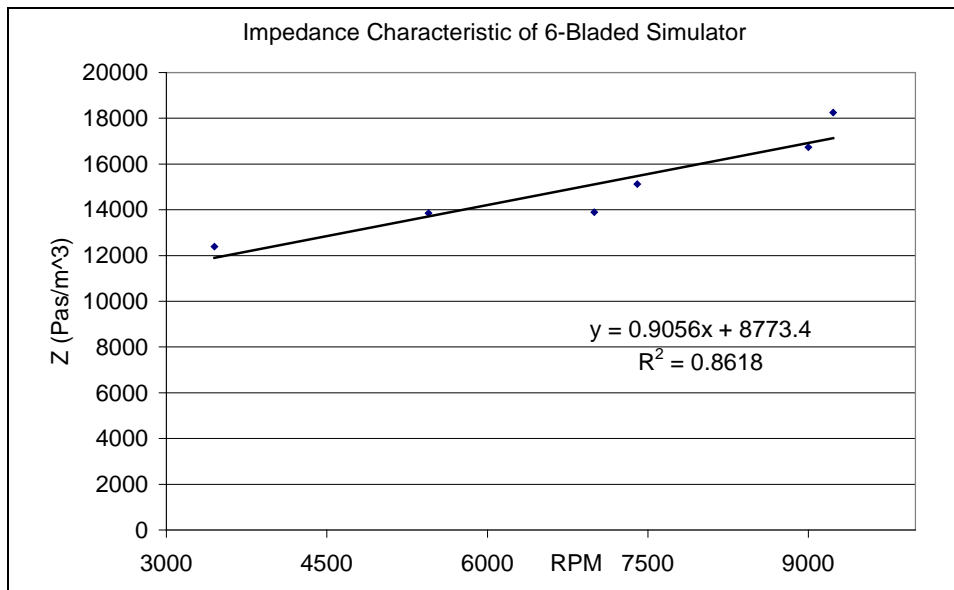


Figure 5.9 Impedance characteristic of the six-bladed simulator.

Unfortunately, due to logistical problems, the four-slotted simulator could not be calibrated in a similar way so, following the theory detailed in White (1991) and outlined above, the impedance was doubled at each speed as shown in Figure 5.10. The formula generated was then extrapolated into the region of higher speeds and this relationship used when choosing impedances for this simulator during testing.

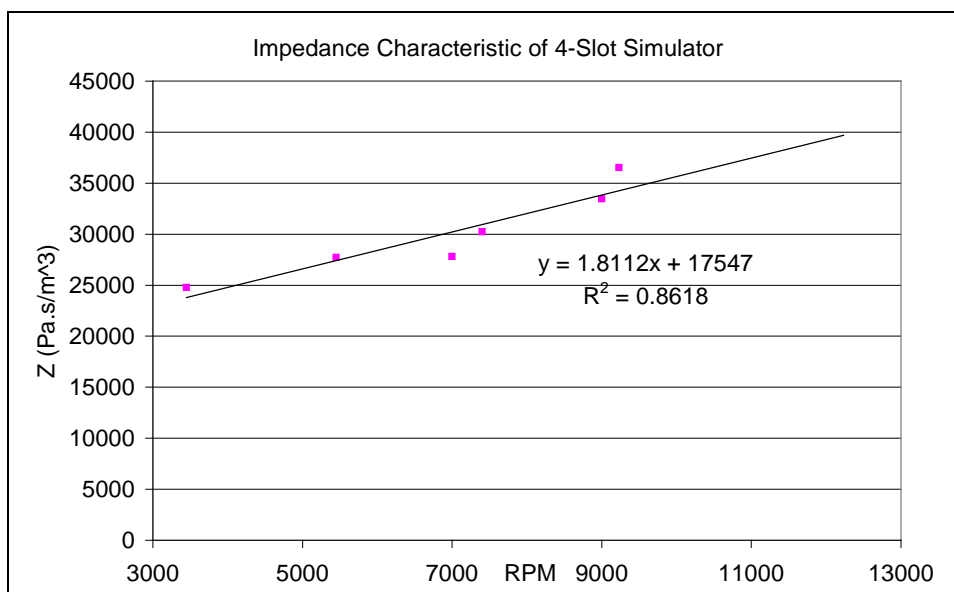


Figure 5.10: Impedance characteristic of the four-slotted simulator.

Estimating the error in Z_{S_2}

The calibration curves in Figure 5.8 should pass through the origin as there is no pressure drop without any flowrate and vice-versa. The straight fitted lines of Figure 5.8 have been replaced with lines following a power relationship (between pressure drop and flowrate) in Figure 5.11, to illustrate the possible error.

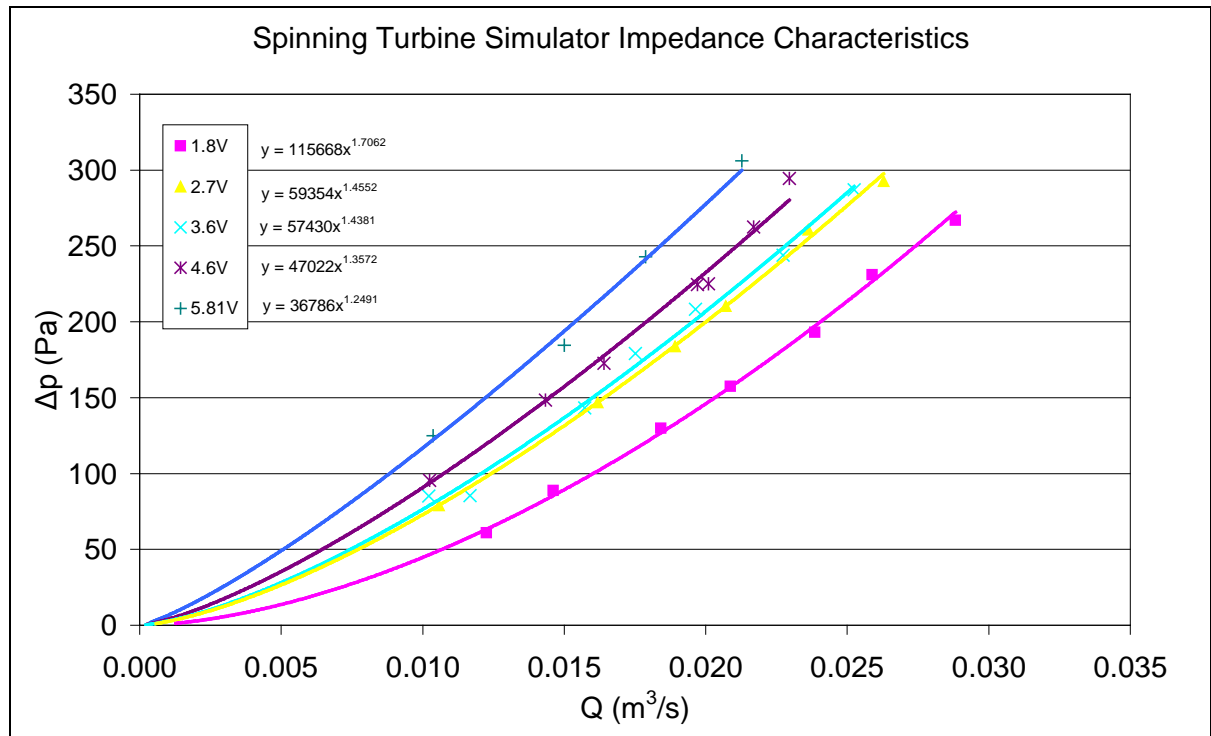


Figure 5.11 Extrapolated calibration curves showing the possible relationship in the operating region 0 to 0.003 m³/s.

For the purposes of this error estimation, it is assumed that the characteristic curves in Figure 5.11 are accurate in the operating region. It is of course possible that the gradients in the operating region are lower than those shown here, but it is considered unlikely that they would be higher. The errors estimated below are therefore a lower bound.

By differentiating the equations of the lines in Figure 5.11, the gradient of the line can be evaluated at any point. This was done for a flowrate of $0.001\text{m}^3/\text{s}$ and $0.003\text{m}^3/\text{s}$ to give the impedance of the turbine in this region.

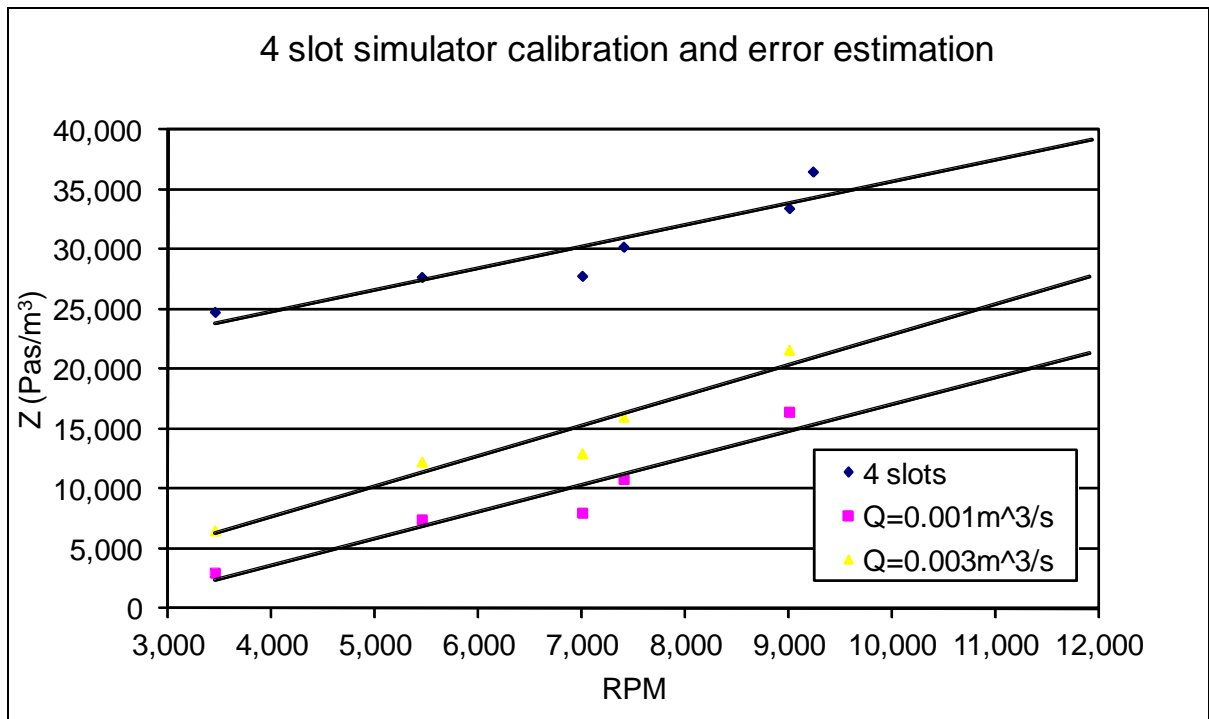


Figure 5.12: Comparison of impedance in the calibrated region with that in the operating region.

The spinners were used in the range 6,000 to 11,000 RPM, and lower impedances were used in the resonant region than outside it. The flowrate was larger in the resonant region, so the error is likely to have been close to the difference between the 4 slots line and the $0.003\text{m}^3/\text{s}$ line at about 7,000 RPM for resonant regions. From Figure 5.12, this is $30,000/12,500 = 2.4$.

Outside the resonant region, 11,000 RPM was used for all of the tests, and the flowrate was lower, so the error is likely to be closer to the difference between the 4 slots line and the $0.001\text{m}^3/\text{s}$ line at 11,000 RPM is a factor of $37,500/19,000 = 1.97$.

5.1.6.4. P_{air} Errors

The power in the air, calculated from equation 5.1, was underestimated for two reasons:

1. The pressure was slightly underestimated as taps were 0.5D either side of the simulator and the highest pressure drop occurs when one tap is 0.5D upstream, and the other is 1D downstream (BS 1042, 1987)
2. The calibration of the simulator led to high values of Z_s , as described above, reducing the value by a factor of between 2 and 2.5.

In fact, the flowrate varies during each cycle, so the factor will vary between these values. As mentioned above, 2 and 2.5 are likely to be lower bounds of the error since the actual shape of the calibration curve is not known. The gradient could have been lower, which would give a lower impedance value, and increase these two factors.

These systematic errors were carried through to the efficiency in equation 5.3, meaning that all P_{air} and η values were underestimated by the same factor of 2 to 2.5. The errors were very similar for all of the models (when tested in the same conditions), so the comparative results are still valid.

The important criterion for the simulators was that they could be used to determine peak performance for each of the models in such a way that results obtained in one run could be compared confidently against those of any other run. The spinners described here do give repeatable and steady impedances that are quick to change between tests.

5.1.7. Setup

A bracket was fabricated that could be fixed to the walkways surrounding the tank. As the precise location of the model was not known in advance, a set of threaded hooks was designed to allow firm but flexible mounting.

It was important that the model draft could be adjusted quickly, so a three-point mounting was designed to firmly fix the model within the fixed frame (Figure 5.13). The three adjustable screws gave a high degree of accuracy when setting the draft, which was done by lining up the still water level with a line drawn onto the model. The model could be swapped rapidly for another and was fixed to the bottom of the duct containing the simulator.

The six-bladed simulator can be seen spinning in Figure 5.13 and the wave probe is attached to the vertical white rod in the background.

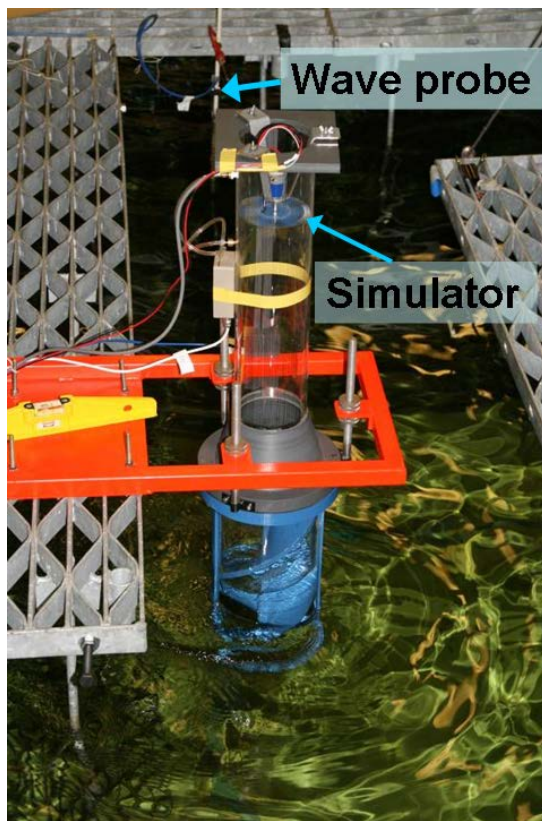


Figure 5.13 The experimental setup in the Edinburgh University wave tank showing the Single twist model.

5.1.8. Edinburgh University Tank

The tank at Edinburgh University was conceived by Prof Salter of Edinburgh University (Salter 2001) and is curved in order that multi-directional waves can be generated in a small tank (Taylor and Mackay 2001). Edinburgh Designs (a university spin-off company). Designed the yellow wave-makers which can be seen

under the walkway on the right of Figure 5.14 and the absorbing beaches are under the walkway on the left.

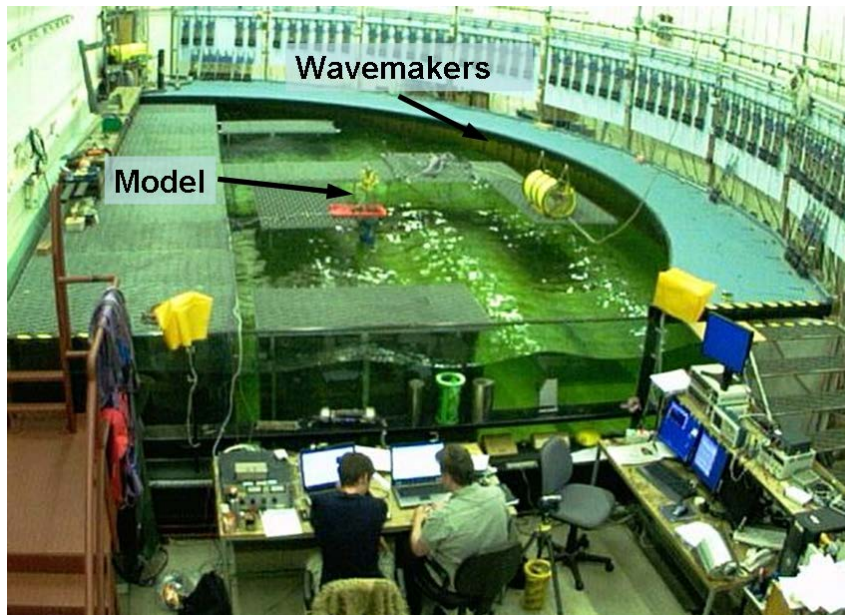


Figure 5.14: Edinburgh University's curved tank with the single twist model under test.

Two additional absorbers were placed on the near and far sides of the tank to absorb any cross waves formed, and increase the quality of the incident waves.

Waves are created using a series of paddles, hinged at the bottom, around the curved edge of the tank. Each paddle has a sensor to measure the force of the water acting on it. This sensor is used to ensure that the correct force to create a given wave is applied to the water at any given instant. In turn, this means that waves reflected onto the paddles are absorbed giving good quality, repeatable waves at the model under test.

Experience has shown the Edinburgh University team that there is a 'sweet spot' that is best for repeatable waves, and the model was positioned at this spot.

The range of periods available from the tank is given as 0.5-2.5s. In fact, the lowest practical period is about 0.67s as the waves break below this value since the waves

have a steepness of about 1:12. Above 2s, the waves do not form well since the paddles are only 0.7m high and can't generate long wavelength waves with the heights required. In addition, there is a lot of reflection from the beach (up to 25% at 2.5s). This means that the effective range of periods is 0.67s to 2s. 30 periods were chosen with a distribution designed to give a better defined region of readings around the expected peak performance where higher resolution is desirable. This spread can be seen in the spacings between the points in Figure 5.15 below.

The height of the incident waves was limited by the height and stroke of the paddles for low periods and to prevent them from breaking for high period waves. For this set of tests, the largest wave that could be made at each period was chosen. This would give the best chance of getting a measurable Δp . This was a concern since the previous pressure gauges were oversized as discussed in Chapter 3, and the waveheights were chosen to ensure that the maximum possible range of the pressure sensors was used.

Figure 5.15 shows the wave heights chosen at each wave period for the first set of tests. In the event, the tank control wasn't perfect, and specifying a wave height did not guarantee that that wave height would be produced in the tank. This set of waves was produced:

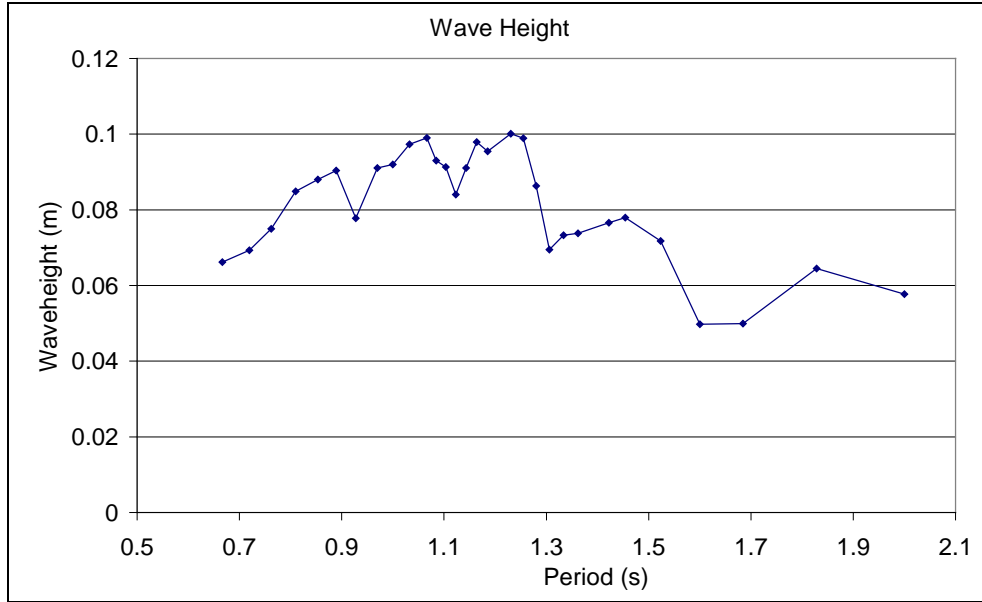


Figure 5.15: Wave heights for the first set of tests in the wide tank.

The irregularity of the curve in Figure 5.15 proved to be a problem as it made identifying resonant effects difficult due to the peaks and dips in wave height being associated with peaks and dips in performance. It was determined that a smoother set of curves would be tried for the next set of tests.

Accordingly, a day was spent achieving the waves (shown in Figure 5.16), at the beginning of the second tests. This was done by adjusting the input waves, and measuring them. The goal was to achieve a similar wave height for the range of periods where resonance was expected, i.e. $0.85s < T < 1.2s$, to give some confidence that the results in that region were comparable. The incident power was then calculated using equation 2-6 modified to show the power in a width of wave equal to the model diameter, $D=0.14m$:

$$P_i = D \cdot \left(\frac{\rho g^2}{32\pi} \right) TH^2 \approx 0.14 \cdot 0.98 TH^2 (kW / m)$$

The wave heights and incident power for the second set of tests at Edinburgh are shown in Figure 5.16:

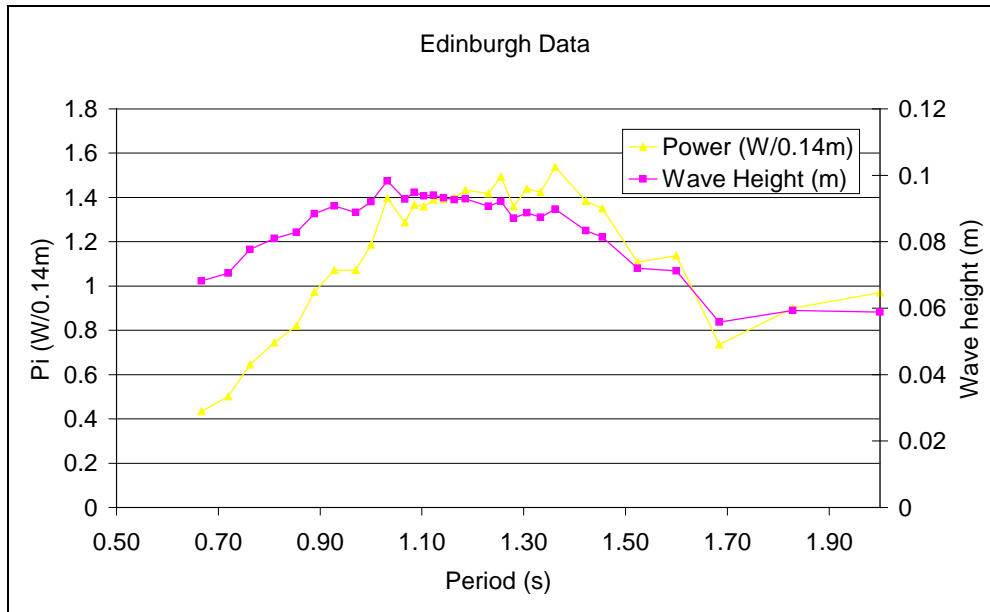


Figure 5.16 Incident wave height and power plotted against incident wave period.

It should be noted that the incident power is proportional to the square of the wave height, so when this is plotted, the peaks and dips are exaggerated.

5.1.8.1. Non-linear waves

About half of the waves created in the tank were non-linear. Waves that have a wavelength < depth/2 are considered to be in shallow water and the interactions of the seabed affect their shape and motion. The tank at Edinburgh was 1m deep, so any waves with a wavelength over 2m can be considered a shallow water wave. From Figure 5.17 this is all waves where $T > 1.12s$. Waves with a steepness of 1:10 or more are also non-linear as they begin to break. It can be seen from Figure 5.17 that the first few low period waves are close to this figure.

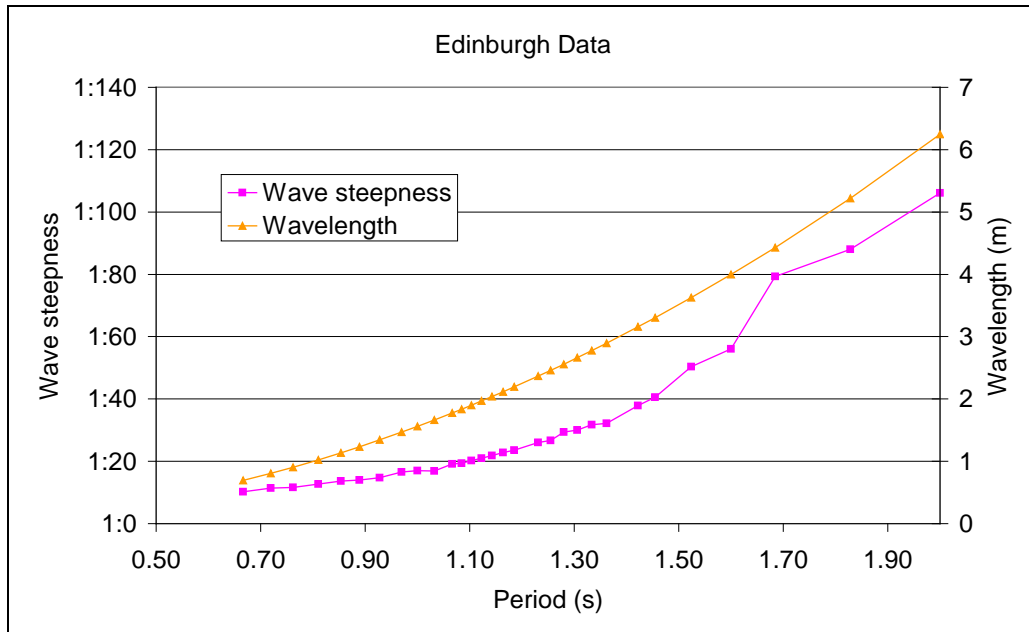


Figure 5.17 Wave steepness and wavelength plotted to identify non-linear waves.

The non linear waves used at Edinburgh are repeatable, and so they don't affect the comparison of the models, however they are not straightforward to model mathematically, and this is discussed in Chapter 6.

5.1.8.2. Repeatability and errors

The tank was found to provide very repeatable waves, in terms of waveheight and period, which were measured three times at the beginning of the tests. No difference was measured between the same repeated periods, and the waveheight varies by 2% over a 1 minute test, and this decreases to 0.5% for a three minute test. This repeatability was mirrored in the performance of the models. Figure 5.18 shows a typical sample of repeatable runs.

In order that only useful data were recorded, the Δp RMS cache could be reset on demand to eliminate data resulting from the initial, non-fully developed waves.

Errors were due to:

1. Speed fluctuations in the range $20\text{rpm} < \text{Speed} < 50\text{rpm}$

2. The operator's ability to read the fluctuating efficiency figure was limited to about +/- 0.02% of efficiency.
3. +/-1% of the full scale of 5mbar = error in measuring the pressure (from the sensor datasheet)
4. The wave height repeatability was about 2% for 1 minute tests, decreasing to 0.5% if the average wave height was measured over 3 minutes.

The partial differentiation method was then used to estimate the cumulative error:

The partial derivative of errors can be added together to get the total error for a particular sample. The general form is:

$$df = \frac{\partial f}{\partial a} da + \frac{\partial f}{\partial b} db \quad (5-6)$$

Where f is a function defining the variable being measured. And a and b are variables in that function.

In this case the function is,

$$\eta = \frac{\Delta p^2 / Z_s}{0.98 H^2 T} \quad (5-7)$$

No error in T was measured, so the partial differential is:

$$d\eta = \frac{2\Delta p / Z_s}{0.98 H^2 T} d\Delta p + \frac{2\Delta p^2 / Z_s}{0.98 H^3 T} dH + \frac{\Delta p^2 / Z_s^2}{0.98 H^2 T} dZ_s \quad (5-8)$$

Substituting in efficiency on the right gives:

$$d\eta = \frac{2\eta}{\Delta p} d\Delta p + \frac{2\eta}{H} dH + \frac{\eta}{Z_s} dZ_s \quad (5-9)$$

The values for the pressure drop, Δp , the wave height, H , and the simulator impedance, Z_s , were taken from each test run, as was the efficiency value. $d\Delta p$ is 1% of the full scale value, dH was taken as 2% of the wave height and dZ_s was calculated using the equation from Figure 5.10 and the RPM error which was in the range ± 20 to ± 50 RPM.

This produced a 6.5% error to which was added the 0.02% operator error in reading the efficiency giving a total error of between 7% and 10% and these are shown as error bars in Figure 5.18. The red triangles show the 11 repeatability tests, all of which fall well within the error range.

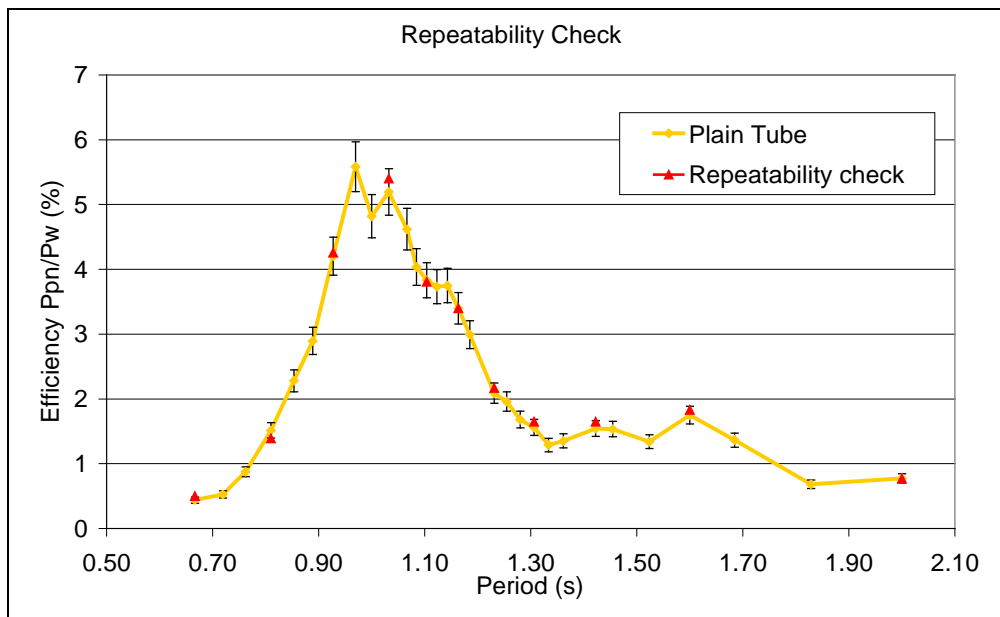


Figure 5.18 Whole system repeatability check.

This level of repeatability was considered acceptable and error bars are shown for the results obtained to give confidence in the conclusions drawn.

5.2. Test protocol

A test protocol is important as it defines the tests to be run and helps to define the quickest sequence of tests. Test protocols also define the priorities of the

programme and having a clear understanding of these aids decision making during the tests when the pressure is often on to finish in a certain time. In this case, Jamie Taylor of Edinburgh University generously allowed me to test in their curved tank on two separate week long visits.

250 test configurations were planned, and a schedule arranged to minimise test times. It would have been useful to test more data points for each model, however there was not enough time available in the tank.

1. Set draft (long process, so do least often)
2. Set wave $H=\text{const}$; 30 periods in the range $0.67\text{s} < T < 2.00\text{s}$
3. Test min 5 turbine settings
4. For 30 H/T Combinations
5. For 7 model configurations: Models at resonant draft. All models at shortest draft.

The test protocol is shown as a flow diagram in Figure 5.19:

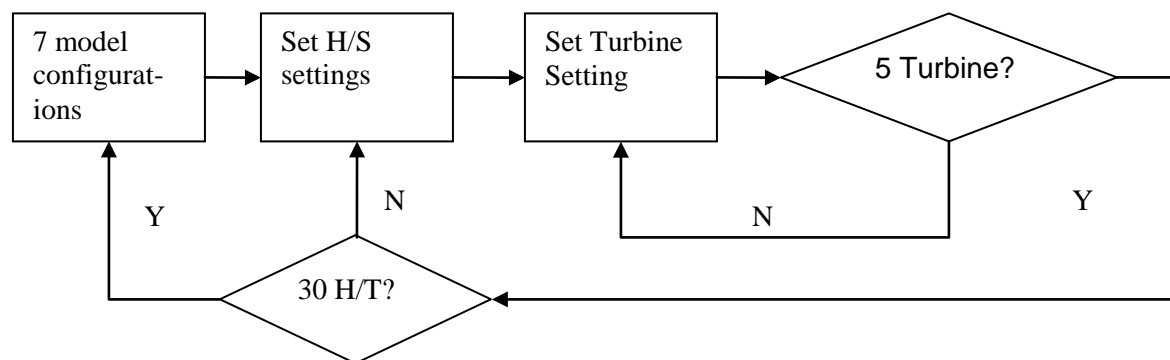


Figure 5.19 Test protocol flow diagram.

Evaluating these flow diagrams and breaking them down into tasks led to an estimation of 33 hours for the first set of tests and 43hours for the second set of tests

Inevitably there were delays, but all of the tests were completed in about 45 hours during the first visit and 55 hours during the second, and Edinburgh University was

kind enough to allow the author stay on site to complete the tests.

Clear goals are important as they aid decision making during a pressurised period of testing. The Goals for the tests were:

1. Test all models with same coupling length
2. Test all models with same draft
3. Plot P vs. Z to determine optimum Z.
4. Compare performance of optimised models with same draft, d, and same resonant length, L_c
5. Compare performance of Plain Tube with different drafts.
6. Eliminate ineffective models.

5.2.1. Key

A shorthand to define the different combinations of model, simulator impedance and draft will be used in the rest of this chapter.

Configurations will be given a name in the form:

M Z d

Where

M is the model (P, S, 1.5, or D),

Z is the impedance in kPa.s/m^3 ,

d is the draft in meters

For example, the 1.5 twist model with an impedance of $17,000\text{Pa.s/m}^3$, a draft of 191 mm will be called:

1.5 17 0.191

5.3. Results of the first Edinburgh tests

Two sets of experiments were undertaken in Edinburgh's curved tank during two week long visits. The first visit was designed to gain a preliminary understanding of the models and their characteristics and the experimental equipment. The second set was to generate performance data for comparison of the models.

5.3.1. The Aims of the First Round of Experiments

A preliminary indication of the comparative performance of the models was important and the tests were set up to achieve this. In addition, this first round of testing was largely focused on learning how the test equipment and tank performed. The other important goal was to eliminate one or two models to reduce the number of tests required during the second round of experiments at Edinburgh University.

5.3.2. Time series

The waves incident on the model were measured at a point about 1.2m upstream of the model, and in line with the centre of the model. The wave probe was therefore subject to reflections from the model, but these reflections were considered small compared to the size of the waves, and the data could be used for calculating the phase difference between the wave outside and the wave inside the model. This is useful as it gives an indication of how close to resonance the system is operating. At resonance the water level inside should be 90° behind the incident wave as described by Main (1998) and shown in Figure 5.22.

Air can be considered incompressible for small scale wave energy converter tests (Weber 2007). This is because flows with a Mach number, $Ma < 0.2$ can be considered incompressible, and it is not until the $Ma \geq 0.4$ that compressibility becomes significant (Massey 1989).

The Mach number is defined by Massey as:

$$Ma = \frac{V}{a} \quad (5-10)$$

Where V is the velocity from Table 4-5 and a is the speed of sound in air, where a=343m/s (Massey 1989).

The double model velocity was the largest at 0.335 and using these figures in equation 5-10 gives a Mach number of:

$$Ma = \frac{0.335}{343} = 0.00098$$

This is clearly below the 0.2 value given by Massey, so the flow in this case can also be considered incompressible.

For a stiff system, there is no phase difference between the input and the output signal (Main 1989). The input signal in this case is the wave, and the velocity of the surface of the wave will be in phase with the flow rate. The velocity of the surface inside the model will precede the surface elevation inside the model by 90° and so will the flowrate. The differential pressure is generated by the flowrate and it has its maximum and minimum points at the same time as the flowrate experiences its maximum and minimum flows. The differential pressure is therefore in phase with the flowrate and as the power is a product of differential pressure and flowrate, it will also be in phase with them. The power, differential pressure and flowrate will all precede the internal water surface level by 90°.

It is possible to infer the phase difference between the internal and external levels by adding 90° to the phase difference between the incident wave height and the power / pressure or flow rate plot.

Figure 5.20 below shows a sample plot of wave elevation and power for the plain tube at resonance. The power is the instantaneous power was calculated according to equation 3.6 and is always positive, so it is difficult to see the phase difference from this plot.

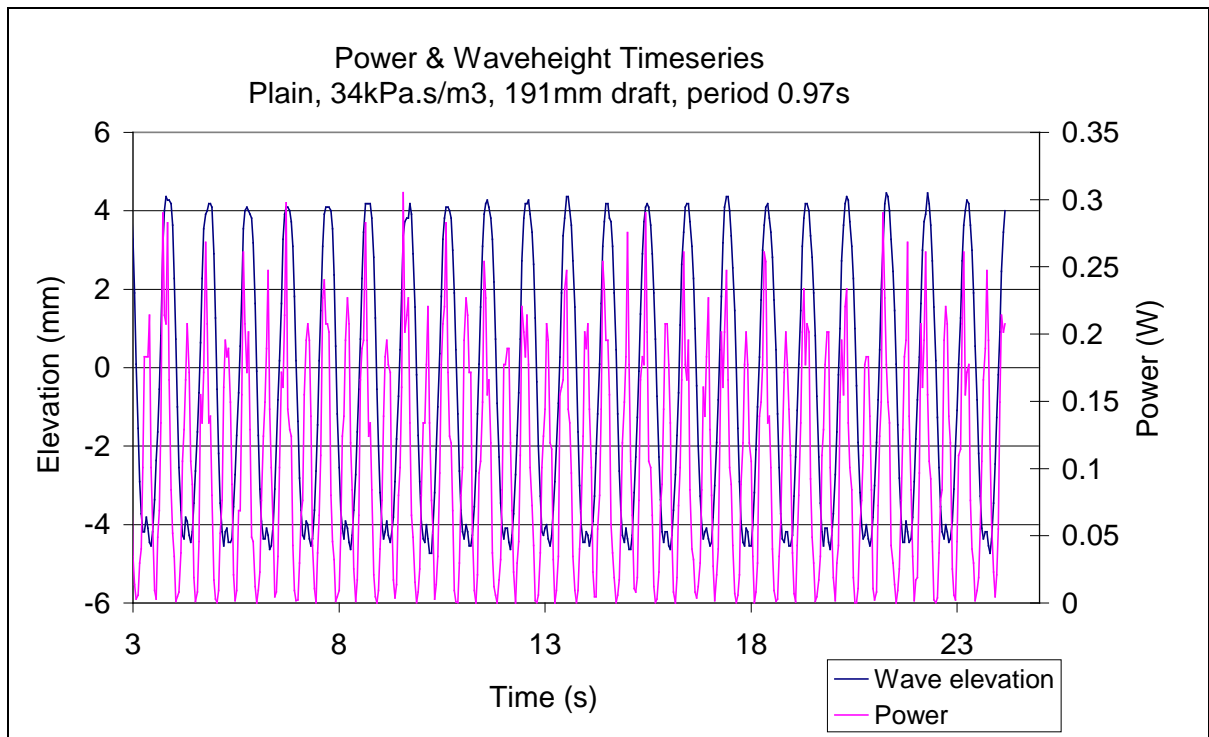


Figure 5.20 Wave elevation vs. Power for the plain model at resonance.

Figure 5.21 is a time series plot of pressure and wave elevation for the same set up as Figure 5.20. Pressure was chosen rather than flow rate as it was the parameter that was actually measured and the relationship with the waveheight is clearer. At $T=0.97s$, resonance is expected (see Figure 5.24), so the phase difference between the external and internal water levels should be about 90° and the phase between the internal water level and the pressure reading should be -90° as well. This gives a 0° phase difference between the external water level and the pressure across the turbine at resonance, which is shown in the pressure plot in Figure 5.21 below.

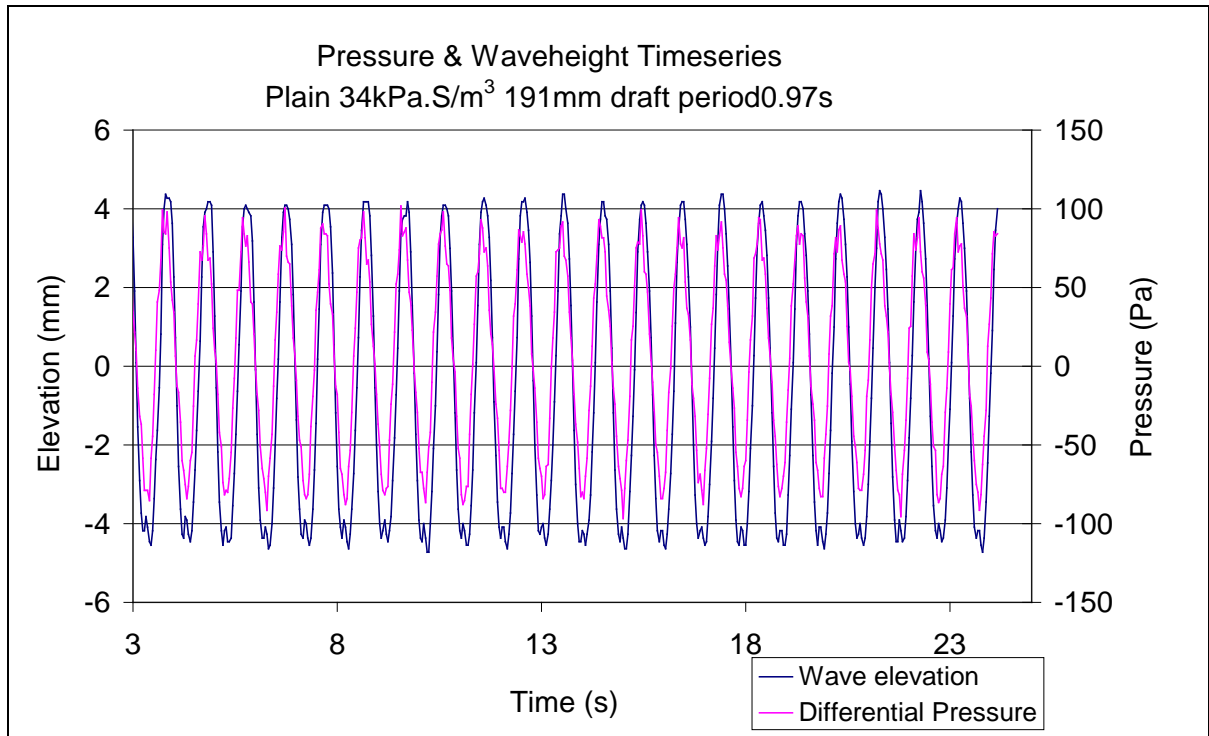


Figure 5.21 Plot of Wave elevation vs. Pressure.

Figure 5.21 shows that the sensors were all working satisfactorily. There is a discrepancy in the wave height which should have been 91mm according to the tank calibration, instead of the ca. 85mm shown here. This discrepancy is probably due to the fact that the wave height in the Edinburgh University tank varies spatially, and additionally the probe would have experienced interference from radiated and reflected waves from the model.

5.3.3. Resonance

In a mass-spring-damper system, resonance occurs when the phase between the forcing function and the moving mass is 90° (Figure 5.22). The peak amplitude and the frequency that that peak amplitude occurs at both reduce as damping is increased.

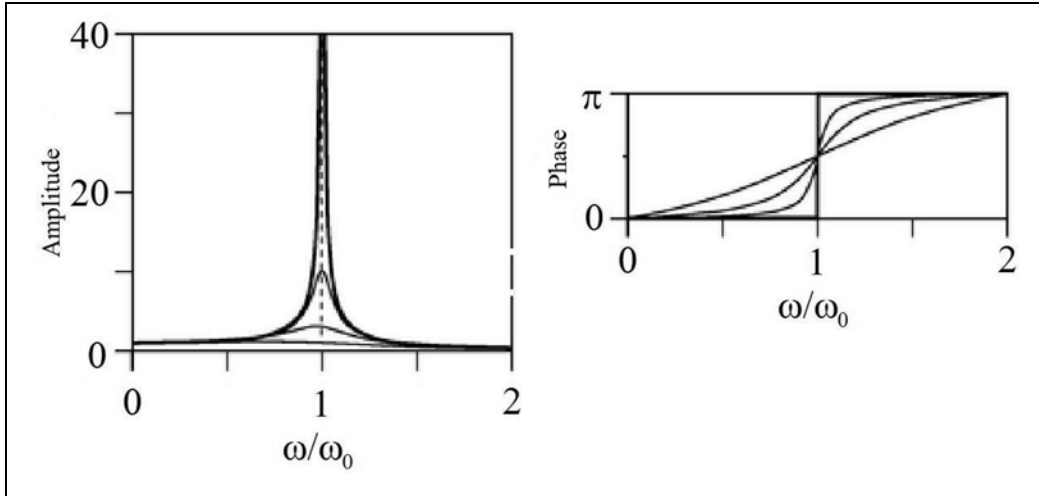


Figure 5.22 Resonance plots for phase and damping (EMEC 2009).

Figure 5.23, shows the phase difference between the external wave elevation and the pressure drop across the turbine, and the inferred the phase difference between the external wave elevation and the internal water elevation.

The plain tube is used in this example, and the phase difference between the external elevation and the pressure drop was calculated from charts like the one in Figure 5.21 for all of the periods. As an example, at 0.97s the phase difference is 14° (from Figure 5.21), and this can be seen in Figure 5.23:

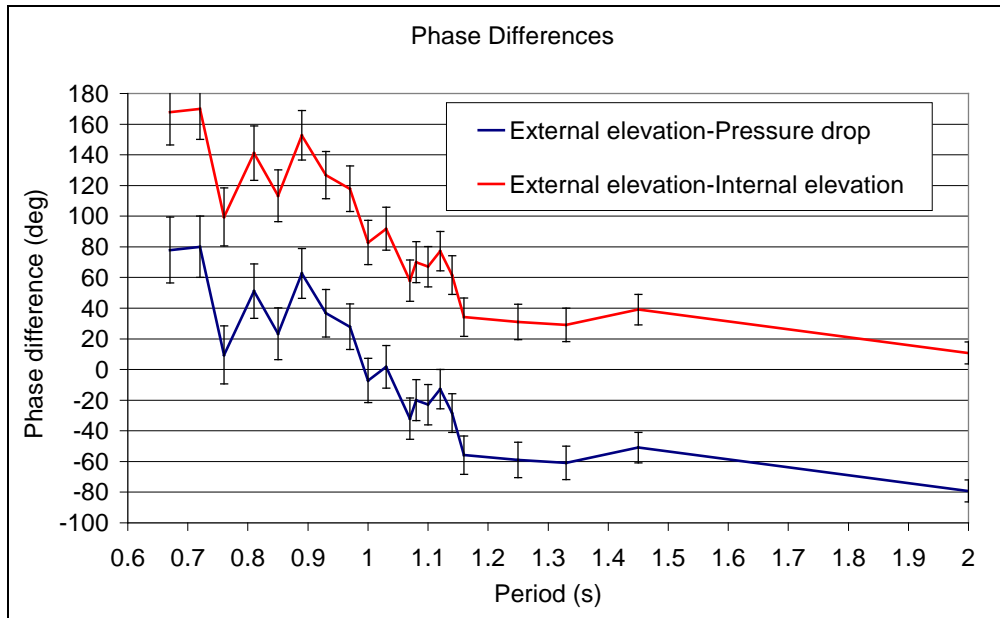


Figure 5.23 Phase difference between incident wave and power produced and inferred phase difference between internal and external water levels.

Figure 5.23 shows that there is good correlation between the phase difference measured, and that predicted for $T=0.97s$. Figure 5.22 shows that a resonant system will tend to 180° for periods lower than the resonant period, and to 0° degrees for periods much higher than the resonant period. This pattern is visible in Figure 5.23, however, at very low wave periods, there is some discrepancy.

All of the models suffered from low turbine simulator damping in this region, however under-damping does not alter the 90° phase shift, only the period of the maximum value (Figure 5.22). This reduction in phase suggests that there may be a harmonic of the main resonant period just outside the range of periods assessed. A performance feature of this nature would be interesting as it may coincide with an area of higher performance and could therefore extend the operating range of a full-size device into the lower period region. A significant amount of additional power could be gained if this were the case since WECs are often designed with cut-in criteria (similar to a wind turbine). Another area of good performance might allow this cut-in to occur in a lower sea state, or improve performance in benign conditions. It was determined to examine this further in the detailed tests that followed.

5.3.4. Impedance

In order to identify the peak performance, a series of impedances were used on the plain tube with a draft of 191mm and at a period of 0.97s (Figure 5.24). In this case, the performance at 0.97s was close to the maximum performance indicated by the variable impedance line, but this maximum was also near to the top end of the impedance range. For this reason it was considered important to extend the range of the simulator as far as possible for the second set of tests in Edinburgh University's test tank.

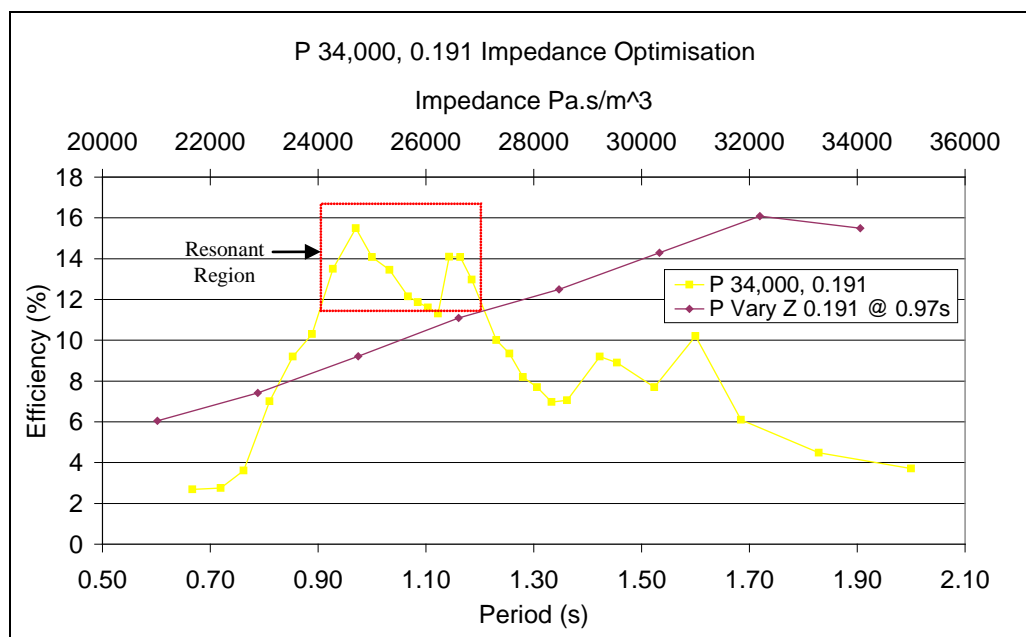


Figure 5.24 Impedance Optimisation.

Figure 5.25 illustrates the importance of finding the correct impedance. The two major peaks of the 34,000Pa.s/m³ results (using the 4-slot spinner) are around the optimum impedance, whereas the lower graphs were the best that could be achieved with the six-slot spinner.

The spinners were handmade, and the out-of-balance forces caused the aluminium bracket to vibrate and the disc to touch the inside of the duct. In turn, this slowed the

disc down, and caused excessive wear on the motor bearing. The maximum operating speed was 9,000rpm giving a maximum impedance of 34,054Pas/m³. Towards the end of the tests, the aluminium bracket was showing signs of fatigue, and the resultant weakening enhanced the vibrations of the original spinner.

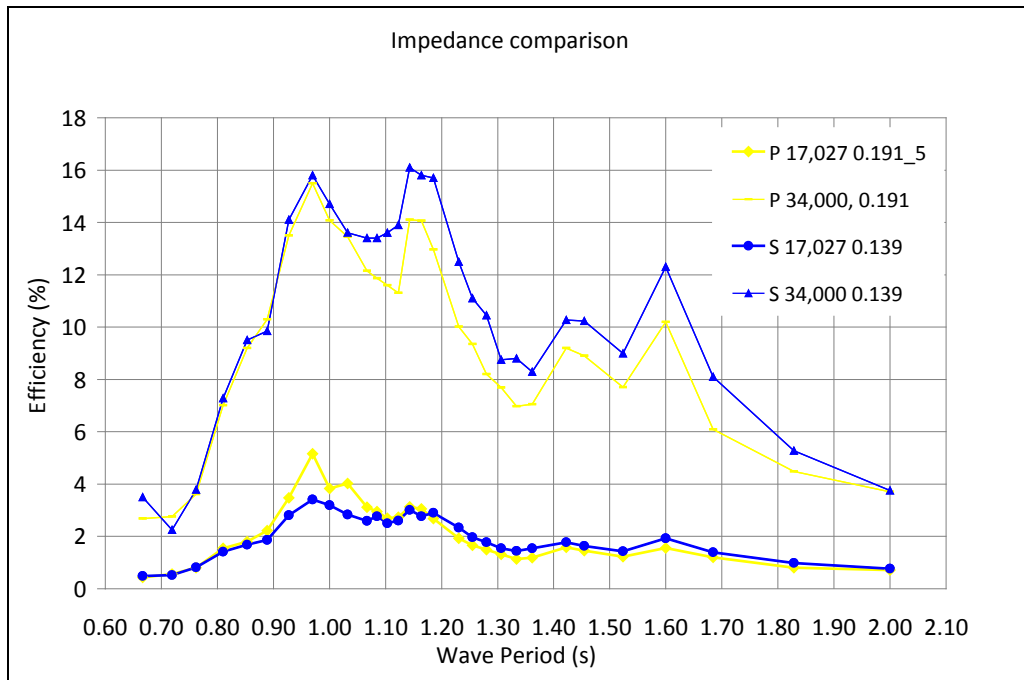


Figure 5.25 Graph demonstrating the importance of impedance optimisation.

The areas under these curves are a measure of comparative performance across the range of waves tested, so the larger the area, the better the performance. The best performance results to date are also shown in Figure 5.25. The area under the single twist graph is larger than that of the plain model by 13.2% across the spectrum. Crucially, it produced higher efficiencies than the plain tube in the resonant region (Figure 5.24) where optimum or close to optimum performance was obtained.

5.3.5. Draft vs. power available.

It is proposed that one reason that a shorter model might be more efficient is that the

OWC opening accesses more energy since it is higher in the water column. Figure 5.26 illustrates this hypothesis (Duckers et al 2008).

The response of the plain tube at two different drafts is shown as solid green and yellow lines. And the dashed yellow line represents the hypothetical device with a 0.139m draft, and a 0.191m coupling length.

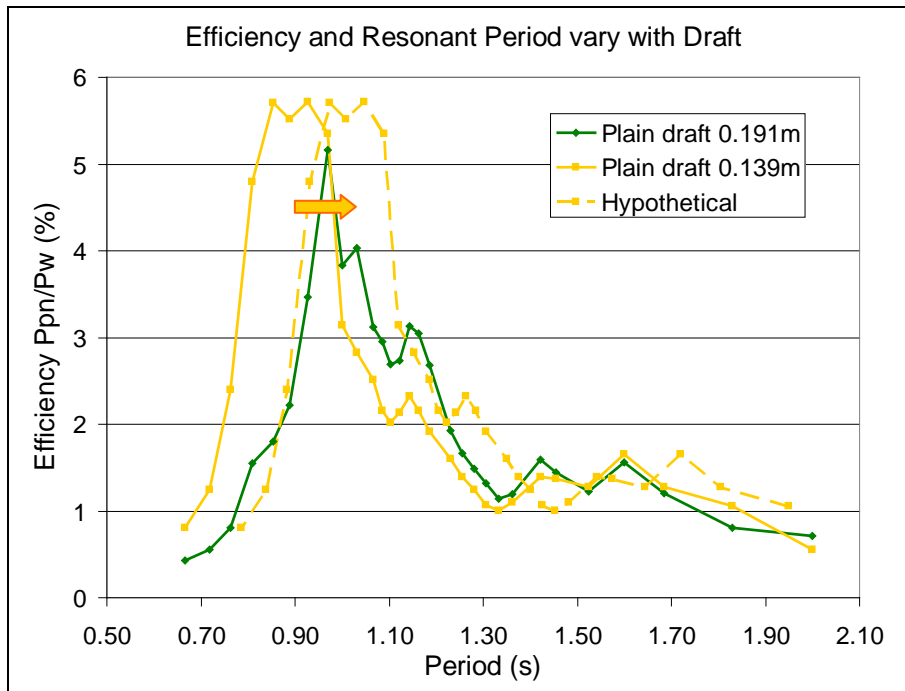


Figure 5.26 Chart showing the effect of reducing draft on power capture.

With the shallower draft of 139mm, the area under the graph is 12% larger than the area under the graph for 191mm. If the 139mm graph could be shifted so that its resonant period matched that of the 191mm model (indicated by yellow arrow), then the hypothetical dotted line would be obtained. In order to achieve this, a longer coupling length would have to be achieved, using such as the helical fins inside the column, or possibly the bent backward duct buoy configuration which has a long tube bent parallel with the water's surface so that the opening is high in the water column (Masuda et al 1999). The results in Figure 5.25, where the resonant periods are the same for all of the models, the device with shallower draft performs best with the optimum turbine setting. This indicates that the effect illustrated in Figure 5.26

may indeed be contributing to the performance of the helical devices.

5.3.6. Determining the resonant period (T_{res}) to draft relationship

Eight tests were run with the 17kPa.s/m^3 turbine simulator impedance setting to determine the characteristics of the models and are shown in Figure 5.27. These were used to determine the relationship between T_{res} and the draft for each of the models. Most of the runs resulted in graphs with more than one peak. In these cases, the first prominent peak was used to derive the relationship between T_{res} and draft. The important relationship is between a region of high performance and the draft, and choosing the first peak gives consistency when there are two peaks of similar efficiency values.

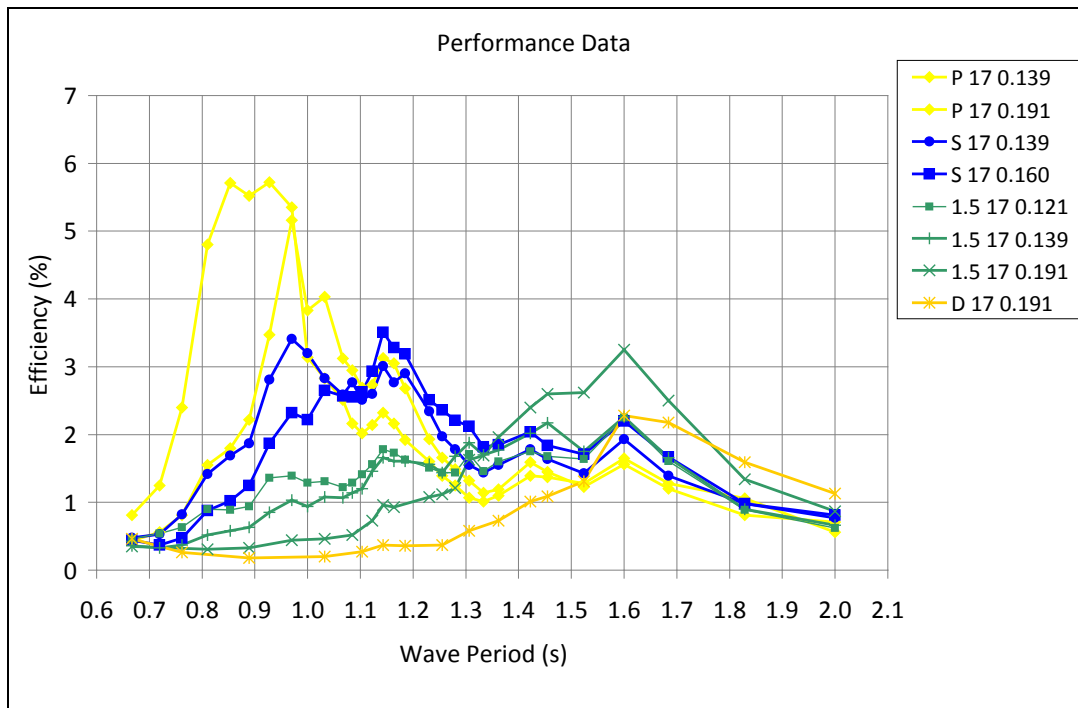


Figure 5.27 Comparative performance of model configurations.

As a result of these tests, it was decided that the double twist OWC would not be tested any further, since it was generally outperformed by all of the other configurations.

5.3.6.1. Resonant Draft

The formula for the coupling length L_c of a resonating U-Tube as a function of wave period T is given by equation 1-1:

$$L_c = \frac{gT^2}{2\pi^2} = 0.497T^2$$

Since both a U-tube and an OWC involve water flowing through pipes, it is expected that the relationship between draft and resonant period will have a similar form to this such that.

$$d = CT^x \quad (5-11)$$

This has the same form as equation 2.17, which adds weight to the hypothesis that an equation like 5-11 will describe the relationship between T_{res} and the draft.

A higher power of x implies a higher rate of change of T_{res} for a given change in draft. Therefore, the more twists in a model, the higher the index should be.

The coefficient, C , is inversely proportional to the number of twists: the more twists, the lower the draft.

Very few data points were available (Table 5-1) to plot the graphs in Figure 5.28, so their accuracy cannot be confirmed at this stage. Analysing the available information is still interesting as it indicates the likely relationship between draft and T_{res} which is the key design point for a full scale device.

	Draft d	T (res)
P	0.139	0.85
P	0.191	0.97
S	0.160	1.03
S	0.139	0.97
1.5	0.121	0.97
1.5	0.139	1.03
1.5	0.191	1.15

Table 5-1 Relationship between T_{res} and draft.

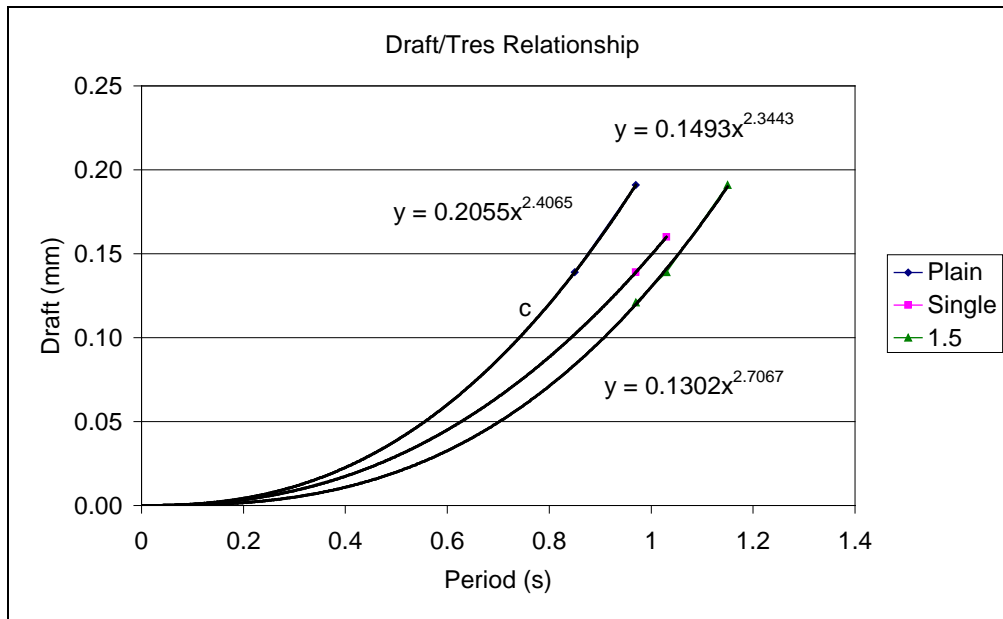


Figure 5.28 Draft vs. T_{res} relationships for the models.

The coefficients shown in Figure 5.28 are in the expected order since the plain tubes $C=0.2$ and is higher than $C=0.15$ for the single twist which is again higher than $C=0.13$ for the 1.5 twist. However, the powers are not. The value of the power of T for the single tube should be between that of the plain and 1.5 twist models. Without more data it is only possible to speculate on the cause of this apparent anomaly, but if true it would be intriguing. It suggests that the internal path of the plain tube is longer than that of the single tube. Water with a free surface flowing down through a tube forms a vortex (as seen in the experiments described in Chapter 4) and it is possible that there is an element of rotation in the flow through the plain tube. If it exists, this rotation may help to define the ideal helix angle, which might well change with period.

As discussed in Chapters 1, 2 and 3, a significant proportion of the coupling length is outside the models. Comparing the plain tube coefficient (0.2055 from Figure 5.28) with that of the U-tube ($g/2\pi^2 = 0.497$ from equation 1-1) gives:

$$\frac{0.2}{0.497} = 40\%$$

This suggests that 60% of the path shown in Figure 1.3 is outside the OWC and 40% is inside. Part of the water flow is certainly outside the device (Knott and Flower 1980), and equation 5-11 describes the part of the “U-tube” system that is enclosed by the model. This shows that the system boundaries extend significantly beyond the device itself, although the diffusion of the external flow seen by Knott and Flower (1980) means that it is probably less than 60% of the coupling length. This is consistent with point absorber theory which suggests that energy is absorbed from waves beyond those that are actually incident on the absorber (Falnes 2002).

By analysing the internal path length of the models, it was shown that the path flows up at a radius of $R/\sqrt{2}$, where R is the radius of the model tube. This is probably because the flow up the tube is affected by centripetal forces due to the rotation introduced by the helical fins. In tests, the surface profile was observed to be similar to that of a forced vortex in a vertical cylinder, which supports the idea that the water was not flowing evenly up the fins, but was distributed a little further out. This explains why the average water path was found at $R/\sqrt{2}$.

5.4. Results of the second Edinburgh tests

5.4.1. Setup

The setup was almost identical as for the first set of tests, but with the improvements listed below:

The main improvement to the system was to machine a new 4-slotted disc to the original specification. This disc was better balanced than the original one, so there were fewer vibrations at the high speeds required.

A steel bracket was fabricated, and this along with the machined disc gave a maximum rotational speed in the model of 11,000rpm, pushing the maximum impedance from 34,054Pa.s/m³ to 37,778Pa.s/m³.

In addition, the incident waves were adjusted to give a smoother input across the spectrum as discussed in section 5.1.8.

It was decided to concentrate on getting results from a sweep of the maximum wave heights, rather than to simulate a real sea-state as described in (IEA OES 2003 and EMEC 2009). Tests in realistic conditions are envisaged as the next stage tests for the concept.

In order to get an appreciation of the effect of wave height on efficiency, a sweep of wave heights at two periods was carried out and are shown in Figure 5.37. Time constraints precluded more being carried out.

Curved entries were designed so that the bottom lip of the models would be close to the Keulegan-Carpenter criteria noted in section 2.4.2. Unfortunately, these were not finished in time for experiments, and this omission could be partially responsible for the low performance of the models.

5.4.2. Results

Time series data were the primary output of the tests in the Edinburgh University wave tank, and these were analysed in several ways, described below.

The pressure and waveheight time series for the plain tube at a period of 1s are shown in Figure 5.29 as an example.

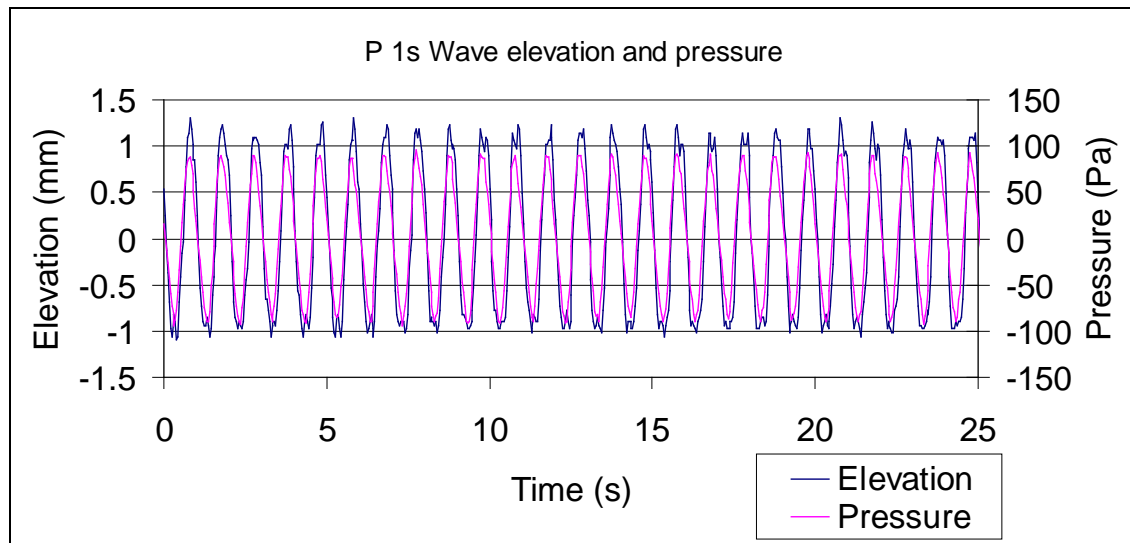


Figure 5.29 Example plot of waveheight and pressure (Plain Tube $T=1s$).

It was immediately clear that there was a problem with the wave probes during this set of tests as they should have been measuring a wave height of 92mm in the case shown. After recalibrating the probes and troubleshooting the system it was thought that the trouble lay in the solid state electronics. Due to time constraints, it was decided not to fix them, but to keep measuring the data as they would still be useful for analysing the phase difference between the external and internal water levels. The internal water level was estimated using the same technique outlined in section 5.3.3.

The pressure sensor performed satisfactorily during the tests and the performance data were derived from it as previously described.

5.4.2.1. Optimised results

The optimum performance for a model in a particular period of wave is governed by

the turbine impedance (Falnes 2002 & Sarmento 1992).

In order to obtain the optimum performance, a sweep of impedances was carried out for a selection of the 30 waves used in the tests to determine which impedance delivered the highest performance (Figure 5.30). This confirmed that impedance was important for performance, and the maximum value of efficiency achieved was taken when comparing the models performance.

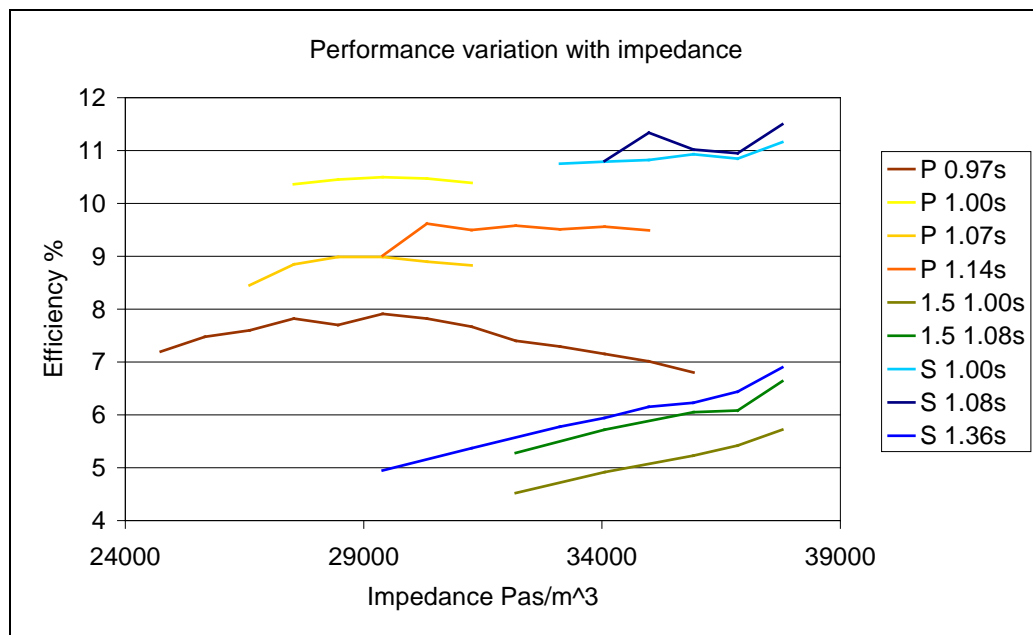


Figure 5.30 Performance variation with simulator impedance.

The peak performance was clearly identified for P 0.97s and for the other results in the resonant region shown in Figure 5.24.

Outside this region, the magnitude of the impedance required was still too great for the turbine simulator so the best performance achievable was used. For example the S 1.36s plot shown above in Figure 5.30. This was also the case for the 1.5 twist model. The single twist mode required a higher turbine impedance than the plain tube to achieve resonance, and the 1.5 twist model a higher impedance again. The improved spinner was not able to achieve the very high impedances required to achieve resonance for the 1.5 twist model. While the 1.5 twist model could not be

ruled out as a viable resonant device it did not appear likely that it would be able to match the performance of the single twist model.

To reduce the time required to carry out the tests, an iterative process was used to find the peak performance. This involved carrying out a large impedance sweep at the beginning of testing for each new setup. Once the optimum impedance was identified, then the search for a local maximum close to that value was conducted for adjacent periods.

The results of the second set of tests at Edinburgh's tank show that the single twist model outperforms the plain model when comparing the areas under the graphs in Figure 5.31. Integrating under the plain and single twist graphs shows that there is 24% more energy transferred across the range of periods by the single twist model. To reiterate, the single twist model required a higher impedance across the range of wave periods to achieve the highest possible performance, so where the models are performing below this optimum performance, the single twist model could always be improved more than the plain tube. This means that the 24% increase in power capture could be improved upon.

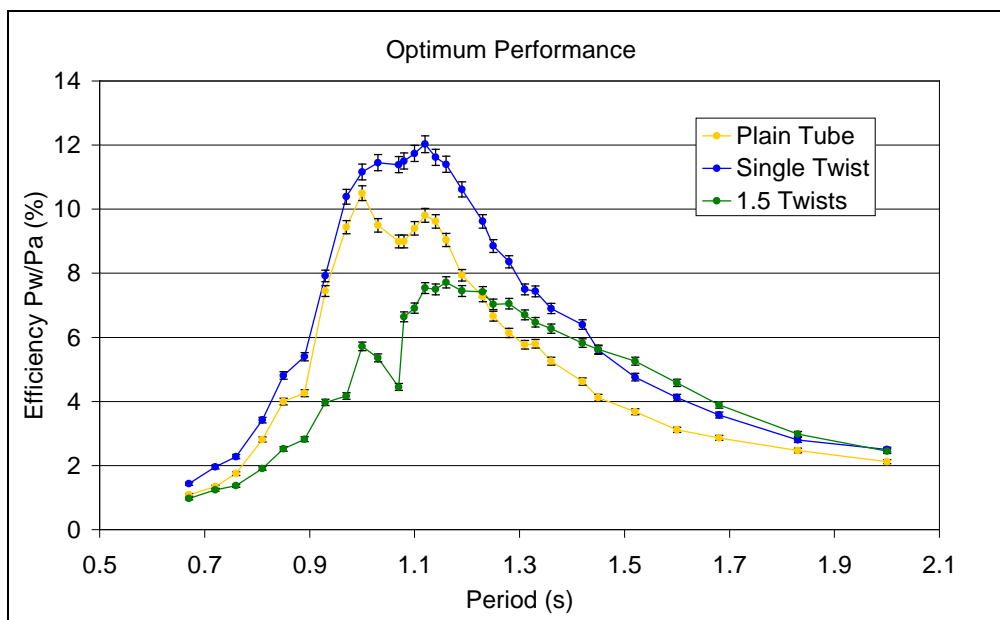


Figure 5.31 Comparative performance between models.

Error bars were calculated as described in section 5.1.8.2 and in this case they range from 2% error to 4% error. The improvement in comparative performance from 13.2% (Figure 5.25) in the first set of tests to 24% in this second set of tests is due to the fact that larger impedances were used, but the impedance error remained the same.

It is interesting to note that the results are lower here than for the earlier set of tests shown in Figure 5.25. The wave height was calibrated more accurately on the second visit to Edinburgh, and this calibration was performed at the actual location in the tank that the models were mounted (instead of some way in front as in the earlier tests). Since almost everything else was identical, this is the most likely explanation of the discrepancy.

5.4.2.2. Maximum theoretical efficiency

The peak theoretical power absorption of a point absorber in heave is 50% of the energy in $\lambda/2\pi$ of wave front (Falnes 2002):

$$P_{(\max)} = 0.5 \frac{\lambda}{2\pi} P_i \quad (5-12)$$

It is usual to calculate the efficiency of a WEC in terms of the width of the device, but it can be seen from equation 5-12 that this will underestimate the incident power considerably, and it is therefore possible to generate figures over 100% which is clearly impossible. The concept of the capture width was invented to solve this conundrum, and the capture width ratio (CWR) is a measure of the efficiency of the device compared to the power incident on its width (equation 3.7). The maximum possible CWR was calculated using:

$$CWR_{\max} = \frac{P_{(\max)}}{D \cdot P_i} \quad (5-13)$$

Figure 10 is a line graph titled "Performance Comparison" showing the Capture Width Ratio (%) on the y-axis (ranging from 0 to 400 in increments of 50) versus the Period (s) on the x-axis (ranging from 0.60 to 2.00 in increments of 0.20). The graph compares three models:

- Theoretical CWR limit:** Represented by a magenta line with square markers. It shows a linear increase from approximately 40% at 0.60s to approximately 355% at 2.00s.
- Single twist model:** Represented by a blue line with circle markers. It shows a slight increase from approximately 2% at 0.60s to approximately 12% at 1.00s, then drops to approximately 1% for periods greater than 1.00s.
- Plain model:** Represented by a dark blue line with circle markers. It remains consistently near 0% across the entire period range.

The legend indicates that the magenta line with squares represents the "Theoretical CWR limit", the blue line with circles represents the "Single twist model", and the dark blue line with circles represents the "Plain model".

For example, the theoretical CWR limit at $T=1s$ is 89%, whereas the models only have an efficiency of about 11%. This suggests that there were significant losses in the system and these were most likely caused by the losses due to the sharp edges at the bottom of the duct – See the discussion of Knott and Flower’s work and the Keulegan-Carpenter number in section 2.4.2.

$$P_{(\max)} = 0.5 \frac{\lambda}{\pi} P_i$$

$$P_{(\max)} = 0.5 \frac{3\lambda}{2\pi} P_i$$

These are plotted in Figure 5.33:

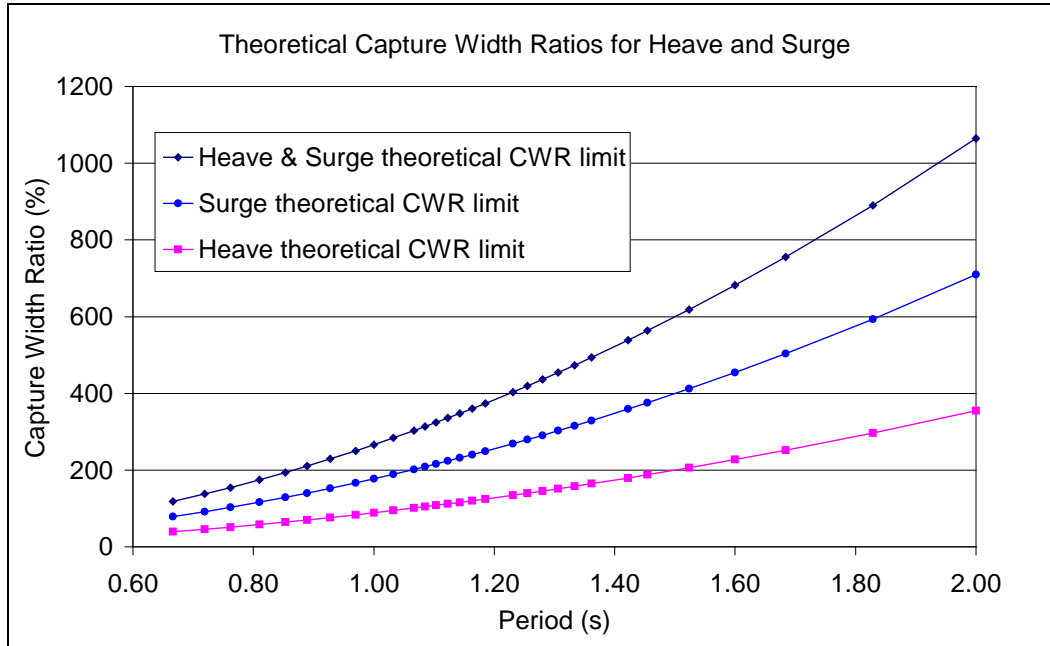


Figure 5.33 Theoretical Capture Width Ratio (CWR) limit for ideal point absorbers operating in different degrees of freedom.

It may be possible to take advantage of the higher efficiencies available to a heaving and surging machine by altering the design. This again raises the interesting question of using side entries instead of an open bottom or a baffle behind the OWC to utilise some of the surge motion in the waves and improve efficiency towards these limits.

5.4.2.3. Impedance relationship to pressure and flowrate

The optimum impedance decreases in the resonant region as shown in Figure 5.34 and this corresponds with the higher flowrates associated with the greater displacements in the resonant region. This suggests that very high impedances might be required for optimum performance when the flowrates are low for $0.8s > T > 1.2s$. This is likely to be a constraint on the turbine if it is to be tuned within

an individual wave cycle since the flowrate is $0\text{m}^3/\text{s}$ twice per cycle, implying very high impedances could be required regularly.

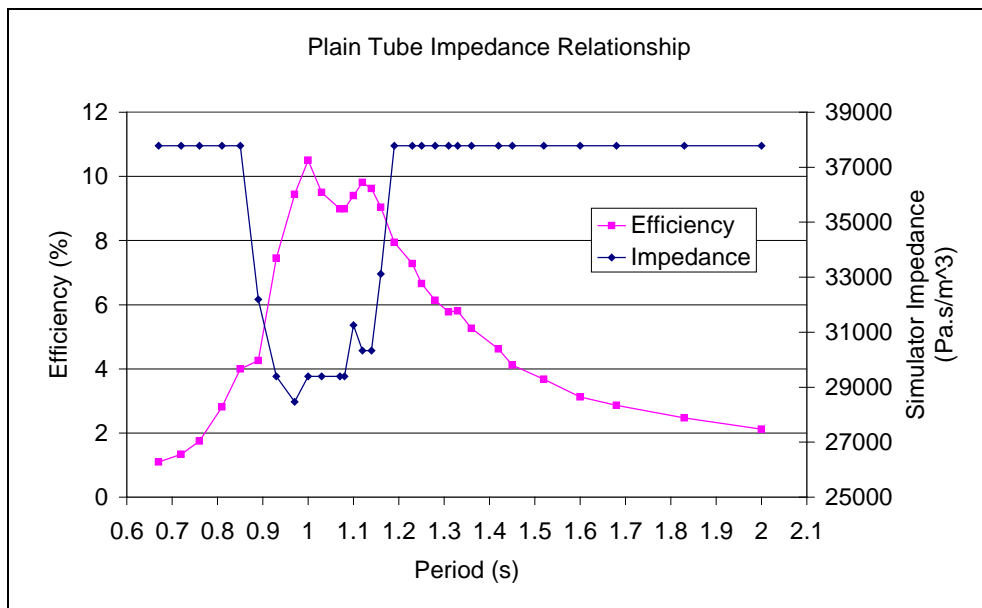


Figure 5.34 Relationship between impedance and efficiency.

5.4.2.4. Wave height sweep

In order to determine whether the wave height would affect the performance of the model, two sweeps were carried out at constant periods, 0.97s and 1.14s (see Figure 5.35). This shows that the efficiency does not vary significantly with wave height, although there is a slight downward trend with increasing wave height. This may be because these higher waves are steeper and more non-linear than the lower waves, and this non-linear input delivers a lower response. This is a subject that should be investigated further in the next stage of development.

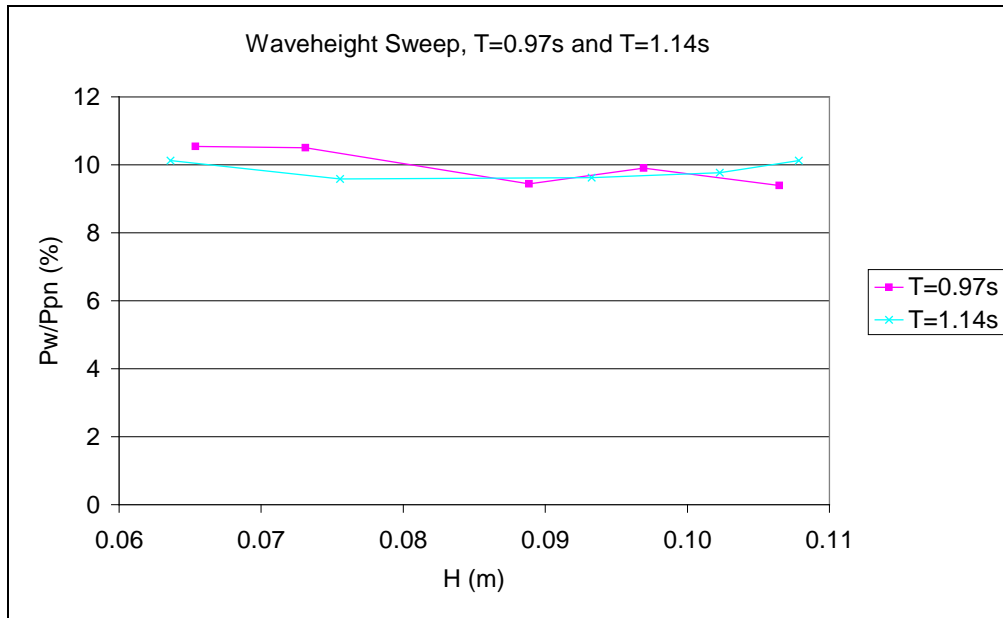


Figure 5.35 Sweep of performance with change in wave height.

This result suggests that the efficiencies can be expected to remain similar for all wave heights, and will only vary with period. It is assumed that this is the case for the helical models too.

Figure 5.36 shows the phase analysis of the internal to external water elevation.

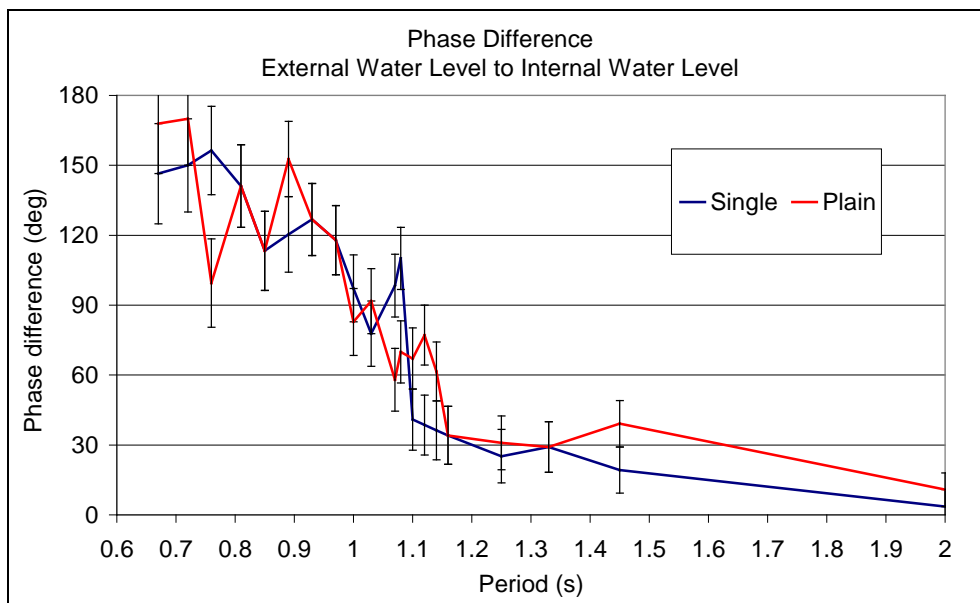


Figure 5.36 Hydraulic phase difference as a function of wave period.

The phase difference between the external and internal water levels as a function of wave period was examined using the same method described in section 5.3.3 above. The results come from the faulty probes referred to in Figure 5.29, however the error was with the height recorded, not with the phase of the measured wave. The results are shown in Figure 5.36 with error bars added in this case. The error bars represent the fact that the estimated error in reading the time that a maximum or minimum in the time series (Figure 5.29) occurred at was about ± 0.08 s. This systematic error has a larger effect for lower periods as it is proportionally larger compared to the wave period.

This analysis shows that the system does perform like a theoretical mass-spring-damper system: Tending towards 180° at low periods, 90° at resonance (about $T=1$ s) and tending to 0° for high periods. Thus a mass-spring-damper analysis would be a suitable method to use for modelling the system and this will be the focus of the following chapter.

5.4.2.5. Scaling of results

As discussed previously, Froude number scaling was used to design the model and test conditions. As an example of how the performance might scale up, a scale factor of 85 has been used to give a diameter of 12m at full scale and to place the optimum performance at the best sea state.

The results were overlaid onto a Bretschneider spectrum (EMEC 2009 and section 2.2.2) as shown in Figure 5.37, representative of a typical wave climate off the west coast of the UK, to show the performance that can be expected at full scale. The red line shows the 1:10 steepness contour, which is upper bound for steepness in a real sea. The Bretschneider spectrum represents a realistic sea with a range of waves, steep and shallow, large and small. Data that follow this pattern have been used to estimate the power output of the plain and single helixes below.

The green 1:20 contour represents fully developed wind-seas and is described by the Pierson-Moskowitz spectrum.

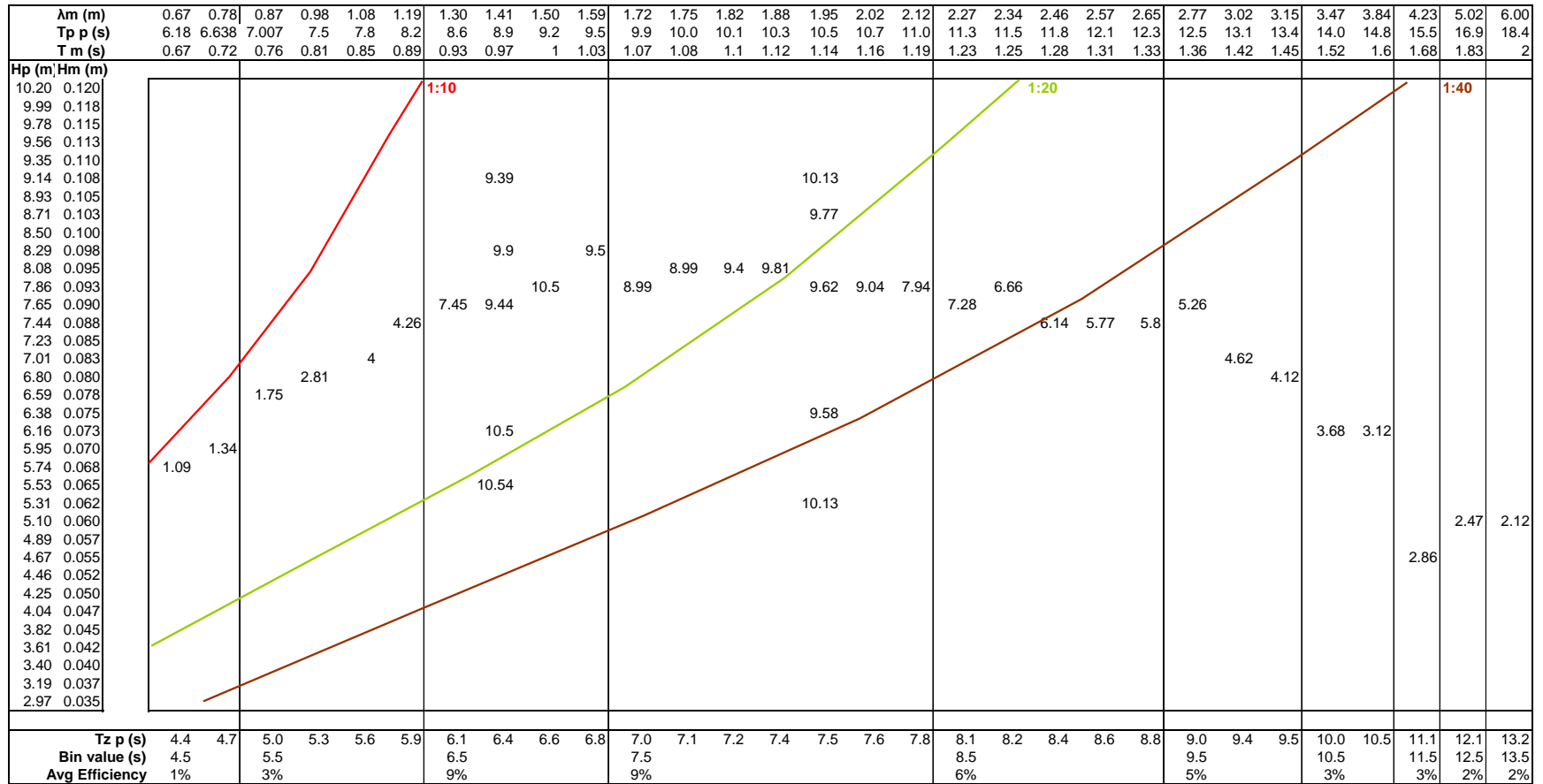


Figure 5.37 Performance of the plain tube with Bretschneider limits indicated (EMEC 2009).

The efficiency figures were mapped using T_m , which is the monochromatic test period, and H_m which is the height of the test wave. The two sweeps of waveheight can be seen at $T_m=0.97s$ and $T_m=1.14s$

The vertical lines separate the bins in Figure 5.39 that the efficiencies fall into and. the average efficiency for these bins is shown in the bottom line.

This shows that the results are largely within the usable Bretschneider range. There is likely to be a practical limit to the wave height that a machine of this type would operate in. The largest H_s in Figure 5.37 is 10.2m, which represents a severe storm, and it is very likely that an OWC would be shut down in these conditions to protect it and especially the turbine from damage. These results can therefore be used to predict the performance of a full scale device.

Figure 5.38 shows the single twist performance data overlaid onto the same outline of a Bretschneider spectrum.

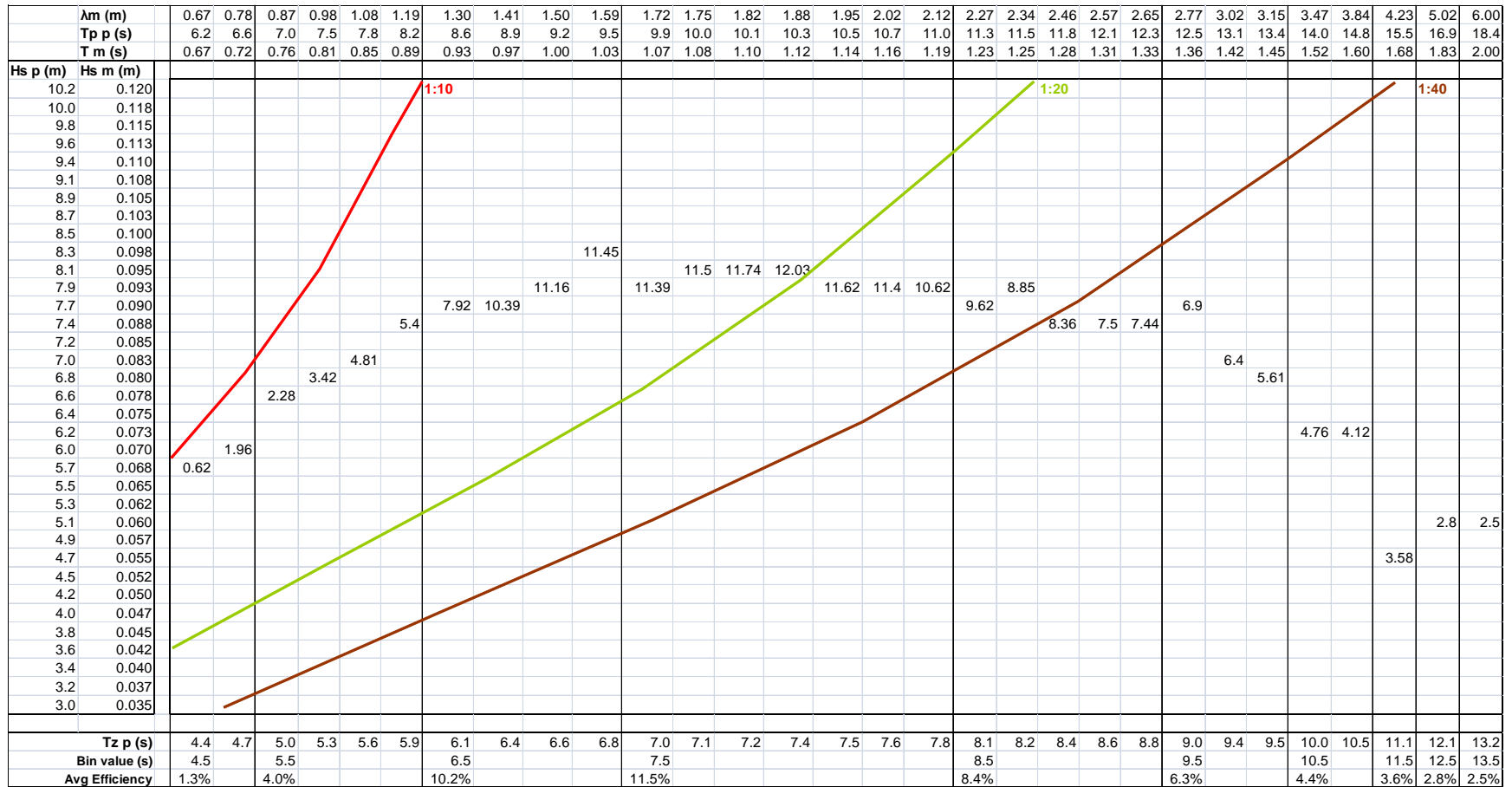


Figure 5.38 Performance of the single twist model with Bretschneider limits indicated (EMEC 2009).

It must be noted that the experimental results are monochromatic, and the sea state would be polychromatic. This means that some assumptions were necessary in order that the data could be used:

1. The monochromatic period can be scaled to the Peak period (T_p). The author's experience of comparing monochromatic results and polychromatic results elsewhere suggests that this is the best match.
2. It must also be assumed that the efficiency is the same in monochromatic and polychromatic conditions; in fact devices of this type (OWCs) often perform better in polychromatic conditions. This is because they tend to be designed to extract energy at a certain period, and a component of any given wave spectrum is likely to be at this period (EMEC 2007).
3. Finally, the assumption is made that the efficiency does not change with wave height as discussed in 5.4.2.4.

The wave climate at the Wave Hub site off the south-west coast of the UK was chosen (SWRDA 2006) as this is a typical mid-range wave climate and would be a suitable site for deployment of a prototype device or farm.

		3	4	5	6	7	8	9	10	11	12	13	
	Tz range	4	5	6	7	8	9	10	11	12	13	14	
	Tz Bin	3.5	4.5	5.5	6.5	7.5	8.5	9.5	10.5	11.5	12.5	13.5	Total
Hs range	Hs bin												
12.5 13	12.75											1	1
12 12.5	12.25												0
11.5 12	11.75										4		4
11 11.5	11.25									2	1		3
10.5 11	10.75									2	3		5
10 10.5	10.25								1	9			10
9.5 10	9.75									13			13
9 9.5	9.25							1	2	11			14
8.5 9	8.75							1	18	7			26
8 8.5	8.25							4	50	2			56
7.5 8	7.75					1		44	60	1			106
7 7.5	7.25						6	102	29	4			141
6.5 7	6.75						36	205	12	2			255
6 6.5	6.25					2	126	213	5				346
5.5 6	5.75					16	432	93	8				549
5 5.5	5.25					100	669	31	6	1			807
4.5 5	4.75				7	549	604	19	6	3			1188
4 4.5	4.25				62	1307	161	36	11				1577
3.5 4	3.75				527	1401	99	33	11	2			2073
3 3.5	3.25			36	2067	647	107	48	11	4			2920
2.5 3	2.75			669	3061	375	124	33	7	6	3		4278
2 2.5	2.25		45	3748	1466	338	142	54	21	6	1		5821
1.5 2	1.75	20	1528	4929	937	306	140	54	18	8	3	1	7944
1 1.5	1.25	242	6035	2615	1028	396	122	80	31	15	6	2	10572
0.5 1	0.75	1623	4403	1695	734	299	107	27	22	4	3		8917
0 0.5	0.25	429	464	210	106	41	26	13	4				1293
Total		2314	12475	13902	9995	5778	2901	1091	333	102	24	4	48919

Figure 5.39 Joint probability wave height – wave period scattergram for the Wave Hub site (SWRDA 2006) showing the number of occurrences of each wave.

T_z is the mean zero upcrossing period. Multiplying the power (equation 2-7) available in each of the bins in Figure 5.39 by the probability (occurrence/total number of samples) that it will occur gives a weighted energy scattergram for the site as shown in Figure 5.40: The units are W/year indicating that Wave hub has an average of power 23kW/m over one year.

		T range	3.0	4.0	5.0	6.0	7.0	8.0	9.0	10.0	11.0	12.0	13.0	Total
		Tz	4.0	5.0	6.0	7.0	8.0	9.0	10.0	11.0	12.0	13.0	14.0	
H range	Hs		3.5	4.5	5.5	6.5	7.5	8.5	9.5	10.5	11.5	12.5	13.5	
12.5	13.0	12.8											22	22.0
12.0	12.5	12.3												0.0
11.5	12.0	11.8										69		69.1
11.0	11.5	11.3									29	16		45.0
10.5	11.0	10.8									27	43		70.0
10.0	10.5	10.3								11	109			120.0
9.5	10.0	9.8									142			142.4
9.0	9.5	9.3							8	18	108			134.6
8.5	9.0	8.8							7	145	62			214.0
8.0	8.5	8.3							26	358	16			399.5
7.5	8.0	7.8					5		251	379	7			641.9
7.0	7.5	7.3						27	510	160	24			721.6
6.5	7.0	6.8						140	889	58	10			1096.5
6.0	6.5	6.3					6	419	792	21				1237.2
5.5	6.0	5.8					40	1216	293	28				1576.2
5.0	5.5	5.3					207	1570	81	17	3			1878.9
4.5	5.0	4.8				10	931	1160	41	14	8			2163.9
4.0	4.5	4.3				73	1774	248	62	21				2176.8
3.5	4.0	3.8				483	1480	119	44	16	3			2144.8
3.0	3.5	3.3			21	1421	513	96	48	12	5			2117.4
2.5	3.0	2.8			279	1507	213	80	24	6	5	3		2116.2
2.0	2.5	2.3		10	1045	483	129	61	26	11	3	1		1769.9
1.5	2.0	1.8	2	211	832	187	70	37	16	6	3	1	0	1364.3
1.0	1.5	1.3	13	425	225	105	46	16	12	5	3	1	0	852.0
0.5	1.0	0.8	32	112	53	27	13	5	1	1	0	0		244.0
0.0	0.5	0.3	1	1	1	0	0	0	0	0				3.8
			51	762	2460	4302	5433	5202	3141	1298	580	147	36	23,322

Figure 5.40 Weighted energy scattergram for wave hub.

This scattergram shows that the bin ($H_s=4.25\text{m}$, $T_z=7.5\text{s}$) has the most power during the year, and it is likely that this will be used as the design wave in order to maximise the energy conversion.

Full scale efficiency

The model efficiencies will have to be modified to take account of scaling effects and power conversion efficiencies.

Weber (2007) has shown that compressibility of air reduces power performance by about 10.6%, on average, if Froude number scaling is used.

It has been assumed that a Wells turbine would have an efficiency of 60% on average (Tease 2005), and that an electrical generator would be 95% efficient.

These efficiencies were applied to the average bin efficiencies of the single twist model shown in Figure 5.38. to produce the efficiencies in Figure 5.41. As discussed in section 5.4.2.4, the assumption has been made that the efficiency does not change significantly with waveheight, so the efficiencies have been copied so that each period has the same efficiency regardless of height. This is the efficiency map for the single twist prototype:

T range			3.0	4.0	5.0	6.0	7.0	8.0	9.0	10.0	11.0	12.0	13.0
T z			4.0	5.0	6.0	7.0	8.0	9.0	10.0	11.0	12.0	13.0	14.0
T z			3.5	4.5	5.5	6.5	7.5	8.5	9.5	10.5	11.5	12.5	13.5
H range	Hs												
12.5	13.0	12.75											1.3%
12.0	12.5	12.25											
11.5	12.0	11.75										1.4%	
11.0	11.5	11.25									1.8%	1.4%	
10.5	11.0	10.75									1.8%	1.4%	
10.0	10.5	10.25								2.3%	1.8%		
9.5	10.0	9.75									1.8%		
9.0	9.5	9.25							3.2%	2.3%	1.8%		
8.5	9.0	8.75							3.2%	2.3%	1.8%		
8.0	8.5	8.25							3.2%	2.3%	1.8%		
7.5	8.0	7.75					5.9%		3.2%	2.3%	1.8%		
7.0	7.5	7.25						4.3%	3.2%	2.3%	1.8%		
6.5	7.0	6.75						4.3%	3.2%	2.3%	1.8%		
6.0	6.5	6.25					5.9%	4.3%	3.2%	2.3%			
5.5	6.0	5.75					5.9%	4.3%	3.2%	2.3%			
5.0	5.5	5.25					5.9%	4.3%	3.2%	2.3%	1.8%		
4.5	5.0	4.75					5.2%	5.9%	4.3%	3.2%	2.3%	1.8%	
4.0	4.5	4.25					5.2%	5.9%	4.3%	3.2%	2.3%		
3.5	4.0	3.75					5.2%	5.9%	4.3%	3.2%	2.3%	1.8%	
3.0	3.5	3.25				2.0%	5.2%	5.9%	4.3%	3.2%	2.3%	1.8%	
2.5	3.0	2.75				2.0%	5.2%	5.9%	4.3%	3.2%	2.3%	1.8%	1.4%
2.0	2.5	2.25		0.7%	2.0%	5.2%	5.9%	4.3%	3.2%	2.3%	1.8%	1.4%	
1.5	2.0	1.75	0.3%	0.7%	2.0%	5.2%	5.9%	4.3%	3.2%	2.3%	1.8%	1.4%	1.3%
1.0	1.5	1.25	0.3%	0.7%	2.0%	5.2%	5.9%	4.3%	3.2%	2.3%	1.8%	1.4%	1.3%
0.5	1.0	0.75	0.3%	0.7%	2.0%	5.2%	5.9%	4.3%	3.2%	2.3%	1.8%	1.4%	
0	0.5	0.25	0.3%	0.7%	2.0%	5.2%	5.9%	4.3%	3.2%	2.3%			

Figure 5.41 Single twist performance map adjusted for system efficiencies.

A similar performance map was produced for the plain tube model and these maps were applied to the energy in each of the bins in Figure 5.40 to give the full scale power maps in Figure 5.42 and Figure 5.43.

T range			3.0	4.0	5.0	6.0	7.0	8.0	9.0	10.0	11.0	12.0	13.0	Total
Tz			4.0	5.0	6.0	7.0	8.0	9.0	10.0	11.0	12.0	13.0	14.0	
Hs			3.5	4.5	5.5	6.5	7.5	8.5	9.5	10.5	11.5	12.5	13.5	
H range	Hs													
12.5	13.0	12.8										0.3		
12.0	12.5	12.3												0.0
11.5	12.0	11.8										1.0		1.0
11.0	11.5	11.3									0.5	0.2		0.8
10.5	11.0	10.8									0.5	0.6		1.1
10.0	10.5	10.3							0.3		2.0			2.3
9.5	10.0	9.8									2.6			2.6
9.0	9.5	9.3						0.3	0.4		2.0			2.7
8.5	9.0	8.8						0.2	3.3		1.1			4.7
8.0	8.5	8.3						0.8	8.2		0.3			9.3
7.5	8.0	7.8				0.3		8.1	8.6		0.1			17.2
7.0	7.5	7.3					1.2	16.5	3.7		0.4			21.7
6.5	7.0	6.8					6.0	28.7	1.3	0.2				36.2
6.0	6.5	6.3				0.3	18.0	25.6	0.5					44.4
5.5	6.0	5.8				2.3	52.1	9.5	0.6					64.5
5.0	5.5	5.3				12.2	67.3	2.6	0.4	0.1				82.6
4.5	5.0	4.8			0.5	54.8	49.7	1.3	0.3	0.1				106.8
4.0	4.5	4.3			3.8	104.4	10.6	2.0	0.5					121.3
3.5	4.0	3.8			25.3	87.1	5.1	1.4	0.4	0.1				119.4
3.0	3.5	3.3			0.4	74.6	30.2	4.1	1.6	0.3	0.1			111.3
2.5	3.0	2.8			5.7	79.1	12.5	3.4	0.8	0.1	0.1	0.0		101.8
2.0	2.5	2.3		0.1	21.3	25.4	7.6	2.6	0.8	0.3	0.1	0.0		58.1
1.5	2.0	1.8	0.0	1.4	17.0	9.8	4.1	1.6	0.5	0.1	0.1	0.0	0.0	34.6
1.0	1.5	1.3	0.0	2.8	4.6	5.5	2.7	0.7	0.4	0.1	0.0	0.0	0.0	16.9
0.5	1.0	0.8	0.1	0.7	1.1	1.4	0.7	0.2	0.0	0.0	0.0	0.0		4.4
0.0	0.5	0.3	0.0	0.0	0.0	0.0	0.0	0.0	0.0					0.1
W/m absorbed														966

Figure 5.42 Single twist power map (full scale).

T range			3.0	4.0	5.0	6.0	7.0	8.0	9.0	10.0	11.0	12.0	13.0	Total
T z			4.0	5.0	6.0	7.0	8.0	9.0	10.0	11.0	12.0	13.0	14.0	
Hs			3.5	4.5	5.5	6.5	7.5	8.5	9.5	10.5	11.5	12.5	13.5	
H range	Hs													
12.5	13.0	12.8										0.2		
12.0	12.5	12.3												0.0
11.5	12.0	11.8										0.9		0.9
11.0	11.5	11.3									0.4	0.2		0.6
10.5	11.0	10.8									0.4	0.6		0.9
10.0	10.5	10.3							0.2	1.6				1.8
9.5	10.0	9.8									2.1			2.1
9.0	9.5	9.3						0.2	0.3	1.6				2.1
8.5	9.0	8.8						0.2	2.5	0.9				3.6
8.0	8.5	8.3						0.6	6.2	0.2				7.1
7.5	8.0	7.8				0.2		6.0	6.6	0.1				12.9
7.0	7.5	7.3					0.9	12.2	2.8	0.4				16.2
6.5	7.0	6.8					4.5	21.3	1.0	0.2				27.0
6.0	6.5	6.3				0.3	13.6	19.0	0.4					33.2
5.5	6.0	5.8				1.9	39.5	7.0	0.5					48.8
5.0	5.5	5.3				9.7	51.0	1.9	0.3	0.0				63.0
4.5	5.0	4.8			0.5	43.7	37.7	1.0	0.2	0.1				83.2
4.0	4.5	4.3			3.5	83.2	8.0	1.5	0.4					96.6
3.5	4.0	3.8			23.1	69.4	3.8	1.1	0.3	0.0				97.8
3.0	3.5	3.3			0.3	68.2	24.1	3.1	1.2	0.2	0.1			97.2
2.5	3.0	2.8			4.6	72.3	10.0	2.6	0.6	0.1	0.1	0.0		90.2
2.0	2.5	2.3		0.1	17.2	23.2	6.0	2.0	0.6	0.2	0.1	0.0		49.3
1.5	2.0	1.8	0.0	1.3	13.7	9.0	3.3	1.2	0.4	0.1	0.0	0.0	0.0	29.0
1.0	1.5	1.3	0.1	2.6	3.7	5.0	2.2	0.5	0.3	0.1	0.0	0.0	0.0	14.6
0.5	1.0	0.8	0.2	0.7	0.9	1.3	0.6	0.2	0.0	0.0	0.0	0.0		3.9
0.0	0.5	0.3	0.0	0.0	0.0	0.0	0.0	0.0	0.0					0.1
W/m absorbed														782

Figure 5.43 Plain tube power map (full scale).

This Helical OWC was conceived as a simple reliable machine, so an availability of 90% was chosen to estimate the energy produced in a year. In reality, the generator would most likely be shut down for survival when the wave height reached a critical value. However the goal is to generate in as many sea states as possible, so all of the data have been used here to calculate the maximum theoretical annual energy capture for the single twist and plain tube OWCs shown in Table 5-2.

11.9m dia.	Single	Plain
Rated power (kW)	104	83
Average output kW	11.49	9.31
kWh/year	90,615	73,401

Table 5-2 Comparative output of single twist and plain tube OWC prototypes.

The rated power is taken from the $H_s=4.25\text{m}$ $T_e=7.5\text{s}$ bin in Figure 5.42 and Figure 5.43.

Table 5-2 shows once again that the single twist design will produce 23.4% more energy than the plain tube version.

5.5. Conclusions

1. It has been shown that the energy available to OWC's rises significantly with reducing draft. When this phenomenon is combined with the helical design, then the resonant period can be matched with a deeper plain tube model. This gives the combined benefits of 24% more efficiency with 26% less draft.
2. The spinner is suitable for scale testing of wave energy converters with an air turbine, especially where there is a requirement to determine the optimum turbine impedance. It gives a very quick and simple method for obtaining a fixed impedance. Attention must be paid to the spinner bearing, the bracket and the power of the motor to ensure that very high impedances can be achieved. With a powerful motor or some system that allows rapid and accurate acceleration and deceleration of the spinning simulator, it might also be possible to simulate adjusting the turbine impedance during a wave cycle.
3. Deficiencies in the spinner calibration may have led to significant overestimation of the impedance. This in turn would have reduced the value of P_{air} meaning that the efficiencies were underestimated. The magnitude of this error is not known as the precise relationship between pressure drop and flow rate couldn't be established for the spinners.
4. The important design characteristic of the T_{res} – draft relationship has been

investigated and a preliminary definition derived. This will allow the confident design of larger models for future tests.

5. Analysis of the phase difference between the external and internal water surfaces shows that the system behaves like a theoretical mass-spring-damper system. This shows that a numerical model based on this theory will give a suitable mathematical representation of the physical system.
6. Scaling the results to a 12m device fixed in deep water gives an OWC rated at 104kW producing 90,615kWh/year. This is not very much, but it is hoped that the performance can be significantly improved if the optimum impedance can be achieved over a range of periods, and suitably rounded entries to the lower end of the duct employed. The theoretical maximum power absorbed is about 9 times higher than 104kW at resonance (Figure 5.32), so there is room for improvement.

Chapter 6: Mathematical Modelling of a model OWC

6. Introduction

The purpose of the analysis presented in this chapter was to mathematically replicate the performance of the OWC models described in the preceding chapters, and then use the mathematical model to predict full scale performance.

In addition, an analysis of the radiation damping was carried out in order to try to predict the turbine damping for future models.

The mathematical model used in this chapter is based on Watabe's model for the Mighty Whale (Watabe 2007) and modified using Brendmo et al's (1996) linear OWC model.

6.1. Mathematical model

6.1.1. Overview:

The water is induced to move by a sinusoidal wave input, with values set to represent the wave height, H , and period, T , and this in turn causes air to flow through a linear damper across which the air power is measured. Efficiencies are then calculated in the same way as in Chapters 3 and 5, and compared to the results from the second set of tests at Edinburgh described in section 5.4.

Watabe splits the model into two sections

- “ G_1 ”, motion of the water (described below in section 6.1.2) and
- “ G_2 ”, the motion of the air plus the turbine interaction (described below in section 6.1.3)

Both G_1 and G_2 are complex and their solutions are polar values where:

$|G1|$ is the reciprocal of the oscillating wave force (1/N)

$\angle G1$ is the phase angle between the internal and external water elevations.

$|G2|$ is the peak air flowrate (m^3/s)

$\angle G2$ is the phase angle between the internal water level and the air flow at the turbine.

The use of these four parameters is given in section 6.2 below.

6.1.2. Evaluating “ G_1 ”, the wave interaction with OWC

The movement of the water is based on the formula for a forced oscillator as described in section 2.4.6.2. Equation 2-22 can be rewritten as:

$$F_0 \cos \omega t = m\ddot{x} + b\dot{x} + Kx \quad (6-1)$$

Where ω is the frequency of the incident wave in rad/s, t is time, \ddot{x} is the acceleration of the water within the OWC, \dot{x} is the velocity of the water inside the OWC, and x is the displacement of the water inside the OWC. F_0 , m , b and K are described below.

Using a sinusoidal input to the mathematical model is an approximation to physical waves but should give a good correlation with the regular waves used to test the models in Chapter 5. These sinusoidal inputs will deviate from the actual waves in the tank, many of which were non-linear. In the case of the physical models, all of the waves in the resonant region are close to linear as discussed in section 5.1.8.1. Sinusoidal inputs have been used successfully elsewhere to simulate waves (e.g. Falcao and Justino 1999 and Korde 1997 as well as Brendmo et al 1996).

The initial displacing force F_0 is due to the vertical displacement of water in the wave, and the force is generated by gravity acting on the water displaced to restore it to its original mean water level position (Brendmo et al 1996):

$$F_0 = m_d g \quad (6-2)$$

Where g is the acceleration due to gravity, and m_d is the mass of water above the mean water level inside the model when the internal water surface has the same amplitude of excursion as the wave:

$$m_d = S_a \rho \frac{H}{2} \quad (6-3)$$

Where S_a is the horizontal cross sectional area of the interior of the model, ρ is the density of water and H is the wave height.

The next variable from equation 6-1 is m which is the mass of moving water. In this case it is the sum of the mass of the water inside the OWC, m_w , and the added mass, m_a :

$$m = m_w + m_a \quad (6-4)$$

Where

$$m_w = \rho \cdot S_a \cdot (d + x) \quad (6-5)$$

Where d is the at-rest draft of the OWC and x is the excursion of the internal water surface. x is measured from the mean water level and up is positive.

The added mass is given by:

$$m_a = \frac{\text{Im}\{Z_w\}}{\omega} \quad (6-6)$$

Where Z_w is the model damping (Brendmo et al 1996):

$$Z_w = Z_r + R_f \quad (6-7)$$

Where Z_r is the radiation damping and R_f is the viscous resistance. Z_r must be measured, and is discussed in section 6.1.2.2 below.

Returning again to equation 6-1 (Brendmo et al 1996) b is defined as:

$$b = Z_w = Z_r + R_f = 2\sqrt{mK_w}\xi \quad (6-8)$$

Where K_w is the spring constant for water and arises from the fact that the water has been displaced vertically from its at-rest position and that gravity therefore acts on it to return it to its at-rest state. ξ is the damping coefficient and was set to 0.2 following both Watabe (2007) and Brendmo et al (1996).

The last undefined variable in equation 6-1 is:

$$K = K_w + K_a \quad (6-9)$$

Where K_a is the spring constant of air (Watabe 2007):

$$K_a = \frac{S_a \Delta p}{x} \quad (6-10)$$

Where K_a is the spring rate of Air, S_a is the horizontal surface area of the inside of the chamber, Δp is the change in pressure in the chamber and x is the change in internal water level. Although air is incompressible at model scale (section 5.3.2), it is not at full scale, and so it is included in the mathematical model.

Empirical data used to calculate G_1

Some empirical data was required to calibrate the model and ensure that G_1 was calculated correctly. It is described here:

6.1.2.1. Empirical water excursion

It must be noted that for a linear system, x can be described using (Watabe 2007):

$$x = \frac{F_0}{\sqrt{\{(K_w + K_a) - m_a \omega^2\}^2 + Z_w \cdot \omega)^2}} \quad (6-11)$$

However some of the waves were in shallow water, and some were steep (Figure 5.17) and in addition, the mass of the water m_w varies with the displacement of the water inside the machine, x , and this is constantly changing. This means that equation 6-11 cannot be used, and the values for x were taken from the physical test results.

6.1.2.2. Empirical model damping

Equation 6-7 shows that the total model damping is:

$$Z_w = Z_r + R_f$$

Where R_f is the viscous resistance (Brendmo et al 1996):

$$R_f = \frac{\rho g S_a k}{\omega_0^2 + k^2} \quad (6-12)$$

Where ω_0 is the natural frequency and k is the decay constant describing how the oscillations of the unforced system (in this case the water oscillating vertically in the model) die down over time after being given an initial displacement.

Brendmo et al (1996) gives the radiation damping Z_w as

$$Z_w(\omega) = \frac{-\rho g S_a}{j\omega - x_0 / \tilde{x}} \quad (6-13)$$

Where $j\omega$ is a complex frequency and x_0 is the surface elevation at rest and the excursion of the surface for linear conditions, x is (Brendmo et al 1996):

$$x = x_0 e^{-kt} \cos \omega_0 t \quad (6-14)$$

\tilde{x} is a Fourier transform of 6-14 (Brendmo et al 1996):

$$\tilde{x} = x_0 \left[\frac{j\omega + k}{-\omega + 2jk\omega + \omega^2 + k^2} \right] \quad (6-15)$$

Equation 6-14 describes the exponentially decaying sinusoidal wave generated using a transient experiment proposed by Sarmento (1991) detailed in section 6.3.1. Using this experiment, ω_0 was determined empirically and k derived from the form of the exponential curve of x_{\max} plotted as a function of time.

6.1.3. Evaluating “ G_2 ”, modelling the air flow and turbine simulator.

The model has so far dealt with the moving water, and Watabe (2007) describes the movement of the air with this expression:

$$G_2 = \frac{\omega^2 \frac{S_a p_0}{Z_s (V_c - 2\Delta V_1)} + \left(\frac{S_a p_0}{Z_s (V_c - 2\Delta V_1)} \right)^2 \frac{\omega j}{S_a}}{\omega^2 + \left(\frac{S_a p_0}{S_a Z_s (V_c - 2\Delta V_1)} \right)^2} \quad (6-16)$$

Where Z_s is the turbine impedance (equation 3-5):

$$Z_s = \frac{\Delta p}{Q}$$

P_0 is atmospheric pressure, V_c is the volume of the air chamber and ΔV is the change in volume inside the chamber. The other variables are described above.

ΔV is calculated using the excursion, x , from the physical models (section 6.1.2.1) and the horizontal cross-sectional area S_a of the models.

6.2. Calculation of pneumatic power and efficiency

In order to derive useful results from the model, the power extracted by the system is required. The first step is to calculate the flowrate:

$$Q_{\max} = F_0 |G_1| |G_2| \quad (6-17)$$

As shown in previous chapters and by Watabe, the pneumatic power is given by:

$$P_{air} = \Delta p \cdot Q = Q^2 Z_s \quad (6-18)$$

Substituting Q_{\max} from equation 6-17 in equation 6-18, gives a figure for the peak power, whereas it is the RMS power that is used when calculating the usable power delivered by the system. The mathematical model is in the frequency domain, so no time series exist to analyse the RMS value of P_{air} . For a sinusoid, the relationship between the maximum value and the RMS value is (Croft et al 2001):

$$Maximum = \sqrt{2} \cdot RMS \quad (6-19)$$

Thus the power in the air, P_{air} , is:

$$P_{air} = \frac{Q_{max}^2 \cdot Z_s}{\sqrt{2}} \quad (6-20)$$

Using this value and the same 30 monochromatic waves as those used in chapter 5, an efficiency value was derived. This was then compared to the empirical results.

The model was written in Microsoft Excel, and an electronic copy has been deposited with this thesis at Loughborough University.

6.3. Radiation damping and turbine damping

Since $Z_w = Z_r + R_f$, (equation 6-7), and Z_w was calculated in section 6.1.2.2, the calculation of R_f allows the determination of Z_r . This is useful as $Z_r = Z_s$ for maximum power conversion (Falnes 2002).

Equation 6-12 shows that R_f is:

$$R_f = \frac{\rho g S_a k}{\omega_0^2 + k^2}$$

The decay constant, k , is not known and an experiment to determine it is described in section 6.3.1.

6.3.1. Experiment to determine R_f

Sarmiento's experiment (Sarmiento 1991) involves displacing the water inside the OWC (using low pressure air and a seal across the exhaust at the top). The seal is then removed and a note is taken of the average period of the oscillations. This gives the resonant period of the OWC, T_{res} .

This experiment was carried out for the plain tube and a resonant period of 0.97s was observed, which was identical to that observed in the tests described in Chapter 5.

The displacement was also measured, and the time at which each maximum displacement occurs was noted. These were then plotted (Figure 6.1) and exponential curves fitted to determine the oscillation decay constant k .

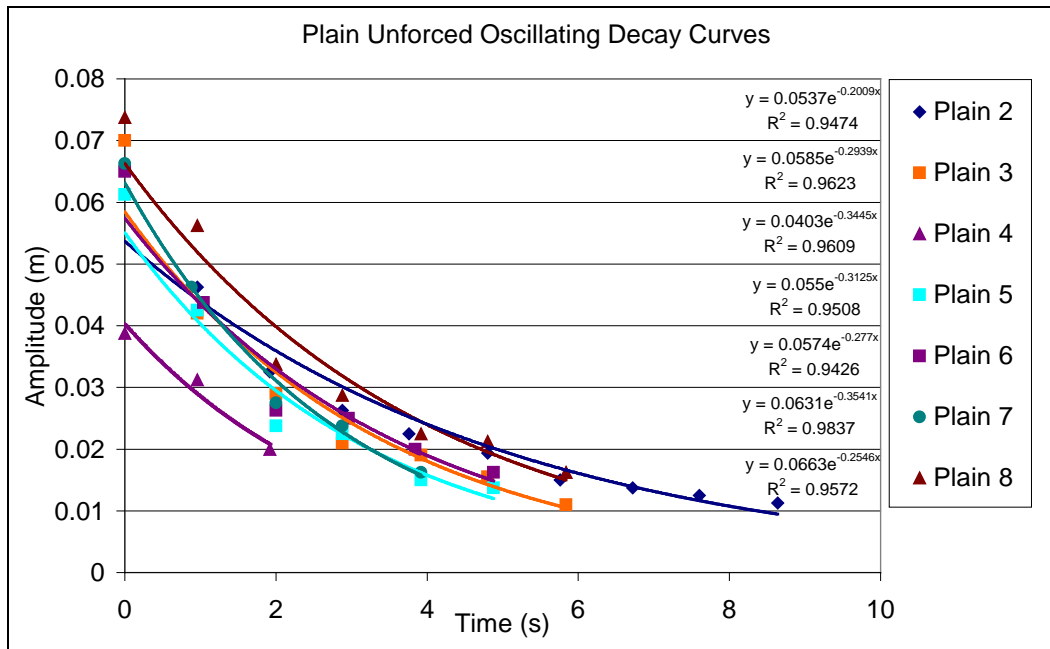


Figure 6.1: Plain Tube unforced oscillating decay including fitted curves.

The average of these k values was taken, and used to determine \bar{x} and thus $Z_w(\omega)$ was calculated (section 6.1.2.2).

This value was then used to compare the impedance of the turbine and the radiation damping.

6.4. Results and discussion

The model was written in Microsoft Excel as described above, and the graph in Figure 6.2 below was produced for the plain tube OWC model.

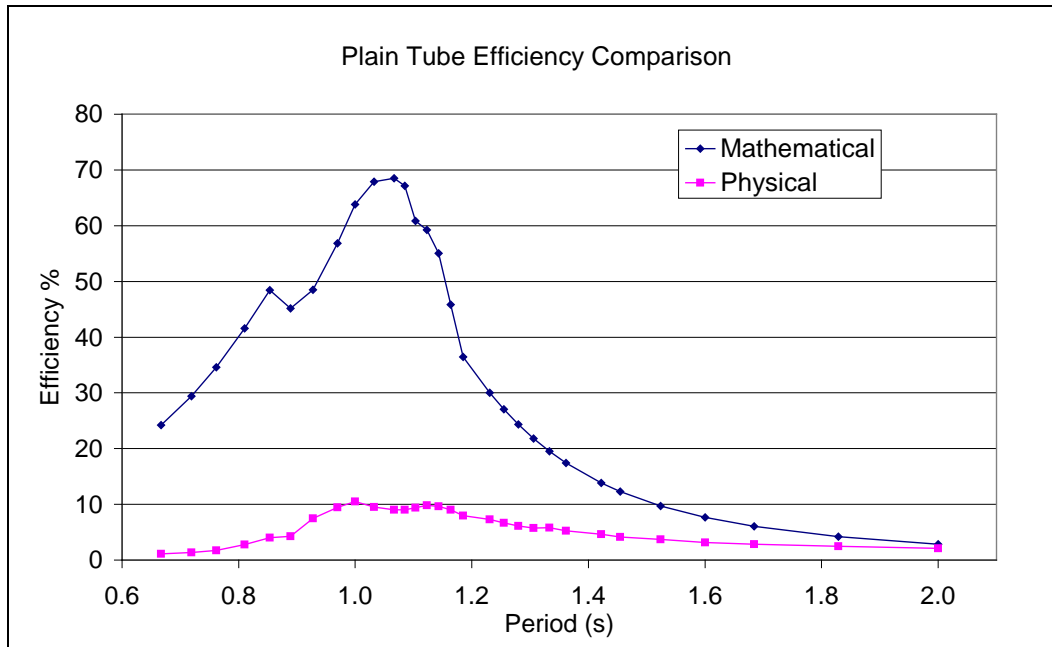


Figure 6.2: Comparison of theoretical and measured results for the plain tube model efficiency as a function of wave period.

The most striking difference between the graphs is the peak value of efficiency.

The mathematical model predicts much better performance than was actually achieved and some possible reasons for this are outlined below:

6.4.1. Adjustment of ω_0

In order for the peak performance of the numerical model to be at the same period as that of the physical models, the resonant period, ω_0 , was set to 1.2s. This is higher than the expected 0.97s (from the physical models), and is probably due to the fact that, at resonance, the excursion of the internal water surface, x , is greater than at other frequencies. This additional excursion implies more water reciprocating, and the extra mass of this water moved the model's resonant peak to a higher period (equation 3-10).

The peak efficiency occurs in the same place as the empirical results, but with only one major peak, instead of two. There are two correctly aligned peaks in Figure 6.5,

suggesting that the discrepancy in the damping of the physical and numerical models has distorted the response curves in Figure 6.2 and Figure 6.3.

The single twist OWC model was also analysed with similar results (Figure 6.3):

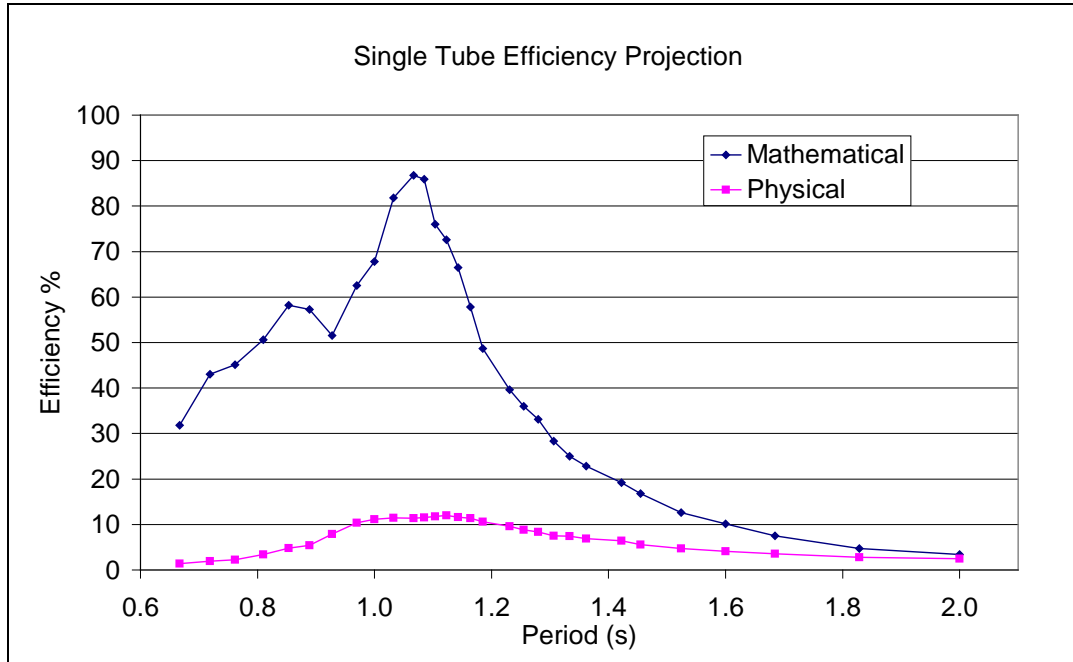


Figure 6.3: Single twist efficiency comparison.

As previously noted, the theoretical maximum power converted by an OWC of the sort tested was given by equation 5-12 (Falnes 2002):

$$P_{(\max)} = 0.5 \frac{\lambda}{2\pi} P_i$$

The power converted at resonance by the model is about 9 times less than this theoretical limit (from Figure 5.32), whereas the efficiency predicted by the mathematical model in Figure 6.4 is about 70% of this limit in the resonant region.

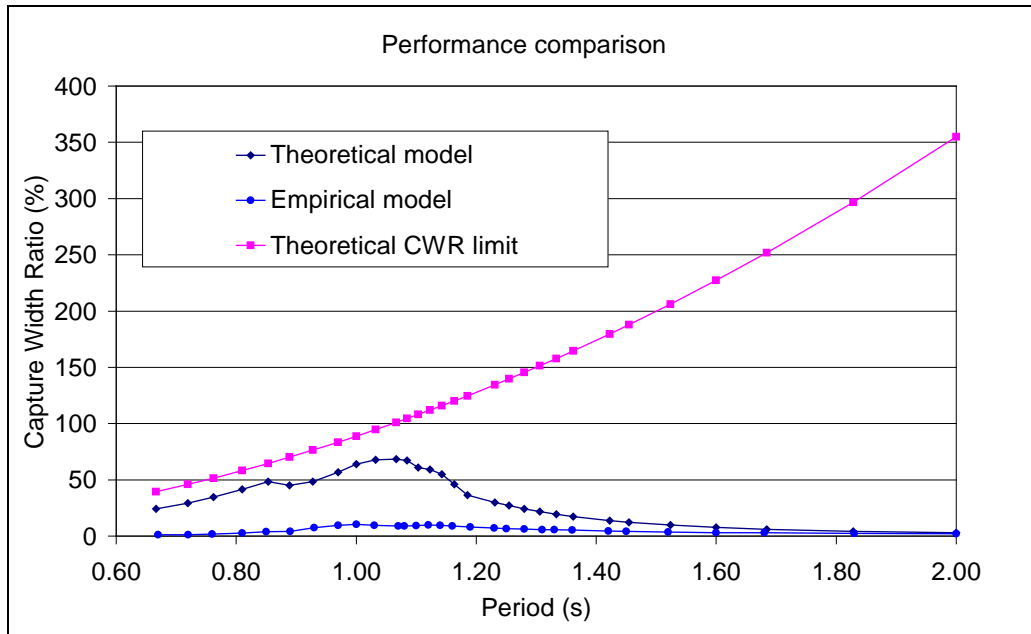


Figure 6.4 Plain tube performance (theoretical and empirical) compared to the theoretical maximum efficiency for a point absorber in heave from Figure 5.32.

This shows that both the theoretical model and physical model are within the bound set out by Falnes (2007), but that the physical model has delivered very low performance.

In any case there is clearly a large discrepancy between the mathematical and the physical results in Figure 6.3. This is probably partially attributable to the error in calculating efficiency discussed in Chapter 5, but also to losses in the physical model that were not accounted for in the mathematical representation.

6.4.2. Vortex shedding

In order to test this, the overall system damping, ξ , from equation 6-8, was increased from 0.2 to 0.55 making the two curves virtually identical. Figure 6.5 shows the empirical results for the plain tube model described in Chapter 5 and the mathematical result with $\xi=0.55$.

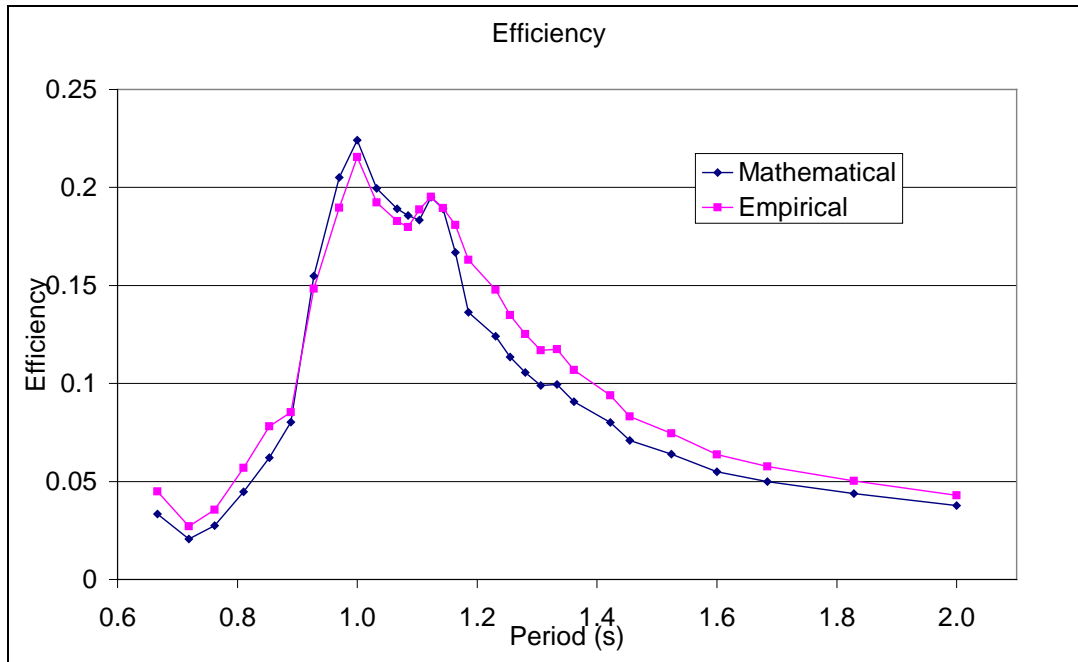


Figure 6.5: Results with high damping coefficient, $\xi=0.55$.

However this requires an excessive amount of damping in the system: both Watabe (2007) and Brendmo use $\xi=0.2$. Furthermore, other indicators, such as the phase angle between the internal and external water level, $\angle G_1$, cease to look realistic (which it does in Figure 6.6) compared to the observed behaviour of the model.

The results do in fact indicate that either the system damping has not been modelled properly in the numerical model, or that the physical models experienced a much higher level of damping than expected, for example due to vortex shedding from the bottom rim of the tube.

A potential major source of losses already identified is due to the sharp edges at the entry to the OWC (Knott and Flower 1980).

As described in Chapter 2, the Keulegan-Carpenter number (N_{KC} , equation 2-9) can be used to identify whether there is likely to be vortex shedding at the entry (Falnes 2007):

$$N_{KC} = \pi \frac{|\hat{x}|}{r_{entry}}$$

Where $|\hat{x}|$ is the excursion of the water particles and r_{entry} is the radius of the entry to the OWC.

When $N_{KC} < \pi$, laminar flow occurs, but if $N_{KC} \geq \pi$, then vortex shedding will occur with significant viscous losses.

Recalling equation 2-10 shows that

$$\frac{|\hat{x}|}{r_{entry}} < 1$$

for laminar flow.

The Keulegan Carpenter number is discussed in section 2.4.2.1 and a full explanation including the effect it has on OWCs can be found in Falnes (2007) and Knott and Flower (1980).

The radius of entry was $\frac{1}{2}$ the width of the Perspex tube = 3mm, whereas $10 < |\hat{x}| < 70$ mm across the period range. Thus there must have been significant vortex shedding at the entry and a resultant drop in efficiency, especially around peak performance with the larger values of x . This would have led to a decrease in the effective area of the entry to the models (as described by Knott and Flower (1980) and Muller and Whittaker (1995)) which would lead to an increase in the damping for the model as a smaller entry has more resistance to the flow. This would account for much of the discrepancy between the curves in Figure 6.2 and Figure 6.3.

A radius of 70mm would be too large to use on the model, or on a scaled up prototype, but something like a 35mm radius would certainly be achievable, and

could be incorporated into a buoyant jacket surrounding a large scale floating OWC. The company Embley Energy have done this with their large scale floating OWC design (Embley Energy n.d.).

There have been various other studies of this phenomenon with reference to wave energy machines, and the sloping IPS buoy incorporated a bell mouth and an angled tube to reduce the effect (Chia-Po 1999). Another solution was incorporated into the NEL OWC and the Mighty Whale (Watabe 2007): a side opening was used instead of a bottom one, allowing a more natural path for the water.

It is regrettable that the teardrop entries described in section Chapter 5 were not available for the final round of tests, as the model results may well have displayed a greater correlation with the theoretical ones.

6.4.3. Error in calculating the simulator impedance, Z_s .

In section 5.1.6.3 the error due to the incorrect calibration of the simulator impedances was estimated as a systematic factor of 2-2.5. This would bring the peak performance in Figure 6.2 to 20-25% and to 24-30% in Figure 6.3. As discussed in section 5.1.6.3, the factors of 2 and 2.5 are considered to be lower bounds, and if this is the case, then correct calibration could have given even higher results for the physical models.

In conclusion it is not possible to estimate what proportion of the error is due to N_{KC} losses, and what proportion is due to the calibration error, but it is likely that they were each responsible for about half of the discrepancy.

Comparisons of physical and numerical results in previous studies show good correlation between the physical and numerical results, however, they use small amplitude waves to keep them in the linear region, and are therefore easier to model. These small amplitude waves give small excursions within the model, and therefore the N_{KC} criteria are met and vortex shedding does not occur.

Sarmiento uses an energy balance approach to show that eddy losses are the main reason that the full theoretical efficiency of a physical OWC cannot be achieved (Sarmiento 1992), as they were not modelled using the techniques common at the time. The effects of turbulence were also not explicitly modelled in the mathematical model discussed in this chapter.

6.4.4. Phase difference between the internal and external surface elevation, $\angle G_1$

Figure 6.6 is a plot of $\angle G_1$ vs. period and shows the phase lag between the internal and external water surfaces. It shows that resonance, indicated by a 90° lag, of the water part of the system is $T=1.07s$

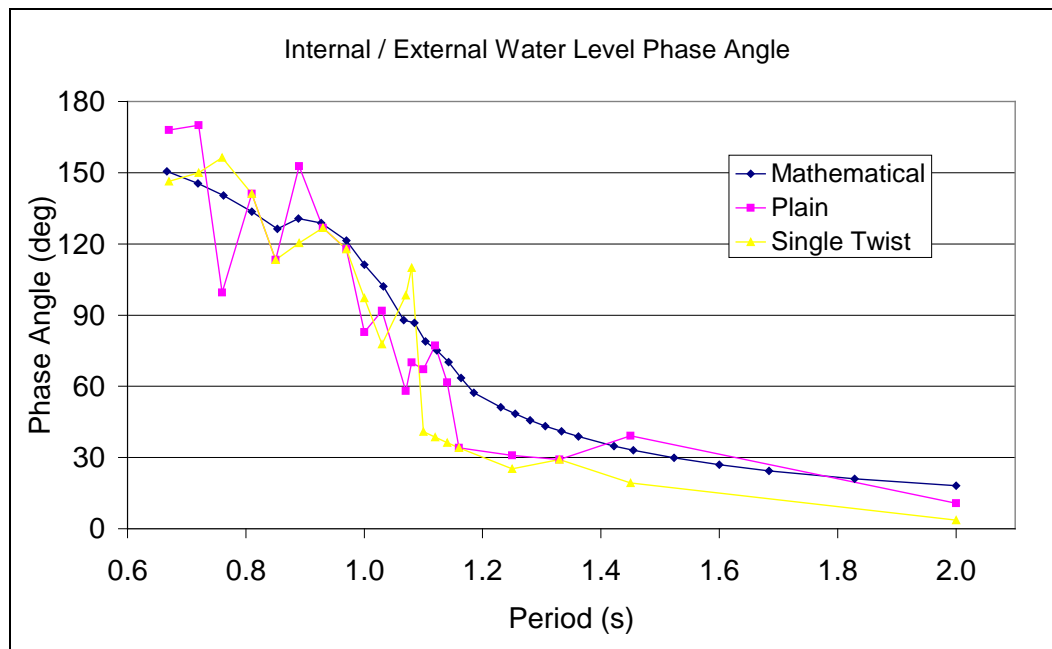


Figure 6.6: Mathematical Internal / external water phase angle: $\angle G_1$ with the phase angles for the physical models (from Figure 5.33).

Figure 6.6 gives confidence that the calculated results are realistic as they replicate those observed in the tank and discussed in chapter 5.

The phase angle between the internal and external water levels shown in Figure 6.6 suggests a slightly higher T_{res} than that of the physical model (1.07s instead of 0.97s), but the agreement is close nonetheless.

The dip in phase angle matches the position of the secondary peak in both the plain tube and single twist tube simulations, suggesting that there is some secondary resonant feature associated with 0.85s. This may be associated with a harmonic or the diameter of the models. This would be worthy of further investigation as the phenomenon was not observed in the experimental measurements.

6.4.5. Scaling of numerical results

Performing the same scaling analysis as described in Chapter 5 on these mathematically predicted efficiencies would give the single twist design a rated power of 643kW, with a 66kW average output which would deliver 517,536kWh/year for a 12m diameter machine with an 11.8m draft. This is much more attractive and indicates that the design should be pursued. It is likely that all of the losses are not accounted for in this mathematical model, and so the scaled output is an upper limit on the power that can be extracted.

6.4.6. Impedance matching.

Falnes (2002) shows that the ideal turbine damping should be the same as the radiation impedance, Z_r .

In order to test this, the optimum impedances of the turbine used in Chapter 5 had to be converted to the same units as those used in Brendmo's model. Using dimensional analysis, it was determined that the turbine damping, Z_s , in Pa.s/m^3 from Chapter 5 should be divided by S_a^2 (the cross sectional area) to give kg/s , the units used by Brendmo et al (1996).

This yields a figure comparable to the values derived using Brendmo's model.

Only those turbine damping values that produced the maximum power transfer as described in Chapter 5 have been compared here as the theoretical method is intended to predict the optimum values. The values of Z_s that did not achieve the maximum power transfer cannot be used for comparison.

Only the real component of the turbine damping is known as it was calibrated in incompressible, steady flow conditions. This is valid for small scale models where the air is considered incompressible, and therefore does not have an imaginary component. Thus, the real components of the empirical and theoretical values are compared in Figure 6.7 below. The theoretical damping is a plot of Z_r as described in section 6.1.2.2. The theoretical damping is the spinner impedance shown in Figure 5.34 and translated as described above. The flowrate is taken from the physical test results from Chapter 5.

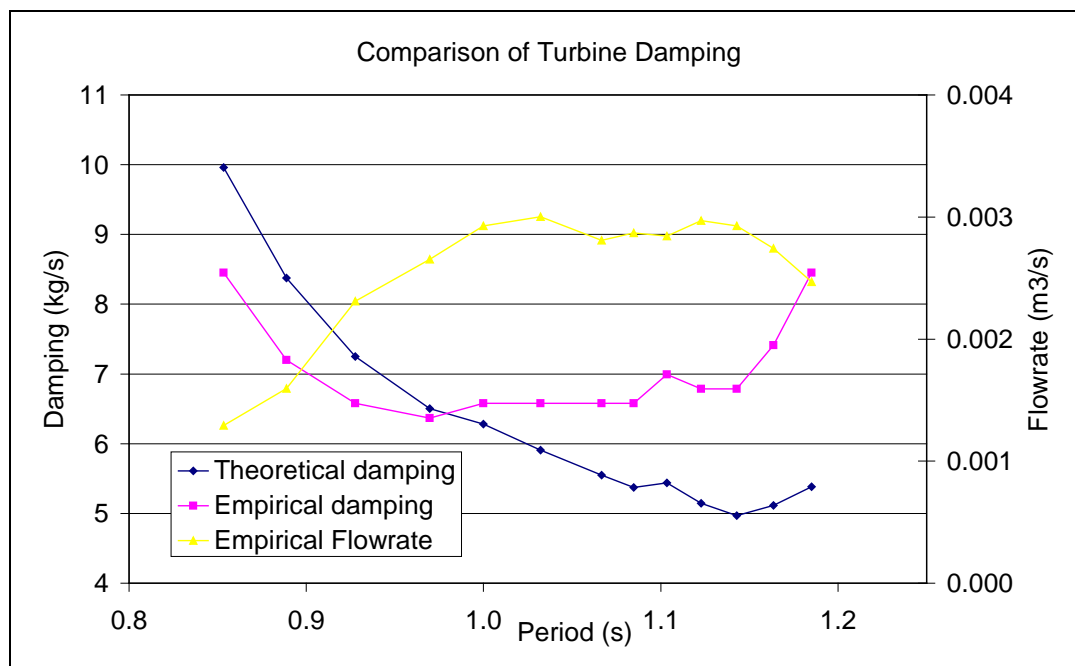


Figure 6.7: Comparison of measured and theoretical optimum turbine damping values.

Although there is some discrepancy, the curves do show some similarities in the resonant region with a minimum optimum damping when the flowrate is at a maximum.

The empirical flowrate shows a much better correlation (they are almost mirrored) with the empirically derived damping values than with the theoretically derived values. This may be because the resonant period of the mathematical model was set to 1.2s which was reflected in the calculation of both R_f (equation 6-12) and Z_w (equation 6-13) and thus Z_r (equation 6-7), the theoretical damping shown here. This may be why the minimum is at a higher period than that of the empirical results. Apart from that, the values are of the same order of magnitude, and very similar around the resonant region near 0.97s.

If the models could be adjusted to be more similar in output, the differences in the physical and theoretical damping values could be reduced, and this method could be used to predict the optimum damping for larger scale models in varying sea states.

6.5. Conclusions

The results of the mathematical model show significant discrepancies to the measured results, despite the fact that the model is partially based on the empirical results. In fact, Watabe, upon whose analysis this mathematical model was based, was modelling a fixed, open fronted machine operating like a terminator, rather than an open bottomed machine operating like a point absorber, giving a higher theoretical maximum efficiency.

The discrepancies can be removed by altering the system damping term and this indicates that there are significant losses not accounted for. This reinforces the case for tilting the models and improving the hydrodynamic shape of the inlet.

Watabe's model was designed to simulate a full scale OWC with a front opening, and the results here show that a modified design with side openings should be tested further. Other models, such as those outlined by Falnes (2002) or McCormick (1981), could be tried to see if better correlation can be achieved between the mathematical and physical models.

It was shown that a reasonable correlation can be achieved between the theoretically predicted and empirically derived values of turbine damping, especially close to resonance. With the improvements to the models outlined above, it is expected that this correlation would improve, and this could be used to predict the optimum characteristics of a full scale turbine.

Using the mathematically derived results to predict full scale performance gave a modest size of machine.

The mathematical model has given an insight into the challenges of designing and operating of an OWC. In particular, it has identified that the physical models were suffering from significant over-damping, and this is most likely due to the shape of the opening causing large eddies to form within the OWC. This highlighted the necessity for correctly designed openings, and using the Keulegan-Carpenter number, the optimum radius of the entry for the physical models was determined.

Chapter 7: Conclusions and further research

7. Introduction

There is a good case for developing wave energy devices as about 16% of the UK's electricity could be produced from wave energy, and there are many more potential markets around the world. The improvements to an OWC presented here could enhance the chance of a successful to this vision.

7.1. General

It is important to test with all parameters optimised to ensure valid comparison. Small scale models should always use the PTO impedance that gives the maximum power for the input wave conditions and the configuration of the model. If this is not done, then comparing sub-optimal results from one machine with optimal results from another could lead to incorrect conclusions. It is also important to test in realistic waves in a basin that represents the proposed deployment site. Examples of the errors that can arise from not doing this are described in Chapter three when the effect of using a flume altered the resonant properties of the model and in Chapter 5 where monochromatic results were used to estimate full scale output in polychromatic conditions.

7.2. Helical Configuration

It has been hypothesised in section 5.3.5 that the energy available to OWCs rises significantly with reducing draft, and it is thought that this is a contributing factor to the performance of the single twist model. When this phenomenon is combined with the helical design, then the resonant period can be matched with a deeper plain tube model. This gives the combined benefits of 24% more efficiency with 26% less draft. The models were scaled using Froude number criteria. The relative performance of the models will scale up, so the helical configuration will also be advantageous at full scale.

The important design characteristic of the T_{res} – draft relationship has been investigated in section 5.3.6, and a preliminary definition derived. This should allow the confident design of larger models for future tests. To understand this relationship it is important to understand how the water behaves inside the OWC. Introducing the helices introduced an element of centrifugal force to the water motion; this may have extended the effective internal water path somewhat by moving the centre of mass of the water towards the outside of the helix. Tests indicate that the centre of mass is at $R/\sqrt{2}$ (section 5.3.6.1) which corresponds to the radius that bisects the plan area of the model into a circle and concentric annulus.

The viscous resistance, R_f , of the single twist tube model was shown to be lower than that of the plain tube model and the 1.5 twist model. This is one reason that it performed better under ideal conditions than either of the other models. Since the tube is not converting any energy itself, its resistance, R_f , should be lowered as much as possible to allow the energy to reach the turbine.

At full scale, achieving optimum performance is the goal of the control strategy. As changing Z_s affects the overall performance of the system considerably, it is likely to form a significant part of the control system. If Z_r is known, it is possible to design for a particular Z_s by choosing an appropriate turbine specification. With the correct control mechanism (e.g. variable pitch turbine and or variable speed generator), it will be possible to alter Z_s in service, and possibly even within a wave cycle, to optimise performance.

7.3. Spinning Simulator

The spinner is suitable for tests, like those described in chapter 5, where there is a requirement to determine the optimum turbine impedance. It gives a method for quickly obtaining a known impedance. Attention must be paid to the spinner bearing, the bracket and the power of the motor to ensure that very high impedances can be

achieved. With a powerful motor or some other system that allows rapid and accurate acceleration and deceleration of the spinning simulator, it would also be possible to simulate adjusting the turbine impedance during a wave cycle.

Deficiencies in the spinner calibration may have led to significant overestimation of the impedance. This in turn would have reduced the value of P_{air} meaning that the efficiencies were underestimated. The magnitude of this error is not known, but has been estimated to be a factor of 2 to 2.5, however it is a systematic error and did not alter the relative performance of the models. When using a turbine simulator of this nature, it is very important to calibrate it correctly as there are no established theoretical methods for calculating flow from a measured pressure drop – as there are for orifice plates.

7.4. Mathematical Model

The results of the mathematical model do not match the measurements from the empirical model, despite the fact that it is partially based on the empirical results. The discrepancies can be removed by altering the system damping term and this indicates that there are significant losses experienced by the physical model that are not accounted for in the mathematical model. This suggests that the efficiencies of the model could be improved, as there are losses in the physical model that could be reduced. It was shown that a reasonable agreement can be achieved between the theoretically predicted and empirically derived values of turbine damping, especially close to resonance. With the improvements to the physical models outlined in chapters 5 and 6, and the use of correctly calibrated simulators, it is expected that the level of agreement would improve, and this could be used to predict the optimum characteristics of a full scale turbine.

7.5. Further Research

Further tests at this scale would be worthwhile with suitably hydrodynamically shaped inlets. These could be tested against models with side-openings, and also a tilting

version like the sloped IPS buoy. These tests should also fully define the relationship between draft and resonant frequency. In addition, more tests to determine optimum helix angle should be carried out.

Further tests are worthwhile at larger scale and using a well calibrated spinning simulator to confirm the actual performance of the models at large scale.

Scaling the results to a 12m diameter device fixed in deep water gives an OWC rated at 104kW producing 90,615kWh/year. This is not a commercially attractive figure, but it is thought to be an underestimate due to the error in calibrating the spinner. In addition, it is expected that the performance can be significantly improved if the optimum impedance can be achieved over a wider range of periods. Turbulent losses could be reduced by adding suitably rounded entries to the bottom of the duct. The theoretical maximum rated power is about 10 times more than that absorbed by the models, so there is significant room for improvement on this 104kW figure. Using the mathematically derived results to scale up to full scale, gave a modest size of machine that could be commercially viable.

Watabe's mathematical model could be refined further to give a good impression of the full scale power output and to compare various other configurations.

7.6. Final Thoughts

Overall the helical concept shows great promise and the author will continue its development to improve the performance of OWC's as they are deployed around the world.

Appendix A: References

1. AHLUWALIA, A. (2006). *Developing a wave power concept*, M.Eng. Loughborough University.
2. BABARIT, A. HALS, J. MULIAWAN, M.J. KURNIAWAN, A. MOAN, T. KROKSTAD, J. (2012). Numerical benchmarking study of a selection of wave energy converters, *Renewable Energy*, 41, pp.44-63, ISSN 0960-1481.
3. BABARIT, A. AND CLÉMENT, A.H. (2006). Optimal latching control of a wave energy device in regular and irregular waves. *Applied Ocean Research*, 28(2) pp.77–91.
4. BELLAMY, N.W. (1985). *Development of the “sea clam” wave energy device for small scale use*. Report for the Wave Energy Steering Committee of the Department of Energy.
5. BERR, (2008). *Supply Chain constraints on the deployment of renewable electricity technologies* (by Douglas Westwood) [online] Available at: www.berr.gov.uk/files/file46792.pdf [Accessed 15/11/10].
6. BRADDICK, H.J.J. (1965). *Vibrations, waves and diffraction*, McGraw-Hill ISBN: 9780000000002.
7. BRENDMO, J. FALNES, J. & LILLEBEKKEN P. M. (1996). Linear modelling of oscillating water columns including viscous loss *Applied Ocean Research* 18(2-3) pp. 65-75.
8. BRITO-MELO, A. GATO, L.M.C. SARMENTO, A.J.N.A. (2002). Analysis of Wells turbine design parameters by numerical simulation of the OWC performance, *Ocean Engineering* 29(12), pp.1463–1477.
9. BRITISH STANDARDS INSTITUTION, (1987). BS 1042, Measuring fluid flow in closed conduits.
10. BWEA, (2009). *Predictors for wave and tidal: Installed capacity of marine energy projects to 2020*. [Online] www.bwea.com/pdf/marine/Marine_report_enteclogo.pdf [Accessed 10/11/10].
11. CARBON TRUST, (2006). *Future Marine Energy*. [Online] www.oceanrenewable.com/wp-content/uploads/2007/03/futuremarineenergy.pdf [Accessed 15/11/10].
12. CARBON TRUST, (2011), *Accelerating Marine Energy*. [Online] www.carbontrust.com/media/5675/ctc797.pdf [Accessed 15/11/12].
13. CARBON TRUST (2007) [http://www.carbontrust.co.uk/SiteCollectionDocuments/Various/Emerging technologies/Technology_Directory/Marine/Technical_guidelines/Ocean Waves and wave design.pdf](http://www.carbontrust.co.uk/SiteCollectionDocuments/Various/Emerging%20technologies/Technology_Directory/Marine/Technical_guidelines/Ocean%20Waves%20and%20wave%20design.pdf) [Accessed 08/10/07].
14. CAREY, J. PEMBERTON, M. (2001). A Fully Submerged Oscillating Water Column, *Marine Renewable Energy Conference* Newcastle upon Tyne, UK 27-28 December 2001.
15. CHAKRABARTI, S.K. (1994). *Offshore Structure Modelling* Singapore, World Scientific ISBN: 9810215134.
16. CHANSON, H. (1999). *The Hydraulics of Open Channel Flow* Oxford, Arnold

ISBN 978 0 7506 5978 9.

17. CHIA-PO, L. (1999). *Experimental studies of the hydrodynamic characteristics of a sloped wave energy device* PhD The University of Edinburgh.
18. CROFT, A. DAVISON, R. HARGREAVES, M. (2001). *Engineering Mathematics 3rd ed*, Harlow, Pearson Education Ltd ISBN 0-130-26858-5.
19. CRUZ, J. (2008). *Ocean Waves Energy, Current Status and Future Perspectives*, Berlin, Springer, ISBN3540748946.
20. CUAN, B. BOAKE, T. J. WHITTAKER, T. FOLLEY, M. ELLEN, H. (2002). Overview and Initial Operational Experience of the LIMPET Wave Energy Plant. *Proceedings of The Twelfth International Offshore and Polar Engineering Conference* Kitakyushu, Japan May 26-31, 2002 ISSN 1098-6189.
21. CURRAN, R. STEWART, T.P. WHITTAKER, T.J.T. (1997). Design synthesis of oscillating water column wave energy converters: Performance matching *Proceedings of the Institution of Mechanical Engineers, Part A: Journal of Power and Energy* September 1, 1997 vol. 211 no. 6 489-505.
22. CURRAN, R. WHITTAKER, T.J.T. STEWART, T.P. (1998). Aerodynamic conversion of ocean power from wave to wire. *Energy Conversion and Management*. 39(16–18), November–December 1998, Pages 1919-1929, ISSN 0196-8904.
23. DALTON, G.L. LEWIS, T. (2011). Performance and economic feasibility analysis of 5 wave energy devices off the west coast of Ireland. *European Wave and Tidal Conference 2011*. [Online]
[https://www.see.ed.ac.uk/~shs/TidalStream/EWTEC 2011 full/papers/36.pdf](https://www.see.ed.ac.uk/~shs/TidalStream/EWTEC2011full/papers/36.pdf) [Accessed 12/01/12].
24. DIZADJI, N. SAJADIAN, S.E. (2011). Modelling and optimisation of the chamber of owc system. *Journal of Energy* 36 pp2360-2366.
25. Dresser Rand (2010) *HydroAir Flyer* [Online]. Available at:
<http://www.dresser-rand.com/products/hydroair> [Accessed 12/10/10].
26. DUCKERS, L. (2004). *CREST MSc Hydro Notes Chapter 9*. Loughborough University, unpublished, but available on request.
27. DUCKERS, L. MINNS, N. HAKEN, R. WATSON, S. (2008). A Novel, Compact Wave Energy Converter, *Proceedings of the 10th World Renewable Energy Congress*. Glasgow, UK 19-21 July 2008.
28. Embley Energy (n.d.). [online] <http://www.sperboy.com/index.html> [Accessed 10/10/10].
29. EMEC, (2009). *Tank Testing of Wave Energy Conversion Systems*. BSI ISBN 970-0-580-67262-0.
30. EVANS, D.V. (1978). The Oscillating Water Column wave energy device, *IMA J. Inst Appl Math*, 22, pp423-433.
31. EVANS, D.V. PORTER, R. (1995). Hydrodynamic Characteristics of an oscillating water column device, *Appl Ocean Res* 17(155-164) 1995
32. Eumetsat, (2009) [online] <http://www.eumetsat.int/jason/print.htm> [Accessed 15/10/10].
33. FALCÃO, A. DE O'. (2004). First generation wave power plants: current

- status and R&D requirements, *Journal of Offshore Mechanics and Arctic Engineering ASME*, 126 pp384-388.
34. FALCÃO, A. F. DE O'. (2010). Wave energy utilization: A review of the technologies, *Renewable and Sustainable Energy Reviews* 14pp899–918.
 35. FALCÃO, A. F. DE O'. (2007). Modelling and control of oscillating-body wave energy converters with hydraulic power take-off and gas accumulator *Ocean Engineering* 34(14–15), pp2021–2032.
 36. FALCÃO, A. F. DE O'. JUSTINO, P.A.P. (1999). OWC wave energy devices with air flow control, *Ocean Engineering*, 26(12) pp1275-1295, ISSN 0029-8018.
 37. FALCÃO, A. F. DE O'. PEREIRA, P.E.R. HENRIQUES, J.C.C. GATO, L.M.C. (2010). Hydrodynamic simulation of a floating wave energy converter by a U-tube rig for power take-off testing, *Ocean Engineering*, 37(14–15) pp1253-1260, ISSN 0029-8018.
 38. FALNES, J.F. (2007). A review of wave-energy extraction. *Marine Structures*, 20(4), pp185-201.
 39. FALNES, J.F. (2002). *Ocean Waves and Oscillating Systems*, Cambridge University Press, ISBN 0 521 78211 2.
 40. FALNES, J.F. (2002a). Optimum control of oscillation of wave energy converters. *International Journal of Offshore and Polar Engineering*, 12 pp 47–155.
 41. GATO, L. M. C. FALCÃO, A. F. DE O'. (1998). Aerodynamics of the Wells Turbine, *Int. J. Mech. Sci.* 30 (6) pp. 383-395.
 42. GERVELAS, R. TRARIEUX, F. PATEL, M. (2011). A time domain simulator for an oscillating water column in irregular waves, *Ocean Engineering* 38 pp1007-1013.
 43. GUNN, K. TAYLOR, C.J. (2008). Genetic algorithms for the development and optimisation of wave energy converter control systems. *23rd European Institute for Applied Research Workshop on Advanced Control and Diagnosis*. Coventry, UK, 1 January 2000.
 44. HUGHES, E. (2002). *Electrical and Electronic Technology*, 8th ed, Harlow, Pearson Education Ltd, ISBN 0582 40519 X.
 45. HULME, M. JENKINS, G.J. LU, X. TURNPENNY, J.R. MITCHELL, T.D. JONES, R.G. LOWE, J. MURPHY, J.M. HASSELL, D. BOORMAN, P. MCDONALD, R. HILL, S. (2002). *Climate Change Scenarios for the United Kingdom: The UKCIP02 Scientific Report*, Tyndall Centre for Climate Change Research, School of Environmental Sciences, University of East Anglia, Norwich, UK. pp 120.
 46. HUNTER, R.S. (1991). Future possibilities for the NEL oscillating water column wave energy converter, *Paper for the energy committee of the IMechE*.
 47. IEA-Ocean Energy Systems, Annex II report (2003). [online] www.ocean-energy-systems.org/library/annex_ii_reports/development_of_recommended_practices_for_testing_oes_2003/ [Accessed 15/10/10].
 48. IPCC, (2007a). *Working Group One: Summary For Policy Makers Fourth*

- Assessment Report, IPCC [online] www.ipcc.ch/pdf/assessment-report/ar4/wg1/ar4-wg1-spm.pdf [Accessed 12/09/10].
49. IPCC, (2007b). *Climate change 2007: Mitigation. Contribution of Working group III to the Fourth Assessment Report of the Intergovernmental Panel on Climate Change* Metz, B. Davidson, O. R. Bosch, P. R. Dave, R. Meyer L. A. (eds), Cambridge and New York, Cambridge University Press.
 50. IPCC, (2007c). *Summary for Policymakers. In: Climate Change 2007: Impacts, Adaptation and Vulnerability. Contribution of Working Group II to the Fourth Assessment Report of the Intergovernmental Panel on Climate Change*, Parry, M.L. Canziani, O.F. Palutikof, J.P. van der Linden P.J. Hanson, C.E. Eds. Cambridge, Cambridge University Press, pp7-22.
 51. JOHNSON, F. DAI, Y.M. CHUDLEY, J. (2001). Design and feasibility study of a tethered multiple oscillating water column (MOWC) pilot unit wave energy device, *Marine Renewable Energy Conference* Newcastle upon Tyne, UK 27-28 December 2001.
 52. KNMI (n.d.): *Wave Atlas* [online] <http://www.knmi.nl/onderzk/oceano/waves/era40/climatology.html> [Accessed 22/10/08].
 53. KNOTT, G.F. FLOWER, J.O. (1980). Measurement of energy losses in oscillatory flow through a pipe exit, *Applied Ocean Research*, 2(4) pp 155-164, ISSN 0141-1187.
 54. KNOTT, G. F. MACKLEY, M.R. (1980). On eddy motions near plates and ducts, induced by water waves and periodic flows Royal Society (London), *Philosophical Transactions*, Series A. 294(1412) pp. 599-623.
 55. KOFOED, J.-P. FRIGAARD, P. (2006). *Experimental testing for Wave Energy Utilisation and Coastal Engineering*. Aalborg University Course Notes, unpublished.
 56. KORDE, U.A. (1997). Performance of a wave energy device in shallow-water nonlinear waves: part I, *Applied Ocean Research*, 19(1) pp1-11, ISSN 0141-1187.
 57. LEIPZIG UNIVERSITY (n.d.). [online] http://www.uni-leipzig.de/~grw/lit/texte_099/59__1999/59_1999_hansa.htm [Accessed 2/10/10].
 58. LOPES, M.F.P. HALS, J. GOMES, R.P.F. MOAN, T. GATO, L.M.C. FALCÃO, A.F.DE O'. (2009). Experimental and numerical investigation of non-predictive phase-control strategies for a point-absorbing wave energy converter. *Ocean Engineering*, 36(5) pp386-402, ISSN 0029-8018.
 59. MAIN, I.G. (1998). *Vibrations and waves in Physics*, 3rd ed. Cambridge, Cambridge University Press, ISBN 0521447011.
 60. MARSHAL, P. (2007). *Wave probes for a model oscillating water column*. M.Eng. Loughborough University.
 61. MASSEY, B.S. (1989). *Mechanics of Fluids*, 6th ed, London, Chapman and Hall, ISBN 0412342804.
 62. MASUDA, Y. (2001). Design Study of a BBDB (Bent Backward Duct Buoy) *Marine Renewable Energy Conference* Newcastle upon Tyne, UK 27-28 December 2001.

63. MASUDA, Y. KUBOKI, T. RAVINDRUM, M. PATHAK, A.G. JAYASHANKAR, V. XIANGUANG, LIANG. (1999). Development of Backward Bent Duct Buoy (BBDB) *Proc Ninth international offshore and polar engineering conference*. Brest, France, May 30–June 4, 1999 ISSN 1098-6189.
64. MCCABE, A.P. AGGIDIS, G.A. (2009). A preliminary study into optimising the shape of a wave energy collector using a genetic algorithm *SUPERGEN International Conference on Sustainable Power Generation and Supply*. Nanjing 6-7 April 2009. ISBN: 978-1-4244-4934-7.
65. MCCORMICK, M.E. (1981) *Ocean Wave Energy Conversion*, John Wiley & Sons inc. 1981 ISBN 0-471-08543-X.
66. MÜLLER, G. WHITTAKER, T.J.T. (1995). Visualisation of flow conditions inside a shoreline wave power-station. *Ocean Engineering*, 22(6) pp 629-641, ISSN 0029-8018.
67. MUNDON, T. MURRAY, HALLAM, PATEL, (2005). Causal Neural Control of a Latching Ocean Wave Point Absorber. *International Conference on Artificial Neural Networks (ICANN)* Warsaw, Poland. LNCS 3697, pp. 423-429.
68. OCEAN ENERGY (n.d.). [online] www.oceanenergy.ie/gallery/ [Accessed 02/10/10].
69. OCEANLINX (2010). [online] <http://www.oceanlinx.com> [Accessed 2/10/10].
70. ONS, (2012). *Preliminary estimate of GDP*. [online] <http://www.ons.gov.uk/ons/rel/gva/gross-domestic-product--preliminary-estimate/q2-2011/preliminary-estimate-of-gdp.html> [Accessed 17/02/12].
71. OPEN UNIVERSITY (1989). *Waves, Tides and Shallow-Water Processes*. Oxford, Pergamon Press, ISBN: 0080363725.
72. OWER, E. PANKHURST, R.C. (1997). *The Measurement of Air Flow*, 5th ed. Oxford, Pergamon 1977, ISBN 0080212824.
73. PACALA, S. SOCOLOW, R. (2004). *Stabilisation Wedges Solving the Climate problem for the next 50 years with current technologies*. Science Magazine August 2004.
74. PRICE A.A.E. DENT C.J. WALLACE A.R. (2009), On the capture width of wave energy converters, *Applied Ocean Research*, 31(4) pp 251-259, ISSN 0141-1187.
75. RAO, N. (1996). Dimensional Analysis, Keeping track of mass, length and time, *Resonance (Journal of Science Education)* Indian Academy of Science, pages 29-41 November 1996.
76. ROSS, D. (1981). *Energy From Waves* 2nd ed. Oxford, Pergamon Press ISBN 0080267157.
77. SALTER, S.H. (2001). Proposals for a combined wave and current tank with independent 360° capability, *Marine Renewable Energy Conference* Newcastle upon Tyne, UK 27-28 December 2001.
78. SARMENTO, A.J.N.A. Gato L.M.C. FALCÃO A.F.DE O'. (1990). Turbine-controlled wave energy absorption by oscillating water column devices, *Ocean Engineering*, 17(5), pp 481-497, ISSN 0029-8018.
79. SARMENTO, A.J.N.A. (1991). Semi-empirical simulation of a 0.3 MW OWC

- power plant. *Proceedings 3rd Symposium on Ocean Wave Energy Utilization*, JAMSTEC, Japan, pp. 385-393.
80. SARMENTO, A. J. N. A. (1992) Wave flume experiments on two-dimensional oscillating water column wave energy devices *Experiments in Fluids* 4(12) pp 292-286 ISSN 0723-4864.
 81. SENSOR TECHNICS datasheet for BSDX 0010d4d: [online]
<http://www.sensortecnics.com/index.php?fid=300&fpar=YToxOntzOjQ6InBjaWQiO3M6MzoiMTcyIj9&isSSL=0&aps=0&blub=427034b7f02c92e64c378cfd5bee1755> [Accessed 15/01/12].
 82. SETOGUCHI, T. (2003). Air Turbine with staggered blades for wave energy conversion, *International Journal of offshore and polar engineering*, 13 pp 316-320.
 83. SETOGUCHI, T. (2004). Study of an impulse turbine for wave power conversion: Effects of Reynolds number and hub to tip ratio on performance, *Journal of Offshore Mechanics and Arctic Engineering ASME*, 126 pp137-140.
 84. STERN, N. (2006). The economics of climate change, executive summary [online] http://www.hm-treasury.gov.uk/d/Executive_Summary.pdf [Accessed on 02/10/10].
 85. SWRDA, (2004). *SeapowerSW Review, Appendix A, for RegenSW*. [online] http://wavehub.co.uk/information_for_developers/future_developments_in_the_sw.aspx [Accessed 12/11/10].
 86. SWRDA, (2006). *Wave Hub Development and Design Phase Appendix-A Coastal Processes Study Report*, Halcrow for SWRDA. [Online] www.wavehub.co.uk/wp-content/uploads/2011/06/Appendix-A-Coastal-Processes.pdf [Accessed 12/11/10].
 87. SWRDA, (2010). *Offshore Renewables Resource Assessment and Development (ORRAD)*. [online] http://www.southwestrda.org.uk/news_and_events/2010/october/offshore_renewables_study.aspx [Accessed 19-10-10].
 88. TAYLOR, J.R.M. MACKAY, I. (2001). The Design of an eddy current dynamometer for a free-floating sloped IPS buoy. *Marine Renewable Energy Conference* Newcastle upon Tyne, UK 27-28 December 2001.
 89. TEASE (2005). Wavegen, Dynamic Response of a Variable Pitch Wells Turbine. [online] http://www.wavegen.co.uk/research_papers.htm [Accessed 02/11/11].
 90. TUCKER, M.J. PITT, E.G. (2001). *Waves in Ocean Engineering*. Oxford, Elsevier 2001, ISBN 0080435661.
 91. VASSALOS, D. (1999). Physical Modelling and similitude of marine structures, *Ocean Engineering* 26 pp 111-123.
 92. WARD-SMITH, CHAPTER H, A. J. (1980). *Internal fluid flow: the fluid dynamics of flow in pipes and ducts* Oxford: Clarendon Press, ISBN: 0198563256.
 93. WATABE, T. (2007). *Utilization of the Ocean Wave Energy*. FUJI Print Press Co. Ltd.
 94. WAVEGEN (n.d.) [online]

- http://www.wavegen.co.uk/what_we_offer_limpet_islay.htm [Accessed 2/10/10].
95. WEBER, J. AND THOMAS, G.P. (2001). Optimisation of the hydro-aerodynamic coupling of a 2-D onshore and a 3-D nearshore OWC wave energy device. *Marine Renewable Energy Conference*. Newcastle upon Tyne, UK 27-28 December 2001.
 96. WEBER, J. (2007). Representation of non-linear aero-thermodynamic effects during small scale physical modelling of OWC wave energy converters. *7th European Wave and Tidal Energy Conference*. Porto, Portugal, 11-14 September 2007.
 97. WEBSOCKETS (n.d.). *Moody Diagram*. [online] <http://webscripts.softpedia.com/scriptScreenshots/Moody-Diagram-Screenshots-33418.html>. [Accessed 12/11/10].
 98. WHITE, P.R.S. (1991). A phenomenological design tool for wells turbines, *Wave Energy, IMechE* 1991 ISBN 0852987889.
 99. WHITE, P.R.S. (1985). *Development of the Sea Clam wave energy device for small scale use*. Commercial report for the DTI by Coventry Polytechnic, 1985 unpublished.
 100. ZHANG, Y.L. ZOU, Q.-P. GREAVES, D. (2011). Air-water two-phase flow modelling of hydrodynamic performance of an oscillating water column device, *Renewable Energy*, 14 pp 159-170.
 101. ZONDERVAN G.-J. HOLTROP J. WINDT J. VAN TERWISGA T. (2011). On the Design and Analysis of Pre-Swirl Stators for Single and Twin Screw Ships. *Second International Symposium on Marine Propulsors*. Hamburg, Germany, June 2011.

Appendix B: Nomenclature and acronyms

Symbol	Description	units
A	Wave amplitude	m
a	speed of sound	m/s
A_c	Amplitude captured (amplitude of internal water level relative to OWC structure) $= A - A_d$	m
A_d	Amplitude of displacement of OWC structure	m
C	circumference	m
c	wave phase speed	m/s
CW	Capture width $= \lambda/2\pi$	m
CWR	Capture width ratio $= P_{\max}/(D \cdot P_i)$	
d	draft	m
D	diameter of OWC	m
D_h	Hydraulic diameter Analogous to D for Re calculations	m
f	frequency	Hz
f	friction factor $= 2hDg/LV^2$	
F_0	Displacing force acting on an OWC	N
F_d	Damping force	N
F_e	Excitation force	N
F_m	Inertial force	N
f_p	frequency for which S(f) is maximum	Hz
Fr	Froude number $= u/gL$	
F_s	Spring force	N
g	acceleration due to gravity	m/s ²
G_1	Complex number describing the movement of the water in the OWC	1/N
G_2	Complex number describing the movement of the air in the OWC	m ³ /s
H	monochromatic wave height	m
H_f	head loss due to friction	m
H_s	significant wave height	m
j	$\sqrt{-1}$	
K	spring constant	N/m
k	exponential decay constant	
K_a	Spring rate of air	N/m
K_w	Spring rate of water	N/m
L	internal water path length	m
L_c	Coupling length	m
m	mass	kg
m (subscript)	denotes that variable relates to model scale	
Ma	Mach number $= V/a$	
m_a	Added mass of water	kg
m_d	Mass of water above the mean water level inside the model when the internal water surface has the same amplitude of excursion as the external wave	kg

Symbol	Description	units
m_w	Mass of water in the OWC when at rest	kg
MWL	mean water level	
n	number of turns of the helical fins	
N_{KC}	Keulegan Carpenter number =	
OWC	Oscillating Water Column	
P	power	W
p	pressure	Pa
p (subscript)	denotes that variable relates to prototype scale	
p_0	Atmospheric pressure	Pa
P_{air}	Power in air flow	W
P_i	Incident wave power	W/m
PTO	Power take off	
Q	volume flow rate	m^3/s
Q_{max}	peak flowrate	m^3/s
r	relative roughness = ε/D_h	
R	Radius of OWC	m
Re	Reynolds number =	
r_{entry}	radius of the entry	m
R_f	Resistance due to friction	$Pa.s/m_3$
RMS	root, mean, square value	
$S(f)$	Spectral variance density	m^2/Hz
S_a	horizontal sectional area of the OWC at the MWL	m^2
T	Wave period	s
t	time	s
T_e	Energy period	s
T_{res}	Period for which η is a maximum	s
u	velocity	m/s
v	velocity	m/s
X	Physical scale factor between a model and a prototype	
x	displacement	m
\hat{x}	maximum displacement of the reciprocating flow	m
\dot{x}	velocity	m/s
\ddot{x}	acceleration	m/s^2
z	mean water depth	m
Z	impedance	$Pa.s/m_3$
Z_r	Radiation impedance	$Pa.s/m_3$
Z_s	Turbine simulator impedance	$Pa.s/m_3$
Z_{tot}	Total impedance = $Z_r + R_f + R_s$	$Pa.s/m_3$
Z_w	Total model damping = $Z_r + R_f$	kg/s
Δp	differential pressure	Pa
ε	absolute roughness	mm

Symbol	Description	units
ζ	vertical displacement of water particles	m
η	efficiency	
κ	wave number = $2\pi/\lambda$	1/m
λ	wavelength	m
μ	dynamic viscosity	Pa·s
ξ	OWC damping coefficient	
ρ	density	kg/m ³
ρ_a	density of air	kg/m ³
ω	frequency	rad/s
ω_0	natural frequency	rad/s
ν	kinematic viscosity	m ² /s
χ	horizontal displacement of water particles	m

Appendix C: List of papers

L DUCKERS, **N MINNS**, A AHLUWALIA AND S WATSON (2008). A Novel, Compact Wave Energy Converter, *Proceedings of the 10th World Renewable Energy Congress*, Glasgow, UK, 2008.

M. LEYBOURNE, W.M.J. BATTEN, A.S. BAHAJ, J. O'NIANS AND **N. MINNS** (2009). A Parametric Experimental Study of the 2D Performance of a Ducted Wave Energy Converter. 8th European Wave and Tidal Energy Conference, Uppsala, Sweden, 2009.

M. LEYBOURNE, W.M.J. BATTEN, A.S. BAHAJ, J. O'NIANS AND **N. MINNS** (2010). Experimental and Computational Modelling of the OWEL Wave Energy Converter. 3rd International Conference on Ocean Energy, Bilbao, Spain, 2010.

M. LEYBOURNE, W.M.J. BATTEN, A.S. BAHAJ, **N. MINNS** AND J. O'NIANS (2011). Preliminary design of the OWEL wave energy converter commercial demonstrator, World Renewable Energy Congress, Linköping, Sweden, 2011.

A Novel, Compact Wave Energy Converter

Les Duckers¹, Ned Minns², Robert Haken² & Simon Watson²

¹ Faculty of Business, Environment and Society, Coventry University, Coventry, UK, Tel: 44-24-7688-8283, Fax: 44-2476888679, Email: l.duckers@coventry.ac

² Centre for Renewable Energy Systems Technology, Loughborough University, Loughborough, UK LE11 3TS, Tel: 01223 242 848, Email: n.minns@lboro.ac.uk

1 Introduction

This paper describes a novel oscillating water column which is designed for simple deployment as a floating device. Waves in the Sea of Japan have average periods of around 7s, whereas in the North Atlantic they are more typically 10s.

Figure 1. Annual average wave power (kW/m) for various locations round the world (adapted from [1])



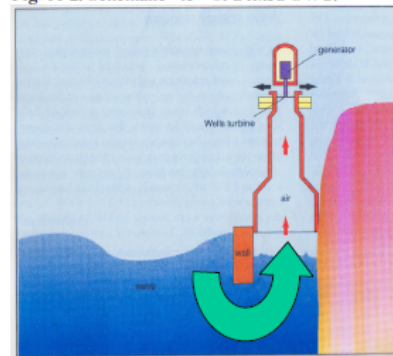
Oscillating water columns respond to waves in a resonant manner, and are best thought of as a U tube, half of which is outside the device and unconstrained. The OWC can be tuned to the incident wave climate using $L = gT^2/2\pi^2$, where L is the length of the liquid in the tube, or the coupling length [2].

2 Oscillating Water Columns (OWC)

OWCs are probably the most popular type of wave energy converter and have been considered in many countries: Australia, India, Japan, China, Norway, Ireland, Portugal and the UK. Their simplicity is a major attraction, and the single moving component of a shaft linking an air turbine to a generator leads to a high reliability and ease of maintenance. The initial concept was a fixed structure with a mouth or opening beneath the surface through which water flows into and out of the column driven by the wave crest and trough. As the water rises and falls within the column it drives the air in the column through an air turbine and the draws it back on the return stroke. The use of a self rectifying air turbine running at high speed gives good conversion without the need

for rectifying valves or complex and expensive power conversion machinery. The linear pressure-flow characteristics, that is to say -the impedance- of the "Wells" turbine, for example, permit it to be designed for optimum matching to the incoming waves. The low drag of the Wells symmetrically shaped blades allow it to rotate at synchronous speeds such as 1500rpm, thereby obviating the need for a gearbox as it can drive the generator directly. The OWC operates best when it is tuned to the incident wave climate and this is achieved by setting the coupling length to be $L = gT^2/2\pi^2$ [2]. This implies that for the Sea of Japan the coupling length is of the order of 24m, whereas for the North Atlantic it is around 49m. Even with around half of this length outside the device, the need to design a structure to accommodate such a long length has resulted in many being fixed to the sea bed or rock face. There have been variations on this theme: multi-resonant devices incorporating harbour walls or multiple tubes; focusing devices and floating OWCs including the Bent Backward Duct Buoy. In all arrangements the coupling length has to be of the order of tens of metres and this dictates the physical size of the structure (see Figure 2).

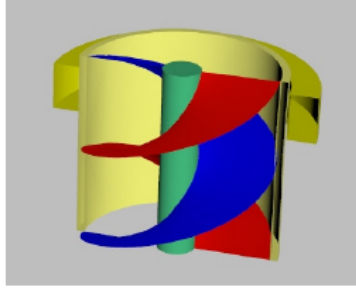
Figure 2. Schematic view of a fixed OWC.



Aim of the Present work

The present work employs a helical path for the internal movement of water which causes the water oscillations to execute a longer length.

Figure 3. Twin start, single twist helix inserted into OWC tube.



The coupling length necessary for resonant oscillations is therefore achieved with a device having a smaller draft than that of the equivalent plain tube. This leads to a reduction of the overall length of the device and hence to a compact OWC. The ultimate concept is that this device would be small enough to be factory produced, transported by lorry/boat and deployed easily and quickly as a floating wave energy converter in almost any shallow water (<50m) location around the world. It would be anchored to the seabed, with a flexible cable delivering the electrical output to land. Since the design length is of the order of 8m draft, it is anticipated that maintenance would be done on a remove and repair/replace basis.

Computation of Coupling length.

The water inside the device has to travel up a helical path l described by:

$$l = \sqrt{(nC)^2 + D^2} \quad (1)$$

Where l is the distance that the water travels through the helix, C is the resonant circumference ($=\pi\delta$, where δ = resonant diameter) and D is the draft when the device is at rest (all in meters) and n is the number of turns made by the helix from the bottom of the tube to the mean water level in the tube.

The resonant diameter is illustrated in Figure 4 which shows a large portion of the water flowing up the helix along a path close to the internal surface of the tube.

Figure 4. Internal water path of the single twist helix.



From the experimental results it was deduced that $\delta \approx 0.8 \times \text{internal diameter}$.

For a normal OWC, with a plane tube,
 $L \approx 2D + 0.25C$, (2)

but using a helix gives:
 $L \approx D + l$ (3)

or

$$L \approx D + \sqrt{(nC)^2 + D^2} \quad (4)$$

Which means that a prescribed value of L is obtained with a smaller values of D for $n > 0$. It is possible to reduce the draft by up to 40% by choice of n . Above 40%, at the model scale, the impedance of the model seriously affects the performance of the OWC.

Impact of the helix on performance of an OWC.

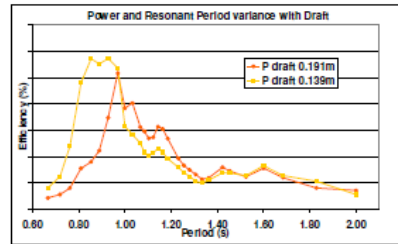
The introduction of the helix into the water flow path can be expected to degrade performance primarily due to the viscous flow along the surface of the helix, and around the internal surface of the tube (since the water is forced towards this surface in its circular motion). On the other hand, for the same coupling length, the entrance to the OWC is now shallower than with the plane tube and so the energy/power intercepted by the OWC is

greater. The fraction of energy between the surface and depth y is given by [3]:

$$F = 1 - \exp\left(-4\pi \frac{y}{\lambda}\right) \quad (5)$$

Tests performed on the models demonstrated that they do indeed become more efficient, as well as moving the resonant period, as the draft is reduced by use of the helical inserts.

Figure 5. Increasing efficiency with reducing draft.



Using a shallower draft increased the power available at the turbine by 10.5% across the spectrum, so using an extremely shallow draft, similar to the wave amplitude for a fixed device, is likely to give the best performance.

Floating OWC.

Floating OWCs of the tube type considered here will respond to heave forces in two modes; the oscillation of water resembling the "U" tube discussed here and the oscillations of the object as a float.

The latter will oscillate with a period, T_f , approximately given by:

$$T_f = 2\pi\sqrt{\frac{D}{g}} \quad (6)$$

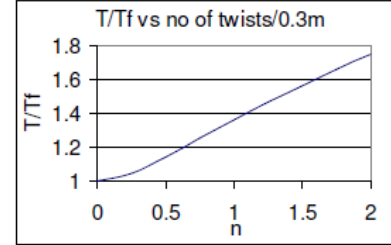
whereas the water oscillations have a period, T , approximately given by:

$$T = 2\pi\sqrt{\frac{L}{2g}} \quad (7)$$

The ratio of these periods is:

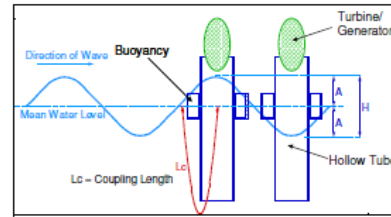
$$\frac{T}{T_f} = \sqrt{\frac{D + \sqrt{(nC)^2 + D^2}}{2D}} \quad (8)$$

Figure 6. Ratio of T/T_f as a function of n . In this case $C=0.349m$, $D=0.139m$ and $n=1.5$.



We can see that the periods become more distinct as the number of turns of the helix increases and therefore the opportunity to have two resonant periods to broaden the response curve. This is a phenomenon that will scale well and could be incorporated into full size devices.

Figure 7. Schematic view of a small floating OWC.



Experimental work.

The work described here has been conducted on four OWC models, all based on a tube of internal diameter 0.14m and so represent a scale of approximately 1:35 for a 5m OWC.

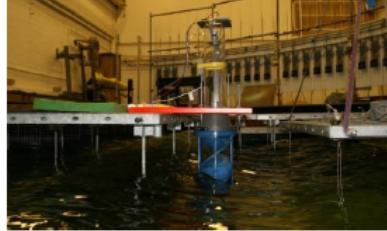
Table 1. List of models used.

Model	Tag	Twists per 0.3m high model
Plain Tube	P	na
Single twist helix	S	1
1.5 twist helix	1.5	1.5
Double twist helix	D	2

All the experiments were conducted with the models held in a fixed position, not floating, in order to achieve results as a function of the water oscillations alone. Initially a narrow wave tank was used, producing monochromatic waves of $T = 0.6$ to $1.65s$, and

with set heights of up to 0.1m. In the later series of tests a wide tank was used (Edinburgh University's curved tank), again using monochromatic waves with periods of 0.67 to 2s and set heights up to 0.11m.

Figure 8. Single twist model under test, with the turbine simulator mounted above, the wavemakers to the right and the beaches to the left.



Instrumentation.

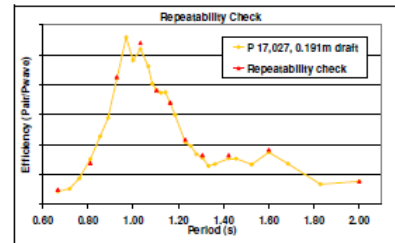
Incident waves were measured with a resistive wave probe. Wells air turbines were simulated using thin rubber sheet with slits cut across them in the narrow tank and then slotted rotating disks resembling a Wells, but without the aerofoil shape were used in the wide tank [4, 5]. A high speed motor was used to drive the rotating disk at a range of known speeds, giving various impedances (Z). These were all calibrated against a standard orifice plate and produced a linear pressure/flow impedance characteristic, unlike the orifice plate which had a square law relationship between pressure and flow. During the experiments the instantaneous pressure drop across the "Wells" was recorded using "sensortech" pressure transducers with a range of ± 2.4 mBar and a sensitivity of 0.0014 mBar and an error of $\pm 1\%$. The pressure taps were mounted 0.5 diameters above and below the simulator to maximise the pressure difference available in the reciprocating flow [6]. The instantaneous air power was then calculated from

$$\text{Pneumatic power} = \Delta P^2 / Z. \quad (9)$$

The waves were measured using Edinburgh University's wave probes. A series of periods and wave heights were chosen to achieve the maximum height available in the tank, without causing the waves to break.

The repeatability of the tank was tested by running 10 tests twice and comparing the efficiency results and the wave heights. The results were very good with the maximum deviation being 3.8% and most of the points nearly identical (Figure 9). At periods above 1.5s, there were considerable reflections from the beach with up to 30% of the energy being reflected [7], this did not seem to affect the repeatability, but data gathered above 1.5s was treated with caution.

Figure 9. Repeatability check



The speed of the simulator was governed by a Hall effect sensor which kept the plate spinning at $\pm 0.5\%$ of the desired speed (2,000-9,000 RPM). These small fluctuations had no measurable effect on the impedance.

Model Impedance.

The impedance to water flow through the tube, and around the helix was measured in a water flume by recording the head necessary to force a known flow rate. At the relatively small scale of these models this impedance is much larger than that due the turbine simulator.

Table 2. Impedance at drafts to give a resonant period of 0.97s

Model	Draft (m)	Z_m (Pa.s/m ³)
Plain	0.191	89,000
Single	0.139	79,000
Double	0.1	200,000

This indicated that the double twist helix has a significantly higher impedance than the other two, so an additional model with 1.5 twists was constructed to fill the gap in the wide tank tests. The fact that the single tube has a lower impedance than the plain tube when set for the

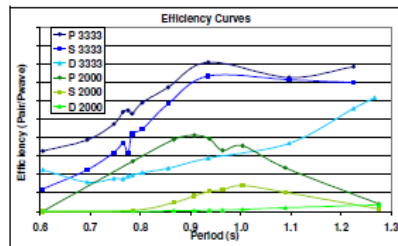
same resonant period showed promise for the concept.

The models were made to scale with Froude number, but not Reynolds number, and since full scale devices would have a Reynolds number about 100 times higher, some more Reynolds scale modelling will have to be devised to investigate the scalability of these results.

Model performance.

Figure 10 shows results obtained using rubber turbine simulators. Here the coupling length was held constant throughout the tests and the data indicate the variation in performance due to the draft difference between the models. Although there was considerable experimental uncertainty we are confident that the inclusion of a helix substantially modified the behaviour.

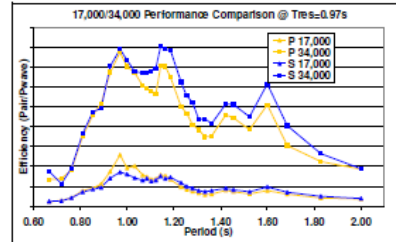
Figure 10. Narrow tank tests using rubber turbine simulators of impedance 2,000 and 3,333Pa.s/m³.



These results indicated that the helix had a detrimental effect on performance, but these results were not trusted as there appeared to be a large amount of interference in the tests due to the small scale of the flume we were using. In addition it was clear that much higher impedances were required, so the rotating disk simulators were developed.

Figure 11 shows the results from the wide tank experiments using the rotating disk simulators. Again, the draft of each model was adjusted to lead to the same notional resonant period. The results show the sensitivity to coupling length, draft and the number of twists in the helices and when the performance of the single twist helix is compared to the plain tube OWC with near optimum impedance of 34,000 Pa.s/m³, the overall performance is very encouraging.

Figure 11. Performance of the plain and single twist helices at two impedances.



At the near optimum impedance (for the plain tube) of 34,000Pa.s/m³, the single twist helix outperformed the plain tube by 13.2%. This improvement in performance is probably due to a combination of two things: the impedance of the shallower helical model is actually lower than that of the plain model, and also the water path may be a more natural one due to the "scooping" effect of the bottom of the helices. This result shows that the helical concept has definite performance benefits over the standard plain tube OWC.

At the lower impedance of 17,000Pa.s/m³, the helical models all underperformed against the plain tube at lower periods, and outperformed it at higher periods. Across the spectrum, the performance of the single helix was 62.7% of that of the Plain tube, but this property may still be useful as there is more energy available in the higher period waves in a polychromatic sea. It could, therefore, translate into better performance in a real sea.

Figure 11 also shows that there are some apparent harmonics at periods of about 1.16, 1.42 and 1.63s that are independent of draft. These were also very clear in results from other tests that have been omitted for clarity. Further work is required to determine if these are harmonics caused by the diameter or some other feature of the model, or some effect associated with the tank and the incident waves.

Conclusion

We have developed a means of effectively reducing the depth of the device under water by introducing a helix into the OWC tube.

Model tests indicate that we could reduce these drafts by 47% by choosing a very tight helix, although an optimum design contains a less tight helix, leading to a 27% - 36% reduction in draft (independent of resonant period chosen). Introducing a single twist helix therefore opens the possibility of fabricating an 8.6m draft, 60kW device (Sea of Japan) or a 17.6m draft, 315kW device (N. Atlantic) in a single piece. The Japanese version, in particular, can be easily transported and deployed using a standard lorry and small vessel. Being compact, fabrication is accessible to a modest facility, possibly located near to the deployment site.

Further tests are needed to validate the preliminary experimental results presented here and to determine the scalability of the results. In addition, a full economic analysis is required to determine whether the reduction in device fabrication and logistical costs is accompanied by a proportional increase in performance at full scale to determine the viability of the concept. If the performance and

cost characteristics are favourable, then the compact OWC could be deployed in large numbers.

References

1. T.Watabe, Utilization of the Ocean Wave Energy, Fuji Print Press, 2008
2. A.P.French, Vibrations and Waves, Van Nostrand Reinhold, 1986 ISBN 0442307845
3. L.J.Duckers, Wave Energy, in "Renewable Energy: Power for a Sustainable Future", Ed G Boyle, OUP 2004 ISBN 0199261784
4. Wave Energy Research Group, Coventry Polytechnic, Development of the "sea clam" wave energy device for small scale use, report for the Wave Energy Steering Committee, March 1985
5. P.R.S.White, A phenomenological design tool for wells turbines, Wave Energy IMechE 1991 ISBN 0852987889
6. Massey, Mechanics of Fluids, 6th Ed, Chapman and Hall 1989, ISBN 0412342804
7. Jorge Lucas, Edinburg University: Private Communication received by email. 31/3/2008

Appendix D: List of promising wave technologies



Courtesy of IT Power Ltd



Introduction



There are almost 1000 Wave technologies that have been conceived over the years [McCormick M, 1981], most of which haven't come to anything. Those in this list have been selected as being possible leaders in the field of wave energy conversion.



In most cases the technology has been selected due to the developers having proved their equipment at large scale. Others have been chosen because the author believes that the technology has good potential and / or the developers have a particularly competent consortium in place.


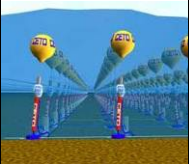
The 16 technologies are detailed below.



WAVE DEVELOPER/ DEVICE	Picture	Operating principle	Operating position	Description	PTO type	Rated power current kW	Rated power - target	TRL	Mass T	Mooring/ foundation type	Scale of current device	Next deployment scale	Company website
PWP/ Pelamis		Attenuator	Offshore	Several cylindrical sections linked by hinged joints, rotation is restrained by hydraulic rams. As sections heave and sway, hydraulic oil is pumped at high pressure via smoothing accumulators to hydraulic motors that drive electrical generators	Hydraulic	750	750	9	750	Catenary mooring system	Full	Full	www.pelamiswave.com
Wavegen/ Limpet		Oscillating water column	Shoreline	Inclined oscillating water column that couples with surge-dominated shoreline wave field. Design of the air chamber maximises capture of wave energy and conversion to pneumatic power. Wells turbines are matched to the air chamber to maximise power output. The blades are fixed, have no pitching mechanism or gearbox.	Pneumatic	500 per set of turbines	2000	7		Concrete structure set into shoreline	Full	Full	www.wavegen.com


WAVE DEVELOPER/ DEVICE	Picture	Operating principle	Operating position	Description	PTO type	Rated power current kW	Rated power - target	TRL	Mass T	Mooring/ foundation type	Scale of current device	Next deployment scale	Company website
OPT/ Powerbuoy		Point absorber	Offshore	Waves cause the PowerBuoy to oscillate, reacting against a submerged mass. The resultant motion is converted via a hydraulic power take-off to drive an electrical generator. OPT and Converteam are currently investigating linear generators. The system automatically locks-up and ceases power production in the event of very large oncoming waves.	Hydraulic	40-150	500	7		Concrete mooring with chain tethering device	Full	Full	www.oceanpowertec.com
Aqua-marine power/ Oyster		Oscillating surge absorber	Nearshore	Consists of a steel flap, fitted with double-acting water pistons, deployed in depths around 10m. Each wave activates the pump, which delivers high pressure water via a sub-sea pipeline to the shore. Onshore, high-pressure water is converted to electrical power using conventional hydro-electric generators. When deployed in multi-MW arrays, several near-shore pumps will feed a single onshore hydro-electric generator attached to a single manifold pipeline.	Hydraulic (onshore)	300-600	600	7		Fixed directly to seabed	Full	Full	www.aquamarinepower.com

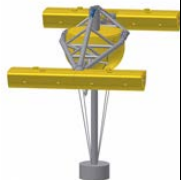
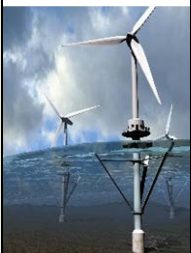
WAVE DEVELOPER/ DEVICE	Picture	Operating principle	Operating position	Description	PTO type	Rated power current kW	Rated power - target	TRL	Mass T	Mooring/ foundatio n type	Scale of current device	Next deploy- ment scale	Company website
Ocean Energy/ OE Buoy		Oscillating water column	Offshore	Device uses wave energy to compress air in a plenum chamber and pump it through an air turbine system. This isolates the power conversion system from the seawater and also provides a high-speed air flow to the turbine. The device is a floating system with the mouth of the OWC facing away from the wave direction.	Pneumatic	16	2000 per turbine pair	6	600	Slack mooring system	1/4	?	www.oceanenergy.ie
Oceanlinx/ OWC DAT		Oscillating water column	Offshore	Parabolic focusing wall used to focus waves onto the oscillating water column, and a two-way variable pitch blade air turbine. The generator, is designed so that the electrical control will vary the speed and torque characteristic of the generator load in real time to maximize the power transfer. An induction machine is used for the generator. The grid interconnection point and the control system are located in a weatherproof building external to the air duct.	Pneumatic	450	1000	7		Slack mooring system	Full	Full	http://www.oceanlinx.com/

WAVE DEVELOPER/ DEVICE	Picture	Operating principle	Operating position	Description	PTO type	Rated power current kW	Rated power - target	TRL	Mass T	Mooring/ foundation type	Scale of current device	Next deployment scale	Company website
Wave Dragon/ Wave Dragon		Overtopping device	Offshore	A floating, slack-moored, overtopper with two curved 'arms' focusing oncoming waves up a central ramp into a reservoir. At the bottom of the reservoir is a set of low-head hydro turbines, through which the collected water flows back out to sea. The reservoir has a smoothing effect and the turbines are coupled directly to variable speed generators. The concept is similar to a hydroelectric power plant.	Hydraulic	20	4000-7000	6		Slack mooring system	1/4	Full	www.wavedragon.net
Fred Olsen/ FO3		Point absorber	Offshore	The FO3, designed to be installed near shore, is a floating system that employs multiple point absorbers mounted on a large floating platform and placed in a grid to extract energy from the waves. Fred Olsen are investigating various hydraulic and other generator systems; current PTO uses timing belts to drive generators, no latching.	Timing belts drive generators	500?	1500	6		Slack mooring system	1/3	Full	http://www.fredolsen-renewables.com/

WAVE DEVELOPER/ DEVICE	Picture	Operating principle	Operating position	Description	PTO type	Rated power current kW	Rated power - target	TRL	Mass T	Mooring/ foundation type	Scale of current device	Next deployment scale	Company website
Wave Star Energy/ WavestarC5		Point absorber	Nearshore	The device is anchored perpendicular to the motion of the waves. On either side of the WaveStar there are several (20) hemispherical floats partially submerged in the water. Waves raise each float in turn which compresses a hydraulic cylinder, forcing fluid into the machine's common transmission system with a pressure of up to 200 bar. The pressure drives a hydraulic motor, which is connected to a generator.	Hydraulic	500	6000	6		Pile mounted into seabed	1/2	?	www.wavestarenergy.com
Carnegie/ CETO		Submerged pressure differential	Nearshore	Seabed-mounted device. It uses a submerged, buoyant, spherical actuator moving with the subsurface water in a cyclical and elliptical manner. This motion is used to pull the pump on the pressure stroke and allows the suction stroke to occur under gravity. Each actuator operates a single pump. The pumps take seawater from a seabed-mounted filter unit, high-pressure water is collected from an array of pumps and fed ashore via a pipe for extraction of energy and/or potable water.	Hydraulic (onshore)	200 (plus fresh water)	50,000 (array)	7		Seabed-mounted, bolted to a stationary concrete clump weight	Full	Full	http://www.carnegie-wave.com/ http://www.reh-plc.com/index.asp

WAVE DEVELOPER/ DEVICE	Picture	Operating principle	Operating position	Description	PTO type	Rated power current kW	Rated power - target	TRL	Mass T	Mooring/ foundation type	Scale of current device	Next deployment scale	Company website
Wave Bob/ Wave Bob		Point absorber	Offshore	Axisymmetric, self-reacting point absorber, primarily operating in the heave mode. Can be tuned to the incident wave action using a proprietary system to change the devices natural resonant frequency, without changing the floats draught. A digitally controlled power take off also allows the device to dynamically change the damping. Power take off is oil hydraulics using bio-degradable fluids. The WaveBob will typically carry three or four motor-alternator sets, all or some of which may be entrained, depending on incident wave energy.	Hydraulic	20	1300	6		Slack moored	?	?	www.wavebob.com
OWEL/ OWEL		Oscillating water column	Offshore	Floating wave energy platform that uses wave action to compress air in several horizontal ducts. The compressed air is then used to drive a unidirectional turbine.	Pneumatic	n/a	5000-12000	4		Slack moored	1/50	1/2	www.owel.co.uk

WAVE DEVELOPER/ DEVICE	Picture	Operating principle	Operating position	Description	PTO type	Rated power current kW	Rated power - target	TRL	Mass T	Mooring/ foundation type	Scale of current device	Next deployment scale	Company website
AWS/ AWSIII (Clam)		Oscillating water column	Offshore	Following "unsatisfactory" Portuguese test results, AWS began redesigning AWSIII, virtually from scratch. New design is based on the 30yr old Coventry Clam - an arrangement of 12 airbags mounted around a hollow circular spine. As waves impact on the structure, air is forced between the bags via the hollow spine which is equipped with self-rectifying turbines. AWS I and II were both submerged point absorbers.	Pneumatic	1000	2500	6		Slack moored	1/9	Full	www.aws-ocean.com
Checkmate Seaenergy/ Anaconda		Pressure differential	Offshore	Large water filled distensible rubber tube floating just beneath the ocean surface and oriented parallel to wave direction. Waves excite a bulge in the tube which travels just in front of the wave rather like a surf-board, picking up energy and increasing progressively in size. The bulge waves are then used to drive a turbine generator located at the stern of the device.	Hydraulic	n/a	1000	4		Slack moored	1/25	1/4	http://www.checkmateuk.com/seaenergy/

WAVE DEVELOPER/ DEVICE	Picture	Operating principle	Operating position	Description	PTO type	Rated power current kW	Rated power - target	TRL	Mass T	Mooring/ foundation type	Scale of current device	Next deployment scale	Company website
Green Ocean Energy/ Wave Treader		Attenuator	Offshore	Comprised of two pontoons at the fore and aft and a spar buoy in the centre. As waves pass along the device, first the fore pontoon lifts and falls, then the spar buoy, and then the aft pontoon, respectively. The relative motion is harvested by hydraulic cylinders that pump fluid hydraulic motors and an electric generator. Electricity is exported via a cable piggy-backed to the anchor cable. In order to weather-vane to the wave direction, it has active onboard adjustment to allow for offset due to the effects of current.	Hydraulic	33?	500	4		Single point mooring system.	1/12.5	Full	http://www.greenoceanenergy.com/
Ecofys/ Wave Rotor		Vertical axis turbine	Offshore	Wave Rotor is designed to capture energy from currents and waves. It utilises combined Darrieus and Wells rotors, which are mounted on the same vertical axle. These are respectively multi- and bi-directional rotors that can operate in multi directional currents. Water motions exert lift forces on the vertical and horizontal blades. Structures are fixed to the sea bed by monopile foundations.	?	30	500	5		Pile mounted into seabed	1/6	Full	http://www.ecofys.nl/expertisegebieden/product_systeemontwikkeling/waverotor.htm

The End!